Universidad Zaragoza

Ph.D. Thesis

Autonomic nervous system biomarkers from multi-modal and model-based signal processing in mental health and illness

Spyridon Kontaxis

Supervisors:

Prof. Raquel Bailón

Prof. Eduardo Gil

Ph.D. in Biomedical Engineering

December, 2020

Autonomic nervous system biomarkers from multi-modal and model-based signal processing in mental health and illness

Spyridon Kontaxis, 2020
Autonomic nervous system biomarkers from multi-modal and model-based signal processing in mental health and illness.

Date of current version: November 2, 2020

This Ph.D. thesis has been developed within the Department of Electronic Engineering and Communications and the Aragón Institute for Engineering Research (I3A) at the University of Zaragoza (Zaragoza, Spain).

The research presented in this thesis was supported by a personal grant to Spyridon Kontaxis by *Gobierno de Aragón* (Spain) and the projects *TIN2014-53567-R* and *RTI2018-097723-B-I00* from the *Ministerio de Economía y Competitividad* (Spain). It was also funded by *Gobierno de Aragón* (Spain) through the project *LMP44_18* and *Reference Group BSICoS (T39-17R and T39-20R)* cofunded by *FEDER 2014-2020 "Building Europe from Aragon"*, and by *CIBER in Bioengineering, Biomaterials & Nanomedicine (CIBER-BBN)* through *Instituto de Salud Carlos III*. The computation of some parts of this thesis was performed at the *High Performance Computing platform of the NANBIOSIS ICTS*, *CIBER-BBN* and *Aragón Institute of Engineering Research (I3A)*, Zaragoza, Spain.

This thesis was printed thanks to the financial support of BSICoS Group at University of Zaragoza.

Abstract

This dissertation is focused on multi-modal and model-based signal processing techniques for deriving physiological parameters, i.e. biomarkers, related to the autonomic nervous system (ANS). The development of novel approaches for deriving noninvasive ANS biomarkers in mental health and illness offers the possibility to improve the assessment of stress and the monitoring of depression. For this purpose, the present document is structured in three main parts. In Part I, an introduction to mental health and illness is provided (Ch. 1). Moreover, a theoretical framework for investigating the etiology of mental disorders and the role of stress in mental illness is presented (Ch. 2). The importance of noninvasive biomarkers for ANS assessment, paying particular attention in clinical depression, is also highlighted (Ch. 3, 4). In Part II, the methodological framework for deriving ANS biomarkers is provided. Signal processing techniques include the joint analysis of heart rate variability (HRV) and respiratory signals (Ch. 6), novel techniques for deriving the respiratory signal from electrocardiogram (ECG) (Ch. 7), and a robust photoplethysmogram (PPG) waveform analysis based on a model-based approach (Ch. 8). In Part III, ANS biomarkers are evaluated in stress assessment (Ch. 9) and in the monitoring of depression (Ch. 10).

Part I: Mental health is not only related to that positive state of well-being, in which an individual can cope with the normal stresses of life, but also to the absence of mental illness. Mental illness or disorder can be defined as an emotional, cognitive, or behavioural disturbance that causes substantial functional impairment in one or more major life activities. The most common mental disorders, which are often co-occurring, are anxiety and major depressive disorder (MDD). Mental illness has a negative impact on the quality of life, since it is associated with considerable losses in health and functioning, and increases significantly a person's risk for cardiovascular diseases. A common instigator underlying the co-morbidity between MDD, cardiovascular pathology, and anxiety is mental stress. Stress is common in our fast-paced society and strongly influences our mental health. In the short term, ANS controls the cardiovascular response to stressful stimuli. Regulation of physiological parameters, such as heart rate, respiratory rate, and blood pressure, allows the organism to respond to sudden changes in the environment. However, physiological adaptation to a regularly occurring environmental phenomenon alters biological systems involved in stress response. Neurobiological alterations in the brain can disrupt the function of the ANS. ANS dysfunction and structural brain changes have a negative impact on cognitive, emotional, and behavioral processes, thereby leading to development of mental illness.

Part II: The development of novel approaches for deriving noninvasive ANS biomarkers offers the possibility to improve the assessment of stress in healthy individuals and ANS dysfunction in MDD patients. Joint analysis of various biosignals (multi-modal approach) allows for the quantification of interactions among biological systems associated with ANS, while the modeling of biosignals and subsequent analysis of the model's parameters (model-based approach) allows for the robust quantification of changes in physiological mechanisms related to the ANS. A novel method, which takes into account both phase and frequency locking phenomena between respiration and HRV signals, for assessing quadratic nonlinear cardiorespiratory coupling is proposed in Ch. 6.3. Novel techniques for improving the monitoring of respiration are proposed in Ch. 7. In Ch. 8, to increase the robustness for some morphological measurements reflecting arterial tone changes, the modeling of the PPG pulse as a main wave superposed with several reflected waves is considered.

Part III: ANS biomarkers are evaluated in the assessment of different types of stress, either physiological or psychological, in healthy individuals, and then, in the monitoring of depression. In the presence of mental stress (Ch. 9.1), induced by cognitive tasks, healthy subjects show an increment in the respiratory rate and higher number of nonlinear interactions between respiration and HRV signal, which might be associated with a sympathetic activation, but also with a less regular breathing. In the presence of hemodynamic stress (Ch. 9.2), induced by a postural change, healthy subjects show a reduction in strength of the quadratic nonlinear cardiorespiratory coupling, which might be related to a vagal withdrawal. In the presence of heat stress (Ch. 9.3), induced by exposure to elevated environmental temperatures, healthy subjects show an increased sympathovagal balance. This demonstrates that ANS biomarkers are able to assess different types of stress and they can be further explored in the context of depression monitoring. In Ch. 10, differences in ANS function between MDD and healthy subjects during a mental stress protocol are assessed, not only with the raw values of ANS biomarkers but also with autonomic reactivity indices, which reflect the ability of an individual to cope with a challenging situation. Results show that depression is associated with autonomic imbalance, characterized by increased sympathetic activity and reduced arterial compliance. Autonomic reactivity indices quantified by changes, from stress to recovery, in arterial stiffness surrogates, such as the PPG amplitude loss in wave reflections, show the best performance in terms of correlation with depression severity, yielding to correlation coefficient $r = -0.5$. The negative correlation implies that a higher degree of depression is associated with a decreased autonomic reactivity. The discriminative power of ANS biomarkers is supported by their high diagnostic performance for classifying subjects as having MDD or not, yielding to accuracy of 80.0%. Therefore, it can be concluded that ANS biomarkers can be used for assessing stress and that impaired arterial compliance might constitute a biomarker of mental health useful in the monitoring of depression.

Resumen y conclusiones

Esta tesis se centra en técnicas de procesado multimodal y basado en modelos de señales para derivar parámetros fisiológicos, es decir, biomarcadores, relacionados con el sistema nervioso autónomo (ANS). El desarrollo de nuevos métodos para derivar biomarcadores de ANS no invasivos en la salud y la enfermedad mental ofrece la posibilidad de mejorar la evaluación del estrés y la monitorización de la depresión. Para este fin, el presente documento se estructura en tres partes principales. En la Parte I, se proporciona una introducción a la salud y la enfermedad mental (Cap. 1). Además, se presenta un marco teórico para investigar la etiología de los trastornos mentales y el papel del estrés en la enfermedad mental (Cap. 2). También se destaca la importancia de los biomarcadores no invasivos para la evaluación del ANS, prestando especial atención en la depresión clínica (Cap. 3, 4). En la Parte II, se proporciona el marco metodológico para derivar biomarcadores del ANS. Las técnicas de procesado de señales incluyen el análisis conjunto de la variabilidad del rítmo cardíaco (HRV) y la señal respiratoria (Cap. 6), técnicas novedosas para derivar la señal respiratoria del electrocardiograma (ECG) (Cap. 7) y un análisis robusto que se basa en modelar la forma de ondas del pulso del fotopletismograma (PPG) (Ch. 8). En la Parte III, los biomarcadores del ANS se evalúan en la quantificación del estrés (Cap. 9) y en la monitorización de la depresión (Ch. 10).

Parte I: La salud mental no solo está relacionada con ese estado positivo de bienestar, en el que un individuo puede enfrentar a las situaciones estresantes de la vida, sino también con la ausencia de enfermedad mental. La enfermedad o trastorno mental se puede definir como un trastorno emocional, cognitivo o conductual que causa un deterioro funcional sustancial en una o más actividades importantes de la vida. Los trastornos mentales más comunes, que muchas veces coexisten, son la ansiedad y el trastorno depresivo mayor (MDD). La enfermedad mental tiene un impacto negativo en la calidad de vida, ya que se asocia con pérdidas considerables en la salud y el funcionamiento, y aumenta significativamente el riesgo de una persona de padecer enfermedades cardiovasculares. Un instigador común que subyace a la comorbilidad entre el MDD, la patología cardiovascular y la ansiedad es el estrés mental. El estrés es común en nuestra vida de rítmo rapido e influye en nuestra salud mental. A corto plazo, ANS controla la respuesta cardiovascular a estímulos estresantes. La regulación de parámetros fisiológicos, como el rítmo cardíaco, la frecuencia respiratoria y la presión arterial, permite que el organismo responda a cambios repentinos en el entorno. Sin embargo, la adaptación fisiológica a un fenómeno ambiental que ocurre regularmente altera los sistemas biológicos involucrados en la respuesta al estrés. Las alteraciones neurobiológicas en el cerebro pueden alterar la

función del ANS. La disfunción del ANS y los cambios cerebrales estructurales tienen un impacto negativo en los procesos cognitivos, emocionales y conductuales, lo que conduce al desarrollo de una enfermedad mental.

Parte II: El desarrollo de métodos novedosos para derivar biomarcadores del ANS no invasivos ofrece la posibilidad de mejorar la evaluacón del estrés en individuos sanos y la disfunción del ANS en pacientes con MDD. El análisis conjunto de varias bioseñales (enfoque multimodal) permite la cuantificación de interacciones entre sistemas biológicos asociados con ANS, mientras que el modelado de bioseãles y el análisis posterior de los parámetros del modelo (enfoque basado en modelos) permite la cuantificación robusta de cambios en mecanismos fisiológicos relacionados con el ANS. Un método novedoso, que tiene en cuenta los fenómenos de acoplo de fase y frecuencia entre la respiración y las señales de HRV para evaluar el acoplo cardiorrespiratorio no lineal cuadrático se propone en el Cap. 6.3. En el Cap. 7 se proponen nuevas técnicas para mejorar la monitorización de la respiración. En el Cap. 8, para aumentar la robustez de algunas medidas morfológicas que reflejan cambios en el tonno arterial, se considera el modelado del pulso PPG como una onda principal superpuesta con varias ondas reflejadas.

Parte III: Los biomarcadores del ANS se evalúan en la cuantificación de diferentes tipos de estrés, ya sea fisiológico o psicológico, en individuos sanos, y luego, en la monitorización de la depresión. En presencia de estrés mental (Cap. 9.1), inducido por tareas cognitivas, los sujetos sanos muestran un incremento en la frecuencia respiratoria y un mayor número de interacciones no lineales entre la respiración y la seãl de HRV. Esto podría estar asociado con una activación simpática, pero también con una respiración menos regular. En presencia de estrés hemodinámico (Cap. 9.2), inducido por un cambio postural, los sujetos sanos muestran una reducción en el acoplo cardiorrespiratorio no lineal cuadrático, que podría estar relacionado con una retracción vagal. En presencia de estrés térmico (Cap. 9.3), inducido por la exposición a temperaturas ambientales elevadas, los sujetos sanos muestran un aumento del equilibrio simpatovagal. Esto demuestra que los biomarcadores ANS son capaces de evaluar diferentes tipos de estrés y pueden explorarse más en el contexto de la monitorización de la depresión. En el Cap. 10, se evalúan las diferencias en la función del ANS entre el MDD y los sujetos sanos durante un protocolo de estrés mental, no solo con los valores brutos de los biomarcadores del ANS, sino también con los índices de reactividad autónoma, que reflejan la capacidad de un individuo para afrontar con una situación desafiante. Los resultados muestran que la depresión se asocia con un desequilibrio autonómico, que se caracteriza por una mayor actividad simpática y una reducción de la distensibilidad arterial. Los índices de reactividad autónoma cuantificados por cambios, entre etapas de estrés y de recuperación, en los sustitutos de la rigidez arterial, como la pérdida de amplitud de PPG en las ondas reflejadas, muestran el mejor rendimiento en términos de correlación con el grado de la depresión, con un coeficiente de correlación $r = -0.5$. La correlación negativa implica que un mayor grado de depresión se asocia con una disminución de la reactividad autónoma. El poder discriminativo de los biomarcadores del ANS se aprecia también por su alto rendimiento diagnóstico para clasificar a los sujetos como MDD o sanos, con una precisión de 80.0%. Por lo tanto, se puede concluir que los biomarcadores del ANS pueden

usarse para evaluar el estrés y que la distensibilidad arterial deteriorada podría constituir un biomarcador de salud mental útil en el seguimiento de la depresión.

Acknowledgments

Once jamón a time ... a journey full of funny moments started for me in Spain. A needlework, in which small pieces of good and bad memories have sewn together for more than 5 years, is finally ready. The reference exclusively to funny moments is because a "strange" sense of humor and a bit of self-sarcasm can convert bad memories to the funniest stories to talk about. But what is more important, the stories, the process that generated them, often called Ph.D., or the audience of these stories? Without any doubt, the last one! Hence, below I dedicate few words to my friends.

I could not start without mentioning the person who fought at my side for solving problems from the very first moment. Raquel, I want to thank you for a lot of things but the most important are letting me be myself, trusting me, and being a calming force when I needed you. Edu, you are the second example of having a supervisor who becomes a friend. Thank you for extending our excellent collaboration from the university to football fields. Pablo, although your name does not appear in the first page, for me you are my third supervisor. Thank you for all the discussions, known as intellectual boxing in our case, and learning. If it is true that hard times reveal good friends, then our friendship is guaranteed. I would like also to dedicate some words to Leif and Vaidotas with whom I had the opportunity to collaborate systematically the last years. Leif, I am grateful for all you have taught me, and I am very happy that I have met the most Mediterranean Swedish man. Vaidotas, I really appreciate your help when I was in Lithuania, and I hope we will continue our fruitful collaboration. I really appreciate the effort that all of you have put into this thesis.

The last years I realized that I have two families, one in Greece and another one in Spain. The family is not always blood, it is also that group of people who supports you in difficult situations and helps you until you can stand on your own feet. I will never forget my first labmates, Sanjuan, one of the smartest and most active guys I have ever met, Mimma, the Italian goddess of wine and espresso, and Jesus, one of the best teachers who accelerated my progress during the first years. You make me feel like my home; Jesus maybe literally. Another person who made me feel like a specific place of my home, the sofa, is you David. Chatting, chilling out, eating Greek gyro (neither here-o, nor yai-ro), and playing biased Catan (Jorge I can understand) are few of the things that I can tell about you. I forgot it! Family also teaches you the language when you are child. I can tell you that I have been classified repeatedly as such based on height criteria. David you were also one of my good teachers. I would not say that I had bad teachers, but big brothers who wanted to teach me "useful" phrases. I am speaking about the freaky triad

Juan, Carlos, and Alex, and our morning coffee meetings. But I cannot remember your laughters because Arantxa was there as well. I cannot dedicate the pages you deserve for describing our relationship because the printing of the thesis is expensive and I have to save money in case I skip Greek military services. I can simply say that you are the administrative of my life.

As they say, it's like a dream job to work with your friends. I am blessed because I worked and I am still working with you, Javi and Arma. Friendship is built on respect and trust, but when there is also kindness and selflessness, this is a relationship between brothers. I hope that our professional and personal life will have a lot of common points in the future; Greece has plenty of ruins to visit! I want to thank all former and actual members of L.3.07 including Cris, Sonia, Diego, Saul, and my RADAR savior, Estela. Many thanks to my Italian friends, Alba (ovviamente), Chiara, Jeni, Luca, Flavio, Max, Giorgio, and Tanja. Tanja, for sure you belong to the Italian rather than the German section, in which, Carmen is now the president. Not to forget, Carmen, and of course Jorge Mario, you will be the admins of my online repository, in which all the novel spanish words, such as papelear, manifiestación, etc, are stored. My thanks list can be extended a lot if I take into consideration the bar owners in Magdalena and the members and visitors of BSICoS group who joined that sect called "juepincho". I want to declare that it was not created by me, as many think, but I am a true believer. Special thanks to COVID-19 that allowed me to finish in time my Ph.D. by minimizing the distractions and my social life during the last months.

I hope one day Greek researchers will be the majority in the group and then you will be obligated to rename it "BS-OIKOS". I am not sure if your Greek sample is representative because Kostas is my twin brother. Kostaki, I believe in you and I am sure with your hard working you will turn your dreams into reality. If not a billionaire at least a millionaire. In a difficult period of my life, I had the fortune to fill a big emotional void with your craziness. I think Mood is karmic.

The following lines are not large mathematical equations, but simply few words for my family. Δεν ξέρω αν πίσω από έναν πετυχημένο άντρα κρύβεται πάντα μια γυναίκα αλλά η οικογένεια σίγουρα. Λαμπράκη, Τζόνη δεν θα είχα φτάσει εδώ που είμαι χωρίς την στήριξή σας. Το ξέρω οτι για σας ήταν αυτονόητο αλλά δεν είναι πάντα εύκολο να δείχνεις κατανόηση σε επιλογές και καταστάσεις που καταλήγουν να είναι δύσκολες για το παιδί σου. Μπίλια μου τώρα για σένα ότι και να πώ θα είναι λίγο. Σε ευχαριστώ μέσα από την καρδιά μου για όλα αυτά τα χρόνια που είσαι δίπλα μου, όχι σαν αδερφός μου, αλλά σαν ο καλύτερος μου φίλος. Αυτό το διδακτορικό είναι και δικό σας.

Σπύρος

"If you are depressed you are living in the past.
If you are anxious you are living in the future.
If you are at peace you are living in the present."

- Lao Tzu

Contents

Part I

Introduction

1

Mental health and illness

1.1 Motivation

Mental health is a level of psychological well-being that is defined in terms of happiness and life satisfaction based on the hedonic approach, or meaningful functioning and self-actualization according to Aristotle's eudaimonic approach. World Health Organism (WHO) describes mental health as that state of well-being, in which an individual realizes his or her own abilities, can cope with the normal stresses of life, can work productively and is able to make a contribution to his or her community [244]. Mental health is not only related to positive states of well-being, but also to the absence of mental illness.

Mental illness is a diagnosable health condition, and is distinct from feelings of sadness, stress or fear that anyone can experience from time to time in their lives. Concretely, it can be defined as an emotional, cognitive, or behavioral disturbance that causes substantial functional impairment in one or more major life activities [244]. A mental illness, due to the associated distress and disability, is also known as a mental disorder. Examples of mental disorders include neurodevelopmental, psychotic, bipolar, depres-

sive, and anxiety disorders. The estimated prevalence of mental disorders, without the inclusion of neurodevelopmental disorders, is 12% of the entire population. The most common mental disorders are depression and anxiety, which cause economy loses about US$ 1 trillion per year in productivity [244]. Depression is the single largest contributor to the non-fatal disease burden and the third largest contributor to the overall disease burden [159]. Depression is also the major contributor to suicide deaths and increases significantly a person's risk for cardiovascular diseases. Moreover, more than 40% of all depressed patients suffer from co-occurring anxiety [112]. A common instigator underlying the co-morbidity between depression, cardiovascular pathology, and anxiety is mental stress [132].

Mental stress is common in our fast-paced society and strongly influences our psychological and physical well-being. Humans exposed to common aversive or stressful experiences exhibit a wide range of physiological and/or psychological responses that can either be adaptive or damaging to the individual. In the short term, the physiological response to acute stress is achieved by changes in the autonomic nervous system (ANS). ANS controls the cardiovascular response that regulates physiological parameters such as heart rate, respiratory rate, and blood pressure. The variation in ANS activity during stressful experiences, which is known as autonomic reactivity, is particularly important for adaptive stress responses, since reflects the ability of an individual to cope with stress. Maladaptive responses may lead to neurobiological alterations in the brain that disrupt the function of ANS. ANS dysfunction and structural brain changes have a negative impact on cognitive, emotional, and behavioral processes, thereby leading to development of mental disorders.

While screening tools used in clinical practice, such as questionnaires, have considerable value, sometimes they are time-consuming and require the willingness of the patients to communicate their symptoms. Screening tools based on noninvasive ANS biomarkers could complement existing psychometric scales for improved accuracy in the assessment and monitoring of depression. The noninvasive assessment of ANS function in mental health and illness constitutes the core of the present dissertation. Physiological parameters, i.e. biomarkers, related to ANS can be derived from multi-modal and model-based signal processing of diverse biosignals, such as electrocardiogram (ECG), photoplethysmogram (PPG), or respiratory signal. Joint analysis of various biosignals (multi-modal approach) allows for the quantification of interactions among biological systems associated with ANS, while the modeling of biosignals and subsequent analysis of the model's parameters (model-based approach) allows for the robust quantification of changes in physiological mechanisms related to the ANS. The development of novel approaches for deriving noninvasive ANS biomarkers offers the possibility to improve the assessment of stress in healthy individuals and ANS dysfunction in depressed individuals. Furthermore, the capacity of adaptation to mental stress quantified by changes in ANS biomarkers (autonomic reactivity) can aid for the monitoring and progression of depression. Wearable devices and smartphones are able to capture or track biometric information, such as heart rate and respiratory rate mainly derived from ECG or PPG

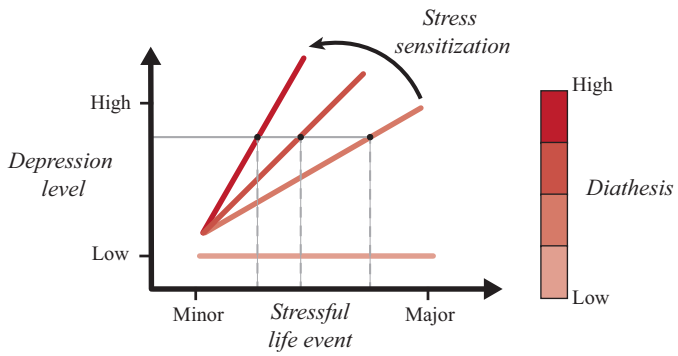

Figure 1.1: Stress-diathesis model of depression. The continuous effect of the diathesis is influenced by the stress sensitization process. Reproduced and modified from [156]

signals, related to health or fitness, offering the possibility to perform a more frequent and massive screening as well as a continuous monitoring of stress and depression level.

1.2 Stress-diathesis model

The stress-diathesis model is a psychological theory that provides a framework for investigating the etiology of various mental disorders [235, 344]. The term diathesis derives from the ancient Greek term ($\delta\iota\acute{\alpha}\theta\epsilon\sigma\iota\varsigma$) for predisposition, yet it can be hereditary or acquired. While not necessarily being the cause of a psychiatric disorder, stress in combination with diathesis contribute to several mental disorders, particularly depression.

A very minimal level of diathesis may be insufficient to produce the disorder even under the most stressful experiences, the often called stressful life events [156]. However, as the predisposition to depressive mood, i.e., diathesis, increases a patient becomes psychologically more vulnerable. Thus, the severity of the life event needed to precipitate an episode of depression decreases [349]. There is also a continuous effect of the diathesis. The likelihood of the diathesis developing, once a minimum threshold is passed, increases as the individual become less resistant to stress through a process called stress sensitization [26,156]. Figure 1.1 shows the stress-diathesis model of depression with the continuous effect of the diathesis.

1.2.1 Stressful life events

Stressful life events have been reported as precipitants for a depressive episode. Life events associated with the onset of depression are mainly external episodes, such as loss events, rather than internal episodes, such as a hormonal challenge or brain injury [349]. Life events are classified in the literature based on their severity, duration and timing in the life course [104]. Major life events either during childhood, including separation

from parents, sexual abuse, and substance abuse among family members [141, 155, 222], or recent occurrences of divorce and loss events [179,180] are the most potent risk factors that predispose an individual to develop depression.

Although, most research has focused on major life events, recent studies attempt to shed light on the role of daily negative life experiences in predicting depression. Long-term difficulties such as poor working conditions and financial difficulties are predictors of depression onsets and temporal changes in depression severity [44, 139, 213, 324]. On the contrary, acute episodic stressors, i.e., life events that have a beginning and ending, are more strongly associated with first episodes of depression than with depression recurrences [44, 138].

1.2.2 Diathesis and its variants

The association between major life events and onsets of depression is not always straightforward [179]. For instance, the specificity of interpersonal loss experiences as predictor of depression is determined partially by the vulnerability of the individual who may interpret the loss experience as highly significant, potentially triggering depression [138]. Depressive symptoms can be understood as the consequence of stressful life events interacting with various types of diathesis including genetic vulnerability (inherited or acquired) and cognitive vulnerability (personality) [106].

Gene-environment interactions during development may lead to changes in the expression of genes in the brain implicated in stress and emotional responses [5, 54]. Epigenetic modifications increase the risk for abnormal brain development, which is associated with behavioral and cognitive changes [177]. Maternal prenatal symptoms of depression and anxiety have been associated with altered neurodevelopmental outcomes in the child [34, 186]. These effects may be mediated in part by altered placental function [36, 120]. Adversity during childhood, including parental stress, low socioeconomic status and abuse, is associated with higher predisposition to depression [37, 204]. However, not all children are affected in the same way and most are not affected at all, since epigenetic modifications are thought to be influenced also by personality and genetics, i.e., inherited from parents [119, 314].

Depression is also consider to be the product of interaction between an individual's cognitive vulnerability and certain environmental conditions that serve to trigger this diathesis into operation [156]. Beck's Cognitive Theory, which is considered a breakthrough in cognitive research, states that depression-prone individuals possess negative self-beliefs, called schemas, which involve depressogenic beliefs about the self, world, and future [23]. Cognitive vulnerability influences how the person perceives information regarding a situation. Individuals have a tendency to filter stimuli from the environment such that their attention is directed toward information that is congruent with their schemas, thereby increasing the risk for depressive mood [123, 320].

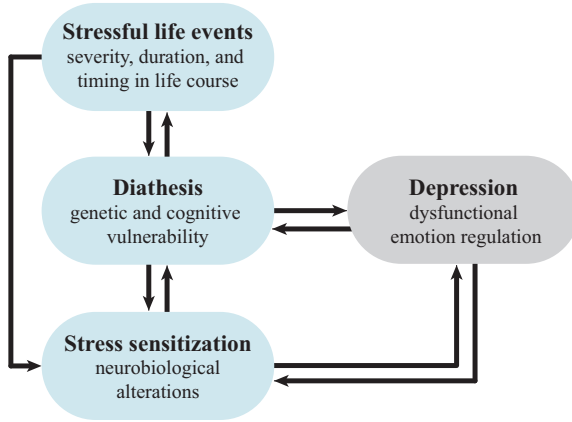

Figure 1.2: Interactions in the stress-diathesis model of depression. Environmental factors (stressful life events) interact with genetic and personality factors (diathesis) to cause reciprocally interactive neurobiological alterations (stress sensitization), which in turn lead to dysfunctional emotion regulation underlying depression.

1.2.3 Stress sensitization

The stress sensitization hypothesis posits that individuals become less resistant to stress due to neurobiological alterations in biological systems that mediate the stress response [267]. Thus, the severity of stressful events needed to trigger depression onsets in stress-sensitized individuals becomes increasingly lower with successive episodes of depression [138, 313]. The pathophysiological disturbances of stress sensitization process impair also the cognitive-affective responses resulting to dysfunctional emotion regulation in depressed individuals [349]. Emotion regulation difficulties and genetic vulnerability in former depressed individuals may continue even while they are in euthimic mood due to the ongoing process of stress sensitization [40, 268, 340].

There is growing interest in moving away from the causal relationship between stress and depression toward a bidirectional association since dysfunctional emotion regulation underlying depression further contributes to stress sensitization [138, 234]. Moreover, diathesis not only interacts with the process of stress sensitization, but also influences the likelihood of stress occurring [90]. Individuals prone to depression have an increase susceptibility to generate interpersonal stressful events [137, 211]. The generation of dependent life stresses may potentially have a role in the maintenance of current depression or increase in the likelihood of subsequent depression onset and recurrence [211,289,320].

Consequently, the effects of either stress or depression are conditional upon the other [234]. Different models have been proposed to describe their association in an attempt to explain the mechanisms behind the predisposition to depression and the progress of the illness [26, 80]. Figure 1.2 illustrates the interacting components in the stress-diathesis model of depression. An understanding of the process, during which individuals become less resistant to stress, and how dysfunctional emotion regulation contributes to this process, are important for the prevention, diagnosis, and treatment of depression.

2

Pathophysiology of stress

2.1 Stress response

The most generic definition of stress is that of, the often called “Father of stress”, Hans Selye: “Stress is the nonspecific response of the body to any demand”. Stress can be viewed as a process with psychological and physiological components that occurs when environmental demands exceed one’s perception of the ability to cope [104].

The acute physiological reaction that occurs in response to a perceived threat, including microbial (infection), physiological (tissue damage), or social (job strain), is known as the "fight-or-flight" response [157]. This involves the integration between outputs of various biological systems, such as the nervous, endocrine, and immune system among others. These systems are working together in an attempt to provide enough energy and beneficial immune responsiveness in order to ensure survival. Once the threat has passed the body returns to "rest and digest" mode restoring homeostasis.

2.1.1 Central nervous system

The nervous system is composed of the central nervous system (CNS) and the peripheral nervous system. CNS consists primarily of the brain and the spinal cord. Spinal cord conducts signals from the periphery of the body to the brain and from the brain to the periphery using the sensory (afferent) and the motor (efferent) neurons of the peripheral nervous system, respectively [163].

One of the most important areas of the brain is the limbic system which is involved in various processes relating to emotion, behavior, memory, attention, and learning. The limbic system is a set of brain structures located on both sides of the thalamus, which acts as a linkage between incoming pathways from the periphery to the cerebral hemispheres. Under the thalamus and at the center for the limbic system is located the hypothalamus, which links the nervous system with the endocrine system via the pituitary gland. The limbic system is also tightly connected to the prefrontal cortex. Both prefrontal cortical and limbic regions, including the amygdala and hippocampus, are important in detecting or recognizing if something in the environment is a stressor [220].

2.1.2 Autonomic nervous system

Autonomic nervous system (ANS) is a division of the peripheral nervous system that controls involuntary responses, such as heart rate (HR), respiration, blood pressure (BP), body temperature, and digestion among others. ANS regulates body's internal environment maintaining the homeostasis via three branches: the sympathetic nervous system (SNS), which is primary mechanism in control of the "fight-or-flight" response, the parasympathetic nervous system (PNS), which is involved in rest and recuperation, and the enteric nervous system, which controls the smooth muscle function of the gut [163].

Autonomic nerves travel to effector organs throughout a sequential two-neuron pathway. The first neuron is called the preganglionic neuron, and the second is the postganglionic neuron. These neurons synapse together in the autonomic ganglia. The exception to this is the adrenal medulla of the endocrine glands called adrenal (or suprarenal) glands. The adrenal medulla is connected directly to the preganglionic neuron [229]. Preganglionic sympathetic neurons are located in the spinal cord, whilst preganglionic parasympathetic neurons lie in the brainstem and in the lower region of the spinal cord. The ganglia of the sympathetic branch are located close to the spinal cord (sympathetic chain), while the ganglia of the parasympathetic branch are located close to the target organ [133]. Figure 2.1 shows the general organization of the sympathetic and parasympathetic branch of ANS. As can be seen, SNS, in contrast with PNS, innervate tissues in almost every organ system.

The effector cells and organs of the sympathetic postganglionic neurons are smooth musculature of all organs (blood vessels, lungs), lymphatic tissues (thymus, spleen, lymph nodes), liver cells, gastrointestinal tract, the heart, and glands such as the sweat gland and,

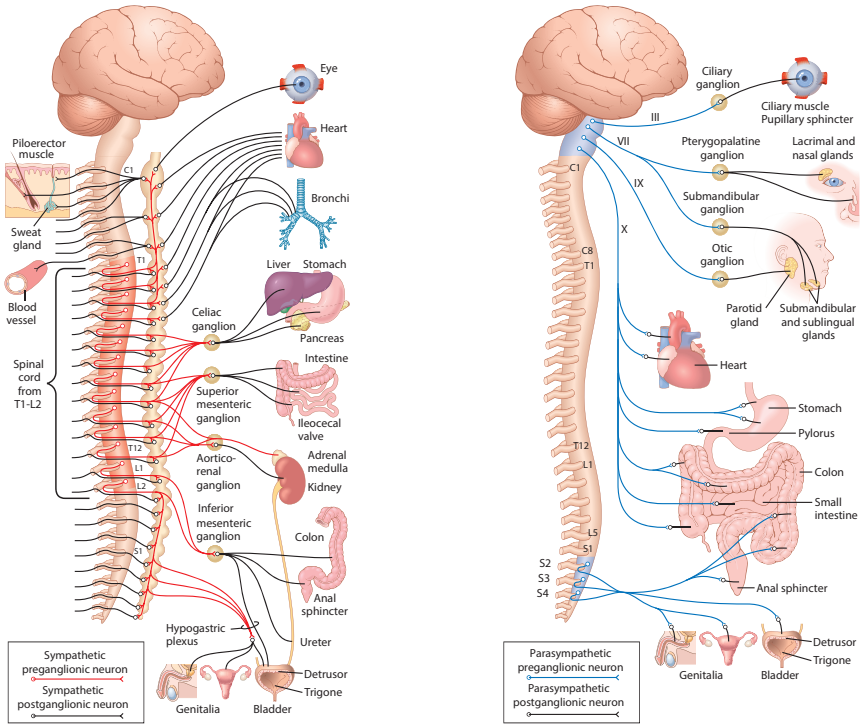

Figure 2.1: Organization of the autonomic nervous system (ANS). The sympathetic (left) and the parasympathetic (right) branch of ANS. Reproduced and modified from [133]

most importantly, the adrenal medulla [163]. Thus, the activation of the SNS enhances the heart activity, through increases in HR and the force of contraction, as well as the respiratory activity, through bronchodilation and increments in the respiratory rate, in order to provide greater amount of oxygenated blood where is needed [133]. Furthermore, the adrenal medulla releases catecholamines, such as adrenaline and noradrenaline (NA), directly into the blood, thereby spreading the effects of sympathetic activation [241].

However, the specific response of the effector organ is dependent on the types of receptors present. The sympathetic postganglionic neurons are adrenergic since use as neurotransmitter NA to activate their adrenoreceptors (ARs), α and/or β, in the target. Sympathetic stimulation of an α-AR results in vasoconstriction which increases BP, while stimulation of a β-AR receptor results in vasodilation [133]. NA binds preferentially to α-ARs, only binding to β-ARs at high concentrations [265]. For instance, to achieve a more efficient blood flow towards the skeletal muscles, blood is diverted away from the skin. This can be accomplished by constricting the blood vessels in the periphery, and dilating the blood vessels of the muscles and the coronary vessels of the heart [133].

Some effector organs will have only one type of the receptors while others a mixture of more than one. For instance, the heart, besides sympathetic, has also parasympathetic innervations. The parasympathetic postganglionic neurons, as well as all the pregan-

glionic neurons, are cholinergic because release acetylcholine molecules as neurotransmitter and typically have the opposite effects of adrenergic neurons [229]. Sympathetic tone elevates the HR while HR decreases with the activation of the vagus nerve (VN), which is the main nerve of the parasympathetic division of the ANS. Thus, the net effect on HR depends on the autonomic balance, which often called sympathovagal balance, which is the relative balance between SNS and PNS activity.

2.1.3 Hypothalamic–pituitary–adrenal axis

The hypothalamic–pituitary–adrenal (HPA) axis together with SNS are the two major stress axes. The activation of these axes provide enough energy via mobilization of energy-rich fuels, such as glucose, amino acids, and lipids. After the enhanced secretion of catecholamines from the SNS, which is faster and occurs first, the HPA axis is activated within seconds [265].

First, the hypothalamus receives information about the context of the stressful stimulus by the amygdala and hippocampus. Then, the hypothalamus releases corticotropin-releasing hormone (CRH) in the anterior pituitary lobe of the pituitary gland, which, subsequently, releases adrenocorticotropic hormone (ACTH) into the systemic circulation. The secretion of ACTH stimulates the adrenal cortex to produce large quantities of glucocorticoids (GCs), especially cortisol. Cortisol stimulates the release of stored energy by various metabolic functions such as hepatic glycogenolysis, lipolysis and protein degradation [241].

There is a close interaction between SNS and HPA axis. The CRH molecules in the brain serve as a neurotransmitter that enhance sympathetic arousal [284]. Although adrenocortical secretion of cortisol is primarily under the influence of ACTH, the adrenal cortex also receives innervation from the SNS. For instance, the adrenal cortical sensitivity to ACTH changes as function of the circadian rhythm [279]. Furthermore, NA-stimulated glycogenolysis is facilitated by GCs [241], providing an important link between the two stress axes.

In addition to facilitating energy mobilization, cortisol returns to the brain to inhibit the stress response. Brain regions are rich in two types of corticosteroid receptors, the mineralocorticoid receptors (MRs) and glucocorticoid receptors (GRs) [284]. At low concentrations, cortisol bind to MRs enhancing excitability, while, at higher concentrations, binds mostly to GRs in the hippocampus and in the cells of the anterior pituitary gland, thereby inhibiting the synthesis and the secretion of CRH and ACTH. This cortisol-mediated feedback inhibition prevents the HPA axis from overshooting [301].

2.1.4 Immune system

The immune system is critical for human health and well-being. Modulation of the immune response by the CNS is mediated by the ANS and the HPA axis, since almost all

immune cells have receptors for one or more of the hormones that are associated with them [118].

Sympathetic influence on immune response can be direct, via adrenoceptors on immune cells, or indirect, through innervation of major immune organs, such as the bone marrow, spleen and lymph nodes, thereby regulating the distribution of immune cells in the body [351]. Immune cells, like macrophages, produce a type of proteins, called cytokines, that mediate and regulate immunity and inflammation. Cytokines that enhance inflammation are referred to as pro-inflammatory, whereas those that down-regulate inflammation are called anti-inflammatory. Pro-inflammatory cytokines are redistributed to screen for pathogens in a process called immunosurveillance and they can recruit other immune cells to the site of inflammatory activity (injury or infection) [300].

Furthermore, pro-inflammatory cytokines, which can be seen as the peripheral immune signals, are pivotal in the communication from immune system to CNS [265]. Cytokines can enter the brain through the blood-brain barrier or can be produced by activated macrophages recruited to the brain [142]. Signalling of brain regions, such as the hypothalamus, is also conducted via activation of related to cytokine receptors in the afferent vagus nerve [219, 258]. Activation of the HPA axis inhibits, via GCs, the efficacy of cytokines and other mediators that promote immune and inflammatory reactions [284, 309]. This glucocorticoid-mediated negative feedback response from the CNS works in favour of more immediate physiological survival needs by suppressing immune system [157].

2.2 Stress sensitization

Homeostasis not only allows the organism to respond to sudden changes in the environment ("reactive homeostasis"), but also initiates the appropriate corrective responses prior to a regularly occurring environmental phenomenon ("predictive homeostasis"). For example, increased gastrointestinal secretion precedes the usual lunch time, thereby anticipating the changes in the content of the digestive tract. Increased plasma cortisol concentration that precedes waking anticipates the energy demands of a changing posture [50]. Predictive homeostasis facilitates physiological adaptation to a regularly occurring environmental phenomenon, such as frequent social threats. However, this alters biological systems involved in stress response, leading to stress sensitization.

Structural changes in the brain owing to reduced neurogenesis, autonomic imbalance due to increased SNS activity, as well as alterations in the cortisol-cytokine dynamics due to the impaired feedback regulation of the HPA axis and low-grade inflammation, disrupt the communication between the biological systems required to maintain homeostasis (see Fig. 2.2) [265, 351]. These neurobiological alterations affect, on the one hand, the cardiovascular system, thereby increasing the risk of developing cardiovascular diseases (CVDs) in patients with depression, and, other hand, the behavioral, cognitive and

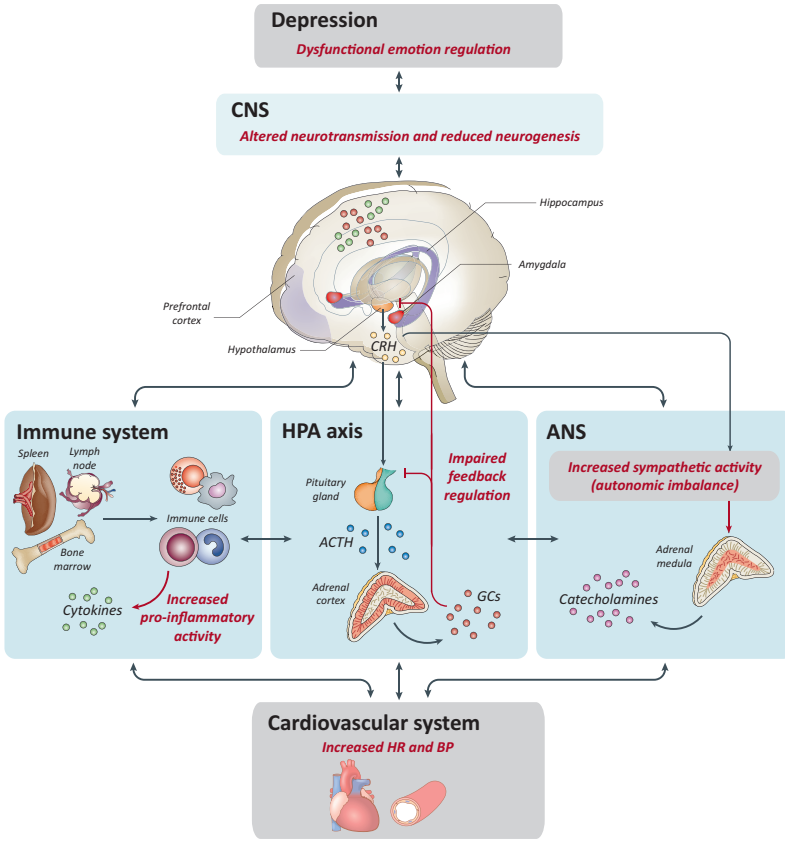

Figure 2.2: Pathophysiology of stress. Alterations in the biological systems involved in stress response, i.e., central nervous system (CNS), autonomic nervous system (ANS), hypothalamic–pituitary–adrenal (HPA) axis, immune system, increase the risk for developing depression and cardiovascular diseases. CRH, corticotropin-releasing hormone; ACTH, adrenocorticotropic hormone; GCs, glucocorticoids. Reproduced and adapted from [252, 309]

emotional responses, which are associated with the psychological symptoms of depression [204, 259].

Altered neurotransmission

A major hypothesis for the pathophysiology of depression, the monoamine hypothesis, posits that depression is caused by an alteration in levels of one or more of the monoamine neurotransmitters, including not only NA, but also serotonin, and dopamine [87]. Serotonin and dopamine play a major role in the feelings of happiness and reward-motivated behavior, respectively. Both of them inhibit the release of NA from adrenergic nerves in blood vessels. Furthermore, serotonin inhibits the secretion of CRH in the hypothalamus and ACTH in the pituitary gland [164].

An alteration in the synthesis, metabolism, or transport in one of these neurotransmitters likely effects the function of the other two, since they are interrelated and effect each other's concentrations in the brain [80]. Monoamine hypothesis posits that depression is associated with decrease levels of serotonin in the brain due to an overactive enzyme, called monoamine oxidase (MAO), which metabolizes monoamines [87]. Other mechanisms involved in alterations of these neurotransmitters are the pro-inflammatory cytokines produced by the SNS. Pro-inflammatory cytokines in low concentration, for instance during exercise, could enhance the dopaminergic neurotransmission [61, 208]. However, a high concentration of pro-inflammatory cytokines in the brain could upregulate the activity of enzymes that induce serotonin depletion, and suppress dopaminergic neurotransmission, thereby enhancing depressive mood [242].

Glucocorticoid resistance

Stress increases local cerebral glucose utilization within seconds, an effect mediated by SNS. Lower levels of GCs at the onset of a stressor enhance hippocampal excitability, memory formation, and synaptic plasticity via the MRs. Rise in GC concentrations has the opposite effects and suppresses the cognitive response via the GRs [284].

In situations, where the organism deals with frequent threats, the requirements for metabolic energy increase. This can be accomplished by reducing the function or expression of the GRs in the brain, a phenomenon called glucocorticoid resistance. The GR resistance to cortisol decreases the inhibitory feedback on the HPA axis [183]. Cortisol provides the organism with the metabolic energy it needs to respond to threats, while elevations in pro-inflammatory cytokines limit infection if an injury occurs. However, GCs have an anti-inflammatory effect. Thus, the immune cells become less sensitive to allow the concurrent increase in the concentration of pro-inflammatory cytokines and cortisol [300].

Reduced neurogenesis

Several limbic and cortical circuits in the brain undergo structural changes due to elevated levels of glucocorticoids and pro-inflammatory cytokines [26]. Brain function is affected at a cellular level, primarily by disrupting neuroplasticity and, accordingly, neurogenesis — the process by which new neurons are generated [252]. Structural and functional brain alterations trigger behavioral, affective, and cognitive changes that play a critical role in the onset, maintenance, and recurrence of depression [219].

2.3 Dysfunctional emotion regulation

Stressful events typically elicit significant emotional responses [68]. Emotion regulation is the capacity to influence the occurrence, duration, magnitude, and expression of an

emotional response [171]. Thus, emotional regulation has been considered as a mediator of stress adjustment. It consists in a complex process that lead to changes in behavioral (verbal and/or facial expressions) and physiological (sympathetic activation) response systems, but, prior to this, the interpretation of the stimulus is required [68].

The appraisal of the situation can be accomplished using either adaptive or maladaptive emotional regulation strategies. Distraction and reappraisal are adaptive strategies that help the individual to avoid the emotional response by reformulating the emotional significance of the situation. Maladaptive strategies include expressive suppression and rumination, which are associated with inhibition of the outward signs of the emotional response and repetitive thinking, respectively [171].

Depression is associated with reduced ability to use adaptive strategies, which require greater levels of cognitive control [171]. Hippocampal shrinkage and smaller volumes in several frontal regions are associated with a reduced cognitive function in patients with depression [29, 164, 351]. Decreased level of hippocampal inhibition of HPA axis activity increases the hormonal stimulation of the amygdala and dampened activity in prefrontal regions reduces the inhibitory control over the amygdala [306,349]. Dominance of lymbic over prefrontal function, due to heightened activation of the amygdala, increase attentional resources to emotionally events [24, 252]. Negative interpretations of emotional experiences in depressed individuals are associated with abnormally increased connectivity between the amygdala and the hippocampus when encoding negative material [30]. Deficits in cognitive inhibition of the prolonged processing of negative material in the working memory affect the long-term memory [169]. Consequently, memory sensitivity to negative affective stimuli is increased [30].

Difficulties in inhibiting the processing of negative material, less use of reappraisal, more use of rumination, and greater expressive suppression are related to higher levels of depressive symptoms [170]. Maladaptive strategies are less effective comparing to adaptive ones and increase physiological arousal [92]. This highlights the fact that dysfunctional emotion regulation mediates the role between depression and further changes in the cardiovascular system [68].

3

Major depressive disorder

Major depressive disorder (MDD), or clinical depression, is a debilitating mood disorder that is characterized by the presence of sad mood accompanied by somatic and cognitive changes that significantly affect the individual's capacity to function. Mood disorders are separated into depressive disorders, with MDD being the most common one, and bipolar related disorders. Depressive symptoms are common in MDD and bipolar disorders, but the latter are also characterized by episodes of abnormally elevated mood, associated with psychosis, which is called mania. Depression without mania, i.e., MDD, is sometimes referred to as unipolar because the mood remains at one emotional state or "pole", i.e., depressed mood [12].

3.1 Course and burden of disease

Based on the the latest set of Global Health Estimates made available by World Health Organization (WHO) in 2015, over 300 million people are estimated to suffer from depression, equivalent to 4.4% of the world's population [244]. Across the lifespan, women are about twice as likely as are men to develop depression [191].

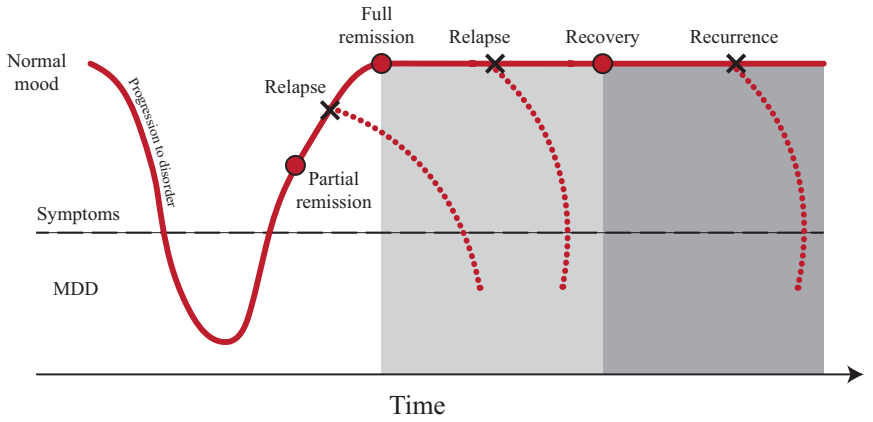

Figure 3.1: Time course of major depressive disorder (MDD). The time occurrence of remission, relapse, recovery, and recurrence. Adapted and reproduced from [192].

The course of MDD is quite variable among patients. The most probable period for the onset of the first depressive episode extends from mid-adolescence to mid-40s and about 40% of these episodes occur before the second decade of life [215]. The resolution of depressive symptoms following an episode is called full remission and it can be either spontaneous or it follows the period of partial remission (2-8 weeks), in which an improvement of sufficient magnitude is observed, but the individual continues to evidence more than minimal symptoms [35]. The end of the depressive episode, where recovery starts, requires an extended period of full remission [273]. Recovery typically begins within 3 months of onset for two in five MDD patients and within 1 year for four in five MDD patients [12]. An early return of symptoms, meeting full syndrome criteria that occurs during the period of remission is called relapse, while a new episode during recovery is referred to as recurrence [273]. Almost 80% of patients with MDD experience at least one further episode in their lifetime [252]. The risk of recurrence is higher in individuals who have experienced multiple episodes and it becomes progessively lower over time as the duration of remission increases [12]. Figure 3.1 illustrates the time course of MDD.

Depressive disorders are associated with considerable losses in health and functioning. MDD is ranked as the single largest contributor to non-fatal health loss [244]. Depression increases the risk of CVDs, such as congestive heart failure [113] and hypertension [105], diabetes mellitus [63], obesity [212], metabolic syndrome [255], cancer [166], respiratory diseases, such as chronic obstructive pulmonary disease [14] and asthma [108], and neurodegenerative diseases, including Alzheimer's and Parkinson's disease [107]. Mental disorders with which MDD frequently co-occurs are, substance use disorders, eating disorders, including anorexia nervosa and bulimia nervosa, obsessive-compulsive disorder, borderline personality disorder, and anxiety disorders, which are the most common ones [12]. In particular, more than 40% of all depressed patients suffer from cooccurring anxiety [112]. Furthermore, depression in adults is more likely to involve personality disturbances than anxiety disorders [12].

The impact of depressive symptoms on emotional and physical functioning has a negative effect on quality of life (QoL). Reduced QoL is related primarily to the dramatic effect of depression on one's ability to work. MDD can significantly reduce the QoL of patients and their families since depression consists in a major risk factor for suicidal ideation and of suicide attempts [252].

3.2 Diagnosis and screening

The diagnostic criteria for MDD, according to the 5th edition of the Diagnostic and Statistical Manual of Mental Disorders (DSM-5) and the 11th version of the International Classification of Diseases (ICD-11), rely on the identification of a number of key symptoms, such as depressed mood (e.g., feelings of sad, empty, hopeless), markedly diminished interest or pleasure in all, or almost all, activities most of the day (anhedonia), feelings of worthlessness or guilt, recurrent suicidal ideation, plan or attempt, fatigue or loss of energy, insomnia or hypersomnia, weight loss/gain or decreased/increased appetite, reduced ability to think or concentrate, or indecisiveness, and psychomotor agitation or retardation [12].

For a diagnosis of MDD, the individual needs to present five (or more) of the above mentioned symptoms, with depressed mood or anhedonia to be at least one of them, for nearly every day during the same 2-week period. Clear-cut changes in emotional, somatic and cognitive symptoms should be accompanied by clinically significant distress (e.g., pain), or functional impairment in social (aggression, passivity, or withdrawal), occupational, physical, or other important areas of functioning [12]. Figure 3.2 illustrates the key symptoms of DSM-5 for MDD [215]. Episodes of MDD can be described in greater depth by specifiers that provide additional information regarding the pattern of the illness and its clinical feature. For instance, based on severity, depressive episodes can be categorized as mild, moderate, or severe. Therefore, anxiety can manifest both as comorbidity and as a predominant feature of MDD. The latter case is termed anxious depression and it is described in DSM-5 with the anxious distress specifier [215]. The specifiers, sometimes, are implicated in the selection of an appropriate treatment method.

Screening tools that are currently used to identify depression include the Hamilton depression rating scale (HDRS) [136] and the Beck's depression inventory-II (BDI) [25], among others. HDRS is a 17-item questionnaire that was designed to measure frequency and intensity of depressive symptoms in individuals with MDD. It is completed by the clinician (see Fig. 1 in Appendix for HDRS questionnaire) and the scores are classified as normal (0 to 7), mild (8 to 13), moderate (14 to 18), severe (19 to 22), and very severe depression (23 to 52). BDI-II is a self-report questionnaire and it consists of 21 items. Higher total scores indicate more severe depressive symptoms, classifying them to as minimal (0 to 9), mild (10 to 16), moderate (17 to 29), and severe (30 to 63). Screening tools are used to assign a score rather than to diagnose depression. If that score is high,

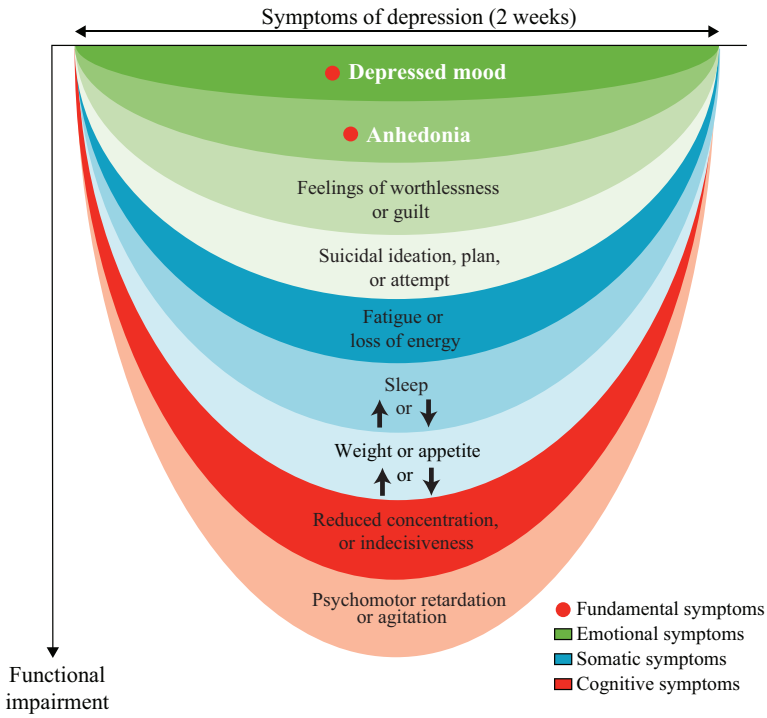

Figure 3.2: The key symptoms of DSM-5 for major depressive disorder (MDD). The symptoms of MDD can be grouped into emotional, somatic, and cognitive domains. For a diagnosis of MDD, the individual needs to present with five or more of any of the symptoms nearly every day during the same 2-week period, provided at least one of these symptoms is a fundamental one. The clinical symptoms of MDD are usually accompanied by functional impairment. Adapted and reproduced from [215].

the person should be evaluated more thoroughly for a depressive disorder diagnosis using the DSM-5 criteria.

3.3 Treatment methods

There are different types of treatment, such as psychotherapy or medication use, that are recommended depending on the severity of the illness and the age of the patient, among others. Antidepressants should not be used for treating depression in children and are not the first line of treatment in adolescents, among whom they should be used with extra caution. They can be an effective form of treatment for moderate-severe depression but are not the first line of treatment for cases of mild depression. For mild cases of MDD, psychological treatment alone can suffice [244].

Psychological treatment

There are several types of psychological treatments for depression that assist the individual to quell rumination and expressive suppression, promoting emotion regulation via reappraisal and distraction techniques [148]. Cognitive behaviour therapy is one of the most effective treatments during which the individual learns to identify and replace negative thinking patterns, which contribute to depression, with more positive thoughts [252]. Mindfulness-based cognitive therapy assists the individual to become aware of all incoming thoughts and feelings and accept them, without grasping onto the need to suppress, fight, or escape them [215]. This approach is achieved by focusing on physical sensations, like breathing, which interrupts the automatic cognitive processes that can trigger a depressive mood. Several initial studies demonstrated that this approach can decrease the recurrence of depression [272]. There is recent evidence that mindfulness component, such as yoga, has mood-enhancing properties. The influence of respiration to VN is associated with its inhibitory effects on physiological stress and inflammation, which are frequently associated with MDD [256].

Antidepressant drugs

In cases of severe depression, medication should be considered as first-line treatment. All antidepressant drugs increase monoamine levels in the synaptic cleft (by blocking reuptake or degradation of monoamines) and induce neural plasticity in the brain areas related to emotions and motivation [252]. The group of antidepressants that are used the most are called selective serotonin re-uptake inhibitors (SSRIs), such as sertraline (Zoloft), escitalopram (Lexapro), and citalopram (Cipramil). Also common are serotonin norepinephrine reuptake inhibitors (SNRIs), such as venlafaxine (Efexor). Some of the older types of antidepressants are called tricyclic antidepressants (TCAs) and monoamine oxidase inhibitors (MAOIs). However, their use is recommended only in severe cases because they have some adverse cardiovascular side-effects. Thus, the most cost-effective approach to treating depression with antidepressants is the newer antidepressant drugs, such as SSRIs and SNRIs [272]. Compounds that are under development include anti-inflammatory agents, hippocampal neurogenesis-stimulating treatments, and antiglucocorticoid therapies, among others [252].

Brain stimulation

There are patients who may be referred to as having treatment-resistant depression (TRD) and they are not obtaining adequate response following a first antidepressant drug treatment [252]. TRD is associated with increased functional impairment, mortality, morbidity and recurrent or chronic episodes in the long term [272]. The most established strategies for treating TRD include the combination of different antidepressants, the combination of pharmacotherapy with psychotherapy, and non-pharmacological biological treatments, such as electroconvulsive therapy (ECT) and vagus nerve stimulation (VNS) [215, 240].

ECT is an non-invasive type of brain stimulation during which an electric current is passed to the brain of the individual through electrodes placed on the head, triggering a seizure, which helps relieve the symptoms of depression. On the other hand, VNS is invasive brain stimulation that involves the surgical implantation of a pacemaker-like pulse generator in the chest, connected to a stimulating electrode attached to the vagus nerve in the neck [252]. VNS is currently being explored as treatment for depression and a variety of other autoimmune and chronic inflammatory disorders, due to its demonstrated anti-inflammatory effects [168]. However, the involvement of surgery has limited VNS only to patients who have failed to respond to multiple treatment options [353].

4

Autonomic nervous system assessment

4.1 Biosignals

Among all biological systems involved in stress response, the noninvasive assessment of autonomic nervous system (ANS) seems the most feasible way to carry out a continuous monitoring of changes in the internal environment of the body. Physiological parameters, i.e., biomarkers, related to ANS, can be derived from the analysis of diverse biosignals.

4.1.1 Electrocardiogram

An electrocardiogram (ECG) describes the electrical activity generated by the cells of the heart muscle. Voltage variations caused by the action potentials of the excitable cells can be recorded by electrodes placed on the body surface. The ECG represents the spatio-temporal sum of multiple action potentials taking place in different regions of the heart (see Fig. 4.1) [305].

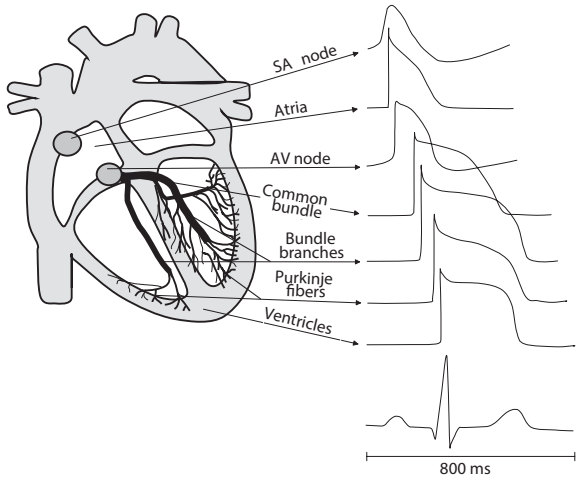

Figure 4.1: Action potentials from different regions of the heart and the surface ECG resulting from their spatio-temporal sum. SA node, sinoatrial node; AV node, atrioventricular node. Reproduced from [305].

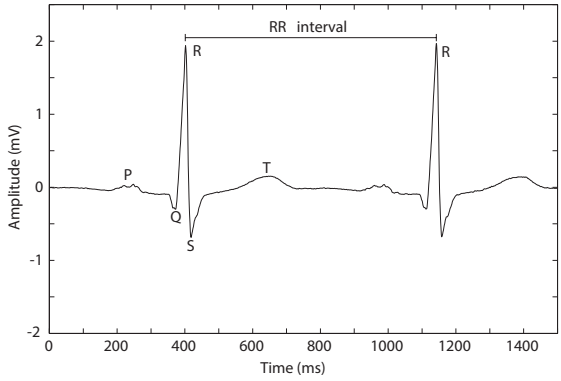

Figure 4.2: Characteristic waves in the ECG. Reproduced and modified from [305].

The cardiac cycle of a normal beat starts with the activation of the sinoatrial (SA) node, situated in the upper part of the right atrium. The SA node consists of pacemaker cells that undergo spontaneous generation of action potentials, i.e., an electrical impulse. The intrinsic rhythm of SA node activation is strongly influenced by the ANS. The morphology and timing of the action potentials generate characteristic waves in the resulting heartbeat (see Fig. 4.2). Electrical impulse generated by the SA node spreads throughout the atria, depolarizing this tissue and causing atrial contraction, which is reflected in the ECG as the so-called P wave. The impulse then travels into the ventricles via the atrioventricular (AV) node, located in the lower back section of the inter-atrial septum, which inserts a small delay in the impulse transmission. This allows the blood to get from atria into ventricles before their contraction. Specialized conduction pathways, including bundle branches and Purkinje fibers, in the ventricular walls rapidly conduct the electrical impulse throughout the ventricles to elicit ventricular contraction. The depo-

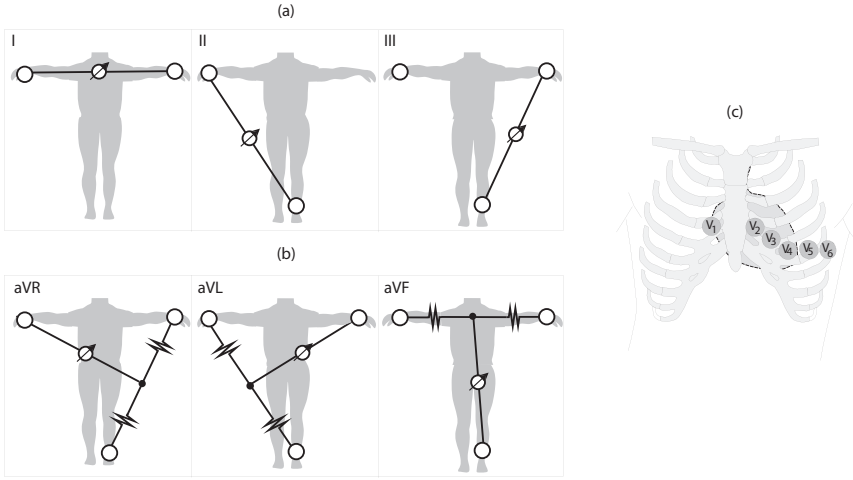

Figure 4.3: Electrode positions for the standard 12-lead electrocardiogram. (a) Bipolar limb leads, (b) augmented unipolar limb leads, and (c) unipolar precordial leads. Reproduced and modified from [305].

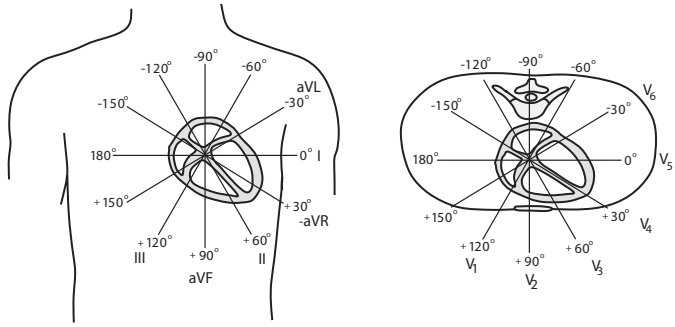

Figure 4.4: Directions of the 12-lead electrocardiogram. Bipolar and augmented limb leads in the frontal plane (left), and precordial leads in the horizontal plane (right). Reproduced from [305].

larization of the ventricles is reflected in the ECG as the QRS complex, which is the result of superposition of 3 waves named the Q, R, and S waves. The cardiac cycle ends with the relaxation of both atria and ventricles. No distinctly visible wave represents atrial relaxation in the ECG because atrial repolarization is masked by ventricular depolarization and is of relatively small amplitude. Ventricular repolarization, which occur during the ventricular relaxation, is reflected at the last wave of the heartbeat, the so-called T wave. Besides the morphology of the ECG waves during a cardiac cycle, the time pattern that characterizes the occurrence of successive heartbeats represents useful information for the heart's electrical activity. The time occurrence of heartbeats in sinus rhythm should be defined based on the time occurrence of the P waves, since depolarization of the cardiac muscle begins at the SA node. However, the P wave is characterized by a very low amplitude and sometimes is completely missing from the heartbeat. Taking into account that the interval between the P and R wave is relatively fixed, R-to-R (RR) intervals are commonly used to characterize the time pattern of successive heartbeats [305].

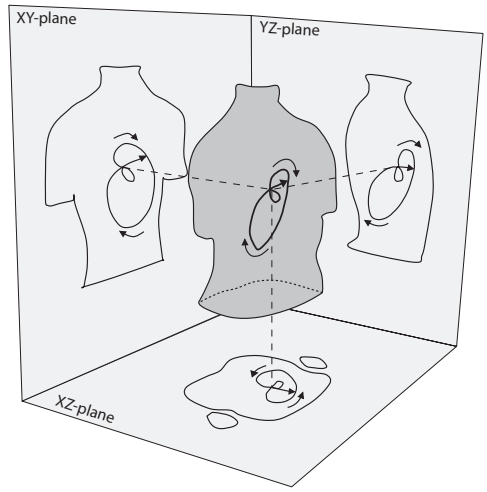

Figure 4.5: A vectorcardiogram loop and its projection onto the three orthogonal planes. The two arrows outside each loop indicate the direction in which the loop evolves. Reproduced from [305].

The number and position of electrodes attached to the body surface for recording the ECG depends on the type of clinical information desired. Different configurations can reveal in more detail specific spatio-temporal variations of the cardiac electrical field. The voltage difference between a pair of electrodes is referred to as a bipolar lead, while the voltage variation of a single electrode in relation to a reference electrode, where the voltage remains almost constant during the whole cardiac cycle, is referred to as a unipolar lead. The ECG is typically recorded with a multiple-lead configuration that includes unipolar or bipolar leads, or both. The most employed lead configuration in the clinical routine is the standard 12-lead ECG (see Fig. 4.3), which is composed of 3 bipolar limb leads (I, II, III), 3 augmented unipolar limb leads (αVF, αVL, αVR), and 6 unipolar precordial leads (V_1,...,V_6). These electrode positions allow for describing the cardiac electrical activity in different directions of the frontal and horizontal plane, as depicted in Fig. 4.4. For instance, in horizontal plane, leads V_1 and V_2 primarily reflect the activity of the right ventricle, while the left ventricle is viewed by the rest of precordial leads. Another lead configuration system, which allows to view the electrical activity in the three perpendicular directions X, Y, and Z, is the orthogonal or Frank lead system. Besides the information of individual orthogonal leads during the cardiac cycle, the visualization of a three-dimensional vectorcardiogram (VCG) loop, together with its projection onto the XY-, XZ-, and YZ-planes (see Fig. 4.5), can provide additional information for tracking the dominant direction of the electrical axis of the heart [305]. When either only the VCG or the 12-lead ECG is available, there are transformations, such as the Dower and the inverse Dower, which allow for the derivation of the orthogonal leads from the 12-lead ECG, and vice versa [86]. Kors transformation is another method used for reconstruction of the VCG from standard 12-lead ECG [190].

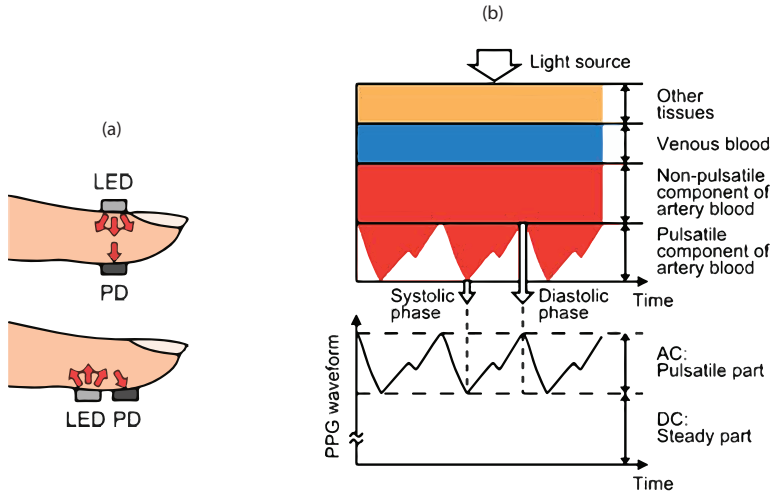

Figure 4.6: Recording of a photoplethysmogram (PPG). (a) Modes of PPG, transmission (top) and reflectance (bottom), and (b) characteristic PPG waveform that arise from light attenuation by tissues. LED, light-emitting diode; PD, photodetector. Reproduced and modified from [316].

4.1.2 Photoplethysmogram

A photoplethysmogram (PPG) is an optical measurement that requires a light source, commonly a light-emitting diode (LED), and a photodetector (PD). It allows to detect blood volume changes in the microvascular bed of tissue by monitoring the light intensity via reflection from or transmission through the tissue [4]. In transmission mode, the PD is placed opposite the light source, detecting the light transmitted through the medium, while in reflectance mode, the PD is placed adjacent to the light source, detecting the light that is back-scattered or reflected from the tissue (see Fig. 4.6(a)). Light sources commonly used for tissue illumination are red, infrared, and green LEDs. Furthermore, PPG measurements can be acquired using a video camera as PD and, as illumination source, normal ambient light for long-distance recordings or phone camera flash (white LED light) for short-distance recordings [316].

The recorded light has a direct relationship with perfusion, since blood absorbs more light than the surrounding tissue [316]. Fig. 4.6(b) shows an example of a characteristic PPG waveform, which is composed of a pulsatile (AC) component superimposed on non-pulsatile (DC) component. The AC component of the PPG waveform is associated with the pressure pulse wave produced by left ventricular contraction with each heartbeat, while the DC component, with the structure of the tissue and the average blood volume. A larger blood volume during the systolic phase leads to greater attenuation of the light source compared to the diastolic phase of the cardiac cycle. The potential of PPG for assessing cardiovascular system and autonomic function has been recognized many decades ago. The DC component is not constant, but changes slowly over time, and reflects autonomic modulation and thermoregulation, among other physiological mechanisms. Besides the fact that AC component is synchronous with the beating heart which

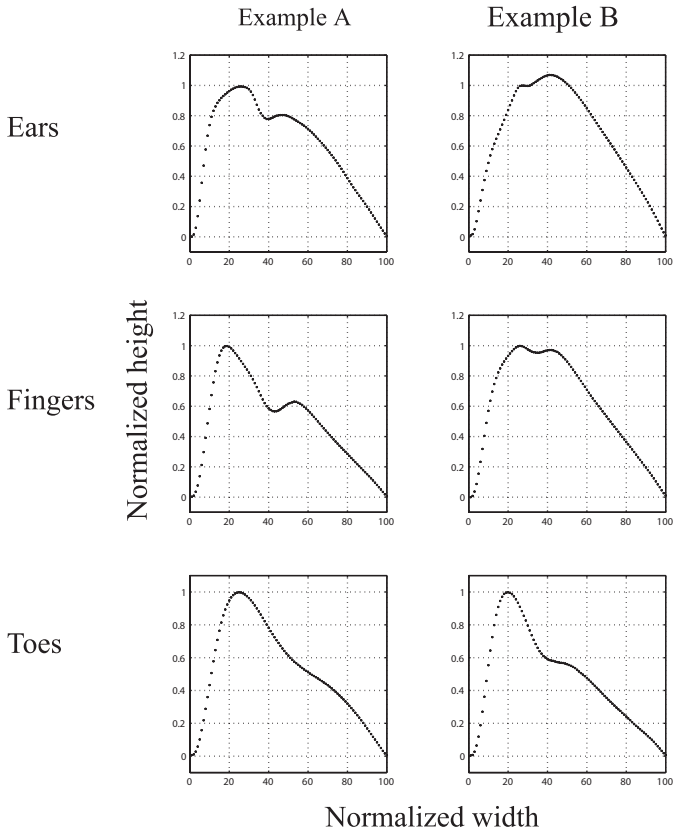

Figure 4.7: Photoplethysmographic pulses recorded at different sites of the body (ears, fingers, toes) for 2 subjects (example A at left and example B at right). Reproduced from [4].

reflects autonomic function, blood volume changes in the systolic and diastolic phase of the cardiac cycle provide additional information about vascular tone and arterial stiffness. The morphological and temporal characteristics of the AC component are associated with changes in pressure pulse wave as it moves toward the periphery. These changes are attributed to wave reflections of the pulse wave in the periphery [4]. Consequently, depending on the site of measurement, PPG waveform morphology can be different. Figure 4.7 illustrates (inverted) PPG pulses of 2 subjects recorded at different sites of the body.

4.1.3 Respiratory signal

A respiratory signal reflects changes in the thoracic cavity or in the airflow of the respiratory system during breathing. Breathing (or ventilation) is a rhythmic process that usually occurs without conscious thought or awareness. It involves the exchange of air between the atmosphere and the lungs, providing oxygen (O_2) to the tissues and remove carbon dioxide (CO_2). The movement of air into the lungs is called inspiration (inhalation) and the movement of air out of the lungs is called expiration (exhalation). During

inspiration, contraction of the diaphragm pulls downward the lower surfaces of the lungs, and contraction of the external intercostal muscles causes rib cage elevation, thereby increasing the vertical and anteroposterior diameter of thoracic cavity, respectively. The contraction of inspiratory muscles creates a negative intra-thoracic pressure that allows the entrance of O_2-rich air into the lungs. During expiration, CO_2-rich air is expelled from the lungs. Relaxation of the external intercostals and upward movement of the diaphragm due to the elastic recoil of the lungs compress the chest wall. When the elastic forces are not powerful enough for rapid expiration, contraction of expiratory muscles, including internal intercostal and abdominal muscles, can further reduce the duration of the expiration phase [299].

Contraction of muscles related to respiration is controlled by groups of neurons, known as the respiratory center, in the distal part of the brain, the brainstem. The respiratory center in the brainstem is divided into three major groups of neurons (see Fig. 4.8): the ventral respiratory group (VRG) and the dorsal respiratory group (DRG) in the medulla, and the pontine respiratory group (PRG) in the pons. VRG initiates inspiration via spontaneously firing neurons, forming the pre-Bötzinger complex, which gradually increase stimulation of DRG. DRG controls the inspiratory muscles, while VGR is mainly in charge of the control of the expiratory muscles. Most of the DRG neurons are located within the nucleus of the tractus solitarius (NTS), which is the sensory termination of both the vagus and the glossopharyngeal nerves. The NTS receives sensory information from peripheral chemo- and mechanoreceptors, including baroreceptors, atrial stretch, and pulmonary stretch receptors [103]. The NTS in combination with CO_2-sensitive central chemoreceptors located in the medulla provide continuous input into PRG that operates as control network for the coordination of breathing process. PRG integrates the sensory information and feedback impulses from limbic and cortical regions of the brain and interacts with medullary neurons to influence the speed of inhalation and exhalation. [299].

The respiratory neurons interact, within the medulla, with both sensory afferent inputs and premotor neurons that form synapses with autonomic pregaglionic neurons, thereby adjusting autonomic function [15,84,127]. Vasomotor sympathetic tone depends on the activation of sympathetic premotor neurons in the rostral ventrolateral medulla (RVLM), while parasympathetic premotor neurons in the nucleus ambiguus control the vagal tone by sending inhibitory signals to the SA node via the vagus nerve [1, 109]. Medullary interconnections of the NTS with the pre-Bötzinger complex, and both RVLM and nucleus ambiguus provide an anatomical substrate for cardiorespiratory interactions [69, 82, 318]. The most known type of such interactions is the phasically inhibition of cells in nucleus ambiguus during inspiratory bursts from the pre-Bötzinger complex [109]. This phenomenon is known as respiratory sinus arrhythmia (RSA), and it is characterized by higher HR during inspiration than during expiration. RSA is hypothesized to improve energetic efficiency of gas exchange [115] or alternatively, to assist in reducing cardiac work while maintaining low levels of CO_2 in the blood [31].

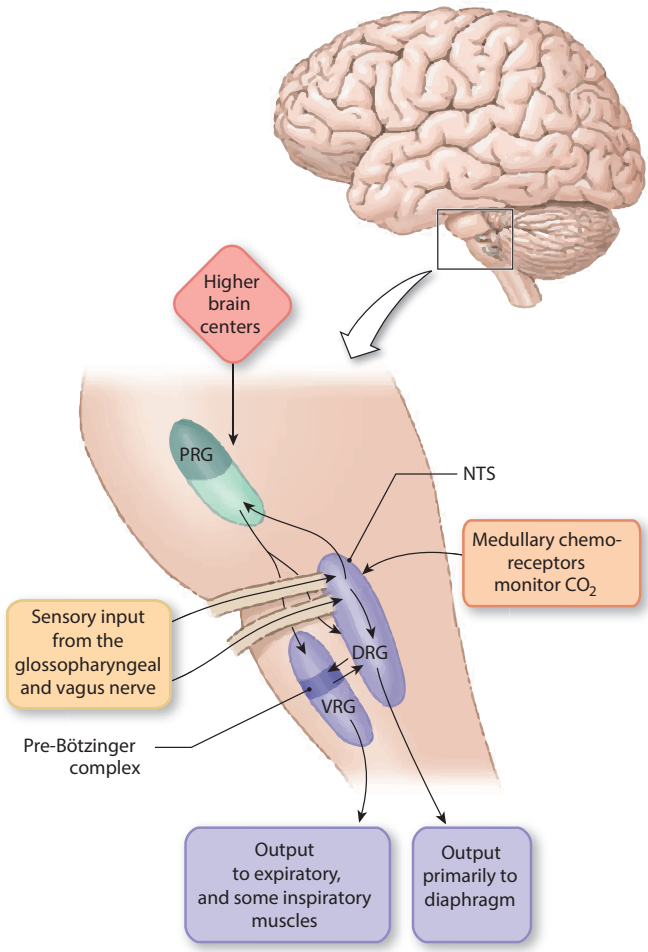

Figure 4.8: Neural control of respiration in the brainstem. The respiratory center is composed of the the ventral respiratory group (VRG) and the dorsal respiratory group (DRG) in the medulla, and the pontine respiratory group (PRG) in the pons. NTS, nucleus of the tractus solitarius. Reproduced and modified from [299].

Respiratory related chest or abdominal movements can be measured using a respiratory belt made from an extendible conducting material, which changes the electrical charge concentration in response to externally applied strain. Nasal or oral airflow related changes can be detected using a pressure transducer sensor incorporated to a facemask or using a thermistor that detects changes in temperature and humidity between the inhaled and exhaled air [2, 217]. Furthermore, respiratory signals can be derived indirectly from other biosignals that contain respiratory influences (see Fig. 4.9) [59]. The modulation on beat-to-beat or pulse-to-pulse intervals due to RSA mechanism is evidenced as a frequency modulation (FM) in ECG and PPG signals, respectively. Furthermore, amplitude modulation (AM) phenomena arise from hemodynamic changes that occur in synchrony with respiration [308]. During inspiration, expansion of the chest wall and lowering of the diaphragm increase venous return to the right atrium. Subsequent ex-

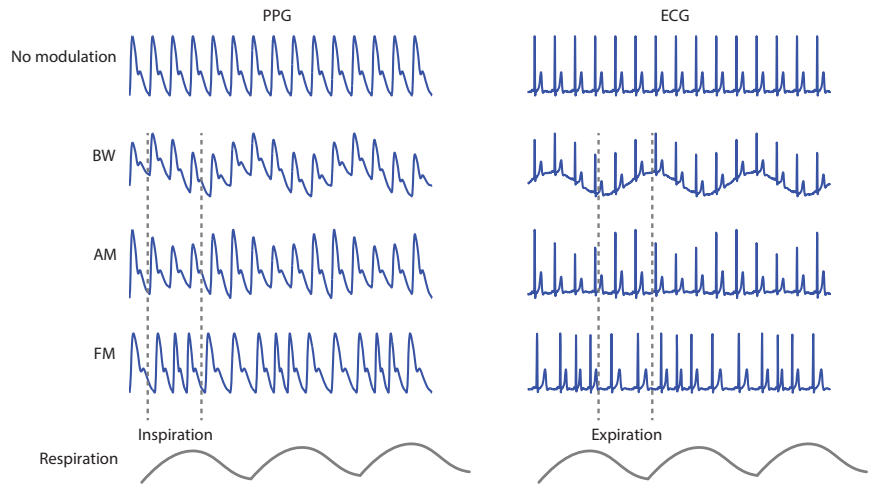

Figure 4.9: Illustrative respiratory modulations of a photoplethysmogram (PPG) (left column) and electrocardiogram (ECG) (right column). From top: no modulation, baseline wander (BW), amplitude modulation (AM), frequency modulation (FM), and the respiratory signal. Reproduced and modified from [59].

pansion of the right ventricle causes displacement of the intra-ventricular septum. This process is known as ventricular interdependence and it reduces the pressure and volume in the left ventricle [283]. Reduced stroke volume reduces blood flow towards the periphery and diminishes surface electrical potentials due to lower blood-related conductivity in the left ventricular chamber [43, 197, 227, 278]. Thus, amplitude in both ECG and PPG signals decreases during inspiration. Baseline wander (BW) contamination is another typical modulation, which, however, is caused by multiple factors besides respiration [4].

It should be noted that additional electro-physiological mechanisms are implicated in the modulating effect of respiration on the ECG morphology. Changes in the orientation of the heart relative to the ECG electrodes due to the movement of the diaphragm, and changes in heart-to-electrode distances and impedance distribution due to filling and emptying of the lungs, alter electrical propagation that influences the beat morphology [16]. ECG can be used to indirectly estimate a respiratory signal, known as the ECG-derived respiration (EDR). EDR signals reflect either RSA information or changes in beat morphology, including the QRS amplitude, the amplitude difference between the R and the S waves [346], and the up- or downslope of the QRS complex [202]. Rotation angles of successive VCG loops of the QRS complex are other characteristics which reflect respiration-induced changes [16]. Respiratory signals can be also derived from changes in pulse-to-pulse intervals and PPG morphology, e.g., pulse amplitude and width, among others [59, 200].

4.2 Noninvasive biomarkers and clinical significance

Noninvasive biomarkers related to ANS can be derived from the analysis of diverse biosignals, such as respiration, ECG and PPG. Such biological parameters reflect autonomic influences on the respiratory center, the SA node, and the peripheral vasculature, and they are valuable in a variety of clinical applications.

The respiratory center in the brainstem can alter the rhythmicity and intensity of ventilation, leading to changes in the number of breaths per minute, the so-called respiratory rate, and the volume of each inspiration, known as tidal volume. Chemical, mechanical, and corticolimbic inputs to the respiratory center determine ventilation, which plays a key role in autonomic regulation [42]. For instance, heighten limbic input during psychological stress causes an increase in ventilation, while, during sleep, reduced cortical input leads to a decrement of ventilation [85, 326]. Various diseases can increase ventilatory needs, stimulate respiratory drive and alter respiratory control, creating characteristic changes in breathing pattern [71]. Alterations in the normal respiratory rate (12-18 breaths per minute) is often a clinical manifestation of pathological conditions, such as airway obstruction in respiratory diseases, reduced oxygenated blood flow in CVDs, or increase acidity of the blood in metabolic acidosis [146, 276]. Increased respiratory rate is an independent predictor of long-term cardiovascular mortality [22, 88]. Abnormal respiratory rate, either elevated or decreased, is an important biomarker of potentially adverse clinical events in elderly people and critical ill patients [3, 73]. Respiratory parameters can be estimated indirectly from the ECG and PPG, without the need of additional sensors [59, 202, 230].

Autonomic influence on the SA node can alter its depolarization periodicity, leading to changes in the number of beats per minute, the so-called mean HR, and in the beat-to-beat variations, known as heart rate variability (HRV) [305]. Increased variability is usually associated with a good health condition, whereas lowered variability signifies pathological changes associated with autonomic dysfunction [96]. HRV is the most extended biomarker used for non-invasive assessment of the ANS and it can be influenced by various biological, physiological, or psychological factors. For instance, HRV differs between wakeful and sleep stages [41], males and females [343], and between young and elderly people [359]. Moreover, HRV is altered by physical [224, 327] or mental stress [315]. It has been also used as an index of emotional responding and cognitive function in both healthy individuals [7, 67, 322] and patients suffering from mental disorders [8, 48, 83]. HRV has been found to be altered in various CVDs, including hypertension [339], coronary artery disease [81], and sudden cardiac death [214], and in pathological conditions related to respiratory disorders, such as chronic obstructive pulmonary disease [334], asthma [205] or sleep apnea [307].

Research integrating HRV has increased in the last decades, particularly given the fact that HRV is able to index cardiac vagal tone, which represents the contribution of the PNS to cardiac regulation [193]. The beat-to-beat fluctuation in HR at the frequency of the respiratory cycle (RSA component) is mediated by the PNS [33, 198]. However, changes

in respiratory parameters, such as respiration rate and tidal volume, can confound the relationship between RSA and cardiac vagal tone [126, 275]. To reduce respiratory confounding effects on RSA, subjects are sometimes asked to breath at a constant respiratory rate [198]. This approach, however, removes variability associated with neural control over the cardiac vagal tone [193]. During spontaneous breathing, the inclusion of respiratory rate information in HRV analysis can improve the ANS assessment [145]. Furthermore, if a respiratory signal is available, there are also mathematical tools that can be employed to extract, and study separately, the respiratory influences from HRV [338]. In summary, it is of paramount importance to simultaneously consider respiration when analyzing HRV-related ANS biomarkers.

Besides HRV analyses guided by respiration, a significant amount of research has been dedicated to the joint analysis of HRV and respiration to derive clinically meaningful ANS biomarkers that assess interactions between the cardiac and respiratory rhythms [21]. The cardiorespiratory system is characterized by a complex interplay of several linear and nonlinear subsystems in the brain networks that interact via feed-forward and feed-back mechanisms [288,293]. Cardiorespiratory interactions give rise to several types of cardiorespiratory coupling phenomena characterized either by phase and/or frequency locking between respiratory and cardiac rhythms, or time differences between the heartbeats and the onsets of respiratory cycles [95, 292]. Cardiorespiratory indices have been reported to be altered in respiratory and cardiovascular diseases [150, 172], in some mental disorders [32, 262, 360], and during physical [110, 332], cognitive [348], or affective stressful stimuli [178, 331].

Biomarkers related to HR and HRV can be also derived from PPG signals assessing pulse-to-pulse interval variations [116]. Besides heart rhythm, PPG waveform morphology can provide great amount of information about vascular tone that is influenced by the sympathetic branch of the ANS [4]. Morphological characteristics based on amplitude ratio or time delay between the systolic and diastolic peak have been used in clinical practice as an index of arterial stiffness [342,354]. The reduced ability of the arteries and veins to stretch in response to pressure has a large effect on BP, and it is a flag for hypertension underlying CVDs [78,173,187,231]. A variety of morphological characteristics of the PPG waveform, including those related to arterial stiffness, have been used to quantify mental stress [60, 114, 341], and assess mental disorders, such as anxiety or depression [182, 296]. However, ANS biomarkers that rely on the detection of the diastolic peak in elderly people or under stressful situations can be challenging. Reduced compliance of the elastic arteries results in faster propagation and early return of the wave reflections from the periphery, which are more prominent in the systolic phase instead of the diastolic phase. Modeling the PPG pulse as a main wave superposed with several reflected waves can aid for measuring morphological characteristics in a more robust way [203].

4.3 Noninvasive biomarkers in mental illness

While screening tools used in clinical practice, such as questionnaires, have considerable value, sometimes they are time-consuming and require the willingness of the patients to communicate their symptoms. Biological and/or physiological information offers the possibility to complement existing psychometric scales for improved accuracy in the assessment of MDD. Screening tools based on noninvasive biomarkers allow for a more frequent and massive screening. Biomarkers are not only useful in distinguishing the presence or absence of an illness but they are able to predict treatment response [291]. Promising peripheral/blood-based biomarkers for depression in association with treatment outcomes are inflammatory proteins, cortisol levels, metabolic factors, and concentration of various neurotransmitters [312]. However, these biomarkers are obtained using invasive methods.

Biomarkers derived from the analysis of diverse biosignals might be useful for an noninvasive monitoring of depression progression/severity. Analysis of speech signals seems promising for the screening of depression and assessment of suicide risk [75]. Speech features, such as shimmer and jitter of vocal-fold vibration, and dynamics of the fundamental frequency (pitch), are able to quantify alterations in motor control of voice generation process. Reduced control of speech production in MDD patients is related to cognitive dysfunction, which affects motor coordination (laryngeal control), and autonomic imbalance, which causes disturbances in muscle tension and respiratory rate [51, 251].

Autonomic imbalance in MDD patients has been reported in various studies exploring HRV indices. Reduced HRV and elevated HR have been widely used as noninvasive biomarkers of the ANS for depression assessment. Individuals with greater levels of resting HRV have greater emotion regulation and executive functioning [135]. Autonomic reactivity in response to mental or physical stressors is hypothesized to be associated with the ability of an individual to cope with stress [52, 250]. Similar to reactivity, recovery plays a crucial role regarding the adaptability of the organism, to face an event and then return to resting level. Variations in the ANS before, during, and after the demands induced by the stressful event, represent different levels of adaptability. A higher resting cardiac vagal tone or HR is hypothesized to promote a more adaptive functioning and it is often accompanied by fast return to initial level [194]. On the one hand, reduced HRV reactivity to cognitive load is a common feature among various mental disorders [6, 57, 117, 135]. On the other hand, exaggerated stressor-evoked BP reactivity and delayed stress recovery increase the risk for developing CVDs [62, 134].

Thus, current research focuses on the autonomic reactivity to stress response as a potential biomarker for MDD. Depression is associated with reduced autonomic reactivity to mental stress induced by cognitive tasks, evidenced by blunted HRV reactivity [290]. The majority of reactivity studies have measured changes in HR, HRV, and BP. Respiratory parameters and morphological PPG characteristics have been seldom analyzed in the context of autonomic reactivity to mental stress [207]. Respiratory activity has emerged as an objective measure of mood regulation since the action of the diaphragm can be

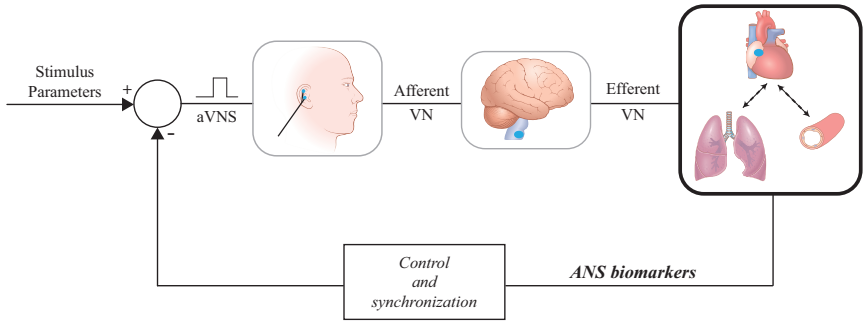

Figure 4.10: Auricular vagus verve stimulation (aVNS) with plethysmographic biofeedback as treatment method in major depressive disorder. Autonomic nervous system (ANS) biomarkers allow for control and synchronization of stimulation of the afferent vagus nerve (VN), which, in turn, modulates the heart rhythm via efferent pathways of parasympathetic branch of the ANS. Adapted and reproduced from [176].

altered by emotional states such as sadness and anxiety [38]. Other ANS biomarkers related to vascular characteristics, such as surrogates of arterial stiffness or BP derived from PPG signals, could provide additional information for the dynamics of the cardiovascular system in MDD [296]. Electrodermal activity, which reflects the activity of sympathetic branch of ANS, is also a valuable biomarker for stress and depression assessment [285].

ANS biomarkers might be also important in some treatment methods. Auricular VNS (aVNS) is a relatively new, noninvasive VNS method based on the rationale that there is afferent/efferent vagus nerve distribution on the surface of the ear. Clinical improvement of depression was shown when treated with aVNS, whereas depression scores as well as remission rates improved [175]. The safe and low-cost characteristics of aVNS have the potential to significantly expand the clinical application of VNS [101]. A systematic approach is required to identify the optimal stimulation parameters (e.g., intensity, frequency) that provides the greatest clinical benefit [353]. This may require participant-specific adjustment of parameters in a closed-loop setup, where stimulation parameters are set in real time based on ANS biomarkers [176]. Furthermore, aVNS gated to the exhalation phase of respiration is suggested to be more efficient in the activation of parasympathetic branch of ANS [294]. Figure 4.10 illustrates a closed-loop aVNS with ANS biomarkers serving for control and synchronization of stimulation process. This requires the development of robust and computationally simple methods for ANS assessment in mental health.

5

Objective and outline of the thesis

The main objective of this thesis is to derive ANS biomarkers from multi-modal and model-based signal processing techniques for assessing stress and monitoring depression. This dissertation is structured in four parts:

- **Part I**: In the present part, an introduction to mental health and illness is provided. Moreover, a theoretical framework for investigating the etiology of mental disorders and the role of stress in mental illness is presented. The importance of noninvasive biomarkers for ANS assessment, paying particular attention in clinical depression, is also highlighted.

- **Part II**: In this part, the methodological framework for deriving biomarkers related to the ANS from multi-modal and model-based signal processing techniques is provided. Such methodologies include the joint analysis of HRV and respiratory signals (Ch. 6), novel techniques for deriving the respiratory signal from ECG (Ch. 7), and a robust PPG waveform analysis based on a model-based approach (Ch. 8).

  A multi-modal approach allows for the modification of classical HRV analyses either including respiratory information or extracting, and analyzing separately, the respiratory influences from the HRV signal. Respiratory information is characterized either by the respiratory rate or the linear dynamics between respiratory and HRV signals. Nonlinear cardiorespiratory interactions are also investigated in the context of HRV analysis. A novel method, which takes into account both phase and frequency locking phenomena between respiration and HRV signals, for as-

sessing quadratic nonlinear cardiorespiratory coupling is proposed. The research described in this chapter generated the following publications:

- **Kontaxis, S.**, Lázaro, J., Hernando, A., Arza, A., Garzón, J. M., Gil, E., Laguna, P., Aguiló, J., and Bailón, R. Mental Stress Detection Using Cardiorespiratory Wavelet Cross-Bispectrum. *2016 Computing in Cardiology Conference (CinC)*, Vancouver, BC, 2016, pp. 725-728. DOI: 10.22489/CinC.2016.211-454.
- **Kontaxis, S.**, Orini, M., Gil, E., Posadas-de Miguel, M., Bernal, M. L., Aguiló, J., de la Camara, C., Laguna, P., and Bailón, R. Heart Rate Variability Analysis Guided by Respiration in Major Depressive Disorder. *2018 Computing in Cardiology Conference (CinC)*, Maastricht, Netherlands, 2018, pp. 1–4. DOI: 10.22489/CinC.2018.319.
- **Kontaxis, S.**, Lázaro, J., Gil, E., Laguna, P., and Bailón, R. Assessment of Quadratic Nonlinear Cardiorespiratory Couplings During Tilt Table Test by Means of Real Wavelet Biphase. *IEEE Trans Biomed Eng*, 2019. vol. 66, n. 1, pp.187–198. DOI: 10.1109/TBME.2018.28211827.
- **Kontaxis, S.**, Bailón, R., Rapalis, A., Brazaitis, M., Cernych, M., Lázaro, J., Laguna, P., Gil, E., and Marozas, V. Autonomic Nervous System Response to Heat Stress Exposure by Means of Heart Rate Variability. *2019 Computing in Cardiology Conference (CinC)*, Singapore, 2019, pp. 1–4. DOI: 10.23919/CinC49843.2019.9005474.
- **Kontaxis, S.**, Laguna, P., García, E., Posadas-de Miguel, M., Siddi, S., Bernal, M. L., Haro, J. M., Aguiló, J., de la Camara, C., Bailón, R., and Gil, E., Blunted Autonomic Reactivity to Mental Stress in Depression Quantified by Nonlinear Cardiorespiratory Coupling Indices. *2020 Computing in Cardiology Conference (CinC)*, Rimini, Italy, 2020. Accepted for publication.

In order to reduce the number of sensors needed to perform HRV analysis that requires simultaneously respiratory information, the ECG can be used to indirectly estimate the respiratory rate. Moreover, in ambulatory monitoring, the usage of ECG to derive respiratory parameters is more favorable than the current techniques which either interfere with normal breathing or cause discomfort. Although retrieving respiratory parameters from EDR signals during sinus rhythm has been widely studied, EDR methods in arrhythmia remains largely unexplored. Novel techniques for improving the monitoring of respiration in cardiac arrhythmias, is also important in the field of mental disorders, since previous studies have found a high degree of comorbidity between MDD and CVDs. A novel EDR signal and a technique for estimating the respiratory rate from EDR signals is proposed. The research described in this chapter generated the following publications:

- **Kontaxis, S.**, Lázaro, J., Corino, V. D. A., Sandberg, F., Bailón, R., Laguna, P., and Sörnmo, L. ECG-derived Respiratory Rate in Atrial Fibrillation. *IEEE Trans Biomed Eng*, 2019. vol. 67, n. 3, pp.905–914. DOI: 10.1109/TBME.2019.2923587.

  - **Kontaxis, S.**, Yebra, A. M., Petrėnas, A., Marozas, V., Bailón, R., Laguna, P., and Sörnmo, L. Investigating Respiratory Rate Estimation During Paroxysmal Atrial Fibrillation Using an Improved ECG Simulation Model. *2020 Computing in Cardiology Conference (CinC)*, Rimini, Italy, 2020. Accepted for publication.

Furthermore, PPG signals can be used to perform HRV analyses. PPG waveform morphology can also provide great amount of information about ANS function. However, deriving ANS biomarkers that rely on the detection of inflection points, which might not be always visible in the PPG waveform (e.g. under stressful situations), can be challenging. Modeling the PPG pulse as a main wave superposed with several reflected waves can increase the robustness for some morphological measurements. The research described in this chapter generated the following publication:

  - **Kontaxis, S.**, Gil, E., Marozas, V., Lázaro, J., García, E., Posadas-de Miguel, M., Siddi, S., Bernal, M. L., Aguiló, J., Haro, J. M., de la Camara, C., Laguna, P., and Bailón, R. Photoplethysmographic Waveform Analysis for Autonomic Reactivity Assessment in Depression. *IEEE Trans Biomed Eng*, 2020. DOI:10.1109/TBME.2020.3025908.

- **Part III**: This part is dedicated to the main objective of the thesis, i.e., the use of ANS biomarkers from multi-modal and model-based signal processing techniques, described in **Part II**, for assessing stress and monitoring depression. First, ANS biomarkers are evaluated in the assessment of different types of stress, either physiological or psychological, in healthy individuals (Ch. 9). Then, biomarkers sensitive to stress are evaluated in the monitoring of depression (Ch. 10). Respiratory information has seldom been taken into account by former HRV approaches in depression. Similarly, nonlinear cardiorespiratory coupling and PPG morphological indices are scarcely considered in depression screening. Finally, autonomic reactivity to mental stress in the monitoring of depression is investigated. Variation in ANS biomarkers before, during, and after a stressful task, can be a tool for assessing depression severity. The capacity of adaptation to stress might be useful in the monitoring of depressive mood.

- **Part IV**: This part contains the final discussion, the main conclusion and the future research lines (Ch. 11).

Part II

Autonomic nervous system biomarkers

6

Joint analysis of heart rate variability and respiratory signals

The purpose of HRV analysis is to investigate the influence of ANS on the SA node based on the time occurrence of heartbeats during sinus rhythm. The net effect of ANS on the SA node depends on the relative balance between SNS and PNS activity. There is a close relationship between HRV and respiration, since the VN is the main nerve of the parasympathetic division of the ANS. Respiratory information, which can be included in HRV analyses for improving the estimation of sympathovagal balance, can be obtained from respiratory signals or indirectly from the ECG.

HRV representations

The time pattern that characterizes the occurrence of successive heartbeats is reflected by the RR interval. A variety of methods have been proposed for beat detection including first order derivative techniques, Hilbert transform, and empirical mode decomposition, among others [271]. In this dissertation, a wavelet-based detector is employed [216].

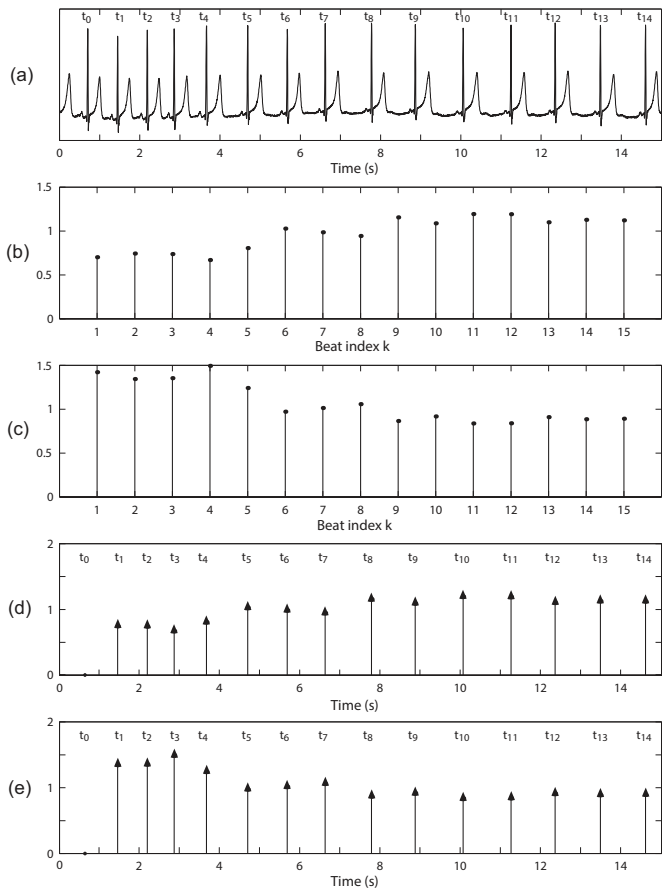

Figure 6.1: Different heart rhythm representations. (a) Example of an ECG signal with the beat occurrence times $t_0, \ldots, t_{14}$, (b) interval tachogram, (c) inverse interval tachogram, (d) interval function, and (e) inverse interval function. Adapted and reproduced from [305].

However, not all RR intervals can be used for a HRV analysis. False detections or miss-detected beats, due to low-amplitude QRS complexes or artifacts, result to RR interval series with invalid intervals. Another aspect of abnormal changes in RR intervals is the fluctuations due to the generation of an electrical impulse in a region of the heart different than SA node. These heartbeats, which can have a supra-ventricular or a ventricular origin, are called ectopic beats and they do not reflect ANS modulation on the SA node depolarization pattern [305]. Thus, RR intervals adjacent to an ectopic or mis-detected beat cannot be used for HRV analysis. Such beats can be identified and removed using an algorithm described in [218], which imposes a threshold for the maximum deviation that can be caused by a beat location belonging to sinus rhythm. The resulting interval series are denoted normal-to-normal (NN) intervals [305].

The NN intervals consist in the simplest representation of heart rhythm, the so-called interval tachogram (Fig. 6.1(b)). Another representation based on inverse of the RR in-

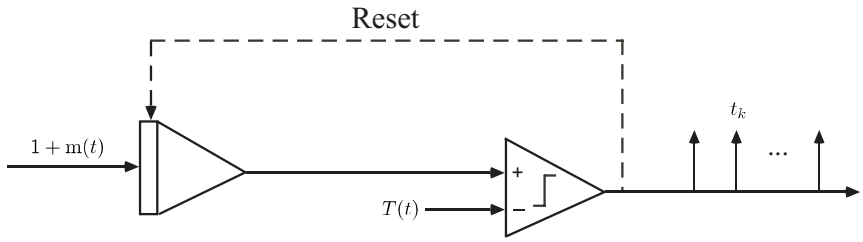

Figure 6.2: The time-varying integral pulse frequency modulation (TVIPFM) model. The generation of an event series, i.e., t_k, from a continuous-time modulating signal $m(t)$ when the time-varying threshold $T(t)$ is reached. Adapted and reproduced from [19].

tervals, which is called the inverse interval tachogram, reflects information about rate instead of time (Fig. 6.1(c)). Both representations are discrete signals that represent different amplitudes related to the NN interval series at each heartbeat. Taking into account the time instant when each heartbeat occurs, the unevenly sampled continuous-time version of the interval and the inverse interval tachogram, named the interval function (Fig. 6.1(d)), and the inverse interval function (Fig. 6.1(e)), can be defined, respectively [305].

Another representation of HRV based on the time-varying integral pulse frequency modulation (TVIPFM) model, which assumes that ANS modulation on the SA node can be represented by a band-limited signal $m(t)$, can be estimated from the beat occurrence time series. A schematic of the TVIPFM model is displayed in Fig. 6.2. The input signal, consisting in $m(t)$ superimposed to a DC level, is integrated until the threshold $T(t)$, which represents the time-varying mean heart period, is reached. Then, a beat occurs and the integration process is reset. The relation between the modulating signal $m(t)$ and the beat occurrence time series $t_k, \forall k$, is given by,

$$k = \int_0^{t_k} \frac{1 + m(t)}{T(t)} dt = \int_0^{t_k} d_{\mathrm{HR}}(t) dt, \tag{6.1}$$

where $d_{\mathrm{HR}}(t)$ refers to the instantaneous HR that is composed by rapid variations, $m(t)/T(t)$, superposed to a slow-changing mean HR, $d_{\mathrm{HRM}}(t) = 1/T(t)$. Thus, $m(t)$ is derived from,

$$m(t) = \frac{d_{\mathrm{HR}}(t) - d_{\mathrm{HRM}}(t)}{d_{\mathrm{HRM}}(t)}, \tag{6.2}$$

where $d_{\mathrm{HRM}}(t)$ is obtained by low-pass filtering $d_{\mathrm{HR}}(t)$. The normalization term in eq. (6.2) allows for comparison of HRV measurements with different mean HR levels. Note that the TVIPFM model accounts for the presence of gaps in the beat occurrence time series, created by deleting ectopic and wrong detections [218]. Finally, a discrete-time version of the modulating signal, $m(n)$, is obtained by resampling $m(t)$ at 4 Hz.

Time-domain indices will be computed based on the tachogram, while frequency-domain indices will be computed from the modulating signal $m(n)$.

6.1 Classical HRV analysis

Time-domain measures of HRV can be divided into two categories, those derived from direct measurements of the NN intervals (or instantaneous HR), and those derived from the differences between NN intervals [317]. The standard deviation of the NN intervals (SDNN) is measured in ms and reflects both SNS and PNS activity. The root mean square of successive differences between NN intervals (RMSSD) is measured in ms. The effect of the difference operation accentuates the high-frequency content of the NN interval series, and thus, RMSSD reflects vagally mediated short-term variations in HRV, in contrast with SDNN that reflects the overall HRV. While the conventional short-term recording standard for time domain indices is 5 min, researchers have proposed ultra-short-term recording periods even lower than 60 s [297].

Frequency-domain indices are estimated from the power spectral density (PSD) of $m(n)$, denoted $S(f)$. Various methods, including Welch's periodogram or autoregressive models, can be used for PSD estimation. From short-term recordings of 2 to 5 min, two main spectral components are distinguished in the low-frequency (LF) band Ω_{LF}, which extends from 0.04 up to 0.15 Hz, and in the high-frequency (HF) band Ω_{HF}, which goes from 0.15 to 0.4 Hz. The power in the LF, P_{LF}, and HF band, P_{HF} varies in relation to changes in autonomic modulation. HF spectral power is considered a measure of PNS activity, mainly due to the RSA, while LF fluctuations in HRV have been suggested to represent both sympathetic and parasympathetic modulations. Attempting to estimate the balance between SNS and PNS activity, LF to HF power ratio has been proposed as an index of the sympathovagal balance. However, to obtain an index of sympathovagal balance in normalized units (n.u.), the relative value of the LF power in proportion to the total power ($P_{\text{TOT}} = P_{\text{LF}} + P_{\text{HF}}$) is sometimes used. The normalized LF power ($P_{\text{LFn}} = P_{\text{LF}}/P_{\text{TOT}}$) is preferred because normalization tends to minimize the effect of changes in P_{TOT} on the LF component [317].

6.2 HRV analysis guided by respiration

Inclusion of respiratory rate information

Changes in ANS can alter, besides LF and HF power distribution, the main frequency of the HF component, the so-called RSA component. The power related to RSA is centered around the respiratory rate, which, however, is not contained always in the classical HF band. In order to account for the respiratory-related power outside the classical HF band, the limits of this band must be redefined. In the literature, different approaches have been proposed for the estimation of HF band boundaries [17, 18, 121, 330]. These definitions take the respiratory rate into account, and the boundaries can be either fixed or they can be defined considering the power spectrum of the respiratory signal. In this dissertation, the limits of the new HF band $\Omega^{c}_{\text{HF}} = \left[f_r^l, f_r^u\right]$, which is centered around the

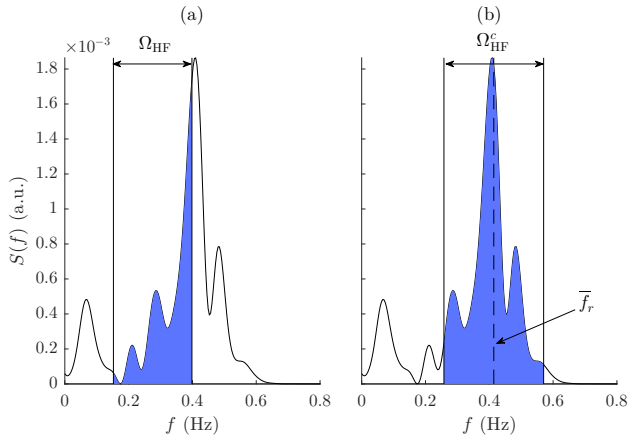

Figure 6.3: Definitions of HF bands. For the same spectrum, (a) the classical HF Ω_{HF}, and (b) the HF band Ω^c_{HF} centered around the mean respiratory rate $\overline{f}_r$ with bandwidth parameter $\Delta f = 0.15$ Hz.

mean respiratory rate $\overline{f}_r$, are given by [145],

$$f_r^l = \max\{0.15, \overline{f}_r - \Delta f\}, \tag{6.3}$$

$$f_r^u = \min\{\overline{f}_r + \Delta f, \overline{f}_{HR}/2\}, \tag{6.4}$$

where f_r^l is limited by the upper limit of Ω_{LF}, and f_r^u is limited by the half the intrinsic sampling frequency of HRV, i.e., the mean HR $\overline{f}_{HR}$ in the analyzed interval. The bandwidth of this guided by respiration band is controlled by the Δf parameter, which is fixed and it is set depending on the application, i.e., age and health condition of the subjects [121]. The definition of Ω^c_{HF} requires the estimation of the respiratory rate that can be derived from the ECG without the need of registering a respiratory signal. The use of the power in Ω^c_{HF}, P^c_{HF}, instead of P_{HF}, allows for a more robust quantification of the RSA-related power, when the respiratory rate is close to the upper limit of Ω_{HF} (see Fig. 6.3). In this case, a more robust estimation of sympathovagal balance can be obtained based on P^c_{HF}:

$$P^c_{LFn} = \frac{P_{LF}}{P_{LF} + P^c_{HF}}. \tag{6.5}$$

However, if respiratory rate is below 0.15 Hz a reliable estimation of RSA is still hindered.

Linear cardiorespiratory coupling

The joint analysis of HRV ($x(t)$) and respiratory ($y(t)$) signals can reveal all those frequencies related to PNS activity. A time-frequency (TF) analysis allows for defining a HF band with variable bandwidth at each time instant based on the TF regions where both signals are linearly coupled [245]. The respiratory influences on HRV can be assessed using the TF coherence (TFC) $\gamma(t,f)$ [246]:

$$\gamma(t,f) = \frac{|S_{XY}(t,f)|}{\sqrt{S_{XX}(t,f)S_{YY}(t,f)}}, \tag{6.6}$$

where $S_{XX}(t,f)$, $S_{YY}(t,f)$, $S_{XY}(t,f)$ are time-varying PSDs defined based on the Cohen's class distributions:

$$S_{XY}(t,f) = \mathcal{F}_{(v,\tau)\rightarrow(t,f)}\left\{A_{XY}(v,\tau)\,\Phi(v,\tau)\right\}, \tag{6.7}$$

with $A_{XY}(v,\tau)$ being the cross-ambiguity function of $x(t)$ and $y(t)$, given by,

$$A_{XY}(v,\tau) = \mathcal{F}_{t\rightarrow v}\left\{x\left(t+\frac{\tau}{2}\right)y^{*}\left(t-\frac{\tau}{2}\right)\right\}, \tag{6.8}$$

and $\Phi(v,\tau)$, a simplified version of the multiform-tiltable exponential kernel:

$$\Phi(v,\tau) = \exp\left\{-\pi\left[\left(\frac{v}{v_0}\right)^2+\left(\frac{\tau}{\tau_0}\right)^2\right]^{2\lambda}\right\}. \tag{6.9}$$

This method offers an excellent temporal resolution, and it is used for tracking transient changes of HRV. The parameters of $\Phi(v,\tau)$ are set to $v_0 = 0.045$, $\tau_0 = 0.05$, and $\lambda = 0.3$, allowing the suppression of the interference terms [247]. The Fourier transform operator $\mathcal{F}$ is used to pass from the ambiguity function domain (v,τ) to the TF domain (t,f).

Estimation of TF regions, characterized by a significant coherence level, is established based on a surrogate data analysis. To do that, $x(t)$ and $y(t)$ are defined as two white gaussian noises and a TFC statistical threshold ($\gamma_{TH}(t,f)$) is constructed based on the distribution of coherence values corresponding to 250 repetitions of those uncorrelated processes with 1% risk of concluding that $x(t)$ and $y(t)$ are coupled when there is no actual coupling (null hypothesis). Regions with statistically significant coupling, i.e., $\gamma(t,f) \geq \gamma_{TH}(t,f)$, are identified by a TF mask $M(t,f)$ of logical values, where 0 and 1 mean lack and presence of coupling, accordingly. The portions of $M(t,f)$ that are smaller than a rectangle of sides 2 s x $\Delta_f/2$ Hz are removed, with Δ_f being a term related to the frequency resolution (see [246]), adding robustness to the final estimates.

The joint analysis of respiration and HRV can be also used to identify overlaps occurring between components at frequencies with different physiological meaning, e.g. LF and respiratory-related components. Vagal activity can easily generate oscillations in the heart rhythms that cross over into the LF band during low respiratory rates or when one sighs or takes a deep breath [297]. The set of time instants where respiration and HRV signal are coupled, denoted Ω_M, and when those coupling regions are overlapping with the LF band for a bandwidth percentage higher than 25%, i.e. 0.0275 Hz, denoted Ω_M^{LF}, can be easily derived through the TF regions where $M(t,f) = 1$. The subset of time instants where HRV indices can be measured is $\Omega_r \equiv \{t \in \Omega_M; t \notin \Omega_M^{LF}\}$. The time percentages where $t \in \Omega_M$, $t \in \Omega_M^{LF}$, and $t \in \Omega_r$ are abbreviated as $\mathcal{T}_M$, $\mathcal{T}_M^{LF}$, and $\mathcal{T}_r$, respectively. Parasympathetic activity, which refers to all respiratory-driven components in HRV, is measured by:

$$P_{HF}^{r}(t) = \int_{0.04}^{f_{HR}(t)/2} S_{XX}(t,f)M(t,f)df, \;\; \forall\; t \in \Omega_r, \tag{6.10}$$

where no estimation is conducted during overlapping ($t \in \Omega_M^{LF}$) and the maximum analyzed frequency at each time instant is half the instantaneous HR ($f_{HR}(t)$). Sympathetic

activity is measured in the LF band as:

$$P^r_{\mathrm{LF}}(t) = \int_{0.04}^{0.15} S_{\mathrm{XX}}(t,f)\,(1-M(t,f))\,df,\ \forall\ t \in \Omega_r, \tag{6.11}$$

where those frequencies related to respiration are excluded through the term $(1-M(t,f))$. Using the eq. (6.10) and (6.11), the normalized LF power (see Fig. 6.4) is defined as:

$$P^r_{\mathrm{LFn}}(t) = P^r_{\mathrm{LF}}(t)/(P^r_{\mathrm{LF}}(t) + P^r_{\mathrm{HF}}(t))\,,\ \forall\ t \in \Omega_r. \tag{6.12}$$

Separating respiratory influences from HRV signal

Although, time instants where respiratory-related components lay within the LF band can be detected and discarded from subsequent analysis, such approach may not be adequate in short recordings, if an important percentage of data is removed. To avoid an underestimation of RSA and, thus a biased sympathovagal balance, respiratory influences can be extracted from the HRV signal. The residual, being a component that do not reflect respiratory information, can be used to estimate, mainly, SNS activity. In a comparison study [347], from all methods proposed for separating respiratory influences from HRV, the orthogonal subspace projection (OSP) showed one of the most robust performance in classifying stress periods based on the residual tachogram. In [338], using previously known monocomponent or broadband respiratory signals and simulated HR profiles, an OSP-based approach resulted to decomposition errors lower than 1%, and improved the estimation of sympathovagal balance.

In order to extract all dynamics of a HRV signal $\mathbf{X}$ $(N \times 1)$ that are linearly related to the respiratory signal $\mathbf{Y}$ $(N \times 1)$, with N being the length of the signals, $\mathbf{X}$ can be projected onto a subspace $\mathbf{V}$ composed of all respiratory variations. In this study, the subspace $\mathbf{V}$ $((N-q)\times(q+1))$ is defined by $q+1$ delayed versions of $\mathbf{Y}$, which are constructed by selecting intervals of length $N-q$ on a sample-to-sample basis. The value of q is the model order and is defined as the minimum amount of delays obtained using both the Akaike information criterion and the minimum description length principle. The delay q is limited to 25 s, which corresponds to the lower limit of LF band i.e., 0.04 Hz. After creating the subspace $\mathbf{V}$, the projection matrix $\mathbf{P} = \mathbf{V}\left(\mathbf{V}^T\mathbf{V}\right)^{-1}\mathbf{V}^T$ can be used to estimate the respiratory component of HRV as [338]:

$$\mathbf{X}_r = \mathbf{P}\mathbf{X}, \tag{6.13}$$

where $\mathbf{X}_r$ contains all dynamics of $\mathbf{X}$ linearly related to respiration. The residual component is given by,

$$\mathbf{X}_{\tilde{r}} = \mathbf{X} - \mathbf{X}_r, \tag{6.14}$$

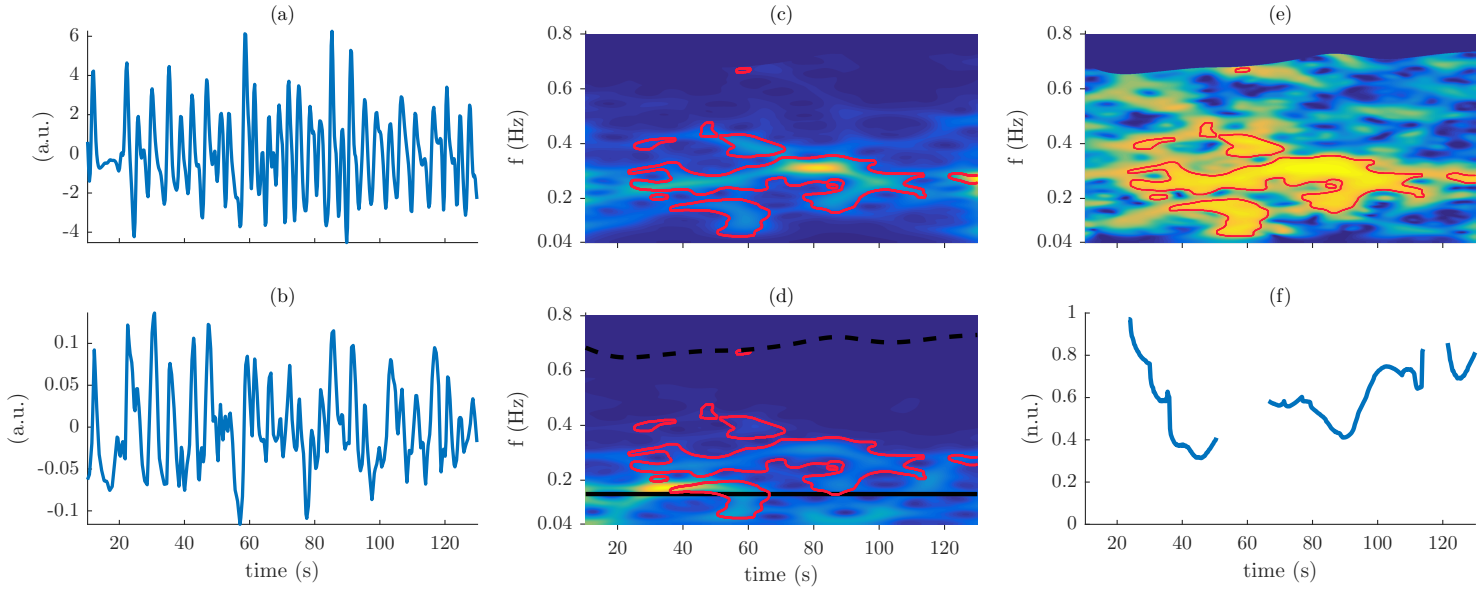

Figure 6.4: An example of TFC between respiration and HRV. (a) Respiratory signal $y(t)$, (b) HRV signal $x(t)$, (c) PSD of $y(t)$, (d) PSD of $x(t)$, (e) TFC $\gamma(t,f)$, and (f) normalized LF power $P^r_{\mathrm{LFn}}(t)$. In red are marked the areas with significant coupling defined by the TF mask $M(t,f)$ ($\mathcal{T}_{\mathrm{M}}$ = 73.6%). The black solid line denotes the upper limit of LF band, i.e. 0.15 Hz, while the dashed line denotes $f_{\mathrm{HR}}(t)/2$. The estimation is conducted for $\mathcal{T}_r$ = 62.3% due to the overlapping between the areas defined by $M(t,f)$ and LF band ($\mathcal{T}^{\mathrm{LF}}_{\mathrm{M}}$ = 11.3%).

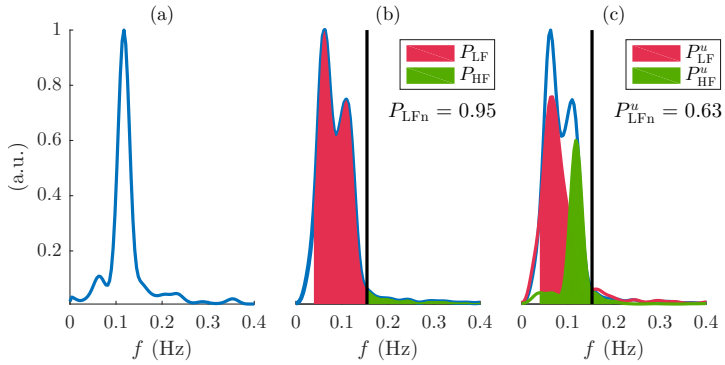

Figure 6.5: Estimation of sympathovagal balance using OSP decomposition. (a) PSD of the respiratory signal, (b) estimation of sympathovagal balance P_{LFn} using the classical definition of the spectral bands in $S(f)$, and (c) unconstrained estimation of sympathovagal balance P^u_{LFn} based on $S_r(f)$ (in green) and $S_{\tilde{r}}(f)$ (in red).

where $\mathbf{X}_{\tilde{r}}$ contains all other, not related to respiration, modulations on HRV. In this way, unconstrained estimation of LF and HF power is obtain from,

$$P^u_{\mathrm{HF}} = \int_{0.04}^{\overline{f}_{\mathrm{HR}}/2} S_r(f)df, \tag{6.15}$$

$$P^u_{\mathrm{LF}} = \int_{0.04}^{0.15} S_{\tilde{r}}(f)df, \tag{6.16}$$

where $S_r(f)$ and $S_{\tilde{r}}(f)$ are the PSDs of $\mathbf{X}_r$ and $\mathbf{X}_{\tilde{r}}$, respectively. Unconstrained estimation of sympathovagal balance can be derived from eq. (6.15) and eq. (6.16) as:

$$P^u_{\mathrm{LFn}} = P^u_{\mathrm{LF}}/(P^u_{\mathrm{LF}} + P^u_{\mathrm{HF}}). \tag{6.17}$$

An example of OSP decomposition when the respiratory rate lies in the LF band is displayed in Fig. 6.5.

Table 6.1 summarizes the indices derived from different HRV analyses guided by respiration.

6.3 Quadratic nonlinear cardiorespiratory coupling

Respiratory information, besides the fact that it can be included in HRV analyses for improving the estimation of sympathovagal balance, may provide additional information for the cardiorespiratory coupling function. Anatomical studies have demonstrated that synaptic interactions between cardiac and respiratory rhythm generators in the brainstem give rise to cardiorespiratory coupling phenomena [15, 84, 102]. The cardiorespiratory system is characterized by a complex interplay of several linear and nonlinear subsystems that interact via feed-forward and feed-back mechanisms [288, 293]. Thus, it has been hypothesized that HRV includes various oscillations that might be nonlinearly related to respiration [158, 288, 293]. Various methods have been proposed to assess

Table 6.1: Indices derived from HRV analyses guided by respiration

Inclusion of respiratory rate information	
A new HF band Ω^c_{HF} of fixed width centered around the mean respiratory rate is used to account for the respiratory-related power outside the classical HF band	
P^c_{HF}	The RSA-related power contained in Ω^c_{HF}
P^c_{LFn}	Normalized LF power using P^c_{HF}
Linear cardiorespiratory coupling	
TF regions where HRV and respiratory signal are linearly coupled are used to reveal those frequencies related to respiration and those time instants where LF and respiratory-driven components are overlapping	
$P^r_{\mathrm{HF}}(t)$	The instantaneous power of all respiratory-driven components in HRV
$P^r_{\mathrm{LF}}(t)$	The instantaneous power in the LF band, excluding respiratory-related components
$P^r_{\mathrm{LFn}}(t)$	Sympathovagal balance index based on $P^r_{\mathrm{LF}}(t)$ and $P^r_{\mathrm{HF}}(t)$
Separating respiratory influences from HRV signal	
Decomposition of HRV into a respiration-related and -non related component by means of OSP	
P^u_{HF}	The power of the respiration-related component
P^u_{LF}	The LF power of the non-related to respiration component
P^u_{LFn}	Unconstrained sympathovagal balance index using P^u_{LF} and P^u_{HF}

nonlinear cardiorespiratory coupling [56, 149, 160], including nonlinear prediction [97], entropy [348], symbolization [21], phase synchronization [195] and recurrence quantification analysis [55]. Information theory has proven to be useful to evaluate directional interactions in cardiorespiratory data [98] and it has been found that those interactions are mostly unidirectional from respiration to HRV [100]. The tendency of unidirectional coupling from respiratory to cardiovascular system has been found also in terms of mutual predictability considering weak coupling between two self-sustained oscillators from bivariate data [254, 277].

Quadratic phase coupling

When oscillations of two signals interact through a nonlinear system new harmonics with frequency and phase correlations will appear. Fig. 6.6 shows a specific class of nonlinear interaction between two oscillations through a Quadratic-Linear (Q-L) system. The resulting components have characteristic phases and frequencies that could not have been produced through a linear system. A component that arises from the interaction of two oscillations f_1 (ϕ_1) and f_2 (ϕ_2) through a Q-L system, is characterized by the same relationship in both frequency and phase, e.g. the phase of the component at the sum

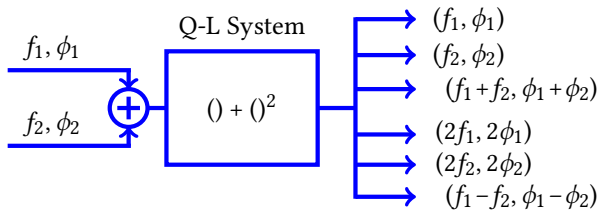

Figure 6.6: The block diagram of a Quadratic-Linear (Q-L) system and the harmonics generated by 2 interacting oscillations f_1 and f_2, with phases ϕ_1 and ϕ_2, respectively.

of f_1 and f_2, i.e., $f_1 + f_2$, is $\phi_1 + \phi_2$, or the phase of the component at $2f_1$, is $2\phi_1$, etc. This phenomenon is known as quadratic phase coupling (QPC). QPC is not detectable by means of power spectral estimation because phase information is suppressed.

6.3.1 Methods

Higher-order spectra

QPC can be revealed using a type of higher-order spectra (HOS), known as the bispectrum that is given by [65],

$$\begin{aligned} B(f_1, f_2) &= E\left[X(f_1)X(f_2)X^*(f_1+f_2)\right] \\ &= E\left[\mathcal{A}_x(f_1)\mathcal{A}_x(f_2)\mathcal{A}_x(f_1+f_2)e^{j(\phi_x(f_1)+\phi_x(f_2)-\phi_x(f_1+f_2))}\right], \end{aligned} \tag{6.18}$$

where $X(f) = \mathcal{A}_x(f)e^{j\phi_x(f)}$ is the Fourier transform (FT) of a segment (or windowed portion) of the signal $x(t)$, with $\mathcal{A}_x(f)$ and $\phi_x(f)$ being the amplitude and phase of the Fourier transform, respectively, and $E[.]$ denotes the window averaging operation. The bispectrum is a function of two frequencies (bifrequency domain) unlike the power spectrum which is a function of one frequency variable (frequency domain). The magnitude of the bispectrum $|B(f_1, f_2)|$ (biamplitude) is considered that reflects QPC. If QPC is present, i.e., $\phi_x(f_1+f_2) = \phi_x(f_1) + \phi_x(f_2)$, the product $X(f_1)X(f_2)X^*(f_1+f_2)$ is positive real number across all segments. In case of linear coupling, where QPC is absent, this product is a complex number. Averaging positive real numbers (QPC case) will lead to higher values of $|B(f_1, f_2)|$, comparing to the averaging of complex numbers with phases that vary randomly across segments (linear case). However, $|B(f_1, f_2)|$ can also get values similar to QPC case, when the phase across all segments is constant, but not zero. This case is referred to as quadratic phase uncoupling (QPU). QPU is different from QPC, since it could arise from linear coupling and a component at $f_1 + f_2$ (not related by anyway to f_1 and f_2) that is stationary. Moreover, the bispectrum depends on both the phase and the amplitude of interacting frequency components across segments. A normalized bispectrum, known as bicoherence, is given by [130],

$$b(f_1, f_2) = \frac{|B(f_1, f_2)|}{E\left[|X(f_1)X(f_2)X^*(f_1+f_2)|\right]}, \tag{6.19}$$

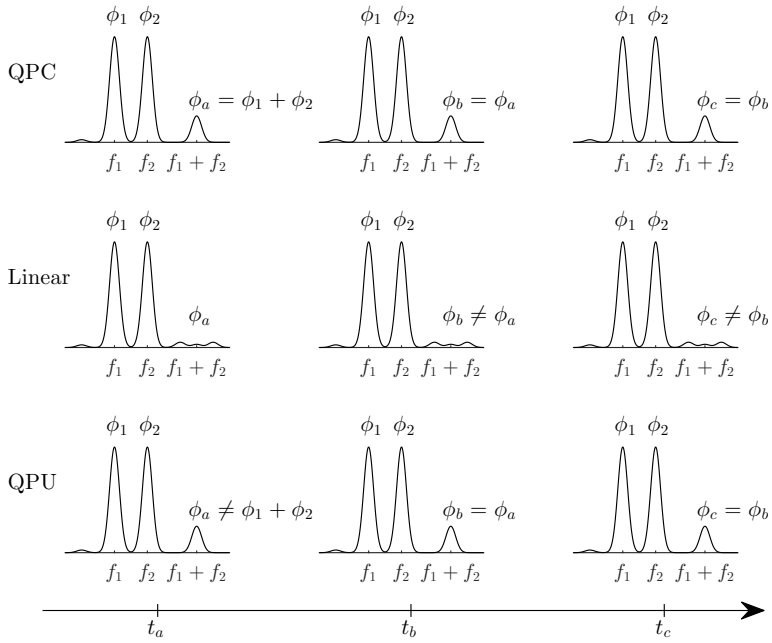

Figure 6.7: An illustrative example of phase evolution in QPC, linear, and QPU case. The phases ϕ_a, ϕ_b, and ϕ_c of a possible nonlinear product ($f_1 + f_2$) between the interacting oscillations f_1 (ϕ_1) and f_2 (ϕ_2) across 3 segments in t_a, t_b, and t_c, respectively.

where the amplitude dependence is removed by normalizing with the bispectrum after setting all phases to 0, thereby ensuring that the phase of the bispectrum (biphase) is zero. Although there are different definitions of the normalization term, this definition is the most intuitive since it corresponds to the case where there is perfect phase coupling, because all of the samples have zero phase. Therefore, the bicoherence has a value between 0 (random phases across segments) and 1 (phase synchronization across segments). However, QPC detection based on bicoherence still presents some limitations [93, 185], because values close to 1 can result from constant phase relationship among interacting oscillations (QPU case), which not necessarily implies QPC.

An illustrative example of phase evolution in QPC, linear, and QPU case is shown in Fig. 6.7. When the oscillations f_1 (ϕ_1) and f_2 (ϕ_2) interact through a Q-L system, the phase of the nonlinear product at $f_1 + f_2$, is constant across all segments and it has the same relationship as frequencies, i.e., $\phi_1 + \phi_2$. Linear and QPU cases do not fulfill these criteria. A numerical example of bispectrum and bicoherence values considering different biamplitude and biphase relationships across 3 segments is given in Table 6.2. As can be seen, $|B(f_1, f_2)|$ is not a reliable measure of QPC since it can be influenced by the amplitude of the interacting oscillations, while $b(f_1, f_2)$ might be suitable for discriminating random phase relationships. However, $b(f_1, f_2)$ is sensitive to constant phase relationships.

Other features that have been proposed to describe the HOS domain are the distribution of local maxima in the biamplitude domain and the regularity of the biphase [238].

Table 6.2: A numerical example of bispectrum and bicoherence values in QPC, linear, and QPU case

	$\lvert B(f_1,f_2)\rvert$	$b(f_1,f_2)$
QPC	$\left\lvert\frac{1}{3}\left(\frac{A}{2}e^{j0}+\frac{A}{2}e^{j0}+\frac{A}{2}e^{j0}\right)\right\rvert=\frac{A}{2}$	$\frac{\lvert B(f_1,f_2)\rvert}{\frac{1}{3}\left(\frac{A}{2}+\frac{A}{2}+\frac{A}{2}\right)}=1$
Linear	$\left\lvert\frac{1}{3}\left(2Ae^{j0}+2Ae^{j\pi/2}+2Ae^{-j\pi/2}\right)\right\rvert=\frac{2A}{3}$	$\frac{\lvert B(f_1,f_2)\rvert}{\frac{1}{3}(2A+2A+2A)}=0.33$
QPU	$\left\lvert\frac{1}{3}\left(Ae^{j\pi/2}+Ae^{j\pi/2}+Ae^{j\pi/2}\right)\right\rvert=A$	$\frac{\lvert B(f_1,f_2)\rvert}{\frac{1}{3}(A+A+A)}=1$

The mean distance D_{M} of the L_{M} local maxima located at $\left(f_1^l, f_2^l\right)$ $(l = 1,\ldots,L_{\mathrm{M}})$ to the largest peak of biamplitude located at $\left(f_1^{\mathrm{M}}, f_2^{\mathrm{M}}\right)$ is given by,

$$D_{\mathrm{M}} = \frac{1}{L_{\mathrm{M}}}\sum_{l=1}^{L_{\mathrm{M}}}\sqrt{\left(f_1^{\mathrm{M}}-f_1^l\right)^2+\left(f_2^{\mathrm{M}}-f_2^l\right)^2}. \tag{6.20}$$

To reduce the influence of spurious components on D_{M}, a peak in the biamplitude is considered local maximum only if it is at least largest than half of $A_{\mathrm{M}} = \left|B\left(f_1^{\mathrm{M}}, f_2^{\mathrm{M}}\right)\right|$. To measure the regularity of the biphase, a vector $\mathbf{v}_\Phi$ with the biphase values at those bi-frequencies, i.e., (f_1, f_2) pairs, that fulfill $|B(f_1,f_2)| \geq 0.5A_{\mathrm{M}}$ is created. Then, $\mathbf{v}_\Phi$ is quantized in N_{E} bins $\mathcal{B}_0,\cdots,\mathcal{B}_{N_{\mathrm{E}}-1}$, sized $2\pi/N_{\mathrm{E}}$ radians, with N_{E} being the number of samples in the analyzed interval. Then, the Shanon's entropy P_{E} is obtained from,

$$P_{\mathrm{E}} = -\sum_{n=0}^{N_{\mathrm{E}}-1} p\left(\mathcal{B}_n\right)\ln\left(p\left(\mathcal{B}_n\right)\right), \tag{6.21}$$

where $p\left(\mathcal{B}_n\right)$ is the relative histogram of $\mathcal{B}_n$, and it is computed by dividing the number of elements in each bin by the total number of bi-frequencies.

Probably one of the most popular application of HOS is in the study of electroencephalogram for depth of anaesthesia [143, 144] and pain characterization [128, 129]. A variety of studies in HOS field have been implemented to analyze cardiac arrhythmias through the nonlinear properties of HRV signals [64, 264]. In [160] and [350], a bispectral analysis has been applied to cardiorespiratory data in order to analyze the coupling mechanisms between respiratory and cardiac systems.

Continuous wavelet transform

Although different techniques have been proposed to deal with the drawbacks of the bispectrum, the main limitation is the signal length requirement for sufficient window averages. Continuous wavelet transform (CWT) introduction in bispectrum field reduced time averages to a minimum, allowing the application of HOS in non-stationary biomed-

ical signals [335]. The CWT of a signal $x(t)$ is defined as [328]:

$$\begin{aligned} W_x(f,\tau) &= \frac{1}{\sqrt{f_c/f}} \int_{-\infty}^{\infty} x(t)\, \psi^*\left(\frac{t-\tau}{f_c/f}\right) \mathrm{d}t, \\ &= \mathcal{A}_x(f,\tau)\, e^{j\phi_x(f,\tau)}, \end{aligned} \tag{6.22}$$

where $\psi(t)$ is the mother wavelet translated by a factor τ and scaled by a factor a, $a = f_c/f$. The parameter f_c is the center frequency of the mother wavelet (see (6.23)). $\mathcal{A}_x(f,\tau)$ and $\phi_x(f,\tau)$ are the amplitude and phase coefficients of the CWT, respectively. In this dissertation, the complex Morlet wavelet is used, due to its good time localization property, which is given by,

$$\psi(t) = \frac{1}{\sqrt{\pi\sigma}} e^{-t^2/\sigma}\, e^{j2\pi f_c t}, \tag{6.23}$$

where σ is the variance parameter that controls the bandwidth of the mother wavelet.

Wavelet bicoherence

To assess time-phase relationships of quadratic nature among interacting oscillations between different signals $x(t)$, $y(t)$, and $z(t)$, with CWT coefficients $W_x(f,\tau)$, $W_y(f,\tau)$ and $W_z(f,\tau)$, respectively, the wavelet cross-bispectrum $B_{\mathrm{W}}(f_1,f_2)$ (WBS) can be employed. WBS consists of the wavelet biamplitude $A_{\mathrm{B}}(f_1,f_2)$ and the wavelet biphase $\Phi_{\mathrm{B}}(f_1,f_2)$, and is defined as [335]:

$$\begin{aligned} B_{\mathrm{W}}(f_1,f_2) &= \int_T W_x(f_1,\tau)\, W_y(f_2,\tau)\, W_z^*(f_{12},\tau)\, \mathrm{d}\tau \\ &= \int_T A_{\mathrm{W}}(f_1,f_2,\tau)\, e^{j\Phi_{\mathrm{W}}(f_1,f_2,\tau)} \mathrm{d}\tau \\ &= A_{\mathrm{B}}(f_1,f_2)\, e^{j\Phi_{\mathrm{B}}(f_1,f_2)}, \end{aligned} \tag{6.24}$$

where $f_{12} = f_1 + f_2$. $A_{\mathrm{w}}(f_1,f_2,\tau)$ and $\Phi_{\mathrm{w}}(f_1,f_2,\tau)$ are the instantaneous wavelet biamplitude and biphase. Note that the expectation operation in eq. (6.18) has been replaced here by the integration over a finite time interval T. The normalized WBS, known as squared wavelet bicoherence (WB), is given by [335]:

$$b^2_{\mathrm{W}}(f_1,f_2) = \frac{|B_{\mathrm{W}}(f_1,f_2)|^2}{B_{\mathrm{N}}(f_1,f_2)}, \tag{6.25}$$

where the dependence of $B_{\mathrm{W}}(f_1,f_2)$ on the amplitude of interacting oscillations is removed by the normalization term:

$$B_{\mathrm{N}}(f_1,f_2) = \int_T \left|W_x(f_1,\tau)\, W_y(f_2,\tau)\right|^2 \mathrm{d}\tau \int_T |W_z(f_{12},\tau)|^2\, \mathrm{d}\tau. \tag{6.26}$$

Although $0 \le b^2_{\mathrm{W}} \le 1$, similar to bicoherence, WB does not reliably measure QPC, since high values are observed also when QPU is present [93].

Biphase randomization wavelet bicoherence

Biphase randomization wavelet bicoherence (BRWB), a modification of WB proposed by Li et al. [206], deal with the problem of the previous definitions of bicoherence. First, a phase randomization term $e^{j\alpha_k \Phi_B(f_1,f_2)}$ is added to bispectral estimation:

$$B_R(f_1,f_2) = E\left[\int_T W_x(f_1,\tau)\, W_y(f_2,\tau)\, W_z^*(f_{12},\tau)\cdot e^{j\alpha_k \Phi_B(f_1,f_2)} \mathrm{d}\tau\right], \tag{6.27}$$

where the randomized WBS $B_R(f_1,f_2)$ is obtained from the ensemble average of $K_R = 100$ realizations of a random variable, α_k, uniformly distributed in $(-\pi,\pi]$. When QPC is present, the wavelet biphase $\Phi_B(f_1,f_2)$ is zero, and thus, the phase randomization term in eq. (6.27) becomes zero regardless the value of α_k. On the contrary, when QPC is absent, the instantaneous wavelet biphase is randomized in $(-\pi,\pi]$. Thus, lower values of $B_R(f_1,f_2)$ are obtained because of the expectation operation in eq. (6.27) [206]. Then, the squared BRWB is obtained from,

$$b_R^2(f_1,f_2) = \frac{|B_R(f_1,f_2)|^2}{B_N(f_1,f_2)}. \tag{6.28}$$

The values of $b_R^2(f_1,f_2)$ close to 1 correspond only to QPC, while lower values are related to linear coupling and QPU cases.

Real wavelet biphase

The BRWB can be used for detecting QPC but increases the computational complexity, since bispectral estimation needs to be repeated for the randomization process. A novel method, named real wavelet biphase (RWB), is proposed in this thesis for QPC detection overcoming the previous limitations and simplifying the computational complexity at the same time. RWB is based on the instantaneous wavelet biphase, which is suggested that carries the information about the nature of quadratic coupling.

Let us consider, the signal $x(t) = Ae^{j(2\pi f_0 t+\phi_0)}$, with fundamental frequency f_0 and initial phase ϕ_0, and without any additive noise for simplification reasons. By doing the variable change $t' = \dfrac{t-\tau}{f_c/f}$ in eq. (6.22) we obtain:

$$\begin{aligned} W_x(f,\tau) &= \frac{Ae^{j\phi_0}}{\sqrt{f_c/f}}\int_{-\infty}^{\infty} e^{j2\pi f_0(t' f_c/f+\tau)}\psi^*\left(t'\right)\mathrm{d}t'\left(\frac{f_c}{f}\right) \\ &= \sqrt{\frac{f_c}{f}}\,Ae^{j(2\pi f_0\tau+\phi_0)}\int_{-\infty}^{\infty}\psi^*\left(t'\right)e^{j2\pi\frac{f_0 f_c}{f}t'}\mathrm{d}t' \\ &= \sqrt{\frac{f_c}{f}}\,Ae^{j(2\pi f_0\tau+\phi_0)}e^{-\pi^2\sigma f_c^2(f_0/f-1)^2}, \end{aligned} \tag{6.29}$$

where $e^{-\pi^2\sigma(f-f_c)^2}$ is the Fourier transform of the complex mother wavelet $\psi(t)$. Based on the above, if two oscillations of $x(t)$ and $y(t)$ at frequencies f_1 and f_2, respectively, interact and produce oscillations at f_{12} in $z(t)$, the instantaneous wavelet biphase, can be written as:

$$\begin{aligned}\Phi_{\mathrm{W}}(f_1,f_2,\tau) &= \phi_x(f_1,\tau)+\phi_y(f_2,\tau)-\phi_z(f_{12},\tau)\\ &= (2\pi f_1\tau+\phi_1)+(2\pi f_2\tau+\phi_2)-(2\pi f_{12}\tau+\phi_{12})\\ &= 2\pi(f_1+f_2-f_{12})\tau+(\phi_1+\phi_2-\phi_{12}),\end{aligned} \tag{6.30}$$

where ϕ_1, ϕ_2, ϕ_{12} are the initial phases of the components f_1, f_2, f_{12}, respectively. When QPC is present (see Fig. 6.6), i.e., $f_{12} = f_1 + f_2$ and $\phi_{12} = \phi_1 + \phi_2$, $\Phi_{\mathrm{W}}(f_1,f_2,\tau)$ is zero. In case of QPU, $f_{12} = f_1 + f_2$ and $\phi_{12} \neq \phi_1 + \phi_2$ lead to $\Phi_{\mathrm{W}}(f_1,f_2,\tau) \neq 0$. Taking into account that, when either frequency or phase requirements are not fulfilled is reflected in $\Phi_{\mathrm{W}}(f_1,f_2,\tau)$, the phase information may suffice for QPC detection.

Based on the aforementioned approach, the mathematical formula of eq. (6.24) is simplified in terms of the complex argument removing directly the amplitude effect:

$$B_\Phi(f_1,f_2) = \int_T e^{j\Phi_{\mathrm{W}}(f_1,f_2,\tau)}\mathrm{d}\tau. \tag{6.31}$$

RWB is defined from the real part of eq. (6.31) with a time normalization term as:

$$\begin{aligned}b_\Phi(f_1,f_2) &= \frac{1}{T}\Re\{B_\Phi(f_1,f_2)\}\\ &= \frac{1}{T}\int_T \cos(\Phi_{\mathrm{W}}(f_1,f_2,\tau))\,\mathrm{d}\tau.\end{aligned} \tag{6.32}$$

This simple computation is the mean cosine value of the instantaneous wavelet biphase in the interval T and is bounded between -1 and 1. Values close to 1 correspond to perfect QPC. High values of RWB imply that $\Phi_{\mathrm{W}}(f_1,f_2,\tau)$ is very small during the whole analyzed interval T, indicating a long lasting phase synchronization.

In order to compare the computed amount of QPC with the other methods, the squared values of RWB ($b^2_\Phi(f_1,f_2)$) are considered:

$$b^2_\Phi(f_1,f_2) = \begin{cases} 0, & b_\Phi(f_1,f_2) < b_{\mathrm{TH}}(f_1,f_2),\\ b^2_\Phi(f_1,f_2), & b_\Phi(f_1,f_2) \geq b_{\mathrm{TH}}(f_1,f_2),\end{cases} \tag{6.33}$$

where the lowest value of $b_{\mathrm{TH}}(f_1,f_2)$ is given by the upper bound of a statistical noise threshold. The statistical noise in the computation of all wavelet-based bispectral measures due to the replacement of the integrals by summations (over N_{T} points) and the use of non-orthogonal mother wavelet is given by [335]:

$$b^2_{\mathrm{TH}}(f_1,f_2) \geq \left[\frac{f_s}{\min(|f_1|,|f_2|,|f_1+f_2|)\cdot 2N_{\mathrm{T}}}\right]. \tag{6.34}$$

Time-varying bispectral analysis

The detection of short-lived couplings requires the computation of bispectral measures to be done in small intervals which, however, reduces the resolution of CWT, causing errors in phase estimation. For a time-varying tracking of QPC the definition of instantaneous bispectra is given by:

$$B_{\mathrm{W}}(f_1, f_2, t) = \int_{t-T'/2}^{t+T'/2} A_{\mathrm{W}}(f_1, f_2, \tau)\, e^{j\Phi_{\mathrm{W}}(f_1, f_2, \tau)} \mathrm{d}\tau, \tag{6.35}$$

$$B_{\mathrm{N}}(f_1, f_2, t) = \int_{t-T'/2}^{t+T'/2} \left| W_x(f_1, \tau)\, W_y(f_2, \tau) \right|^2 \mathrm{d}\tau \int_{t-T'/2}^{t+T'/2} \left| W_z(f_{12}, \tau) \right|^2 \mathrm{d}\tau, \tag{6.36}$$

$$B_{\Phi}(f_1, f_2, t) = \frac{1}{T'} \int_{t-T'/2}^{t+T'/2} e^{j\Phi_{\mathrm{W}}(f_1, f_2, \tau)} \mathrm{d}\tau, \tag{6.37}$$

where CWT computation is done in a window of length T centered at the desired time point t, while the integration is carried out for the T' ($< T$) central seconds. Then, the definition of instantaneous WB ($b^2_{\mathrm{W}}(f_1, f_2, t)$), instantaneous BRWB ($b^2_{\mathrm{R}}(f_1, f_2, t)$) and instantaneous RWB ($b^2_{\Phi}(f_1, f_2, t)$), which allow the detection of couplings with at least duration T', can be done based on eq. (6.35), (6.36), and (6.37). Moreover, $b^2_{\mathrm{TH}}(f_1, f_2, t)$ can be defined for each time instant t. The values of $b^2_{\mathrm{W}}(f_1, f_2, t)$, $b^2_{\mathrm{R}}(f_1, f_2, t)$ and $b^2_{\Phi}(f_1, f_2, t)$ that do not exceed the lower limit of this time-varying statistical threshold are set to zero. The final value of $b^2_{\mathrm{TH}}(f_1, f_2, t)$ is defined based on the surrogate data analysis presented below.

Surrogate data analysis

To obtain a statistically significant estimation of QPC, a surrogate data analysis is conducted. In [323], an approach was described, which takes the Fourier transform of the original data and then assigns a random phase to each frequency component. This results in time series with the same power spectrum as the original data, but they are randomized in every other respect. Regarding HOS-surrogates, surrogate data should have the same amplitude distribution ($A_{\mathrm{W}}(f_1, f_2, \tau)$), as the original data, but any temporal phase relationship ($\Phi_{\mathrm{W}}(f_1, f_2, \tau)$) should be destroyed. A phase-randomized bispectrum for surrogate data analysis ($B_{\mathrm{S}}(f_1, f_2, t)$) has been proposed by Scully et al. [295] by replacing the biphase at each time point in the analyzed interval (T') with a uniform random variable θ in $U[-\pi : -\theta_{\mathrm{TH}}, \theta_{\mathrm{TH}} : \pi]$:

$$B_{\mathrm{S}}(f_1, f_2, t) = \int_{t-T'/2}^{t+T'/2} A_{\mathrm{W}}(f_1, f_2, \tau)\, e^{j\theta(\tau)} \mathrm{d}\tau. \tag{6.38}$$

In [295] a specific threshold $\theta_{\mathrm{TH}} = 1$ was used. The surrogate phase randomized bicoherence (SPRB) is obtained by normalizing $B_{\mathrm{S}}(f_1, f_2, t)$:

$$b_{\mathrm{S}}^2(f_1, f_2, t) = \frac{|B_{\mathrm{S}}(f_1, f_2, t)|^2}{B_{\mathrm{N}}(f_1, f_2, t)}. \tag{6.39}$$

SPRB is calculated for 100 realizations and the mean plus 2 standard deviations is used as threshold at each time point t, substituting, only when it is greater, the value of $b_{\mathrm{TH}}^2(f_1, f_2, t)$ in eq. (6.34). Finally, the original values of $b_{\mathrm{W}}^2(f_1, f_2, t)$, $b_{\mathrm{R}}^2(f_1, f_2, t)$ and $b_{\Phi}^2(f_1, f_2, t)$ greater than this threshold are preserved, otherwise are set to zero.

Cardiorespiratory QPC

The complex structure of HRV includes various oscillations that might be nonlinearly related to respiration [158, 288, 293]. Our hypothesis is that HRV signal might be formed as an output of a quadratic nonlinear system:

$$x_{\mathrm{QPC}}(t) = x_{\mathrm{L}}(t) + x_{\mathrm{R}}(t) + \frac{\varepsilon_{\mathrm{L}}}{\varepsilon_{\mathrm{L,R}}} x_{\mathrm{L}}(t)\, x_{\mathrm{R}}(t) + \frac{\varepsilon_{\mathrm{R}}}{\varepsilon_{\mathrm{R,R}}} x_{\mathrm{R}}^2(t), \tag{6.40}$$

where $x_{\mathrm{L}}(t)$ and $x_{\mathrm{R}}(t)$ represent a LF and HF components of HRV, respectively. If respiration controls HRV, not only via a linear, but also through a nonlinear function additional vagally-mediated components ($x_{\mathrm{L}}(t)\, x_{\mathrm{R}}(t)$, $x_{\mathrm{R}}^2(t)$) will appear in HRV. Interactions of vagal and sympathetic-related components of HRV might be an important aspect of homeostatic mechanism [361]. The coupling strengths ε_{L} and ε_{R} could be different, while $\varepsilon_{\mathrm{L,R}} = \sigma_{\mathrm{L,R}}^2/\sigma_{\mathrm{R}}^2$ and $\varepsilon_{\mathrm{R,R}} = \sigma_{\mathrm{R,R}}^2/\sigma_{\mathrm{R}}^2$ are two normalization terms based on the power of each nonlinear component ($\sigma_{\mathrm{L,R}}^2$, $\sigma_{\mathrm{R,R}}^2$) with respect to the respiratory power (σ_{R}^2).

Based on the above, the most adequate HOS to investigate time-variant nonlinear cardiorespiratory couplings are the instantaneous cross-bispectral definitions in eq. (6.35), (6.36), and (6.37). To detect in a HRV signal, $x(t)$, nonlinearities that are related to respiration $y(t)$, $z(t)$ represents also the HRV signal $x(t)$. Thus, for instance, $\Phi_{\mathrm{W}}(f_1, f_2, \tau)$ in eq. (6.30) is modified as:

$$\Phi_{\mathrm{W}}(f_1, f_2, \tau) = \phi_x(f_1, \tau) + \phi_y(f_2, \tau) - \phi_x(f_1 + f_2, \tau). \tag{6.41}$$

The calculation of all bispectral coefficients is done after energy normalization and mean subtraction from the analyzing signals. Coefficients are computed in the region $\Omega \in \{f_1 + f_2 \leq f_s/2\}$ [335], with f_s being the sampling frequency of the analyzing signals. Considering that a HRV signal is analyzed, the upper limit of Ω might be more restrictive, since the maximum frequency, with physiological meaning, that can be analyzed is half the mean HR. Coefficients of bispectral domains with coordinates that exceed this frequency are set to zero, since they are associated with spectrum repetitions [196].

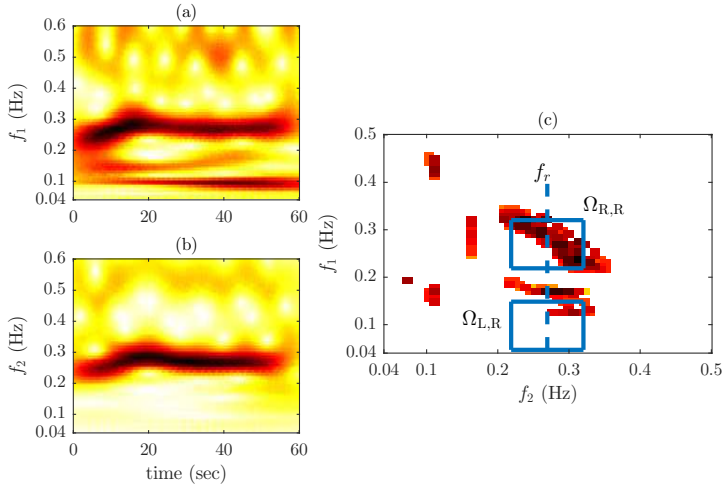

Figure 6.8: Regions for QPC assessment. CWT amplitude coefficients of (a) HRV, and (b) respiration, and (c) RWB domain. The respiratory rate f_r is marked with a dashed blue line, while the regions $\Omega_{L,R}$ and $\Omega_{L,R}$ are marked with solid blue lines.

The regions, where QPC is assessed, are defined based on the respiratory rate $f_r(t)$, which can be derived from $y(t)$ as:

$$f_r(t) = \arg\max_f \left\{ \int_{t-T'/2}^{t+T'/2} \left| W_y(f,\tau) \right| d\tau \right\}. \tag{6.42}$$

QPC between the respiration and the RSA component of HRV is identified in the region $\Omega_{R,R} : \{f_1 \in \Omega_R, f_2 \in \Omega_R\}$, where $\Omega_R = [f_r(t) - 0.05, f_r(t) + 0.05]$ Hz, while QPC between respiration and low frequency components of HRV is identified in the region $\Omega_{L,R} : \{f_1 \in \Omega_{LF}, f_2 \in \Omega_{LF}\}$. An example of the regions where QPC is assessed is shown in Fig. 6.8. QPC-related parameters are estimated for those time instants where $f_r(t)$ is greater than 0.15 Hz. The QPC level and the involved frequencies are given by,

$$C_{\mathcal{I}}^{\Phi}(t) = \max_{f_1,f_2 \in \Omega_{\mathcal{I}}} \{ b_{\Phi}^2(f_1,f_2,t) \}, \tag{6.43}$$

$$\left(\hat{f}_1^{\mathcal{I}}, \hat{f}_2^{\mathcal{I}}\right) = \arg\max_{f_1,f_2 \in \Omega_{\mathcal{I}}} \{ b_{\Phi}^2(f_1,f_2,t) \}, \tag{6.44}$$

where $\mathcal{I} \in \{[L,R], [R,R]\}$ indicates the region $\Omega_{\mathcal{I}}$ in which the parameters are computed; for the simplicity of notation the dependence of $\hat{f}_1^{\mathcal{I}}, \hat{f}_2^{\mathcal{I}}$ on t is omitted. If the region of interest consist in the whole bi-frequency domain Ω then the subscript $\mathcal{I}$ is omitted, i.e., $C^{\Phi}(t)$. QPC detection ($C_{\mathcal{I}}^{\Phi}(t) > 0$) can be performed for WB ($C_{\mathcal{I}}^{W}(t)$) and BRWB ($C_{\mathcal{I}}^{R}(t)$) by replacing $b_{\Phi}^2(f_1,f_2,t)$ with $b_W^2(f_1,f_2,t)$ and $b_R^2(f_1,f_2,t)$, respectively. The bicoherence-based measures, from which the amplitude influence has been removed, cannot be used to quantify QPC strength but only to assess the degree of QPC (phase synchronization). The strength of QPC is assessed using a novel index called normalized wavelet biampli-

Table 6.3: Indices for assessing cardiorespiratory QPC

$\Omega_{\mathrm{R,R}}(t)$	Region in bifrequency domains associated with QPC between respiration and RSA component of HRV
$\Omega_{\mathrm{L,R}}(t)$	Region in bifrequency domains associated with QPC between respiration and LF components of HRV
$C^{\Phi}_{\mathrm{R,R}}(t)$	QPC degree in $\Omega_{\mathrm{R,R}}(t)$ assessed with RWB
$C^{\Phi}_{\mathrm{L,R}}(t)$	QPC degree in $\Omega_{\mathrm{L,R}}(t)$ assessed with RWB
$E_{\mathrm{R,R}}(t)$	QPC strength in $\Omega_{\mathrm{R,R}}(t)$ assessed with NWB
$E_{\mathrm{L,R}}(t)$	QPC strength in $\Omega_{\mathrm{L,R}}(t)$ assessed with NWB

tude (NWB):

$$E_{\mathcal{J}}(t) = \frac{\left|B_{\mathrm{W}}\left(\hat{f}_1^{\mathcal{J}}, \hat{f}_2^{\mathcal{J}}, t\right)\right|}{\int\limits_{t-T'/2}^{t+T'/2} \left|W_x\left(\hat{f}_1^{\mathcal{J}}, \tau\right) W_y\left(\hat{f}_2^{\mathcal{J}}, \tau\right)\right| \mathrm{d}\tau}, \tag{6.45}$$

where the influence of the interacting oscillations amplitudes ($W_x(f_1, \tau)$ and $W_y(f_2, \tau)$) on $|B_{\mathrm{W}}(f_1, f_2, t)|$ is removed. NWB is influenced only by the coupling strength and the amplitude of nonlinear oscillations in HRV ($|W_x(f_1 + f_2, \tau)|$). Moreover, if the phase is not maintained constant at the integration interval, $E_{\mathcal{J}}(t)$ will get lower values. It should be noted that QPC detection is carried out through bicoherence-based measures, while QPC quantification is performed using the WBS ($B_{\mathrm{W}}(f_1, f_2, t)$).

For the estimation of short-live couplings, CWT is carried out in intervals of length $T = 60$ s, while the integration interval for all cross-bispectral measures is set to $T' = 10$ s. The center frequency f_c of the mother wavelet is set to half the sampling rate of respiratory and HRV signals, i.e., 2 Hz, while the parameter σ is set to 1 Hz.

The main contributions, not yet addressed in previous studies, are that the novel RWB method simplifies the computational load associated to BRWB, due to the phase randomization procedure, and as will be shown, it exhibit a more robust performance compared to WB and BRWB in the presence of delays between the interacting components under analysis. Moreover, the novel NWB metric can quantify robustly QPC strength, once detection has been performed by RWB. Table 6.3 summarizes the indices related to cardiorespiratory QPC assessment.

6.3.2 Materials

A simulation is carried out to evaluate the performance of WB, BRWB and RWB in assessing QPC, and their robustness in differentiating QPC from linear coupling and QPU. Based on the model described in eq. (6.40), the two principal components reenacting the sympathetic ($x_{\mathrm{L}}(t)$) and parasympathetic ($x_{\mathrm{R}}(t)$) activity are represented as spectral components at frequencies $f_{\mathrm{L}} = 0.1$ Hz and $f_{\mathrm{R}} = 0.25$ Hz (a common respiratory rate), respectively. To do that, two white gaussian noises are filtered using two autoregressive models, which are designed locating at the polar plane two conjugated poles at LF for sympathetic activity ($p_1^{\mathrm{L}} = 0.95e^{j2\pi f_{\mathrm{L}}/f_s}$, $p_2^{\mathrm{L}} = p_1^{\mathrm{L}*}$) and at HF for RSA component

($p_1^{\mathrm{R}} = 0.95e^{j2\pi f_{\mathrm{R}}/f_s}$, $p_2^{\mathrm{R}} = p_1^{\mathrm{R}*}$) [248]. The two signals $x_{\mathrm{L}}(t)$, $x_{\mathrm{R}}(t)$ are normalized to have the same power and the respiration signal is defined as $y(t) = x_{\mathrm{R}}(t)$.

In earlier works [161, 162], it has been suggested that the nonlinear phase coupling occurs when the systems are in phase (QPC), or there is a small constant phase deviation, i.e., a delay ($\mathrm{QPC_D}$). Time delays arise naturally in coupled systems as a consequence of propagation effects, or may be introduced through closed-loop control schemes [99]. In order to study the effect of constant delays on bispectral measures, a modification of eq. (6.40) is proposed:

$$x_{\mathrm{D}}(t) = x_{\mathrm{L}}(t) + x_{\mathrm{R}}(t) + \frac{\varepsilon_{\mathrm{L}}}{\varepsilon_{\mathrm{L,R}}} x_{\mathrm{L}}(t - t_{\mathrm{L}})\, x_{\mathrm{R}}(t - t_{\mathrm{R}}) + \frac{\varepsilon_{\mathrm{R}}}{\varepsilon_{\mathrm{R,R}}} x_{\mathrm{R}}^2(t - t_{\mathrm{R}}), \tag{6.46}$$

where $t_{\mathrm{L}} = \phi_{\mathrm{D}}/(2\pi f_{\mathrm{L}})$, $t_{\mathrm{R}} = \phi_{\mathrm{D}}/(2\pi f_{\mathrm{R}})$ are the delay parameters, which are defined, for simplicity, based on common phase shift ϕ_{D}. To simulate QPU, the phase dynamics of the nonlinear components should be destroyed, while their second-order spectral properties, i.e., power spectra, are maintained unchanged. The nonlinear components $x_{\mathrm{L}}(t)\, x_{\mathrm{R}}(t)$, $x_{\mathrm{R}}^2(t)$ are subjected to phase randomization using two variables $\phi_{\mathrm{L,R}}$, $\phi_{\mathrm{R,R}}$ uniformly distributed within $(-\pi, \pi]$. Thus, QPU is given by,

$$x_{\mathrm{QPU}}(t) = x_{\mathrm{L}}(t) + x_{\mathrm{R}}(t) + \frac{\varepsilon_{\mathrm{L}}}{\varepsilon_{\mathrm{L,R}}} \mathcal{F}^{-1}\{|X_{\mathrm{L,R}}(f)|\, e^{j\phi_{\mathrm{L,R}}}\} + \frac{\varepsilon_{\mathrm{R}}}{\varepsilon_{\mathrm{R,R}}} \mathcal{F}^{-1}\{|X_{\mathrm{R,R}}(f)|\, e^{j\phi_{\mathrm{R,R}}}\}, \tag{6.47}$$

where $X_{\mathrm{L,R}}(f)$ and $X_{\mathrm{R,R}}(f)$ are the FTs of $x_{\mathrm{L}}(t)\, x_{\mathrm{R}}(t)$ and $x_{\mathrm{R}}^2(t)$, respectively, and $\mathcal{F}^{-1}$ denotes the inverse FT.

Reliability of QPC detection

The first simulation is performed to assess the reliability of RWB ($C_{\mathcal{J}}^{\Phi}(t)$) to detect QPC with low strength ($\varepsilon_{\mathrm{L}} = \varepsilon_{\mathrm{R}} = 0.1$) in the presence of constant delays (ϕ_{D}) based on eq. (6.46). Moreover, the effect of the surrogate data derived thresholds, controlled via θ_{TH}, on the maximum delay that can be detected is investigated. The phase shift term ϕ_{D} varies from 0 to 1.57 rad with a step of 0.31 rad to simulate a progressive deviation from the perfect "phase locking", while the threshold θ_{TH} varies from 0 to 1.25 rad with a step of 0.25 rad. The simulation is repeated 100 times for each case and the median values are obtained for RWB as well as for WB and BRWB for comparison purpose.

Robustness of QPC assessment

A second simulation is carried out to evaluate the robustness of RWB ($C_{\mathcal{J}}^{\Phi}(t)$) and NWB ($E_{\mathcal{J}}(t)$) to quantify QPC under different coupling strengths and to discriminate QPC from linear and QPU relationships. Linear cardiorespiratory couplings are simulated selecting in eq. (6.40) $\varepsilon = \varepsilon_{\mathrm{L}} = \varepsilon_{\mathrm{R}} = 0$, while different levels of QPC are obtained using $\varepsilon = \varepsilon_{\mathrm{L}} = \varepsilon_{\mathrm{R}}$ that varies from 0.2 to 1 with a step of 0.2. The same coupling strengths are considered in QPU, which is obtained using eq. (6.47). The simulation is repeated 100 times for each case and the median values are obtained for RWB as well as for WB and BRWB for comparison purpose.

Table 6.4: The parameter set for simulating time-varying QPC

Intervals (sec)	Duration (sec)	Coupling	Parameters
0 – 60	60	QPU	$\varepsilon_L = 0$, $\varepsilon_R = 0.5$
60 – 85	25	Linear	$\varepsilon_L = \varepsilon_R = 0$
85 – 105	20	QPC	$\varepsilon_L = 0$, $\varepsilon_R = 0 \longrightarrow 0.5$
105 – 125	20	QPC	$\varepsilon_L = 0$, $\varepsilon_R = 0.5 \longrightarrow 0$
125 – 145	20	Linear	$\varepsilon_L = \varepsilon_R = 0$
145 – 170	25	QPC	$\varepsilon_L = 0.25$, $\varepsilon_R = 0$
170 – 185	15	Linear	$\varepsilon_L = \varepsilon_R = 0$
185 – 215	30	QPC	$\varepsilon_L = 0$, $\varepsilon_R = 0.1$
215 – 235	20	Linear	$\varepsilon_L = \varepsilon_R = 0$
235 – 280	45	QPC	$\varepsilon_L = 0.5$, $\varepsilon_R = 0$
280 – 295	15	Linear	$\varepsilon_L = \varepsilon_R = 0$
295 – 335	40	QPC_D	$\varepsilon_L = 0$, $\varepsilon_R = 0.5$
335 – 370	35	Linear	$\varepsilon_L = \varepsilon_R = 0$

Time-varying QPC tracking

This simulation is carried out to investigate the ability of RWB and NWB to detect and quantify, respectively, dynamic changes in QPC. The linear components of HRV $x_L(t)$, $x_R(t)$ are present during the whole simulation, while, at different periods, segments of QPC (6.40), QPC with a constant delay (6.46) and QPU (6.47) are introduced. Table 6.4 describes the duration and coupling strength of the different segments that compose the simulated signal; arrows indicate time-varying coupling phenomena, e.g., (85-125 s). Linear increase/decrease up to the following coupling strength is present at the first and last 5s (transient zone) of the segments with constant coupling, e.g., (145-170 s). For QPC_D, e.g., (295-335 s), ϕ_D is randomly distributed in $[-1.2, 1.2]$ rad, while for QPU, e.g., (0-60 s), $\phi_{L,R}$ and $\phi_{R,R}$ are randomly distributed within $(-\pi, \pi]$ rad in each realization. Note that, in this simulation, one of ε_L or ε_R is set to 0 in QPC intervals for investigating the accuracy of RWB ($C^{\Phi}(t)$) to track the coordinates of a single peak in Ω (instead of a specific subregion Ω_J). For instance, when $\varepsilon_L = 0$ and $\varepsilon_R \neq 0$, the expected maximum value of $C^{\Phi}(t)$ is $b^2_{\Phi}(f_R, f_R, t)$, while for $\varepsilon_L \neq 0$ and $\varepsilon_R = 0$, is $b^2_{\Phi}(f_L, f_R, t)$. The simulated signal is analyzed through overlapped windows of length T with a step factor of 2 s. The simulation is repeated 100 times and the median values of $\hat{f}_1$, $\hat{f}_2$, $C^{\Phi}(t)$ and $E(t)$ are obtained.

6.3.3 Results

Reliability of QPC detection

Fig. 6.9 shows the feasibility of various bispectral methods in detecting QPC as a function of constant delay presence (ϕ_D) and surrogate data analysis parameter θ_{TH}. Phase deviations from the ideal QPC ($\phi_D \neq 0$) reduce QPC degree for BRWB and RWB, while do not

affect WB. Thus, WB cannot be used to estimate properly QPC. The maximum phase shift, for which QPC is still detected, is lower for $\Omega_{L,R}$ than for $\Omega_{R,R}$ due to the worse resolution at lower frequencies. When $\theta_{TH} \longrightarrow \pi$, QPC in $\Omega_{L,R}$ cannot be detected even without any delay influence ($\phi_D = 0$). The optimum threshold θ_{TH} for surrogate data analysis that allows the detection of QPC with the maximum possible delay, is given for $\theta_{TH} = 0$. When $\theta_{TH} \longrightarrow \pi$, the distribution of $\theta(\tau)$ values is narrowed ($U[-\pi : -\theta_{TH}, \theta_{TH} : \pi]$). This could create constant (non-zero) phase relationships in a small integration interval T'. As a consequence, the bicoherence-based surrogate data threshold will be higher and more restrictive [93].

Robustness of QPC assessment

Fig. 6.10 illustrates the performance of bispectral measures in detecting and quantifying QPC. BRWB (C_J^R) and the simplest computation of RWB (C_J^Φ) can detect QPC and discriminate it from linear coupling and QPU. On the contrary, WB (C_J) fails to discriminate between QPC and QPU since high values are maintained in both cases. However, none of the normalized domains is able to quantify the strength of QPC. NWB (E_J) is the only parameter that reflects changes in ε, and thus, it can be used to quantify, once detected, the changes in QPC strength.

Time-varying QPC tracking

Fig. 6.11 illustrates the results of tracking a time-varying QPC. The HRV signal and its spectral components are shown in Figs. 6.11(a)-(b). Low values of $C^\Phi(t)$ for non-QPC waves (Linear, QPU) suggest that RWB could be used to detect QPC with weak coupling strength or in the presence of a certain delay (QPC_D) between the interacting HRV components (Fig. 6.11(c)). As observed from Fig. 6.11(d), the estimated bi-frequencies ($\hat{f}_1, \hat{f}_2$), coincide with the simulated ones ($f_L = 0.1$ Hz, $f_R = 0.25$ Hz). Changes in QPC strength (Fig. 6.11(e)), can be measured using the NWB. The values of $E(t)$ reflect changes of cardiorespiratory coupling across the time, but an underestimation of the coupling strength might occur when the cross-coupling products ($f_2 - f_1 = 0.15$ Hz) between sympathetic ($f_1 = 0.1$ Hz) and parasympathetic-related components ($f_2 = 0.25$ Hz) lie at lower frequencies, where resolution is worse, e.g., in the intervals 145-170 s and 235-280 s.

6.3.4 Discussion

In this simulation study, considering that HRV is formed as the output of a Q-L system with input respiratory oscillations, among others, the reliability of different HOS-based methods to detect QPC was evaluated.

Results from Fig. 6.9 show that WB method cannot be used to estimate properly QPC, since it remains unchanged during phase alternations in the presence of constant

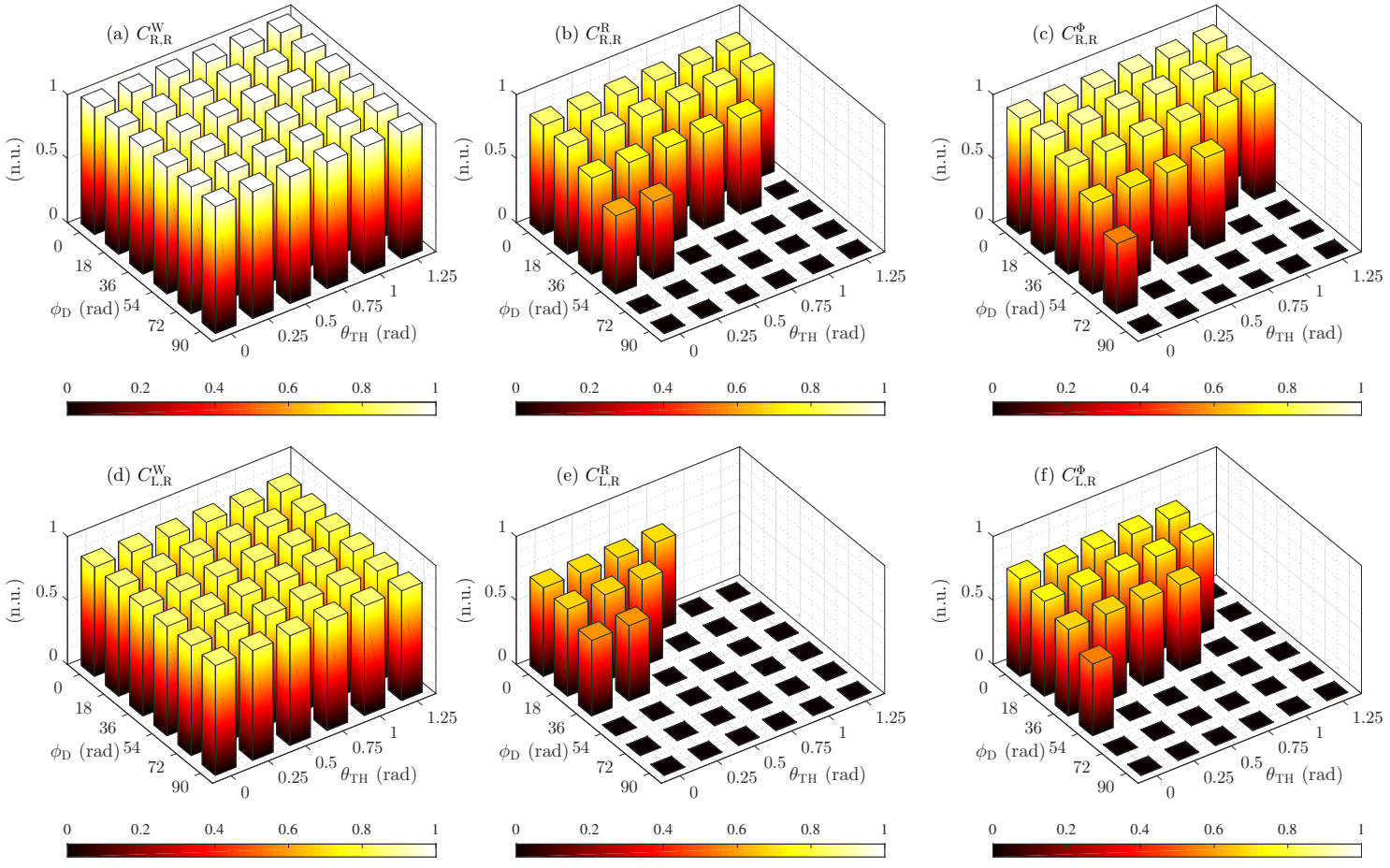

Figure 6.9: Reliability of QPC detection. The influence of delay presence (ϕ_D) and surrogate data analysis parameters (θ_{TH}) on QPC detection. QPC degree in $\Omega_{R,R}$ using (a) WB, (b) BRWB, and (c) RWB, and in $\Omega_{L,R}$ by means of (d) WB, (e) BRWB, and (f) RWB.

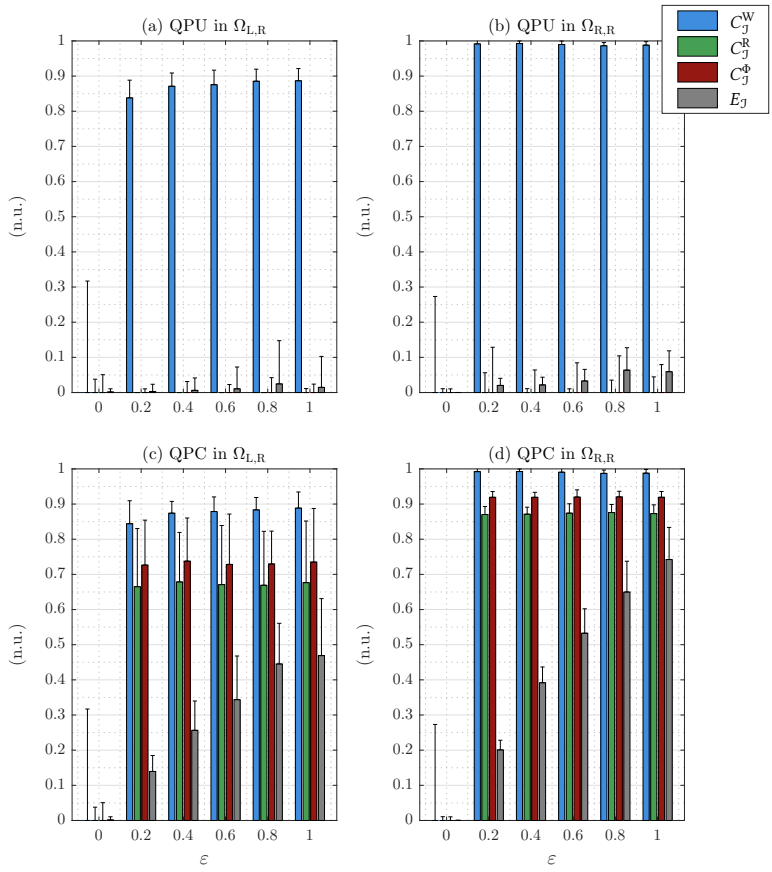

Figure 6.10: Robustness of QPC assessment. Bispectral measures in (a) $\Omega_{L,R}$, and (b) $\Omega_{R,R}$ for QPU case, and in (c) $\Omega_{L,R}$, and (d) $\Omega_{R,R}$ for QPC case.

delays between the interacting oscillations. Moreover, the optimum threshold θ_{TH} for surrogate data analysis that allows the detection of QPC with the maximum delay, is given for $\theta_{TH} = 0$. In BRWB, the maximum phase shift for $x_L(t - t_L)\, x_R(t - t_R)$ is $\phi_D \approx 0.63$ rad, which corresponds to delay $t_L \approx 0.97$ s, and $t_R \approx 0.39$ s, while, for RWB, the maximum delays are $t_L \approx 1.53$ s, and $t_R \approx 0.61$ s ($\phi_D \approx 0.95$ rad). Regarding the nonlinear term $x_R^2(t - t_R)$, the maximum delay in BRWB is approximately $t_R \approx 0.61$ s ($\phi_D \approx 0.95$ rad), while a better performance, $t_R \approx 0.77$ s ($\phi_D \approx 1.26$ rad), is achieved with RWB. These values are in accordance with physiological responses reported in the literature. For example, the response time of a single efferent vagal impulse on the sinus node is very short and affects only 1 or 2 heartbeats after its onset [131]. Considering a vagal arterial baroreflex mechanism, the latencies between systolic pressure fluctuations and RR intervals at low frequencies are up to 2 s, while average latencies between systolic pressures and RR intervals at respiratory frequencies are much less (< 0.5 s) [91]. Delay values in these ranges have been used in the literature for modeling a transfer function between instantaneous vagal firing rate and HR [286].

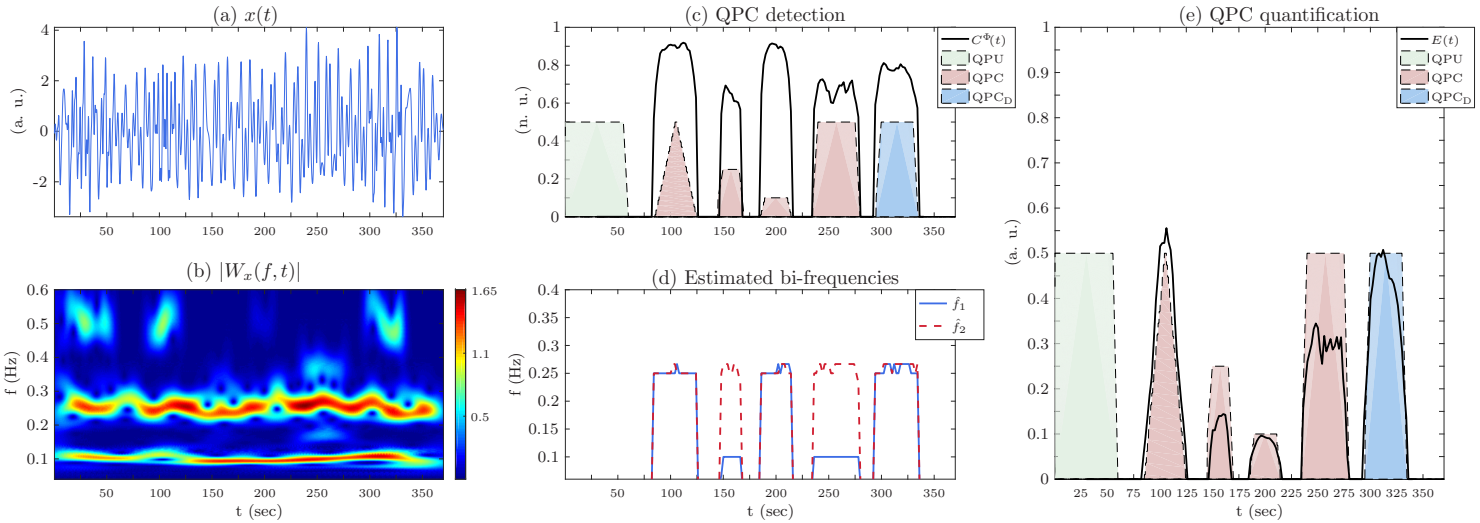

Figure 6.11: Time-varying QPC tracking. (a) Synthesized HRV signal $x(t)$, (b) CWT of HRV , (c) QPC detection by means of RWB ($C^{\Phi}(t)$), (d) bi-frequencies ($\hat{f}_1, \hat{f}_2$) related to QPC, and (e) QPC quantification by means of NWB ($E(t)$).

Results from Fig. 6.10 suggest that the simplest computation of RWB can be used to detect QPC even for weak couplings, while the proposed NWB reflects changes in coupling strength. In a time-varying QPC scenario (Fig. 6.11), the usage of RWB is essential for a correct identification of those bi-frequencies with significant QPC level, discriminating them from QPU and linear coupling. Furthermore, NWB shows a robust performance in quantifying, constant, time-varying, or in presence of delays, QPC strength. It should be noted that a weaker phase synchronization between the interacting oscillations in the analyzed interval, results in lower NWB values. QPC strength depends on the amplitude of the nonlinear oscillations and the degree of QPC. As can be seen from Figs. 6.11(c) and (e), lower values of $C^{\Phi}(t)$ in the intervals 145-170 s and 235-280 s are associated with lower values of $E(t)$.

To sum up, two main contributions, not yet addressed in previous studies, are highlighted. First, the novel RWB method simplifies the computational load associated to BRWB, due to the phase randomization procedure, and it shows a more robust performance in the presence of delays between the interacting components under analysis. Moreover, the novel NWB metric can quantify robustly QPC strength, once detection has been performed by RWB. In this study, the complex Morlet wavelet was used, but different mother wavelets can be considered with optimized parameters, depending on the application.

7

ECG-derived respiration

Respiration plays a key role in autonomic regulation, and alterations in respiratory control are often a clinical manifestation of pathological conditions [42, 71]. Abnormal respiratory rate is an important biomarker of potentially adverse clinical events in elderly people and critical ill patients [3,73]. In clinical practice, respiratory rate is currently measured using techniques which either interfere with normal breathing (nasal thermistors, carbon dioxide sensors) cause discomfort (transthoracic inductance and plethysmography), or do not offer acceptable quality (impedance pneumography) [199,249]. Since these techniques are impractical in monitoring, the ECG can be used to indirectly estimate a respiratory signal. Various EDR methods have explored the idea of retrieving respiratory information, mainly respiratory rate, from the ECG. Such information can be used for improving HRV analyses without the need of registering a respiratory signal. Although retrieving respiratory parameters from EDR signals during sinus rhythm has been widely studied, EDR methods in arrhythmia remains largely unexplored. Novel techniques for improving the monitoring of respiration in cardiac arrhythmias are also important in the field of mental disorders, since previous studies have found a high degree of comorbidity between MDD and CVD [111, 165, 329].

Alterations in respiratory physiology due to a progressive decline in lung function may provoke alterations in cardiac structure and function through changes in atrial elec-

trophysiology, leading to increased incidence of cardiac arrhythmia [298]. Atrial fibrillation (AF) is the most frequently encountered cardiac arrhythmia in clinical practice [209]. Respiratory dysfunction is associated with AF since reduced lung function, decreased oxygenation, hypercapnia, pulmonary hypertension, chronic obstructive pulmonary disease, and sleep-disordered breathing (SDB) have been identified as independent predictors of AF [47, 270, 310, 321]. A variety of pathophysiological mechanisms, including apnea-induced hypoxia and intrathoracic pressure shifts, have been associated with AF in patients with SDB [125], where the risk of new AF episodes is markedly increased shortly after apneas and hypopneas during sleep [233, 243]. Moreover, patients with SDB may be predisposed to arrhythmias because of an increased sympathetic tone. Autonomic imbalance could alter atrial electrophysiology and provoke AF [167].

These clinical observations exemplify the complex interplay between the respiratory, cardiovascular, and autonomic nervous systems, and highlight the need for tools to monitor respiration in patients with AF [345]. It should be noted that methods exploring HR information cannot be used in AF since the rhythm is not controlled by the ANS and thus, RSA is not present. One of the very few EDR studies involving AF patients reported on low detection sensitivity of SDB [263]. The performance of techniques exploring morphology may deteriorate due to the presence of atrial fibrillatory waves (f-waves) which can mask the respiratory information. Therefore, f-wave suppression may have to be performed before respiratory rate estimation. The performance of a novel approach to ECG-derived respiration, named "slope range" (SR), will be compared to that of two well-known methods based on either QRS loop rotation angle (LA) or R-wave angle (RA), which have been reported to be robust in noisy situations, but not during AF. Moreover, a novel technique for selecting the spectral peak related to respiration is proposed, being particularly robust to spurious spectral components caused by f-waves.

7.1 Methods

Suppression of f-waves

In contrast to AF signal processing, where the objective is to extract and analyze the f-waves, the objective is here to suppress the f-waves, while preserving respiratory related QRS variability, before respiratory rate estimation is performed. Signal- and noise-dependent weighted QRS averaging is used for this objective [77], see also [304], being based on the same principle as average beat subtraction (ABS). The i:th observed beat $x_i(n)$ is modeled as:

$$x_i(n) = x_{\mathrm{QRS},i}(n) + x_{f,i}(n), \quad i = 1, \ldots, M, \tag{7.1}$$

where $x_{\mathrm{QRS},i}(n)$ and $x_{f,i}(n)$ are the QRS complex and the f-waves, respectively, and M is the number of beats with dominant morphology. The QRS complex is characterized by the time-dependent variance $\sigma^2_{\mathrm{QRS}}(n)$ and the f-waves by the constant variance σ_f^2. The f-wave suppressed QRS complex of the i:th beat is obtained as a linear combination of M

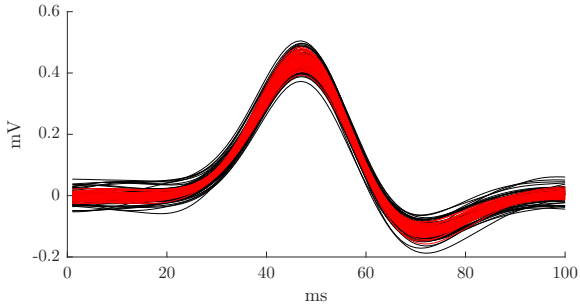

Figure 7.1: Example of f-wave suppression. QRS complexes without ($x_i(n)$) and with f-wave suppression ($\hat{x}_{\mathrm{QRS},i}(n)$) are marked with black and red color, respectively.

beats:

$$\hat{x}_{\mathrm{QRS},i}(n) = \sum_{m=1}^{M} w_{i,m}(n) x_m(n), \tag{7.2}$$

where the weights $w_{i,m}(n)$ are given by [304]:

$$w_{i,m}(n) = \frac{1}{M} \frac{\sigma_f^2}{\sigma_f^2 + \sigma_{\mathrm{QRS}}^2(n)} + \frac{\sigma_{\mathrm{QRS}}^2(n)}{\sigma_f^2 + \sigma_{\mathrm{QRS}}^2(n)} \delta(i - m). \tag{7.3}$$

The f-wave variance σ_f^2 is estimated from the observed signal by computing the sample variance of the concatenated TQ intervals of all beats, following bandpass filtering in the band [0.5, 30] Hz to preserve f-wave related frequency components and reduce the influence of noise [304]. The QRS variance $\sigma_{\mathrm{QRS}}^2(n)$ is estimated by

$$\hat{\sigma}_{\mathrm{QRS}}^2(n) = \max \left\{ \frac{1}{M-1} \sum_{m=1}^{M} (x_m(n) - \bar{x}(n))^2 - \sigma_f^2, 0 \right\}, \tag{7.4}$$

where $\bar{x}(n)$ denotes the ensemble average of $x_1(n), \ldots, x_{\mathrm{M}}(n)$.

This approach uses weights $w_{i,m}(n)$ which not only change from sample-to-sample within each beat given the time-dependent QRS variance $\sigma_{\mathrm{QRS}}^2(n)$, but also from beat-to-beat since more weight is assigned to the i:th beat ($m = i$), thereby accounting for variation in the morphology of the current beat. In this study, M was empirically set to 60. An example of f-wave suppression is illustrated in Fig. 7.1. The derived respiratory signal is computed from the QRS complexes $y_i(n)$ obtained either without or with f-wave suppression:

$$y_i(n) = \begin{cases} x_i(n), & \text{w/o suppression,} \\ \hat{x}_{\mathrm{QRS},i}(n), & \text{with suppression.} \end{cases} \tag{7.5}$$

Derived respiratory signals

1) QRS loop rotation angle d_{LA}: Spatiotemporal alignment between successive, observed QRS loops $\mathbf{Y}_i$ and a reference QRS loop $\mathbf{Y}_{\mathrm{R}}$ is used to estimate a rotation angle

reflecting respiratory information [16], see also [302]. The reference QRS is taken as the average of the first 10 beats of the recording having similar morphology (cross-correlation coefficient higher than 0.8). For two leads, the reference loop $\mathbf{Y}_\mathrm{R}$ contains a two-lead reference QRS complex and the i:th loop $\mathbf{Y}_i$ contains the QRS complexes $y_i(n)$ of two leads. The loop $\mathbf{Y}_i$ is assumed to be a version of $\mathbf{Y}_\mathrm{R}$ but rotated, scaled, and shifted in time. For each beat, the estimated rotation matrix $\hat{\boldsymbol{Q}}_i$ (2×2) is used to extract an angle which forms the EDR signal $d_{\mathrm{LA}}(i)$:

$$d_{\mathrm{LA}}(i) = \arcsin(\hat{\boldsymbol{Q}}_i\,(2,1)). \tag{7.6}$$

2) R-wave angle d_{RA}: The R-wave angle reflects respiratory information in individual leads. First, using the least squares technique, a straight line is fitted to each side of the QRS complex in 8 ms intervals centered at the points of maximum absolute slope, see [202] for details. The R-wave angle is defined as the angle formed by two straight lines fitted to the up- and downslope of the QRS complex:

$$d_{\mathrm{RA}}(i) = \arctan\left(\left|\frac{\mathcal{I}_{\mathrm{US},i} - \mathcal{I}_{\mathrm{DS},i}}{1 + \mathcal{I}_{\mathrm{US},i}\mathcal{I}_{\mathrm{DS},i}}\right|\right), \tag{7.7}$$

where $\mathcal{I}_{\mathrm{US},i}$ and $\mathcal{I}_{\mathrm{DS},i}$ denote the up- and downslope of the two fitted lines, respectively.

3) Slope range d_{SR}: The slope range is a novel parameter which reflects respiratory information in individual leads. It is defined by the difference between the maximum up-slope and minimum down-slope values within the QRS interval, irrespectively of their relative time occurrence:

$$d_{\mathrm{SR}}(i) = \max_n \left\{ y_i'(n) \right\} - \min_n \left\{ y_i'(n) \right\}, \tag{7.8}$$

where $y_i'(n) = y_i(n) - y_i(n-1)$. This definition of the slopes avoids the line fitting used in $\mathcal{I}_{\mathrm{US},i}$ and $\mathcal{I}_{\mathrm{DS},i}$.

The three EDR signals are illustrated in Fig. 7.2.

Outlier rejection and resampling

Outliers in an EDR signal are rejected using a standard deviation (SD)-based rule [16]; the threshold is defined as 5 times the running SD. Since an EDR signal is irregularly sampled, cubic spline interpolation is performed followed by resampling at $f_s = 4$ Hz, where gaps longer than 2 s are excluded from respiratory rate estimation. The resampled EDR signal is indexed with n instead of i and f-wave suppression is indicated with an "s", i.e., $d_{\mathrm{LA},s}(n)$, $d_{\mathrm{RA},s}(n)$, and $d_{\mathrm{SR},s}(n)$.

Respiratory rate estimation

An estimate $\hat{f}_r(k)$ of the respiratory rate is obtained from a smoothed version of the running power spectrum $S_{k,l}(f)$ of the EDR signal, where k and l index the running interval

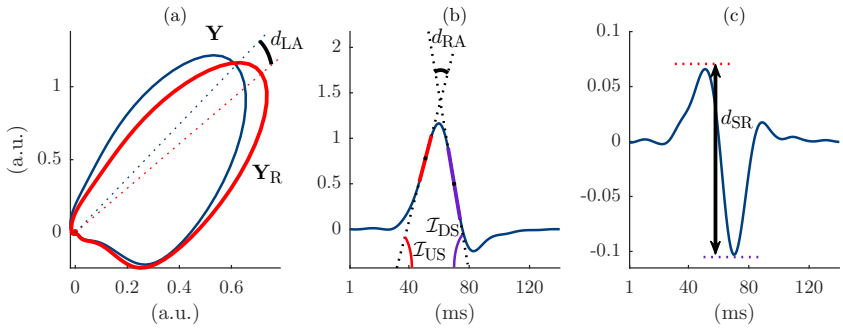

Figure 7.2: Derived respiratory signals. (a) Rotation angle d_{LA} of the observed loop $\boldsymbol{Y}$, in blue, relative to the reference loop $\boldsymbol{Y}_{\mathrm{R}}$, in red, (b) R-wave angle d_{RA} between the lines fitted to the upslope (red) and downslope (purple) of the QRS complex $y_i(n)$, and (c) slope range d_{SR} between the absolute maximum (red) and minimum (purple) of the first derivative $y_i'(n)$ of the QRS complex.

and the analyzed lead[1], respectively. A block diagram of the respiratory rate estimation is shown in Fig. 7.3.

Each power spectrum is obtained using the Welch method and computed every ΔT s in intervals of length T_s s, divided into subintervals of length T_m s with 50% overlap [16]. Before computing the averaged power spectrum of the Welch method, the power spectrum of each subinterval is normalized with respect to power to reduce the influence of spurious spectral peaks due to artifacts and to compensate for lead-to-lead differences in signal power. The power at frequencies exceeding half the mean heart rate is set to zero.

Assuming that respiration is stationary in an interval of T_s s, a smoothed version of $\hat{f}_r(k)$ is obtained by

$$\bar{f}_r(k) = \beta \bar{f}_r(k-1) + (1-\beta)\hat{f}_r(k), \tag{7.9}$$

where β denotes the forgetting factor; the details on how to obtain $\hat{f}_r(k)$ are presented below.

1) Spectral peakedness: A measure of spectral concentration ("peakedness") is introduced to exclude flat spectra and spectra with low power around $\bar{f}_r(k-1)$, defined by

$$P_{k,l} = \frac{\int_{\Omega_p(k)} S_{k,l}(f)df}{\int_{\Omega(k)} S_{k,l}(f)df} \cdot 100\%, \tag{7.10}$$

where both $\Omega_p(k)$ and $\Omega(k)$ are centered around $\bar{f}_r(k-1)$ such that:

$$\Omega_p(k) = [\bar{f}_r(k-1) - \delta_p, \bar{f}_r(k-1) + \delta_p], \tag{7.11}$$

$$\Omega(k) = [\bar{f}_r(k-1) - \delta, \bar{f}_r(k-1) + \delta], \tag{7.12}$$

[1]Note that l refers to the EDR signal(s), not necessarily to the recorded leads. For two leads, two EDR signals can be derived for d_{RA}, and d_{SR}, while only one EDR signal for d_{LA}.

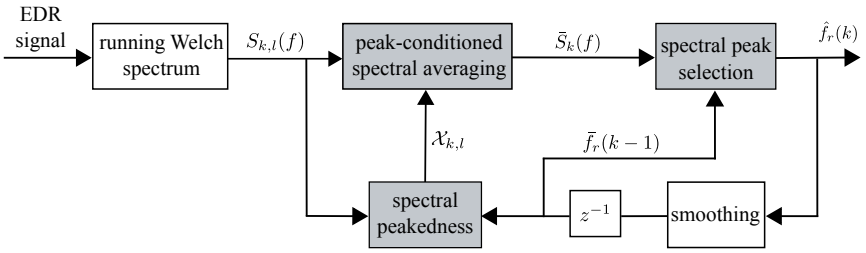

Figure 7.3: Block diagram of respiratory rate estimation. The intermediate steps include computation of the running Welch spectrum, the peakedness measure, the peak-conditioned averaging, and spectral peak selection in the averaged spectrum.

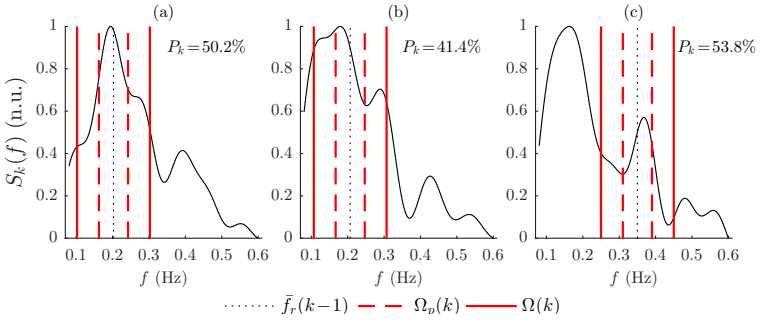

Figure 7.4: Examples of spectral peakedness computed using (7.10). EDR spectrum having a large percentage of its power in $\Omega(k)$ mainly concentrated (a) within $\Omega_p(k)$, (b) outside $\Omega_p(k)$, (c) within $\Omega_p(k)$ although the peak in $\Omega(k)$ is not the absolute maximum of $S_k(f)$. For simplicity, the dependence of l in $S_{k,l}(f)$ and $P_{k,l}$ is omitted.

where $\Omega_p(k)$ is contained in $\Omega(k)$ ($\delta_p < \delta$). Figure 7.4 shows examples of EDR spectra $S_{k,l}(f)$ with different percentages of power concentration $P_{k,l}$ around $\bar{f}_r(k-1)$. Respiratory signals with narrow- and broadband spectra can be also differentiated based on the bandwidth of the respiratory spectrum $B_r(k)$.

The width parameter δ should be selected according to the half-width of the expected respiratory band. It should be noted that while $\Omega_p(k)$ was centered around the local maximum inside $\Omega(k)$ closest to $\bar{f}_r(k)$ in [202], $\Omega_p(k)$ is centered around $\bar{f}_r(k)$ in this study. A search for the local maxima is avoided since the position of local maxima is highly variable across spectra when f-waves are present.

2) Peak-conditioned spectral averaging: The variance reduction provided by the Welch method is complemented with peak-conditioned spectral averaging of K successive running spectra $S_{k,l}(f)$ to further reduce the variance, and thus enhances the frequency component corresponding to the respiratory rate [16]. In addition, averaging is performed across available leads. The spectrum used for respiratory rate estimation is given by

$$\bar{S}_k(f) = \sum_l \sum_{o=0}^{K-1} \mathcal{X}_{k-o,l} \cdot S_{k-o,l}(f), \tag{7.13}$$

where $\mathcal{X}_{k,l}$ is a binary variable indicating the peakedness of $S_{k,l}(f)$, set to 1 when $P_{k,l}$ exceeds the threshold ξ:

$$\mathcal{X}_{k,l} = \begin{cases} 1, & P_{k,l} \geq \xi_p \ \wedge A_{k,l} \geq \xi_a, \\ 0, & \text{otherwise}, \end{cases} \tag{7.14}$$

where

$$A_{k,l} = \frac{\max\limits_{f\in\Omega(k)} \{S_{k,l}(f)\}}{\max\limits_{f\in\Omega_r} \{S_{k,l}(f)\}} \cdot 100\%. \tag{7.15}$$

As shown in Fig. 7.4(c), this restriction is necessary since a large $P_{k,l}$ does not ensure that the spectral peak in $\Omega(k)$ is the largest peak across the whole range of respiratory rates. The range Ω_r is fixed and chosen so that it covers the respiratory rates observed in AF patients.

3) Spectral peak selection: The respiratory rate is selected among the J local maxima $f_1(k), \ldots, f_J(k)$ in $\bar{S}_k(f)$ inside $\Omega(k)$, using minimization of a cost function that quantifies, for each spectral peak, the power deviation from the largest peak and the frequency deviation from $\bar{f}_r(k)$. Assuming that the respiratory rate in the k:th interval corresponds to a peak whose power is similar to the global maximum $\bar{S}_{k,\mathrm{MAX}}$, defined by

$$\bar{S}_{k,\mathrm{MAX}} = \max_j \{\bar{S}_k(f_j(k))\}, \ j = 1, \ldots, J, \tag{7.16}$$

and near $\bar{f}_r(k-1)$, the power deviation from $\bar{S}_{k,\mathrm{MAX}}$ is penalized by the cost $C_p(k,j)$ and the deviation from $\bar{f}_r(k-1)$ by $C_f(k,j)$:

$$C_p(k,j) = 1 - \bar{S}_k(f_j(k))/\bar{S}_{k,\mathrm{MAX}}, \tag{7.17}$$

$$C_f(k,j) = \left|f_j(k) - \bar{f}_r(k-1)\right|/2\delta, \tag{7.18}$$

$$j_c(k) = \arg\min_j \left\{ a_p C_p(k,j) + a_f C_f(k,j) \right\}, \tag{7.19}$$

where a_p and a_f are cost weights. The desired estimate of the respiratory rate is given by

$$\hat{f}_r(k) = f_{j_c(k)} \equiv f_{j_c}(k). \tag{7.20}$$

The cost assignment and the reinitialization of $\bar{f}_r(k)$ (see below for details) for different peak configurations are illustrated in Fig. 7.5. For the computation of $\hat{f}_r(k)$ (Figs. 7.5 (a)–(b)), the cost evaluation is performed for all peaks inside $\Omega(k)$, while, for the reinitialization of $\bar{f}_r(k)$ (Figs. 7.5 (c)–(d)), the cost evaluation is performed inside Ω_r. As observed from Fig. 7.5, rate estimation does not always correspond to the largest peak or the peak closest to $\bar{f}_r(k-1)$, but it combines the information of both peak.

4) Computation of $\bar{f}_r(k)$***:*** The computation of $\bar{f}_r(k)$ involves a number of special cases. At initialization, $\bar{S}_0(f)$ is constructed using $2K$ spectra and Ω_p and Ω are centered around the global maximum of $\bar{S}_0(f)$. Then, $\bar{f}_r(0)$ is determined by finding the highest local maximum in Ω_r.

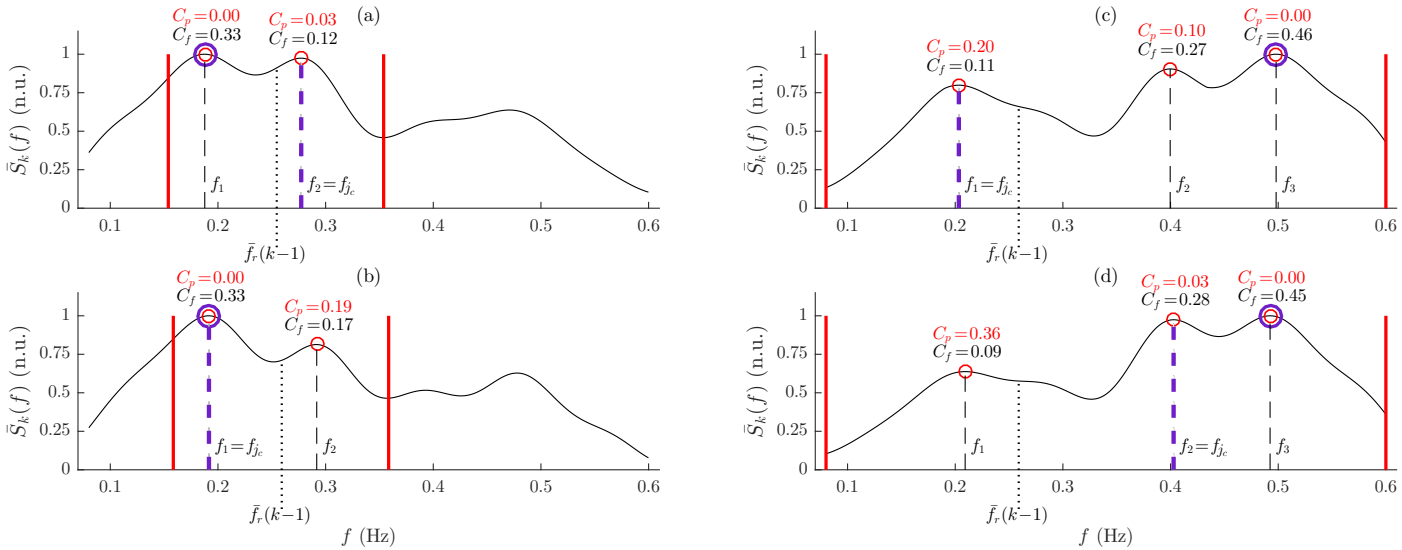

Figure 7.5: Cost assignment in respiratory rate estimation and the reinitialization of $\bar{f}_r(k)$. (a)–(b) Costs used in peak search within $\Omega(k)$ (red solid lines). (c)–(d) Costs used in peak search within Ω_r (red solid lines). The $\bar{S}_{k,\mathrm{MAX}}$ is marked with a purple circle while the estimated respiratory rate with a purple line. The dependence of j or/and k in $f_{j_c}(k)$, $C_p(k,j)$, and $C_f(k,j)$ is for simplicity omitted.

If no spectrum is peaked enough, $\bar{S}_k(f)$ is not defined; thus, $\hat{f}_r(k)$ is not computed and, accordingly, $\bar{f}_r(k) = \bar{f}_r(k-1)$. If no estimate has been produced for the last 15 s, either due to an abrupt change in $f_r(k)$ or incorrect estimation of $f_r(k)$, $\bar{f}_r(k)$ is reinitialized. The reinitialization is performed by finding the local maximum in Ω_r associated with the minimum cost in (7.19), leading to

$$\bar{f}_r(k) = f_{j_c}(k), \tag{7.21}$$

where the bandwidth of the analyzed frequency band in $C_f(k,j)$ is based on Ω_r.

The following parameter values are used when evaluating the performance [202]: $K = 5$, $\Delta T = 5$ s, $T_m = 12$ s, $T_s = 42$ s, $\delta = 0.1$. The parameters $\delta_p = 0.4\delta$, $\beta = 0.8$, $\xi_p = 45\%$, $\xi_a = 85\%$, $\Omega_r = [0.08, 0.6]$, and $a_p = a_f = 1$ are set empirically.

7.2 Materials

Simulated data

To shed light on performance, a model for simulating 12-lead ECG signals in AF is employed [261]. Briefly, the signals, sampled at $f_{s,\mathrm{ECG}}$, are generated by simulating QRST complexes whose morphological variability accounts for respiratory influence (angular variation around each lead), real extracted f-waves, and various types of noise.

1) Ventricular activity: The multi-lead ECG model in [282] is used for simulating QRST complexes with different morphologies, see [261] for further details. A synthesized orthogonal three-lead VCG signal $\boldsymbol{u}_{\mathrm{V}}(n)$ (3x1) is constructed by concatenating a single QRST complex for each lead (X, Y, Z) until the desired length is attained. The Physionet Long Term Atrial Fibrillation Database is used for creating a set of AF rhythms.

2) Atrial activity: A set of 20 segments with real, multi-lead f-waves $\boldsymbol{u}_{\mathrm{A}}(n)$ (12×1) is extracted from a database with 12-lead ECGs acquired from patients clinically diagnosed with persistent AF [260].

3) Noise: A noise component $\boldsymbol{u}_{\mathrm{N}}(n)$ (12×1) is composed of two types of noise frequently encountered in ambulatory recordings, muscle noise and electrode movement artifacts extracted from the MIT BIH Noise Stress Test Database. Noise with 20 μV RMS is included to better mimic real ECGs [261].

4) Respiratory influence: The dynamics of the amount of air in the lungs during the p:th respiratory cycle can be modeled as the product of two sigmoidal functions reflecting inspiration and expiration [13], see also [16, 303],

$$r(n) = m_r(n) \sum_{p=1}^{\infty} \frac{1}{1 + e^{\lambda_{\mathrm{I}}(p)(n - n_{\mathrm{I}}(p))}} \frac{1}{1 + e^{\lambda_{\mathrm{E}}(p)(n - n_{\mathrm{E}}(p))}}, \tag{7.22}$$

where the steepness of the sigmoids during inspiration and expiration are defined by,

$$\lambda_{\mathrm{I}}(p) = -20\frac{f_r(p)}{f_{s,\mathrm{ECG}}}, \tag{7.23}$$

$$\lambda_{\mathrm{E}}(p) = 15\frac{f_r(p)}{f_{s,\mathrm{ECG}}}, \tag{7.24}$$

respectively, $f_r(p)$ is the respiratory rate of the p:th cycle. The midpoint location of the sigmoids related to inspiration and expiration are defined by,

$$n_{\mathrm{I}}(p) = n_{\mathrm{O}}(p) + 0.35\frac{f_{s,\mathrm{ECG}}}{f_r(p)}, \tag{7.25}$$

$$n_{\mathrm{E}}(p) = n_{\mathrm{O}}(p) + 0.6\frac{f_{s,\mathrm{ECG}}}{f_r(p)}, \tag{7.26}$$

respectively, where $n_{\mathrm{O}}(p)$ is the onset of each sigmoid, defined by

$$n_{\mathrm{O}}(p) = \sum_{j=1}^{p-1}\frac{f_{s,\mathrm{ECG}}}{f_r(j)}. \tag{7.27}$$

The function $m_r(n)$ accounts for the amplitude modulation often encountered in respiratory signals. For instance, the modulation observed in periodic breathing can be simulated using $m_r(n) = \beta_r\,(1 + A_m\cos(2\pi f_m/f_s n))$, where $0 < A_m < 1$ and f_m define the amplitude and frequency of the modulating signal, and β_r is a normalization factor ensuring that $r(n)$ is in the interval $[0, 1]$.

The angular variation around each axis is proportional to the amount of air in the lungs. Thus, the time-varying angles $\phi_l(n)$ around each lead l are modeled as,

$$\phi_l(n) = \zeta_l \cdot r(n), \quad l \in \{X, Y, Z\}, \tag{7.28}$$

where ζ_l is the maximum angular variation.

The simulated standard 12-lead ECG, $\mathbf{y}(n)$, is obtained using a linear transformation of the VCG leads [86] and adding atrial activity $\mathbf{u}_{\mathrm{V}}(n)$ and noise $\mathbf{u}_{\mathrm{N}}(n)$:

$$\mathbf{y}(n) = \mathbf{D}\mathbf{Q}(n)\mathbf{u}_{\mathrm{V}}(n) + \mathbf{u}_{\mathrm{A}}(n) + \mathbf{u}_{\mathrm{N}}(n), \tag{7.29}$$

where $\mathbf{D}$ (12×3) is the Dower matrix, and $\mathbf{Q}(n)$ (3×3) is a rotation matrix defined by the angles $\phi_l(n)$. An illustrative example of synthetic ECG components is shown in Fig. 7.6.

The SNR between the QRS complex and the f-waves is defined by

$$\mathrm{SNR} = 20 \cdot \log_{10}\left(A_{\mathrm{QRS}}/A_f\right), \tag{7.30}$$

where A_{QRS} is the peak-to-peak amplitude of the ensemble averaged QRS and A_f is the peak-to-peak f-wave amplitude computed as the mean of the difference between the upper and the lower envelope of the f-wave signal [226]. Using (7.30), a lower SNR implies a larger f-wave amplitude. For multi-lead ECGs, the SNR is given by the lead with the lowest SNR. The minimum and maximum SNRs across leads are denoted $\mathrm{SNR}_{\mathrm{MIN}}$ and $\mathrm{SNR}_{\mathrm{MAX}}$, respectively.

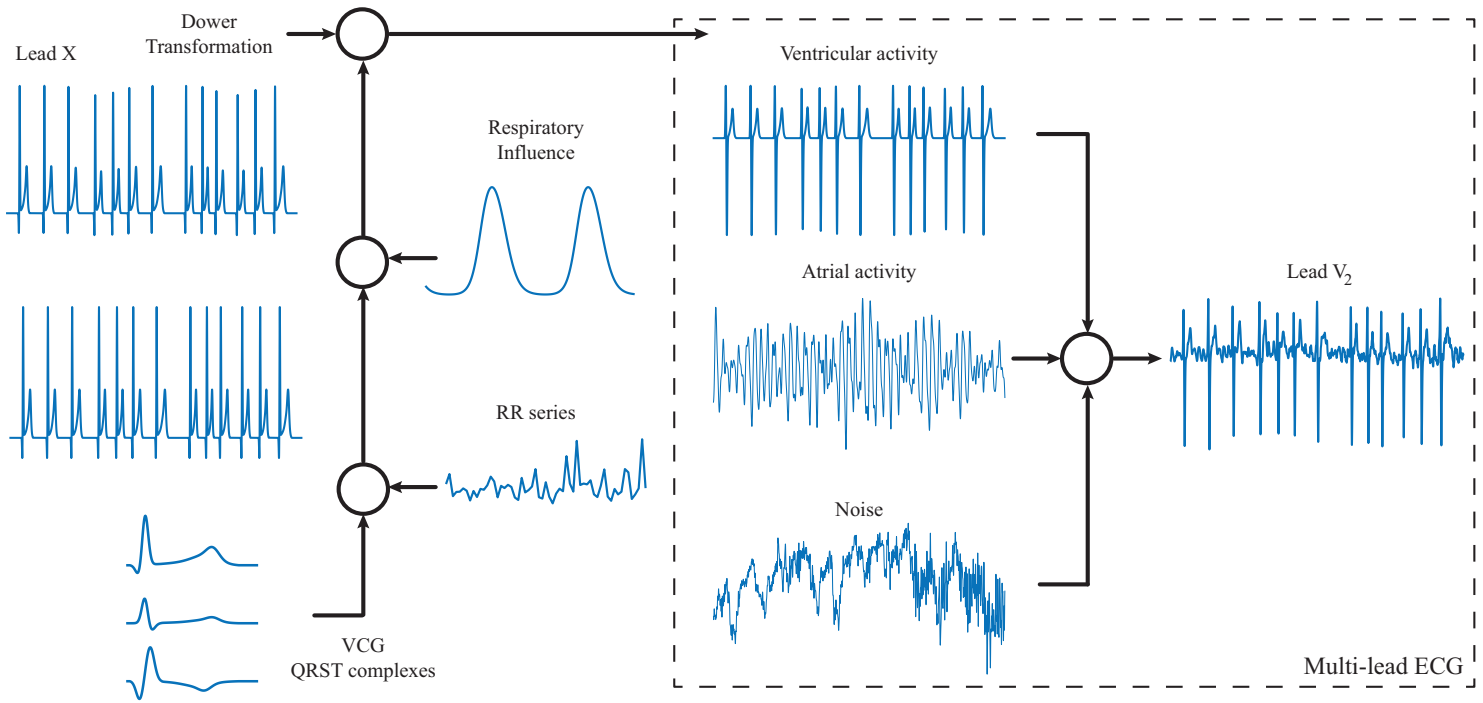

Figure 7.6: Multi-lead ECG modeling. Synthetic ECGs are generated by simulating ventricular activity from VCG QRST complexes, whose morphological variability accounts for respiratory influence, real f-waves for atrial activity and noise often encountered in ambulatory recordings.

Real data

Estimation performance is also evaluated using a database containing recordings from 30 patients with persistent AF (69±15 years, 17 females) acquired at the Department of Cardiology at San Paolo Hospital in Milan, Italy. The patients underwent electrical cardioversion after having had an AF episode lasting longer than 7 days. The morning before electrical cardioversion, recordings were acquired at rest supine position about 15 min. The ECG was recorded using two non-orthogonal leads ($f_{s,\mathrm{ECG}} = 1000$ Hz) and the reference respiratory signal using a belt sampled at 50 Hz, both signals acquired with a Task Force ® Monitor (CNSystem; Graz, Austria) recording system.

Performance evaluation setup

The reference respiratory rate $f_r(k)$ is obtained from the reference respiratory signal by applying the same approach as that used in the EDR signals. To evaluate performance, the mean μ and SD σ of the absolute error $\Delta f(k)$ between $f_r(k)$ and $\hat{f}_r(k)$ and the relative error $\Delta f(k)/f_r(k)$ are considered, provided that both $f_r(k)$ and $\hat{f}_r(k)$ are available. The time during which $\hat{f}_r(k)$ cannot be estimated is denoted $\mathcal{T}$ and is expressed as a percentage of the overall length of the analyzed signal.

Five-minute simulated ECGs are used for estimating the respiratory rate at different SNRs (12, 15, 18, and 21 dB). Two different lead combinations are investigated for simulation, namely (V_1, V_2) and (V_1, V_5). For a maximum respiratory induced angular variation $\zeta_r = 5^o$, three fixed respiratory rates f_r (0.15, 0.25, and 0.35 Hz) are chosen for inducing beat-to-beat changes similar to the respiratory patterns observed in subjects at rest supine position. The peak-to-peak f-wave amplitude in the analyzed leads is presented in Table 7.1. Figure 7.7 illustrates simulated ECGs at different SNRs. Moreover, an additional simulation is carried out to evaluate the performance of SR method obtained either using the first difference or the up- and downslope obtained with line fitting (8 ms). For each combination of f_r and SNR, 200 different simulated signals are analyzed and the gross median error metrics ($\overline{\mu}$, $\overline{\sigma}$) of rate estimation are computed.

When real ECGs are analyzed, the only method previously applied to derive respiratory information in AF patients is studied for comparative purposes [263]. The method, namely QRS area $d_{\mathrm{A}}(n)$, is computed using the trapezoidal method [237].

7.3 Results

Simulated data

Figure 7.8 illustrates respiratory rate estimation on simulated ECGs: f-wave suppression together with $d_{\mathrm{LA}}(n)$ results in cleaner time–frequency (TF) spectra since spurious components in $d_{\mathrm{LA},s}(n)$ are suppressed (Figs. 7.8(a)–(b)). A similar TF pattern is achieved

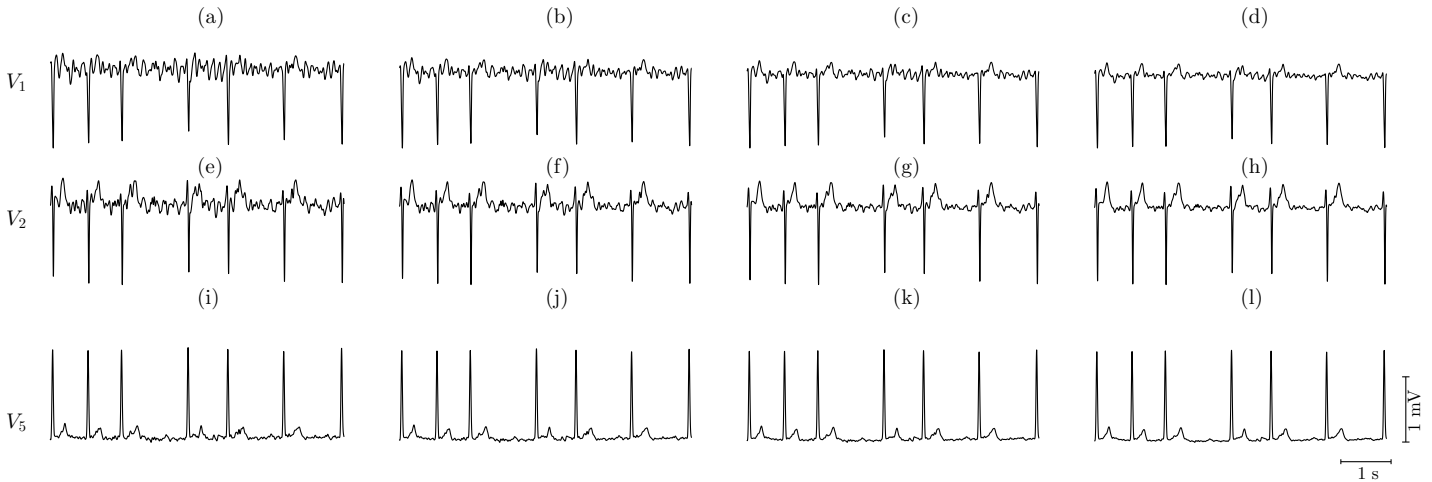

Figure 7.7: Simulated ECGs for f_r = 0.15 Hz in lead (a)–(d) V_1. (e)–(h) V_2, and (i)–(l) V_5. In V_1, the SNR increases from 12 to 21 dB in steps of 3 dB (left to right). Note that a larger f-wave amplitude implies a lower SNR.

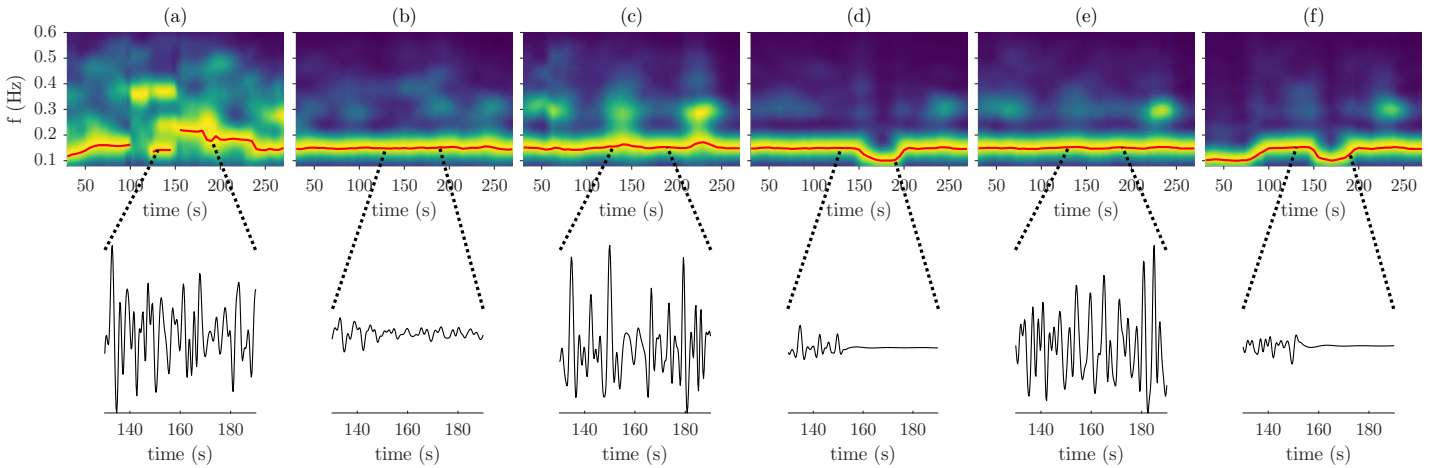

Figure 7.8: Respiratory rate estimation in simulated ECGs for f_r = 0.15 Hz, SNR = 12 dB and (V_1,V_2). Time–frequency spectrum obtained by (a) $d_{\mathrm{LA}}(n)$, (b) $d_{\mathrm{LA},s}(n)$, (c) $d_{\mathrm{RA}}(n)$, (d) $d_{\mathrm{RA},s}(n)$, (e) $d_{\mathrm{SR}}(n)$, and (f) $d_{\mathrm{SR},s}(n)$. The estimated respiratory rate is displayed with a red line. An excerpt of the EDR signal is displayed below each time–frequency spectrum. All EDR signals, with and without f-wave suppression, are plotted with the same amplitude scale.

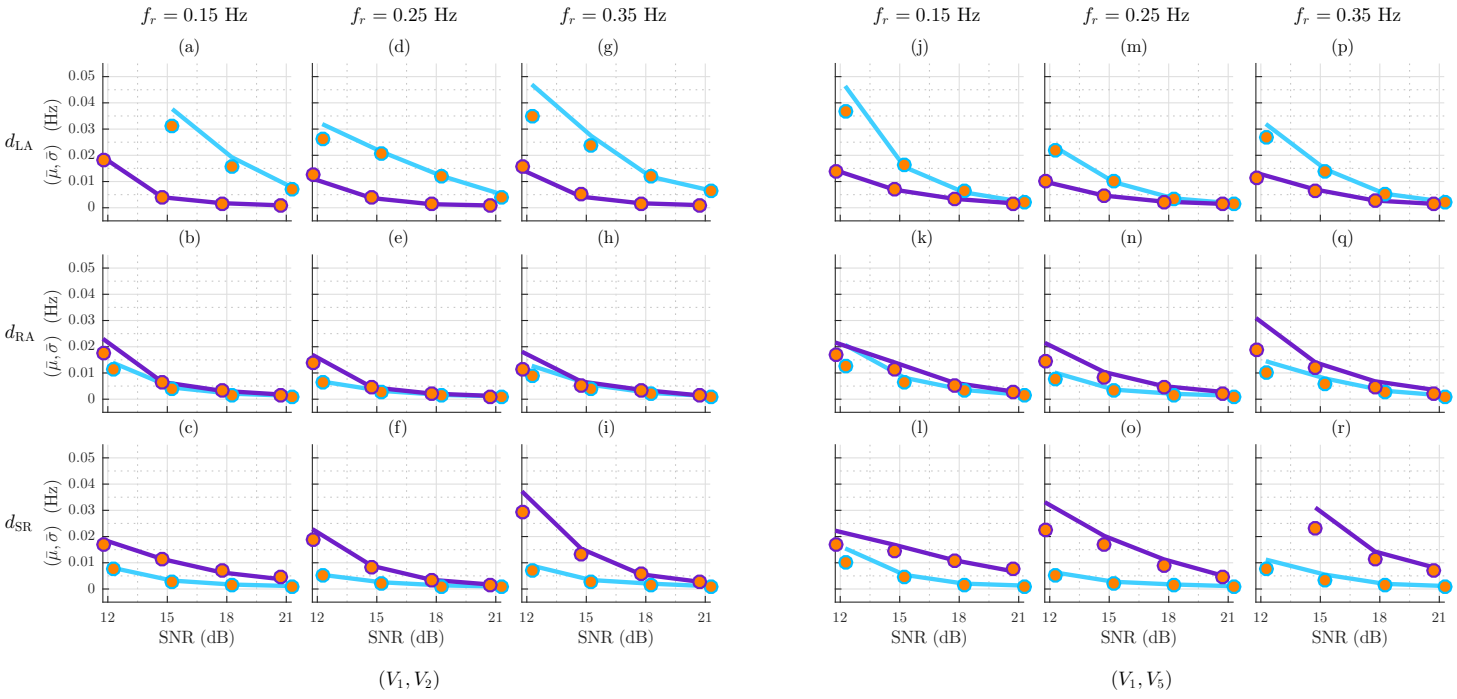

Figure 7.9: Performance in simulated ECGs with different respiratory rates. The median errors for leads (a)–(i) V_1, V_2 and (j)–(r) V_1, V_5. The top row presents to the performance of $d_{\mathrm{LA}}(n)$, and so on. The errors obtained without and with f-wave suppression are marked in blue and purple, respectively. The error metrics $\overline{\mu}$ and $\overline{\sigma}$ are denoted with lines and circles, respectively. Pairs $(\overline{\mu}, \overline{\sigma})$ with errors higher than 0.05 Hz are not shown. The error metrics for the methods with and without f-wave suppression are slightly displaced horizontally to become discernible. Note that a larger f-wave amplitude implies a lower SNR.

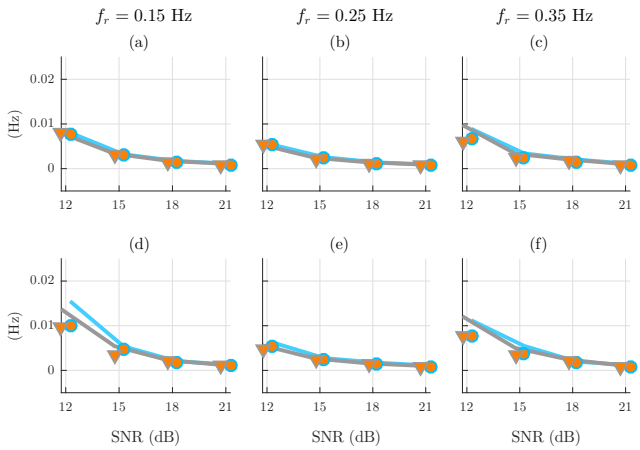

Figure 7.10: Performance in simulated ECGs for different definitions of SR. The median errors for leads (a)–(c) V_1, V_2 and (d)–(f) V_1, V_5. The errors obtained with the use of the first difference and the use of fitting are marked in blue and gray, respectively. The error metrics $\overline{\mu}$ and $\overline{\sigma}$ are denoted with lines and circles, respectively.

using $d_{\mathrm{RA}}(n)$ (Fig. 7.8(c)) and $d_{\mathrm{SR}}(n)$ (Fig. 7.8(e)) without f-wave suppression. On the contrary, the extraction of respiratory information after f-wave suppression does not improve performance (Figs. 7.8(d)–(f)) since the EDR signal, in certain intervals, is almost completely suppressed.

Figure 7.9 shows the results for the lead combinations (V_1, V_2) and (V_1, V_5). It is obvious that f-wave suppression deteriorates the performance of $d_{\mathrm{RA}}(n)$ and $d_{\mathrm{SR}}(n)$, while it significantly improves the performance of $d_{\mathrm{LA}}(n)$. For all considered respiratory rates, the median errors ($\overline{\mu}$, $\overline{\sigma}$) Hz across all respiratory rates are below 0.01±0.01 Hz for SNR> 12 dB without f-wave suppression for SR and RA, while f-wave suppression is required for LA to achieve this particular limit. The median of the time percentage $\mathcal{T}$ during which the respiratory rate could not be estimated was below 10% in all cases.

Table 7.1: Peak-to-peak amplitude A_f (mean±std) of the f-waves in simulated signals

	A_f (μV)		
SNR	V_1	V_2	V_5
12	206 ± 60	160 ± 68	45 ± 24
15	146 ± 42	113 ± 48	32 ± 17
18	103 ± 30	80 ± 34	23 ± 12
21	73 ± 21	56 ± 24	16 ± 8

Regarding lead combinations, the performance does not improve when V_5, having the lowest A_f (cf. Table 7.1), is analyzed instead of V_2. The $\mathrm{SNR}_{\mathrm{MAX}}$ was found to be 3±2 dB higher than $\mathrm{SNR}_{\mathrm{MIN}}$ for (V_1, V_2), while it was 17±4 dB for (V_1, V_5). The QRS amplitude A_{QRS} is equal to 872±208 μV, 908±357 μV, 1195±345 μV in V_1, V_2, and V_5, respectively.

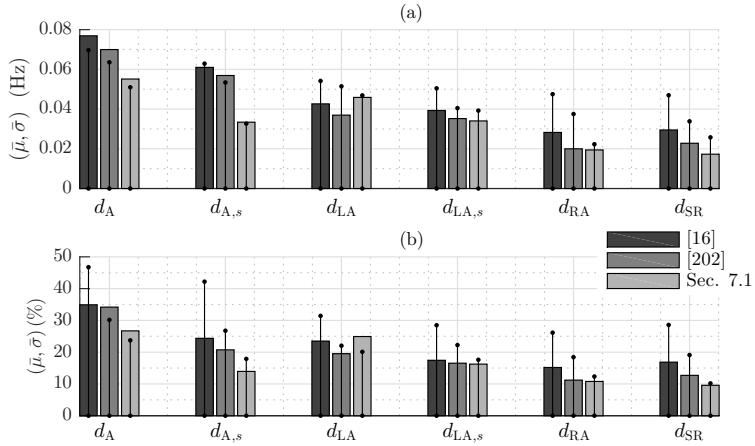

Figure 7.11: Results of respiratory rate estimation in real ECGs using different EDR signals and rate estimation techniques. The (a) absolute error (in Hz), and (b) relative error (in %). The error metrics $\bar{\mu}$ and $\bar{\sigma}$ are denoted with bars and lines, respectively. For each EDR signal, the error metrics of three rate estimation techniques are displayed: the technique in [16] (to the left), [202] (in the middle), and the one presented in Sec. 7.1 (to the right).

Hence, large differences between $\mathrm{SNR}_{\mathrm{MIN}}$ and $\mathrm{SNR}_{\mathrm{MAX}}$ for (V_1, V_5), are associated with low f-wave amplitude and large QRS amplitude.

Regarding the performance for different definitions of SR, results in Fig. 7.10 show that the first difference, which is equivalent to linear fitting with two samples (2 ms), yields to similar errors as the linear fitting with eight samples (8 ms). Thus, the use of the first difference to obtain the SR, apart from its simpler computation, may suffice for a robust performance.

Real data

The rates extracted from the reference respiration signal are characterized by 0.259 ± 0.083 Hz, while $\mathrm{SNR}_{\mathrm{MIN}}$ and $\mathrm{SNR}_{\mathrm{MAX}}$ are 21 ± 7 dB and 26 ± 3 dB, respectively.

Figure 7.11 shows that of the four EDR signals $d_{\mathrm{A}}(n)$ performs inferior, regardless of the rate estimation technique. The rate estimation technique proposed in [16] yield larger errors than do the present technique and the one in [202]. While the latter two techniques have similar performance, the present rate estimation technique achieves the lowest error when $d_{\mathrm{SR}}(n)$ is used, resulting in a median error of 0.015 ± 0.021 Hz ($9.5 \pm 10.2\%$), as well as improves significantly the performance of $d_{\mathrm{A},s}(n)$ resulting in a median error of 0.034 ± 0.033 Hz ($13.5 \pm 17.9\%$). The inter-subject median of $\mathcal{T}$ for $d_{\mathrm{A}}(n)$, $d_{\mathrm{A},s}(n)$, $d_{\mathrm{LA}}(n)$, $d_{\mathrm{LA},s}(n)$, $d_{\mathrm{RA}}(n)$, and $d_{\mathrm{SR}}(n)$ is 9.4%, 3.4%, 11.0%, 5.3%, 3.0%, and 1.9%, respectively. Thus, $d_{\mathrm{SR}}(n)$ is the least affected by the presence of f-waves.

Figure 7.12 shows an example of the respiratory rate estimation in real ECGs. Figure 7.13 shows an example of peak selection using different methods in real ECGs.

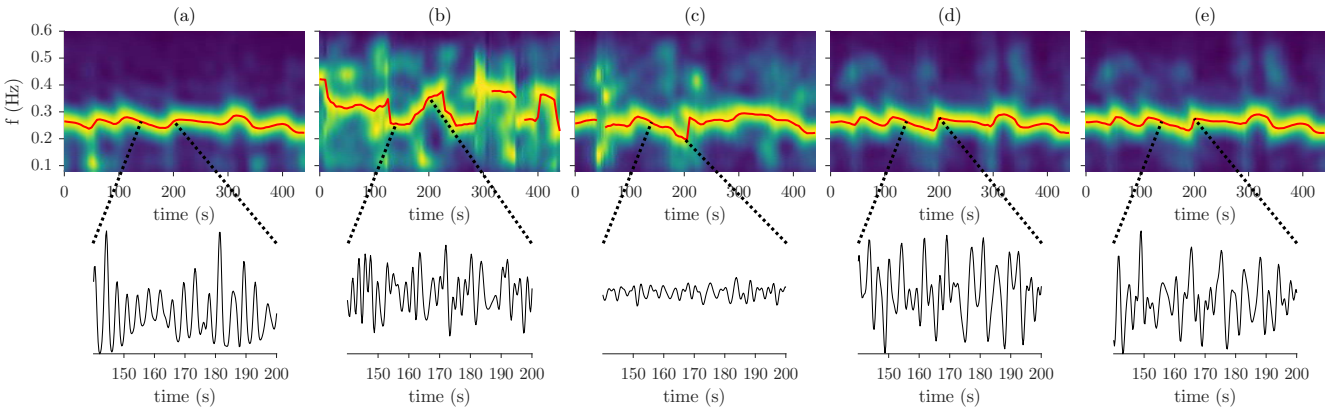

Figure 7.12: Respiratory rate estimation in real ECGs. Time–frequency spectrum obtained from (a) the reference respiratory signal, (b) $d_{\mathrm{LA}}(n)$, (c) $d_{\mathrm{LA,s}}(n)$, (d) $d_{\mathrm{RA}}(n)$, and (e) $d_{\mathrm{SR}}(n)$. The estimated rate is displayed with a red line. An excerpt of the EDR signal is displayed below each TF spectrum.

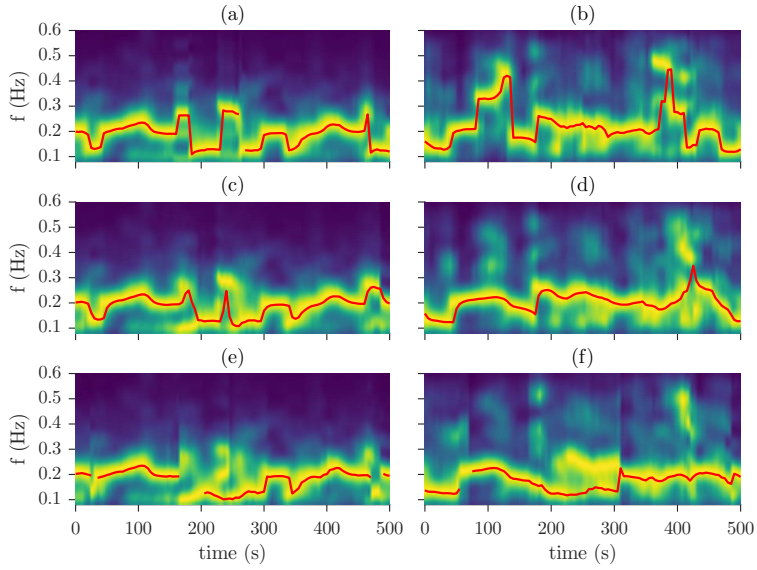

Figure 7.13: Respiratory rate estimation in real ECGs using different methods. The left column presents TF spectra obtained from the reference respiratory signal and the right column from the EDR signal $d_{\mathrm{SR}}(n)$, while each row corresponds to the rate estimation procedure in (a)–(b) [16], (c)–(d) [202], (e)–(f) Sec. 7.1. The resulting intra-subject errors are 0.062 ± 0.063 Hz, 0.040 ± 0.046 Hz, and 0.016 ± 0.017 Hz, respectively. The estimated respiratory rate is displayed with a red line.

7.4 Discussion

The present study addresses the lack of methods for estimating the respiratory rate in AF. The estimation explores beat-to-beat morphological variations induced by respiration which are blurred by the presence of f-waves.

The results obtained on simulated ECGs (Fig. 7.9) show that f-wave suppression improves respiratory rate estimation only for $d_{\mathrm{LA}}(n)$. In the same figure, the worse performance of $d_{\mathrm{RA},s}(n)$ and $d_{\mathrm{SR},s}(n)$ is largely due to that the weighted averaging operation in (7.2) leads to smoothing of QRS complexes which in turn attenuates the respiratory information. As demonstrated in Fig. 7.8, the respiratory information in both $d_{\mathrm{RA},s}(n)$ and $d_{\mathrm{SR},s}(n)$ is sometimes completely attenuated because $\hat{\sigma}^2_{\mathrm{QRS}}(n)$ is much lower than $\hat{\sigma}^2_f$, leading to that $\hat{\sigma}^2_{\mathrm{QRS}}(n)$ is 0 in (7.4). For $\hat{\sigma}^2_{\mathrm{QRS}}(n) = 0$, i.e., the weights in (7.3) are identical to those of ABS, i.e., $w_{i,m}(n) = 1/M$, the averaged QRS complexes lose their morphological variability due to respiration since the relationship between $\hat{\sigma}^2_{\mathrm{QRS}}(n)$ and $\hat{\sigma}^2_f$ determines, through (7.3), the balance between QRS variability preservation ($\hat{\sigma}^2_f \ll \hat{\sigma}^2_{\mathrm{QRS}}(n)$) and f-wave suppression ($\hat{\sigma}^2_f \gg \hat{\sigma}^2_{\mathrm{QRS}}(n)$). The suppression of respiratory information appears to depend on the way in which the methods combine the available leads. While $d_{\mathrm{RA}}(n)$ and $d_{\mathrm{SR}}(n)$ consider respiratory information contained in individual leads, $d_{\mathrm{LA}}(n)$ combines spatial information from two leads. This implies that LA will retrieve respiratory information if it is still present or dominant in one of the leads, whereas, for RA and

SR, the posterior combination of TF–spectra (one spectrum per lead), where the respiratory information is suppressed, can introduce spurious peaks (Fig. 7.8(d) and Fig. 7.8(f)). It should be noted that the estimation of σ_f^2 is also a critical part since, at higher heart rates, the TQ intervals may be too short to contain the needed number of samples for reliable estimation. In addition, it is well-known that the f-wave amplitude changes considerably over time, thus questioning the assumption in [77] of a fixed σ_f^2.

The results obtained from real ECGs (Fig. 7.11) show that the QRS area $d_{\mathrm{A}}(n)$ results in the highest error, thus corroborating the poor performance reported in [263]. More interestingly, using the peakedness proposed in this study, $d_{\mathrm{RA}}(n)$ and $d_{\mathrm{SR}}(n)$ exhibit robust performance without the need for f-wave suppression, yielding median errors of 0.019±0.025 Hz (10.8±12.3%) and 0.015±0.021 Hz (9.5±10.2%), respectively, which are considerably smaller than those of $d_{\mathrm{LA}}(n)$ and $d_{\mathrm{LA},s}(n)$, i.e., 0.046±0.047 Hz (24.9±20.1%) and 0.034±0.039 Hz (16.2±17.6%), respectively. The suppression of f-waves improves the performance of $d_{\mathrm{LA}}(n)$, since variations in the location of the QRS interval, complicating the time alignment between the observed and the reference loop, are reduced. The worse performance of $d_{\mathrm{LA}}(n)$ is mostly attributed to the fact that loop alignment is more difficult to perform in the presence of f-waves, but also to the use of non-orthogonal leads and the way leads are combined.

The slope-based methods $d_{\mathrm{RA}}(n)$ and $d_{\mathrm{SR}}(n)$ are less affected by the presence of f-waves since the differencing operation attenuates lower frequencies where most of the f-wave power is located. Both SR and RA combine estimates of QRS slopes; the combination can be either linear (7.8) or nonlinear (7.7). The use of the first difference is equivalent to use linear fitting with two samples. Computed results evidence that SR obtained either using the first difference or line fitting (8 ms) give equivalent results (see Fig. 7.10). Thus, the slightly worse performance of $d_{\mathrm{RA}}(n)$ relative to $d_{\mathrm{SR}}(n)$ (Fig. 7.11 and Fig. 7.9) should be a consequence of the different ways the slope estimates are combined in (7.7) and (7.8).

The combination of TF–spectra from more than one EDR signal is advantageous when one of the leads is more influenced by respiration than f-waves. The reason is that the peakedness criteria lead to the selection of the TF–spectra with the most dominant frequency component, not necessarily corresponding to the lead with the lowest f-wave amplitude. An ECG lead with large f-waves may be more adequate for respiratory rate estimation if the morphological changes due to respiration dominate over f-waves. Obviously, the peak-to-peak f-wave amplitude is more prominent in V_1 and V_2 than in V_5 (Table 7.1). However, V_5 is less influenced by respiration than V_2 since the performance does not improve when analyzing (V_1, V_2) instead of (V_1, V_5), suggesting that the influence of both respiration and f-waves vary from lead to lead. In [189], a simulation study was designed to evaluate the influence of respiration, measured by QRS ensemble variance, and the f-wave amplitude on EDR performance. Results confirmed that lower errors in leads with similar f-wave amplitude are due to a more pronounced respiratory influence that was larger in V_2, V_3, and V_4 compared to other precordial leads.

In the EDR signals, morphological changes in the QRS complexes due to the f-waves are manifested by additional spectral components complicating the estimation of a time-varying respiratory rate. Moreover, the intrinsic sampling rate of the EDR signal is determined by the heart rate and thus aliasing will occur for components whose frequencies exceed half the mean heart rate. The alias of the first harmonic of the f-waves may lie in the frequency range of respiratory rates and therefore introduce spurious peaks. To address this problem, a novel definition of peakedness is introduced as well as novel criteria for the selection of a spectral peak defining the respiratory rate. In [16], the respiratory rate is determined by the location of the peak with the largest spectral power, while, in [202], by the location of the peak closest to a smoothed respiratory rate estimate $\bar{f}_r(k)$. In this study, respiratory rate estimation is performed through minimization of a cost function which, for each spectral peak, quantifies the power deviation from the largest peak and the frequency deviation from $\bar{f}_r(k)$. The peak selection procedures in [16] and [202] are special cases of the proposed method, obtained by either setting $a_f = 0$ or $a_p = 0$. The significance of the peak selection criteria on performance is evaluated on real ECGs. Analyzing $d_{\mathrm{SR}}(n)$, the results in Fig. 7.11 show that the peakedness measure in (7.10) achieves the lowest error, while similar errors are obtained for $d_{\mathrm{LA},s}(n)$ and $d_{\mathrm{RA}}(n)$ using the peakedness measure in [202]. The peakedness measure in [16] yields a larger error than do the other two measures since its design parameters were chosen to account for the dynamics of a stress test. The results suggest that the technique for respiratory rate estimation proposed in this study perform well in the presence of spectral components caused by f-waves. The technique may provide better tracking of respiratory rate in patients with SDB when the spectral components are caused by either amplitude or frequency modulation in the respiratory signal.

Since the respiratory rate is known to fluctuate on a short-term basis, it is of interest to judge whether the estimation error $\Delta f(k)$ is comparable to the variability of $f_r(k)$, computed from the reference respiratory signal, and thus acceptable for use in clinical applications. In [16], in stress test recordings, the short-term variability was found to be 0.019±0.007 Hz from analysis intervals of 60 seconds. Using the approach in [16], the short-term variability in $f_r(k)$ is in the present study found to be 0.012 ± 0.01 Hz. Since this short-term variability is of the same order of magnitude as the error of the SR method, i.e., 0.015±0.021 Hz, see Fig. 7.11, it can be concluded that SR is suitable for use in clinical applications. Although SR was designed particularly for operation in AF, this novel method was also validated in ambulatory recordings. In collaboration with the Leuven Catholic University (KU Leuven) in Belgium, a review study of ten EDR methods, including SR, was carried out for evaluating the performance on deriving respiratory and cardiorespiratory parameters, under multiple conditions, including normal and abnormal breathing patterns, changes in respiratory rate, noise, and artifacts [337]. Results show that the slope-based methods outperform the other EDR methods in ambulatory recordings, thereby suggesting that SR can be a comfortable, and inexpensive tool for monitoring robustly respiration. Further studies can be done by fusing information from different EDR signals to further improve the accuracy of the respiratory rate estimation, as proposed in [202].

A limitation of the present study is that the performance was studied on only one respiratory rate pattern in simulated signals. Another limitation is that only one f-wave suppression method was investigated. Other methods which better preserve the respiratory information than does signal- and noise-dependent weighted averaging should be investigated.

To sum up, based on real and simulated ECGs, the results show that the slope range method offers the best performance in respiratory rate estimation. Moreover, this method is computationally simple since f-wave suppression is not needed. The R-wave angle method also offers robust performance without needing f-wave suppression, and, therefore, it can be concluded that the slope-based methods are less affected by the presence of f-waves.

8

Model-based photoplethysmographic pulse waveform analysis

8.1 Pulse decomposition analysis

The association between autonomic dysregulation and reduced arterial compliance is commonly observed as a consequence of many disease states, including mental disorders [333, 352]. Arterial stiffness might be a result of prolonged exposure to mental stress [341], and it can also be mediated via inflammatory processes [89]. A great amount of information about the cardiovascular system, including autonomic function and vascular characteristics can be derived from the PPG signal. The speed at which the pressure wave travels along arterial branch is proportional to BP [184]. Thus, multiple vascular parameters in the literature are related to the time that the pressure wave takes to propagate between two points of the arterial branch. However, this type of measurements requires the recording of two signals, at a proximal and distal point, respectively. Taking into account that pulse pressure propagation in arteries causes alterations in blood volume and accordingly changes in the PPG pulse shape, vascular parameters can be derived from a single PPG signal [4]. As a result, the simultaneous measurements at different sites of the body could be avoided.

One of the most recognized methods for deriving non-invasive indexes of arterial distensibility from a single PPG signal is based on the PPG second derivative [94]. However, due to double differentiation, the detection of inflection points can be challenging in the

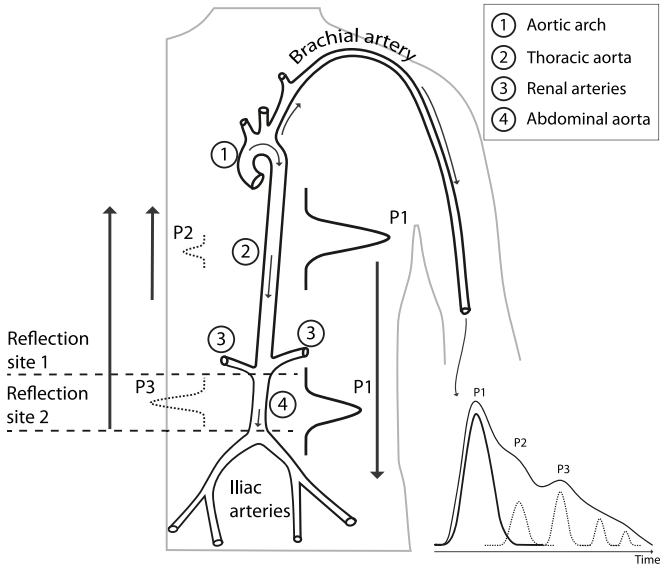

Figure 8.1: Origin of the PPG pulse inner waves. The resulting morphology from the superposition of a forward pulse (P1) and pulses (P2 and P3, among others) reflected at the renal and iliac bifurcations of the arterial tree. Reproduced from [70].

presence of noisy signals. An alternative approach, called pulse decomposition analysis (PDA), has been proposed, as may increase the robustness for some morphological measurements. PDA is based on the hypothesis that the PPG pulse is composed of a single forward wave and its delayed versions, which arise from reflections of the pressure wave at the renal and iliac bifurcations of the arterial branch (see Fig. 8.1). Hemodynamic parameters such as BP and arterial tone changes can be assessed by quantifying time and amplitude relation between the forward and the reflected waves [20]. Several PDA variations have been proposed for modeling the PPG pulse considering different types of morphology (Gaussian, Rayleight and Logarithmic normal function) and number (2 to 5) of inner waves [70, 122, 152]. However, the physiological interpretation of parameters derived from PDA approaches that model the PPG by fitting several waves at once might not be straightforward. In this thesis, an alternative approach [203], where the main and reflected waves are extracted one-by-one from the PPG pulse, is studied, thereby facilitating the interpretation of model parameters based on the pulse wave propagation physiology.

8.1 Pulse decomposition analysis

Intervals of the PPG signal containing artifacts are suppressed using the energy-based approach proposed in [9]. Then, PPG pulse detection is carried out using a low-pass differentiator (transition band from 7.7 Hz to 8 Hz) and a time-varying threshold [201].

For the i:th pulse, the fiducial point $n_{\mathrm{F}}(i)$ consists in the maximum up-slope point of the low-pass differentiator filtered signal.

A pulse decomposition analysis (PDA) technique based on [203] is applied for pulse waveform modeling. Prior to PDA, the raw PPG signal is subjected to low-pass filtering (forth order bidirectional IIR with cut-off frequency of 5 Hz) for attenuating high frequency noise, with $x_{\mathrm{PPG}}(n)$ denoting the filtered signal. In this study, due to low-pass filter operations, a percentage relative to the maximum up-slope value of the first derivative of $x_{\mathrm{PPG}}(n)$ ($x'_{\mathrm{PPG}}(n)$) is used for defining the pulse basal point ($n_{\mathrm{B}}(i)$). The point $n_{\mathrm{B}}(i)$ is searched in the interval $\Omega_{\mathrm{U}} = [n_{\mathrm{U}}(i) - 0.3F_s, n_{\mathrm{U}}(i)]$ around the maximum up-slope point of $x'_{\mathrm{PPG}}(n)$ ($n_{\mathrm{U}}(i)$):

$$n_{\mathrm{B}}(i) = \underset{n\in\Omega_{\mathrm{U}}}{\arg\min} \left\{ \left| x'_{\mathrm{PPG}}(n) - 0.05 \cdot x'_{\mathrm{PPG}}(n_{\mathrm{U}}(i)) \right| \right\}, \tag{8.1}$$

where $x'_{\mathrm{PPG}}(n) = x_{\mathrm{PPG}}(n) - x_{\mathrm{PPG}}(n-1)$. The point $n_{\mathrm{U}}(i)$ is defined as the absolute maximum of $x'_{\mathrm{PPG}}(n)$ in a symmetrical fixed window of 10 msec around the time instant associated with $n_{\mathrm{F}}(i)$. Linear interpolation of $x_{\mathrm{PPG}}(n_{\mathrm{B}}(i))$ series is subtracted from $x_{\mathrm{PPG}}(n)$, yielding $\check{x}_{\mathrm{PPG}}(n)$. Thus, each pulse $x_i(n)$ begins and ends with zero amplitude:

$$x_i(n) = \check{x}_{\mathrm{PPG}}(n + n_{\mathrm{B}}(i)) \quad n \in [0, \ldots, n_{\mathrm{B}}(i+1) - n_{\mathrm{B}}(i)]\,. \tag{8.2}$$

The i:th pulse wave $x_i(n)$ is decomposed into J symmetrical waves $x_{i,1}(n), \ldots, x_{i,\mathrm{J}}(n)$, and a residual signal. The j:th inner wave $x_{i,j}(n)$ is obtained by concatenating the up-slope of the running residual signal $\tilde{x}_{i,j}(n)$ ($\tilde{x}_{i,1}(n) = x_i(n)$) with itself horizontally flipped, assuming that the reflected waves arrive after half of the incident pulse is over:

$$x_{i,j}(n) = \begin{cases} \tilde{x}_{i,j}(n), & n \in [n_{\mathrm{O}_j},\ n_{\mathrm{E}_j}], \\ \tilde{x}_{i,j}(-n + 2n_{\mathrm{E}_j}), & n \in (n_{\mathrm{E}_j}, 2n_{\mathrm{E}_j} - n_{\mathrm{O}_j}], \\ 0, & \text{otherwise}, \end{cases} \tag{8.3}$$

where n_{O_j} and n_{E_j} denote the up-slope onset and end of $\tilde{x}_{i,j}(n)$, respectively; the dependence of i in the up-slope onset n_{O_j} and end n_{E_j} is omitted for simplicity. After the up-slope interval has been defined, the j:th inner wave $x_{i,j}(n)$ is subtracted from the running residual $\tilde{x}_{i,j}(n)$, i.e., $\tilde{x}_{i,j+1}(n) = \tilde{x}_{i,j}(n) - x_{i,j}(n)$, and the $(j+1)$:th inner wave is computed recursively from $\tilde{x}_{i,j+1}(n)$; J is set to 3.

Figure 8.2 illustrates an example of PDA for two different pulse waveform morphologies. The up-slope end n_{E_j} is the position of the first relative maximum of $\tilde{x}_{i,j}(n)$ and the up-slope onset n_{O_j} ($n_{\mathrm{O}_j} < n_{\mathrm{E}_j}$) is the first non-negative-amplitude sample of $\tilde{x}_{i,j}(n)$ [203], e.g., for the main wave $n_{\mathrm{O}_1} = n_{\mathrm{B}}$ (see Fig. 8.2(a)). However, this definition of the up-slope interval may lead to erroneous decomposition results in some morphologies (see Figs. 8.2(a)-(c) and Figs. 8.2(d)-(f)). For instance, relative maxima with low amplitude (see Fig. 8.2(c)) or slope changes prior to the first relative maximum (see Fig. 8.2(e)) can lead to erroneous definition of inner waves. In this dissertation, to deal with these problems, two modifications are introduced. First, an inner wave is considered to exist only if the

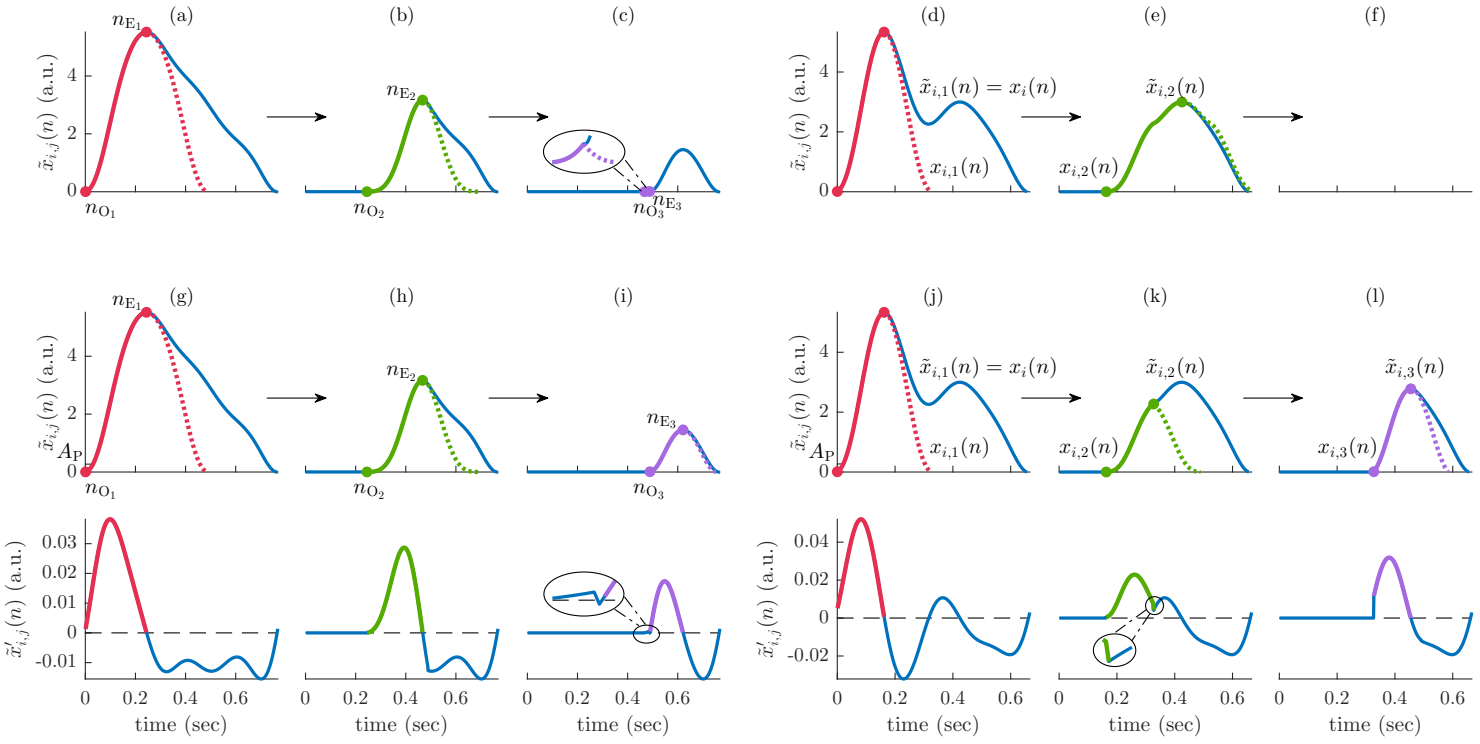

Figure 8.2: Pulse decomposition algorithm. Recursive computation of inner waves for two different pulse morphologies of $x_i(n)$ in (a)-(c), and (d)-(f). The first derivative of the running residual $\tilde{x}_{i,j}(n)$ ($\tilde{x}'_{i,j}(n)$) is displayed below each step of decomposition. The inner waves $x_{i,1}(n)$, $x_{i,2}(n)$, $x_{i,3}(n)$ are marked in red, green, and purple, respectively; the up-slope is marked with solid line, while the horizontally flipped up-slope with dashed line.

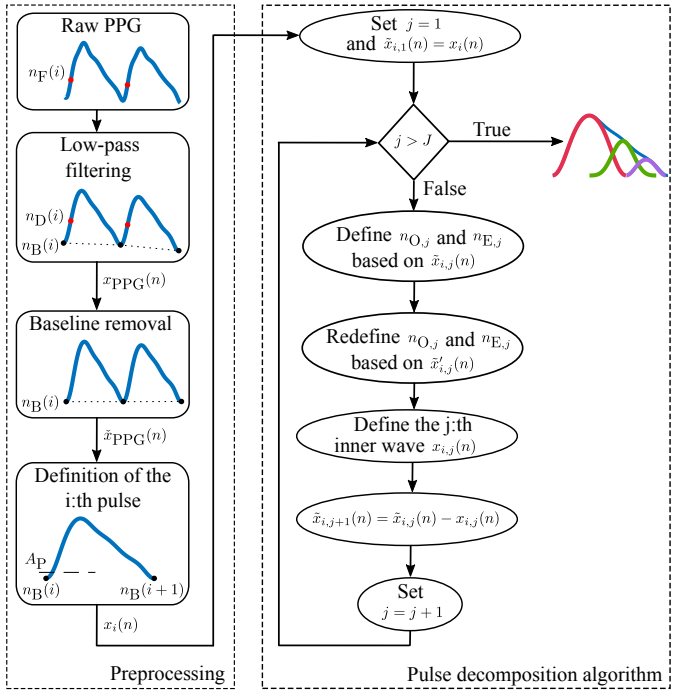

Figure 8.3: Block diagram of the pulse decomposition algorithm.

absolute maximum value of $\tilde{x}_{i,j}(n)$, i.e., $\tilde{x}_{i,j}(n_{E_j})$, exceeds the fixed (for the i:th pulse) amplitude threshold $A_P = 0.05 \cdot \max_n \{x_i(n)\}$. Then, the first derivative of $\tilde{x}_{i,j}(n)$ $\left(\tilde{x}'_{i,j}(n)\right)$ is taken into account for the better identification of the inner waves.

The improvement in decomposition are shown in the Figs. 8.2(g)-(l). When $x_i(n)$ is decomposed to inner waves, the up-slope of the running residual $\tilde{x}_{i,j}(n)$ might not be a strictly increasing function in $[n_{O_j},\ n_{E_j}]$, i.e., $\tilde{x}'_{i,j}(n)$ is not always positive (see Fig. 8.2(i)) or has more than one inflection points (see Fig. 8.2(k)). This is either due to the presence of a relative maximum with amplitude lower than A_P at the beginning of the up-slope interval (see Fig. 8.2(i)), or due to a slope change at the end of up-slope interval which, however, does not appear as a relative maximum in $\tilde{x}_{i,j}(n)$ (see Fig. 8.2(k)). Thus, n_{O_j} is redefined as the next sample after the last negative-amplitude sample of $\tilde{x}'_{i,j}(n)$, so that $\tilde{x}'_{i,j}(n) \geq 0$. Then, n_{E_j} is redefined as the position of the first relative minimum of $\tilde{x}'_{i,j}(n)$ for which $\tilde{x}_{i,j}(n_{E_j}) > A_P$ is fulfilled ensuring that the j:th inner wave can be defined.

Figure 8.3 illustrates a block diagram with the PDA steps.

Pulse waveform characteristics

Several morphological features associated with systolic arterial pressure and vascular compliance measures are extracted from each PDA based modeled PPG pulse. The am-

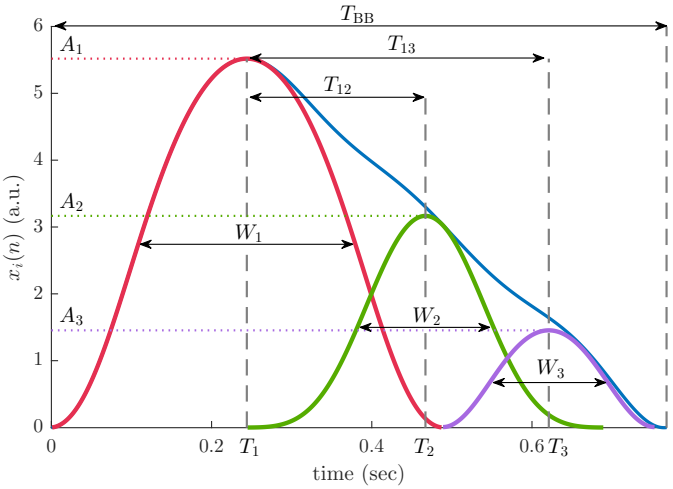

Figure 8.4: Pulse waveform characteristics. Morphological features derived from amplitude A_j, position T_j, and width W_j values of the $J = 3$ inner waves.

plitude $A_j(i)$ and the position $T_j(i)$ of an inner wave are defined as the amplitude and the position of the absolute maximum of $x_{i,j}(n)$, respectively. The width of $x_{i,j}(n)$, denoted by $W_j(i)$, is estimated by the full-width at half maximum. Then, the time delay between the position of the main wave and the first reflected wave $T_{12} = T_2 - T_1$, as well as the percentage of amplitude loss in the first reflection $A_{12} = 100 \cdot (A_1 - A_2)/A_1$ are calculated (the dependence of i is omitted for simplicity). Similarly, T_{13} and A_{13} are calculated for the second reflected wave. The position T_1 and the width W_1 of the main wave are also subjected to analysis. Finally, the instantaneous HR is calculated using the fiducial points $n_F(i)$. Figure 8.4 shows an example of pulse waveform characteristics. The pulse-to-pulse interval for the pulses that were considered in PDA is given by $T_{BB}(i) = (n_B(i+1) - n_B(i))/F_s$.

In this PDA method, distorted pulses are discarded. They are considered as such when at least one of the following criteria are satisfied: (a) the pulse wave is decomposed to less than 3 waves, (b) the amplitude of the main wave is not the largest of the three waves, i.e., $A_2 > A_1$ or $A_3 > A_1$, (c) the second wave is located at the end of the pulse interval, i.e., $T_2 > 0.8\,T_{BB}$, or (d) the third wave occurs earlier than $0.35\,T_{BB}$, i.e., $T_3 < 0.35\,T_{BB}$. For each feature, outlier rejection is complemented with a median absolute deviation (MAD)-based rule [16]; the threshold is defined as 5 times the running MAD of the previous 50 pulses. Modeling the PPG pulse as a main wave superposed with several reflected waves are scarcely considered in mental health. The modeling of PPG and subsequent analysis of the model's parameters allows for the robust quantification of changes in physiological mechanisms related to the ANS, thereby improving the assessment of stress and depression.

Part III

Stress assessment and depression monitoring

9

Biomarkers for assessing stress

Stress is common in our fast-paced society and strongly influences our psychological and physical well-being. Prolonged exposure to stress is a common instigator underlying the co-morbidity between mental disorders and CVDs, thereby highlighting the need of assessing stress [132]. Humans exposed to stressful experiences exhibit a wide range of physiological and/or psychological responses. In the short term, changes in the ANS allow the organism to respond to sudden changes in the environment. Stress response can vary depending on the type of stress, i.e. physiological or psychological, and other factors including mental health or personality [104]. Although focus should be put on behavioral, cognitive, and emotional responses evoked by mental stress, the study of physiological stress, e.g. hemodynamic or heat, that minimize the influence of stress perception on the stress-evoked arousal, can be useful for developing biomarkers of stress. Among all biological systems involved in stress response, the noninvasive assessment of the ANS seems the most feasible way to carry out a continuous monitoring of changes in the internal environment of the body. ANS biomarkers can be derived from the analysis

of diverse biosignals, such as HRV and respiration. Joint analysis of various biosignals allows for the quantification of interactions among biological systems associated with the ANS. The development of novel approaches for deriving noninvasive ANS biomarkers offers the possibility to improve the assessment of stress in healthy individuals and ANS dysfunction in depressed patients.

9.1 Mental stress

A variety of studies have explored the potential use of ANS biomarkers derived from various biosignals, such as HRV, respiratory, and PPG signals, for an objective assessment of stress [114]. In [145], the inclusion of respiratory information in HRV analysis improved the ability of HRV to discriminate stress. Under challenging situations, the nonstationary nature and the interactions between different biosignals might provide useful information [245, 246]. Various methods have been applied to measure cardiorespiratory interactions [100, 149]. To take into account possible nonlinear interactions between respiration and HRV signals, the use of HOS is investigated in healthy subjects during a mental stress protocol.

9.1.1 Materials and methods

Experimental protocol and data acquisition

A database of 80 healthy volunteers (40 women, 21.57 ± 3.97 years), who had not been diagnosed with any comorbidities such as cardiovascular, endocrinological or mental disorders, was recorded in the Autonomous University of Barcelona and University of Zaragoza. The protocol comprises two sessions that were performed on different days but at the same hour for each participant (see Fig. 9.1). The first one, called basal session, consists in an autogenic relaxation condition, where the first 10 minutes is a baseline stage (BL_B) and the next 25 min is a relaxing stage (RS). The second session, called stress session, is composed of the following stages:

i. Baseline stage (BL_S): A 10-minutes length autogenic relaxation condition.

ii. Story Telling (ST): 3 stories, lasting about 1 minute each, with a great amount of details were told to the subject, who was requested to remember as many details as possible.

iii. Memory Test (MT): The subject had to repeat aloud all the remembered details for each story.

iv. Stress Anticipation (SA): The subject was instructed to wait alone during 10 minutes for the evaluation of the previous task.

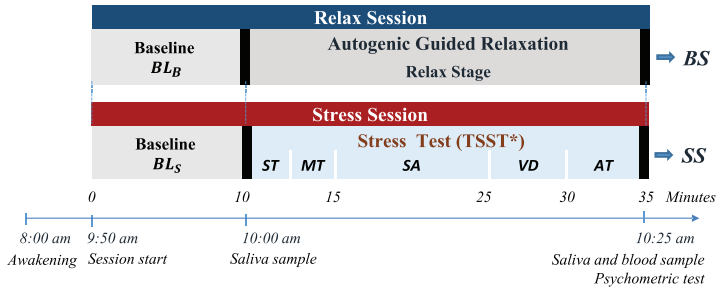

Figure 9.1: Mental stress protocol. The experimental protocol consists of two sessions, the Basal Session (BS) and the Stress Session (SS), recorded on different days. BS consists of a baseline stage (BL_B) and a relaxing stage (RS), while SS is composed of a baseline stage (BL_S) and various stressful tasks including, story telling (ST), memory test (MT), stress anticipation (SA), video display (VD), and arithmetic task (AT).

v. Video Display (VD): The presentation of a video clip from the subject performance in MT was shown. A video of an actor remembering all the details was displayed before that, trying to make the subject believe that his/her performance was very low.

vi. Arithmetic Task (AT): The subject had 5 minutes to perform successive subtractions of 13, starting from the number 1022. In case of calculation error the subject had to restart the countdown from the beginning.

Excluding the first stage of the stress session, BL_S, the rest stages are considered stressful. However, the MT and AT are not examined due to the fact that the interpretation of results is difficult while the subject is speaking. In order to avoid possible transient phenomena between the different stages, only the six central minutes of BL_B, RS, BL_S and SA are analyzed. Due to shorter duration, the whole ST and VE stage are subjected to analysis.

A Medicom system, ABP-10 module (Medicom MTD Ltd, Russia), was used for recording a respiratory signal using a belt at 250 Hz and 3 orthogonal leads of the ECG signal at 1000 Hz.

Bispectral characteristics

A HRV signal $x(t)$, sampled at 4 Hz, is generated based on the IPFM model (see Ch. 6) using the time series of beat occurrence, detected on Z-lead of the ECG. The respiratory signal $y(t)$ is downsampled to 4 Hz. Then, $x(t)$ and $y(t)$ are subjected to bandpass filtering in the intervals $[0.04, 0.8]$ Hz and $[0.08, 0.8]$ Hz, respectively. Based on the definition of WBS $B_{\mathrm{W}}(f_1, f_2)$ in eq. (6.24), different parameters that reflect nonlinear cardiorespiratory coupling are derived from the wavelet biamplitude $A_{\mathrm{B}}(f_1, f_2)$ and the wavelet biphase $\Phi_{\mathrm{B}}(f_1, f_2)$. Such parameters are the distribution of local maxima in $A_{\mathrm{B}}(f_1, f_2)$, quantified by D_{M}, and the regularity of $\Phi_{\mathrm{B}}(f_1, f_2)$, quantified by P_{E}. Note that the coordinate f_2^{M}

of the absolute maximum in $A_B(f_1, f_2)$ is particularly important since reflects respiratory rate-related information.

Statistical analysis

To account for differences in the duration of the protocol stages, the estimation of parameters is performed every 10 s in intervals of length $T = 60$ s, and the mean value, denoted as $\overline{f}_2^M$, $\overline{D}_M$, and $\overline{P}_E$, is considered in the statistical analysis. A paired t-test or a Wilcoxon test, depending on the distribution of the data, Gaussian or not, respectively, with Bonferroni correction is implemented for evaluating individual differences between the basal stage BL_S and the stressful stages ST, SA, and VD. Furthermore, BL_S is compared to BL_B and RS for testing the repeatability of the measurement, since all stages are considered relaxing but they were recorded at different days. The significance threshold is set to $p < 0.01$ (Bonferroni with 5 comparisons).

9.1.2 Results

Fig. 9.2 illustrates an example of bispectral estimation in a subject during a relaxing and stressful stage. It is observed that stress causes an increment in the respiratory rate and increases the number of bispectral peaks. Fig. 9.3 shows the boxplots of bispectral characteristics obtained at different stages of the experimental protocol. Results suggest that $\overline{f}_2^M$ increased significantly at ST and VD, but not at SA, while $\overline{D}_M$ and $\overline{P}_E$ show a statistically significant increment at all stressful stages compared to BL_S. No statistical differences are shown between BL_S and the relaxing stages recorded on different day (BL_B and RS). It should be noted that data of basal session were available only in 63 out of 80 subjects.

9.1.3 Discussion

In this analysis the relation of HRV and respiration by means of WBS has been investigated. Results in Fig. 9.2 show that stress induces amplitude and frequency-related changes in both HRV $x(t)$ and respiratory $y(t)$ signals. Reduction in the peak-to-peak amplitude of $x(t)$ (Fig. 9.2(a),(g)) in the presence of a stressful stimuli might be associated with reduced HRV that implies sympathetic activation. Higher respiratory rate and lower tidal volume in $y(t)$ are observed during stress comparing to basal condition (Fig. 9.2(b),(h)). Although WBS domain cannot be used to estimate properly the degree or strength of cardiorespiratory QPC, bispectral characteristics can be used to quantify changes in the second order properties of the signals. The coupling between respiration and both RSA and LF components in HRV can lead to multiple peaks in the bifrequency domain. Therefore, during relax, a large peak in the biampitude domain and elements concentrated to few phase bins are observed in Fig. 9.2(e) and (f), respectively, while,

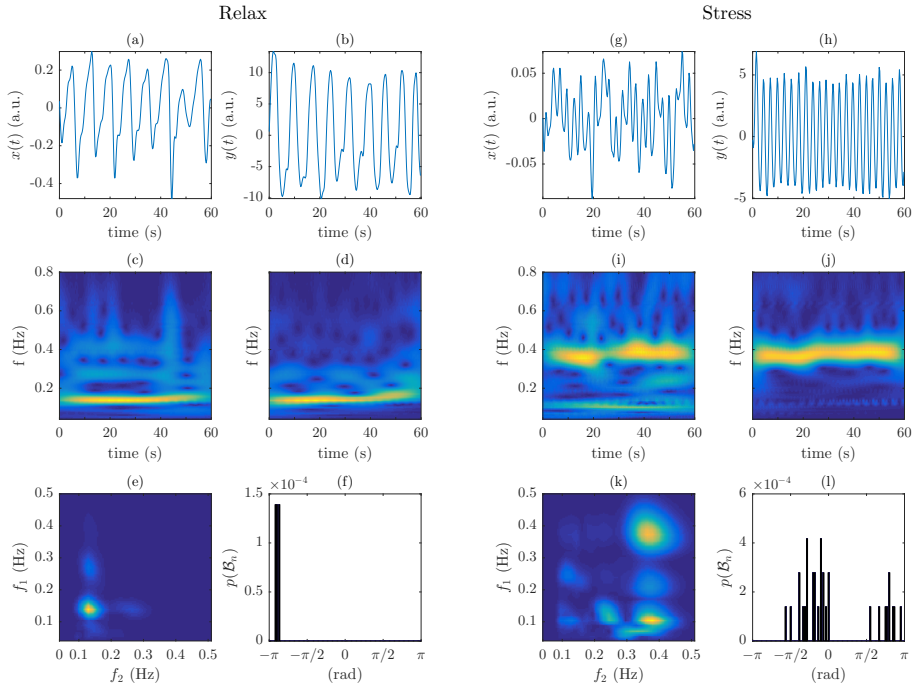

Figure 9.2: Example of bispectral estimation during a relaxing and stressful stage. (a) HRV $x(t)$, and (b) respiration $y(t)$ signal for a subject during $\mathrm{BL_S}$; below are shown their CWT amplitude coefficients in (c) and (d), respectively, (e) the wavelet biamplitude $A_{\mathrm{B}}(f_1, f_2)$, and (f) the normalized histogram of the wavelet biphase $\Phi_{\mathrm{B}}(f_1, f_2)$. For the same subject during ST, similar graphics as those in (a)–(f) are shown in (g)-(l). The values of f_2^{M}, D_{M}, and P_{E}, obtained in the relaxing and stressful stages, are 0.133 Hz, 0 Hz, 3.71×10^{-3} nat, and 0.383 Hz, 0.153 Hz, 0.037 nat, respectively.

during stress, more peaks appear and the phase is distributed to more phase bins (Fig. 9.2(k),(l)).

Results in Fig. 9.3 show that bispectral characteristics based on the distribution of local maxima around the largest peak ($\overline{D}_{\mathrm{M}}$), the regularity of biphase ($\overline{P}_{\mathrm{E}}$), and the coordinate of the absolute maximum related to respiration ($\overline{f}_2^{\mathrm{M}}$) have the capacity to discriminate between relaxing and stressful stages. Stress induction causes an increase in $\overline{f}_2^{\mathrm{M}}$ during ST and VD compared to $\mathrm{BL_S}$. The absence of a specific stressful stimuli in SA, where the subject was waiting for the evaluation of previous tasks, could imply that SA is less stressful than ST and VD. This could explain the absence of significant differences in $\overline{f}_2^{\mathrm{M}}$ for this experimental protocol stage (Fig. 9.3(a)). However, complementary information might be added using $\overline{D}_{\mathrm{M}}$ and $\overline{P}_{\mathrm{E}}$, which show statistically significant differences for all stressful stages. The local maxima representing significant couplings between frequency components are closer to the maximum peak in relax than in stress (Fig. 9.3(b)). Besides lower values of $\overline{D}_{\mathrm{M}}$ during relax, similar phase relationship is expected for adjacent frequency components, fact that is in accordance with lower values of $\overline{P}_{\mathrm{E}}$ (Fig. 9.3(c)).

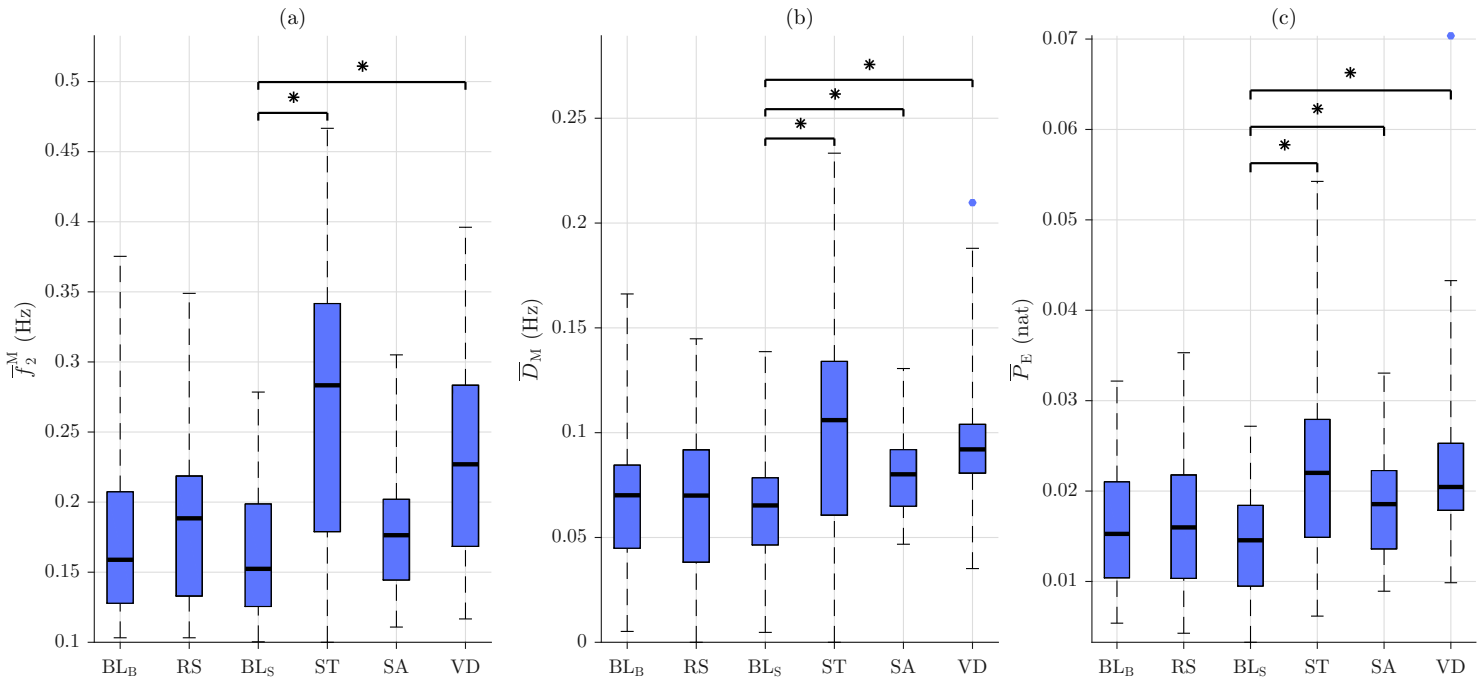

Figure 9.3: Boxplots of bispectral-related characteristics. (a) The coordinate of the absolute maximum in $A_{\mathrm{B}}(f_1, f_2)$ related to respiration, (b) the mean distance of the local maxima to the absolute maximum in $A_{\mathrm{B}}(f_1, f_2)$, and (c) the Shannon entropy of the normalized histogram of $\Phi_{\mathrm{B}}(f_1, f_2)$. Statistical differences between BL$_{\mathrm{S}}$ and various stages ($p < 0.01$) are marked with an asterisk.

Higher values of D_M and P_E during sympathetic activation (stress) could be due to the coupling between respiration and LF components in HRV [160], since additional peaks will appear at higher distance in the bifrequency domain (Fig. 9.2(k)). A less regular breathing during stress might also induce additional peaks. In [145], it was found that the respiratory rate was higher and less stable during stress than during relax. These findings highlight the need for obtaining robust estimates of nonlinear cardiorespiratory interactions and respiratory rate for a better assessment of stress.

Besides HRV and respiration, ANS biomarkers derived from PPG signals can be useful in stress quantification. In collaboration with the Kaunas University of Technology (KTU) in Lithuania, morphological parameters obtained from higher-order derivatives of the PPG signal were studied in a subset of participants subjected to the mental stress protocol [274]. PPG morphology parameters, including the amplitude of forward wave or the time delay between the main and reflected waves have the capacity to discern between stages of stress and relaxation. In [9], other surrogates of arterial stiffness were explored for the same database. Results show that the difference between arrival times of PPG pulses from two different sites of the arterial tree is also sensitive to mental stress.

It can be concluded that ANS biomarkers derived from various biosignals, such as HRV, respiratory, and PPG signals, can aid for an objective assessment of stress.

9.2 Hemodynamic stress

The transition from supine to standing causes hemodynamic stress on the cardiovascular system as blood moves from the central to the peripheral vasculature. A rapid decrease in BP due to the redistribution of the blood is followed by a rapid increase in peripheral vascular resistance, cardioacceleration, and BP overshoot [39]. The cardiovascular system is controlled by the ANS and it continuously monitors and adjusts to conditions in the body and its environment. The tilt-table is an important tool in the evaluation of homeostatic mechanisms controlled by the ANS.

Since the ANS response to hemodynamic stress is well known, the study of nonlinear cardiorespiratory coupling could aid for a better understanding of the nonlinear properties of the cardiovascular system. A variety of studies suggest that the cardiorespiratory system exhibits nonlinear interactions because the generators of cardiac and respiratory rhythm are located in the brainstem [15,84,102]. The cardiovascular and respiratory system interact via feed-forward and feed-back mechanisms, which are influenced by the activity of higher brain regions of CNS [288, 293]. The aim of this study consists in assessing cardiorespiratory QPC during hemodynamic changes induced by a tilt-table test in healthy individuals. Assuming that HRV is formed as the output of a quadratic-linear system with input respiratory oscillations, among others, a simulation study in Ch. 6.3.2 was carried out for assessing cardiorespiratory QPC in a robust and reliable way. Results showed that RWB is able to detect even weak QPC with delays in the range of 0–2 s, which are usual in the ANS control of HR. Once the presence of QPC has been detected,

NWB, which is not influenced by the amplitude of interacting oscillations, can be used to quantify the strength of QPC.

9.2.1 Materials and methods

Experimental protocol and data acquisition

A database of 17 volunteers (6 females, 28.5 ± 2.8 years), who had not been diagnosed with any comorbidities such as cardiovascular, endocrinological or mental disorders, was recorded in University of Zaragoza. Participant underwent a head-up tilt table test that consists of: 4 minutes in early supine position (T_e), 5 minutes head-up tilted to an angle of 70^o (T_h) and 4 minutes back to later supine position (T_l).

A BIOPAC MP 150 system was used for recording the standard 12-lead ECG at 1000 Hz and a respiratory signal using a strain gauge transducer at 125 Hz.

Cardiorespiratory QPC

As in the previous study, a HRV signal $x(t)$, sampled at 4 Hz, is generated based on the IPFM model (see Ch. 6) using the time series of beat occurrence, detected on lead V_4 of the ECG. The respiratory signal $y(t)$ is downsampled to 4 Hz. Then, $x(t)$ and $y(t)$ are subjected to bandpass filtering in the intervals $[0.04, 0.8]$ Hz and $[0.08, 0.8]$ Hz, respectively. The regions, where QPC is assessed, are defined based on the respiratory rate $f_r(t)$ in eq. (6.42). A time-varying QPC tracking is performed using the definition of RWB and NWB in eq. (6.43) and (6.45), respectively, setting $T = 60$ s and $T' = 10$ s (see Fig. 9.4). The time percentage of QPC in $\Omega_{\mathrm{R,R}}$ and $\Omega_{\mathrm{L,R}}$ are denoted as $\mathcal{T}_{\mathrm{R,R}}$ and $\mathcal{T}_{\mathrm{L,R}}$, respectively, while the time percentage of aliasing, i.e., when $f_1 + f_2$ was higher than half mean HR, is denoted $\mathcal{T}_{\mathrm{A}}$.

Statistical analysis

To account for short-lasting QPC, the estimation of NWB is performed every 2 s, and the mean value, denoted as $\overline{E}_{\mathrm{R,R}}$ and $\overline{E}_{\mathrm{L,R}}$, is considered in the statistical analysis. The mean respiratory rate, denoted as $\overline{f}_r$, and the time percentages $\mathcal{T}_{\mathrm{R,R}}$, $\mathcal{T}_{\mathrm{L,R}}$, and $\mathcal{T}_{\mathrm{A}}$ are also subjected to statistical analysis. To avoid transition phenomena between stages the first and last 30 s of T_h are excluded from the analysis. A paired statistical test, t-test or a Wilcoxon test when appropriate, is carried out for evaluating individual differences between the early supine position T_e, which is considered a basal stage, and the stage T_h, where hemodynamic stress was induced, as well as the recovery stage T_l. The significance threshold is set to $p < 0.025$ (Bonferroni with 2 comparisons).

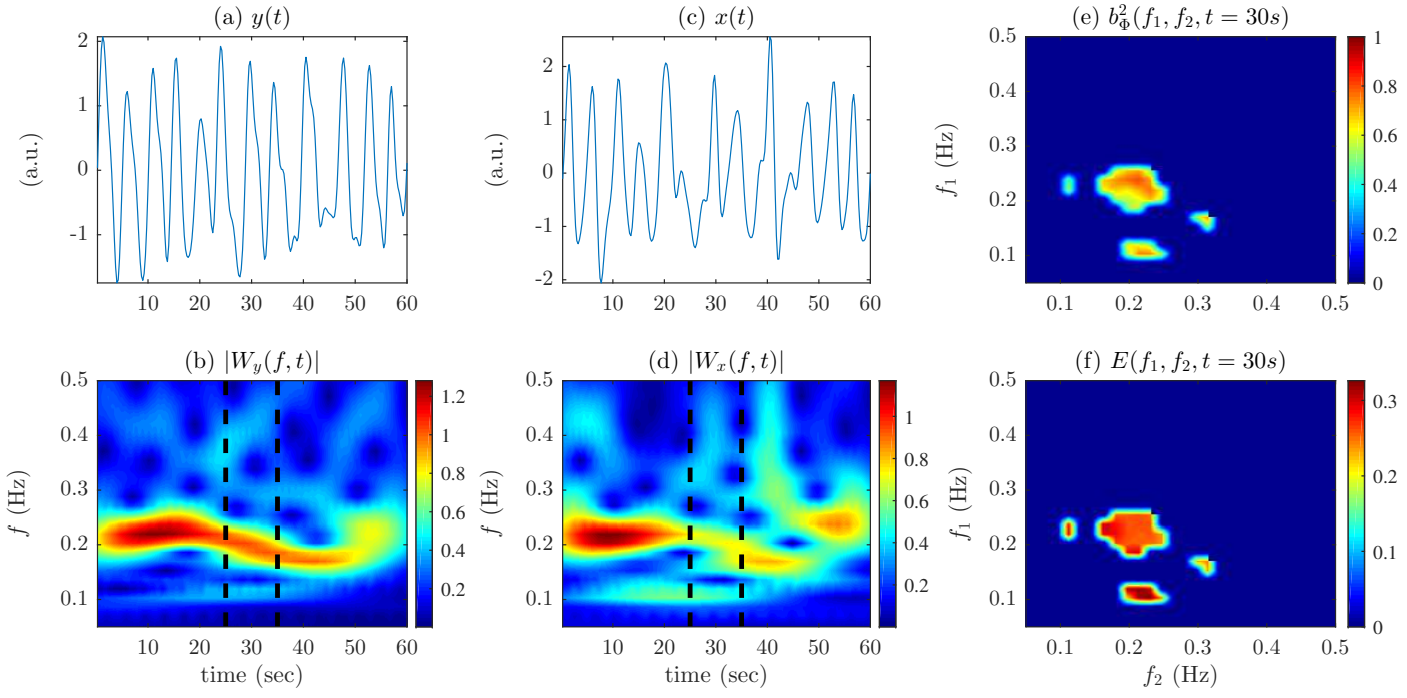

Figure 9.4: An example of QPC assessment from real signals. (a) Respiratory signal $y(t)$, (b) CWT amplitude coefficients of $y(t)$, (c) HRV signal $x(t)$, (d) CWT amplitude coefficients of $x(t)$, (e) instantaneous RWB $b^2_\Phi(f_1, f_2, t = 30s)$, and (f) instantaneous NWB $E(f_1, f_2, t = 30s)$. Bold dashed lines indicate the integration time interval $T' = 10$ s.

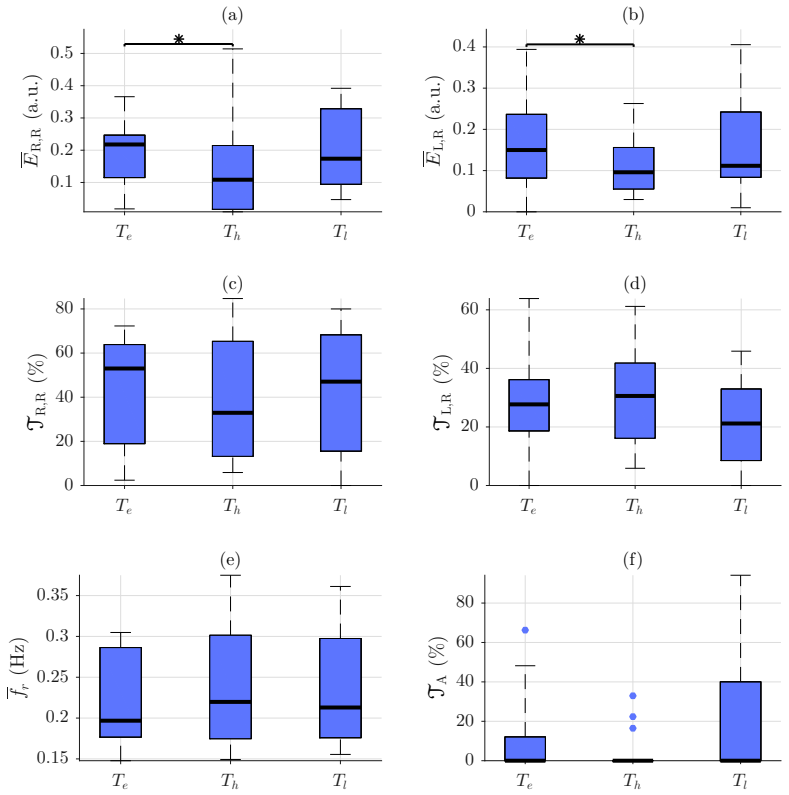

Figure 9.5: Boxplots of cardiorespiratory QPC characteristics across the experimental protocol stages. QPC strength between respiration and (a) RSA component $\overline{E}_{R,R}$, and (b) LF components of HRV $\overline{E}_{L,R}$. Time percentage of QPC in (c) $\Omega_{R,R}$, and (d) $\Omega_{L,R}$. (e) Mean respiratory rate $\overline{f}_r$, and (f) time percentage of aliasing $\mathcal{T}_A$. Statistical differences are marked with an asterisk ($p < 0.025$).

9.2.2 Results

Fig. 9.5 shows the boxplots of the features subjected to statistical analysis. Results show that NWB is reduced significantly during T_h, compared to T_e, in both regions $\Omega_{R,R}$ and $\Omega_{L,R}$ (Fig. 9.5(a)-(b)). This implies that the strength of QPC between respiration and both RSA and LF component of HRV is reduced. However, no significant differences are observed during recovery. The time percentages $\mathcal{T}_{R,R}$ and $\mathcal{T}_{L,R}$ where QPC was present do not change significantly across the whole experimental protocol (Fig. 9.5(c)-(d)). No significant differences are observed neither for the mean respiratory rate $\overline{f}_r$ nor the time percentage of aliasing (Fig. 9.5(e)-(f)). Fig. 9.6 illustrates an example of instantaneous QPC quantification for a subject during the whole experimental protocol.

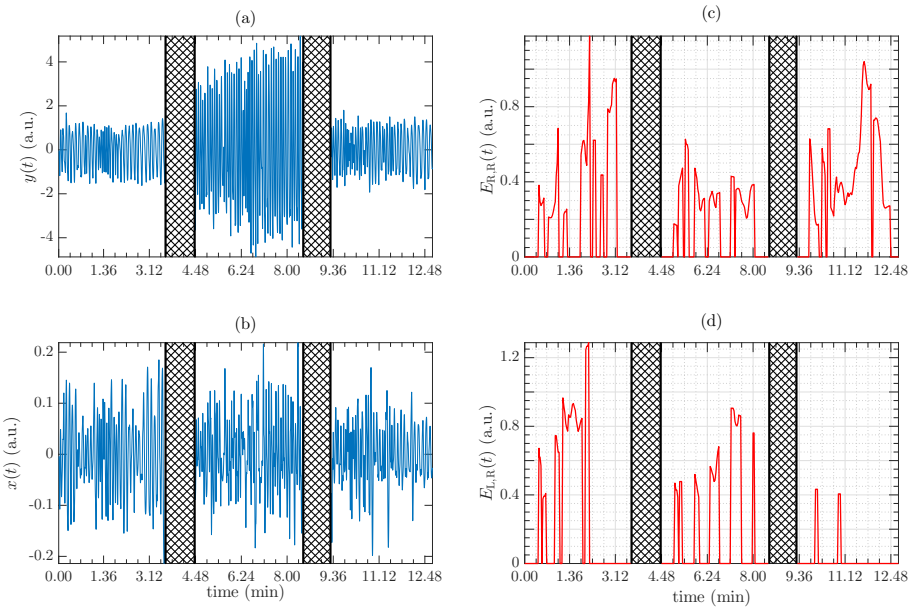

Figure 9.6: Instantaneous quantification of cardiorespiratory QPC for a subject during the whole experimental protocol. (a) Respiratory signal, (b) HRV signal, QPC strength between respiration and (c) RSA component, and (d) LF components of HRV. The black-patterned regions represent the excluded from T_h stage intervals.

9.2.3 Discussion

In this analysis cardiorespiratory nonlinear interactions during ANS changes induced by a tilt table test have been investigated. Results in Fig. 9.5(a)-(b) show that NWB is significantly reduced in head-up tilt position T_h with respect to early supine T_e. The reduction in NWB between respiration and RSA component of HRV ($\overline{E}_{\mathrm{R,R}}$) could be due to a possible vagal withdrawal as previous methods have shown [266]. Changes in $\overline{E}_{\mathrm{L,R}}$ may occur due to reciprocal modulation between respiration and LF components in HRV. The interaction between sympathetic and parasympathetic-related rhythms have been seen on the discharge of central neurons and in peripheral neural outflows [236].

An absence of reduced linear cardiorespiratory coupling during T_h was reported in previous studies analyzing the same database [245], thereby suggesting that nonlinear coupling strength may provide complementary information to the assessment of ANS dynamics. Feedback from pulmonary stretch receptors and direct respiratory-related changes in venous return during head-tilt position could evoke respiratory related fluctuations in HRV, probably through nonlinear processes [225]. Regarding the time percentage of QPC, no significant differences were found neither in $\Omega_{\mathrm{R,R}}$ nor in $\Omega_{\mathrm{L,R}}$ (Fig. 9.5(c)-(d)). Moreover, respiratory rate did not change significantly across the experimental protocol stages (Fig. 9.5(e)). This might be related to the findings of [116], where it was reported that, for the same database, the power content in the HF band of HRV did not change significantly during tilt phase.

One limitation of this study is the exclusion of those peaks where $f_1 + f_2$ was higher than half mean HR. A reduced time percentage of QPC can be attributed either to the absence of QPC or to the fact that QPC is not measurable due to aliasing. In this study the median value of the time percentage where aliasing was present ($\mathcal{T}_A$) is zero for all the stages (Fig. 9.5(f)). For some subjects, $\mathcal{T}_A$ shows higher values in supine positions (T_e and T_l) than T_h. An increased HR during stressful stages, is related to higher intrinsic sampling rate in HRV, and therefore reduced aliasing. The percentage of subjects without aliasing was 65% (T_e), 82.5% (T_h), and 59% (T_l). Generally, the methods for assessment of quadratic nonlinearities could be easily extended to other higher order statistics (cubic), but they cannot be used to detect other general forms of nonlinear couplings [98,154,266].

9.3 Heat stress

Heat stress, during exposure to elevated environmental temperatures and/or exercise, results in pronounced cardiovascular adjustments that are necessary for adequate temperature regulation [72]. Thermal signals originated from thermo-receptors in the skin are transmitted by neurons in the preoptic area of the hypothalamus where transient receptor potential cation channels transduce skin temperature into primary thermoreceptor afferent neuronal activity that controls the autonomic thermoregulation [239].

An increment in body temperature, increases skin blood flow (cutaneous vasodilation) and part of blood volume is diverted from the internal organs to body peripheral parts, where heat transfer occurs in conjunction with sweating [58]. Cardiac output is increased, which is primarily mediated through increases in HR, while cardiac stroke volume remain unchanged and minimal changes are observed for arterial BP, since there is an increased blood flow towards skin [140].

A variety of studies have analyzed the effects of passive (i.e., non-exercising) heat stress on HRV indices, involving protocols of immersion hydrotherapy, wet sauna, and dry sauna. However, few studies have investigated changes in sympathovagal balance at extremely high-temperature and dry environments in healthy subjects. Bruce et al. [45] reported that during a single sauna session HR and sympatho-vagal ratio increased significantly compared to pre-exposure. Zalewski et al. [356] reported an increment in HR and sympatho-vagal ratio immediately after the exposure that lasted up to 3 hours later.

The aim of this study is to investigate ANS responses to pronounced heat stress stimuli induced by repetitive exposures to dry sauna and the respective recovery profile 30 min after the last sauna bathing. An additional novelty of this study is the inclusion of respiratory information, estimated from an EDR method, in HRV analysis [145], since none of the previous sauna studies have considered the potential influence of respiratory rate on spectral-domain indices of HRV.

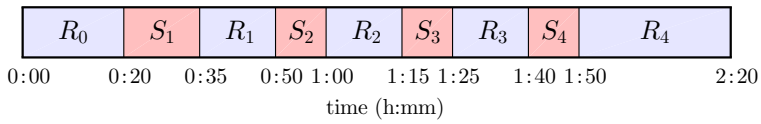

Figure 9.7: Timeline of the heat stress protocol. Rest stages (R_0, R_1, R_2, R_3, R_4) and sauna sessions (S_1, S_2, S_3, S_4) are marked in blue and red, respectively.

9.3.1 Materials and methods

Experimental protocol and data acquisition

Thirteen healthy subjects (all men, mean±standard deviation age 24.61±4.13 years, body mass index 24.43±3.17 kg/m^2) underwent a heat stress protocol which consists of repetitive exposures to sauna characterized by air with a relative humidity of 30% and high temperature 80 – 90 ^{o}C. Before and after sauna exposures, participants were instructed to rest at semi Fowler's position in a neutral temperature environment (25 ^{o}C). The total duration of the protocol was approximately 2 hours and 20 minutes. The timeline of the study protocol is shown in Fig. 9.7.

The experimental procedures were approved by the Lithuanian University of Health Sciences Kaunas Region Biomedical Research Ethics Committee (protocol number BE-2-9). The modified Einthoven leads of ECG (I, II, and III leads) and the chest skin temperature T_c were recorded by using the Nautilus1 (BMII, Lithuania) at a sampling frequency of 1000 Hz and 10 Hz, respectively.

HRV analysis guided by respiration

A HRV signal $m(t)$, sampled at 4 Hz, is generated based on the IPFM model using the time series of beat occurrence, detected on lead II of the ECG. The respiratory rate $f_r(t)$ is estimated from three single-lead EDR signals; the up- and down-slope of the QRS complex defined in eq. (7.7), and the SR defined in eq. (7.8). EDR signals from different leads (lead II and III) are combined to increase the robustness of respiratory rate estimation from EDR spectra. Spectral indices are obtained from the power spectral density of $m(t)$, which is estimated by applying Welch's periodogram (50-s Hamming windows with 50% overlap) in segments of length 5 min every 60 s. For the j:th segment, besides the spectral indices $P_{\mathrm{TOT}}(j)$, $P_{\mathrm{LF}}(j)$, $P^c_{\mathrm{HF}}(j)$, and $P^c_{\mathrm{LFn}}(j)$, the mean HR $d_{\mathrm{HRM}}(j)$ is also calculated. For the estimation of $P^c_{\mathrm{HF}}(j)$ and $P^c_{\mathrm{LFn}}(j)$, Δf is set to 0.15 Hz, and the limits of HF band centered around the mean respiratory rate in the j:th segment $\overline{f}_r(j)$ are given by eq. (6.3) and (6.4).

Statistical analysis

To reduce the parameters variance, the average across segments for 10 min in each stage is used and the features are denoted as $\overline{d}_{\mathrm{HRM}}$, $\overline{F}_r$, $\overline{P}_{\mathrm{TOT}}$, $\overline{P}_{\mathrm{LF}}$, $\overline{P}^c_{\mathrm{HF}}$, and $\overline{P}^c_{\mathrm{LFn}}$. The 10 central

minutes of the stages R_0, R_1, R_2, R_3, and S_1, while the whole stages S_2, S_3, and S_4 are subjected to analysis. Only the last 10 minutes of the recovery phase R_4 are analyzed in an attempt to characterize the late response. Besides HRV parameters, statistical analysis is also conducted for the mean skin temperature $\overline{T}_c$. It should be noted that segments where $\overline{f}_r(j) \leq 0.15$ Hz are excluded for 2 subjects; 50% in S_4 for the first one, while for the second 16%, 50%, and 33% in R_1, R_2, and R_3, respectively.

A paired Wilcoxon signed-rank test is applied after normality rejection (Kolmogorov-Smirnov test) in order to assess intra-subject differences in ANS regulation between R_0 and each stage of the protocol. Considering Bonferroni correction for 8 comparisons, the significance threshold is set to $p < 0.0063$.

9.3.2 Results

Figure 9.8 illustrates the inter-subject mean and standard deviation for all the parameters used in HRV analysis during the whole study. Figure 9.9 shows an example of respiratory rate estimation from EDR signals. Table 9.1 summarizes the results of statistical analysis. Results show that both $\overline{T}_c$ and $\overline{d}_{\text{HRM}}$ increase significantly after basal stage R_0, not only during the sauna sessions (S_1, S_2, S_3, and S_4) but also at the intermediate rest stages (R_1, R_2, and R_3), and recovery phase R_4. No statistically significant differences are obtained for $\overline{f}_r$, although lower median values are observed during stress stages in Fig. 9.10.

A significant reduction in $\overline{P}_{\text{TOT}}$, $\overline{P}_{\text{LF}}$, and $\overline{P}^c_{\text{HF}}$ during most of sauna sessions is observed. An increased $\overline{P}_{\text{LF}}$ is shown only during recovery, although no statistical differences were found. The values of $\overline{P}^c_{\text{LFn}}$ increase significantly after R_0 for all the stages, as it occurs with HR. Note that $\overline{P}^c_{\text{HF}}$ is also significantly lower before last sauna session, i.e., R_3. No significant differences are obtained for $\overline{P}_{\text{TOT}}$ for any intermediate restful stage.

9.3.3 Discussion

In this study, a HRV analysis guided by respiration is conducted to assess changes in ANS regulation during pronounced passive heat stress multi-stage stimuli.

Exposure to repetitive dry sauna sessions alternated with a 15 minute period of rest causes to heat-stressed subjects an increment in $\overline{d}_{\text{HRM}}$, $\overline{T}_c$, and $\overline{P}^c_{\text{LFn}}$, during all stages compared to basal. In this study, the mean respiratory rate most of the times lies in the band [0.15, 0.4] Hz, and thus similar results are obtained for the normalized LF power using the classical HF band [317].

In [45], the exposure to single sauna session led to a minor warming intervention with negligible effects on physiological strain where HR was reported to be increased from 65 to 106 bpm, while in [356] no data were collected during the sauna. In this study, a higher increment of mean HR (up to 133 bpm) in combination with the elevated mean core body temperature (up to 38.7 ^oC) suggests that repetitive exposures to sauna

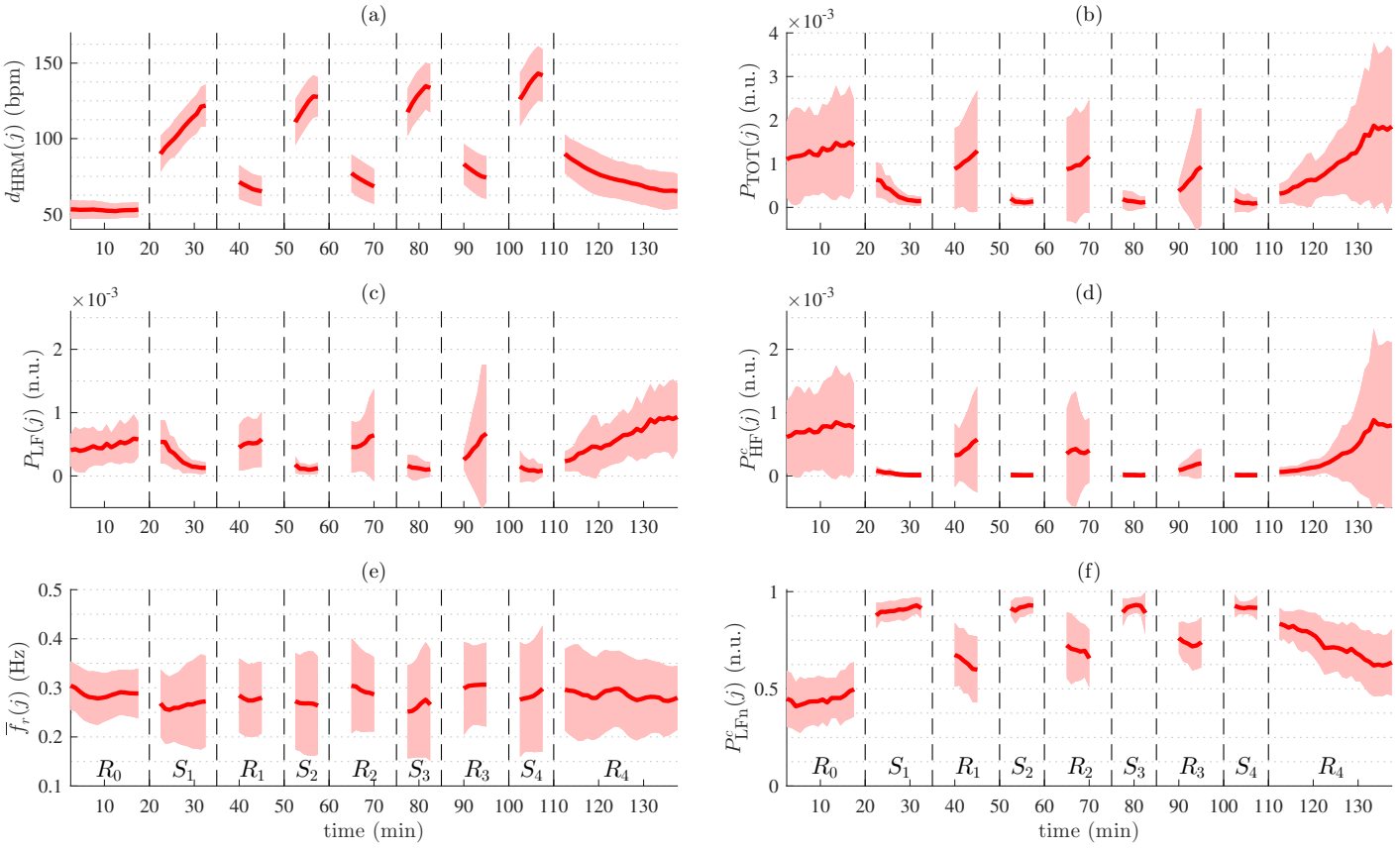

Figure 9.8: Inter-subject mean and standard deviation of all parameters during the heat stress protocol. (a) Mean HR, (b) total HRV power, (c) power at LF band, (d) power at $\Omega^{\mathrm{c}}_{\mathrm{HF}}$ band, (e) mean respiratory rate, (f) normalized LF power.

Table 9.1: Results of statistical analysis in the heat stress study. The values of the intra-subject average parameters are displayed as inter-subject median (interquartile range) and significant differences relative to R_0 are marked with * ($p < 0.0063$).

	R_0	S_1	R_1	S_2	R_2	S_3	R_3	S_4	R_4
$\overline{T}_c$ (^{o} C)	31.0 (2.9)	39.5 (3.7)*	33.7 (3.1)*	38.1 (2.9)*	33.4 (2.8)*	38.7 (2.4)*	34.3 (2.2)*	38.7 (2.0)*	33.3 (2.0)*
$\overline{d}_{\mathrm{HRM}}$ (bpm)	50 (8)	104 (13)*	63 (18)*	118 (17)*	72 (23)*	121 (20)*	73 (22)*	133 (21)*	62 (16)*
$\overline{f}_r$ (Hz)	0.27 (0.07)	0.23 (0.12)	0.27 (0.12)	0.21 (0.14)	0.29 (0.08)	0.23 (0.14)	0.30 (0.01)	0.26 (0.12)	0.26 (0.05)
$\overline{P}_{\mathrm{TOT}} \cdot 10^5$ (n.u.)	80.2 (125.0)	24.8 (28.3)*	64.8 (84.4)	11.2 (15.3)*	58.2 (53.8)	7.6 (13.1)*	44.6 (29.1)	3.7 (8.2)*	134.0 (128.0)
$\overline{P}_{\mathrm{LF}} \cdot 10^5$ (n.u.)	34.8 (39.3)	21.7 (22.0)	42.6 (55.5)	9.1 (12.9)*	31.4 (26.4)	6.7 (10.6)*	28.3 (18.1)	3.2 (7.2)*	95.3 (62.7)
$\overline{P}^c_{\mathrm{HF}} \cdot 10^5$ (n.u.)	45.9 (68.9)	2.1 (3.4)*	19.4 (34.4)	0.9 (1.8)*	15.2 (20.9)	0.7 (1.0)*	11.3 (11.7)*	0.2 (0.7)*	32.0 (44.7)
$\overline{P}^c_{\mathrm{LFn}}$ (n.u.)	0.45 (0.12)	0.91 (0.01)*	0.69 (0.22)*	0.93 (0.06)*	0.74 (0.20)*	0.92 (0.07)*	0.75 (0.08)*	0.92 (0.06)*	0.65 (0.17)*

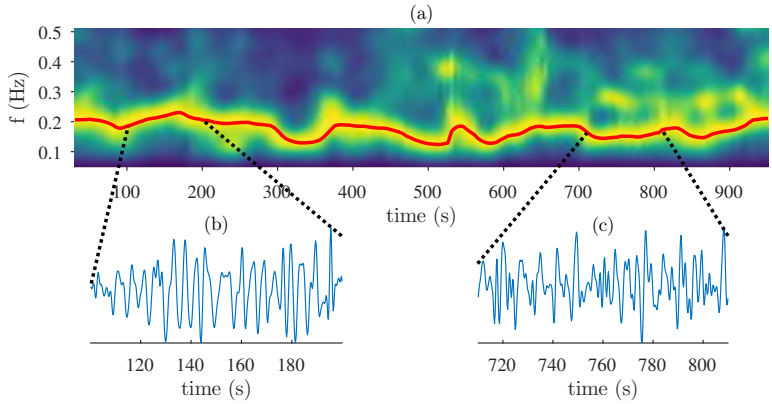

Figure 9.9: Respiratory rate estimation from EDR signals during the heat stress protocol. (a) Time–frequency EDR spectrum, (b)–(c) excerpts of one EDR signal. The estimated respiratory rate is displayed with a red line.

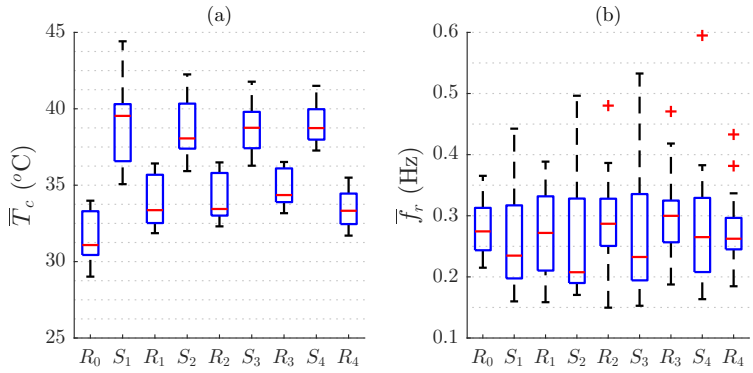

Figure 9.10: Boxplots of parameters across the stages of the heat stress protocol. The mean (a) skin temperature, (b) respiratory rate.

sessions induces internal thermal strain level meeting the criteria of severe whole-body hyperthermia level.

While proceeding to the next sauna exposure, a positive trend from S_1 to S_4 is observed for $\overline{d}_{\text{HRM}}$, while $\overline{P}^c_{\text{HF}}$ follows a negative trend at the intermediate rest stages R_1, R_2, and R_3 (Table 9.1). The short duration of the rest intermediate stages do not allow full recovery, which in turn leads to higher stress of the body in the following sauna session. Lower respiratory rates during sauna (Fig. 9.10) may be a mechanism for avoiding a potential over-activation of the sympathetic branch. During recovery phase, higher values in $\overline{P}_{\text{LF}}$ (relative to R_0) might be related to improved cardiac function after heat exposure since it has been suggested that increased cardiac output and reduced peripheral vascular resistance are the main mechanisms of action for the health effects of frequent sauna bathing [153].

It can be concluded that spectral indices of HRV are able to quantify and monitor shifts of sympathovagal balance toward sympathetic dominance induced by exposure to heat stress multi-stage stimuli with short intermediate rest stages.

9.4 Conclusions

This part of the dissertation explores the idea of assessing stress response in healthy subjects without mental illnesses. ANS biomarkers derived from HRV and respiratory signals are evaluated in the assessment of different types of stress, either psychological or physiological.

The analysis of bispectral characteristics that capture nonlinear interactions between respiration and HRV signals during a mental stress protocol show statistically significant differences between stressful and relaxing stages. In the presence of stressful stimuli, the respiratory rate and the number of bispectral peaks increase, thereby highlighting the importance of respiration and nonlinear cardiorespiratory coupling in stress assessment. A novel strategy, based on RWB and NWB, was used for evaluating cardiorespiratory QPC during hemodynamic stress induced by a postural change. A reduction in the coupling strength between respiration and both RSA and LF components of HRV from supine to tilt position may indicate that changes in quadratic nonlinear cardiorespiratory interactions are useful for quantifying stress. Finally, ANS biomarkers derived from a HRV analysis, taking into consideration the potential influence of the respiratory rate, are also sensitive to sympathovagal balance changes induced by exposures to elevated environmental temperatures.

Therefore, it can be concluded that ANS biomarkers, derived from the joint analysis of HRV and respiratory signals, are able to assess stress and they can be further explored in the context of depression monitoring.

10

Biomarkers for monitoring depression

Depression is a serious mental disorder causing the affected person to suffer from sadness, loss of interest, poor concentration, and feelings of tiredness [244]. Prolonged stress is a crucial factor underlying MDD considering that more than 40% of all depressed patients suffer from cooccurring anxiety [112]. The link between psychological stress and depression can be found in the diathesis-stress model [235]. As the predisposition to depression (diathesis) increases, which can be attributed to either biological or psychological factors, a patient becomes psychologically more vulnerable, and thus the level of stress needed to precipitate an episode of depression decreases [80, 349]. Furthermore, the comorbidity of anxiety and depressive disorders has been associated with poorer trajectories of depressive symptoms [112]. These observations highlight the need of assessing the individual variation in stress susceptibility, resilience, and reactivity in patients with depression [132].

In the short term, the physiological response to acute stress is associated with changes in the ANS. The variation in ANS activity during stressful experiences, which is known as autonomic reactivity, is particularly important for adaptive stress responses, since it reflects the ability of an individual to cope with a challenging situation. Maladaptive responses may have a negative impact on cognitive, emotional, and behavioral processes, thereby leading to development of depression [52, 250]. Current research on stress re-

sponse in MDD patients is focused on HRV, which has been widely used for assessing ANS in a noninvasive way. Recent reviews have pointed out that individuals with greater levels of resting HRV have greater emotion regulation and executive functioning, while hypo-reactivity during stress, evidenced by blunted HRV reactivity, is related to depression [135, 290].

Although autonomic reactivity in MDD patients using HRV indices derived from the ECG has been widely investigated, the use of respiratory and PPG signals in this application remains largely unexplored. Respiratory activity has emerged as an objective measure of mood regulation since the action of the diaphragm can be altered by emotional states such as sadness and anxiety [38]. However, respiratory information has seldom been taken into account by former HRV approaches in depression. One of the very few studies involving MDD patients, showed that entropy measures of cardiorespiratory coupling tend to increase as depression severity increases [360]. In [147], MDD patients showed a reduced high frequency component of the pulse rate variability compared to healthy control subjects during a stressful stimuli. Similar results were reported by [76], where HRV indices derived from a PPG signal were studied before, during, and after executing a mental task. Besides HR information, PPG signals can provide a great amount of information about the cardiovascular system including autonomic function and vascular characteristics. One of the very few studies involving MDD patients investigated the association between autonomic dysregulation and arterial stiffness measured by PPG waveform characteristics but only during resting conditions [182].

In this study, the performance of ANS biomarkers, derived from the joint analysis of HRV and respiratory signals, as well as from a model-based PPG waveform analysis, on the monitoring of depression is evaluated. The novelty of the present study consists in the use of respiratory and PPG signals for assessing autonomic reactivity induced by cognitive tasks in MDD and healthy subjects. The main hypothesis tested in the present study is that the stress response quantified by dynamic changes in ANS biomarkers sensitive to stress is useful for the monitoring of depression.

10.1 Materials and methods

Experimental protocol and data acquisition

A database of 40 MDD patients(white males and females) recruited from consultation as well as from the psychiatric inpatient ward was recorded at the Hospital Clínico Lozano Blesa (Zaragoza, Spain) and the Mental Health Unit of the Parc Sanitari Sant Joan de Deú (Barcelona, Spain). The MDD group consists of subjects with clinically significant depression evaluated with DSM-5 criteria [12]. Depression severity was assessed with the HDRS [136]. Recordings of 40 healthy control (HC) subjects matched by age, sex, race, and body mass index (BMI) were acquired. Only participants without other comorbidities such as cardiovascular, endocrinological or neurological disorders were selected.

Table 10.1 shows the demographic data of the subjects and their medication, including antidepressants (AD) and benzodiazepines (BZ).

Table 10.1: Demographic data (mean±sd) and medication of the participants

	MDD	HC	
Number of subjects	40	40	
Female subjects	24	24	
Unmedicated subjects	3	40	
Subjects with AD and BZ	26	0	
Subjects with only AD	7	0	
Subjects with only BZ	4	0	
Age (years)	45.4 ± 13.35	44.3 ± 12.2	n.s.
BMI (kg/m^2)	27.14 ± 5.16	24.78 ± 4.64	n.s.
HDRS	22.2 ± 6.5	2.1 ± 2.6	*

* $p < 0.01$, n.s. not significant

The experimental protocol had a duration of about 2 hours (starting time between 09:00 a.m. and 11:00 a.m. to avoid circadian rhythm changes) and it consists of three stages. The first stage consists in a basal condition ($\mathcal{B}$), where the subjects were filling psychometric tests including BDI and perceived stress scale (PSS), among others [11], for assessing depression and stress level, respectively. Then, in the second stage, stress was induced to participants by applying two cognitive tasks widely-used in the neuropsychological field for assessing executive function: first the trail making test ($\mathcal{S}_\mathrm{T}$) followed by the stroop color task ($\mathcal{S}_\mathrm{C}$), consisting in a non-verbal and verbal stressor, respectively [223, 287]. The $\mathcal{S}_\mathrm{T}$ consists of two parts. In Part A, the subjects are required to connect, by drawing a line, consecutive numbers, while in Part B, they are required to connect numbers and letters in an alternating progressive sequence. In $\mathcal{S}_\mathrm{C}$, subjects are required to read, as fast as possible in 45 secs, from three different lists, the names of: (a) color-words printed in black ink, (b) different color patches, (c) ink color of color-words printed in an inconsistent color ink (incongruent condition). The total time needed to accomplish both parts of $\mathcal{S}_\mathrm{T}$, denoted $\mathcal{T}_\mathrm{AB}$, and the total number of correct words in the 3 parts of $\mathcal{S}_\mathrm{C}$, denoted W_C, are used for evaluating the performance of the participants in the cognitive tasks [223]. In the third stage, subjects were requested to relax and to remain silent. During this recovery stage ($\mathcal{R}$), of about 5 minutes, individuals were supposed to achieve a resting state.

The duration (mean±SD) of each protocol stage was 11.5 ± 5.0 min ($\mathcal{B}$), 3.5 ± 1.4 min ($\mathcal{S}_\mathrm{T}$), 4.3 ± 1.2 min ($\mathcal{S}_\mathrm{C}$), 5.2 ± 0.5 min ($\mathcal{R}$). This study was carried out in accordance with the recommendations of "Comité Ético de Investigación Clínica de Aragón (CEICA)" and the Ethical Committee of "Fundació Sant Joan de Déu" under clinical studies PI16-0156 and PIC-148-16, respectively, including written informed consent from all subjects in accordance with the Declaration of Helsinki.

During the whole experimental protocol, a non-dominant hand fingertip PPG signal was continuously recorded at a sampling frequency of 250 Hz for each participant using the Medicom system (ABP10 module of Medicom MTD, Ltd, Russia). Three orthogonal

ECG leads were also simultaneously recorded at 1000 Hz, and a respiratory signal with belt at 250 Hz.

ANS biomarkers

To assess depression level, various ANS biomarkers are derived from different analyses (see Ch. 6, 7, and 8), including the classical HRV analysis, the analysis of respiration and EDR signals, the joint analysis of HRV and respiratory signals, and a model-based PPG waveform analysis. A HRV signal, sampled at 4 Hz, is generated based on the IPFM model using the time series of beat occurrence, detected on Y-lead of the ECG. Classical HRV indices, described in Ch. 6.1, in the time domain, i.e., SDNN and RMSSD, and in the frequency domain, including P_{LF}, P_{HF}, P_{TOT}, and P_{LFn}, estimated as described in Ch. 9, are analyzed. Besides the modulating signal of the IPFM model, the time-varying mean HR signal $d_{\mathrm{HRM}}(t)$ is subjected to analysis (see Ch. 6).

To derive indices related to the joint analysis of HRV and respiratory signals, and respiratory parameters, the respiratory signal is downsampled to 4 Hz. The respiratory rate $f_r(k)$ is obtained from the respiratory spectrum and it is also estimated from the novel EDR method, called slope range, described in Ch. 7. The ECG-derived respiratory rate, denoted $f_r^{\mathrm{SR}}(k)$, is obtained by combining the EDR signals from the 3 orthogonal leads to increase the robustness of respiratory rate estimation from EDR spectra. Since stress induction has been associated with a less regular breathing, the bandwidth of the respiratory spectrum, denoted $B_r(k)$, is calculated to differentiate respiratory signals with narrow- and broadband spectra. The parameter $B_r(k)$ is defined as the bandwidth, around the absolute maximum, that contains 50% of the total power of the respiratory spectrum. Fig. 10.1 illustrates an example of $B_r(k)$ estimation during $\mathcal{S}_{\mathrm{T}}$. The definition of the sympathovagal balance P^c_{LFn}, in which the HF band is centered around the mean respiratory rate $\overline{f}_r$ (with $\Delta f = 0.15$ Hz), and the sympathovagal balance indices $P^r_{\mathrm{LFn}}(t)$ and P^u_{LFn}, which take into account respiratory influences by means of TFC and OSP, respectively, as described in Ch. 6.2, are considered ANS biomarkers. Parameters related to strength ($E_{\mathrm{L,R}}(t)$, $E_{\mathrm{L,R}}(t)$) and degree ($C^{\Phi}_{\mathrm{L,R}}(t)$, $C^{\Phi}_{\mathrm{R,R}}(t)$) of cardiorespiratory QPC, described in Ch. 6.3, are also contained in the list of ANS biomarkers, but they are evaluated only for those stages in which the subject is not speaking.

Finally, the instantaneous HR derived from the PPG signal, denoted HR(i), and several morphological features associated with systolic arterial pressure and vascular compliance measures, such as $A_{12}(i)$, $A_{13}(i)$, $W_1(i)$, $T_1(i)$, $T_{12}(i)$, and $T_{13}(i)$, are obtained for the i:th PDA-based modeled PPG pulse, as described in Ch. 8.

Statistical analysis and classification performance evaluation

For each subject, the temporal mean is used for characteristics defined on a beat-to-beat or pulse-to-pulse basis, or with time dependence, to assign a unique value at each condition C, $C \in \{\mathcal{B}, \mathcal{S}_{\mathrm{T}}, \mathcal{S}_{\mathrm{C}}, \mathcal{R}\}$. Only the first 5 minutes of $\mathcal{B}$ are taken into account since the time

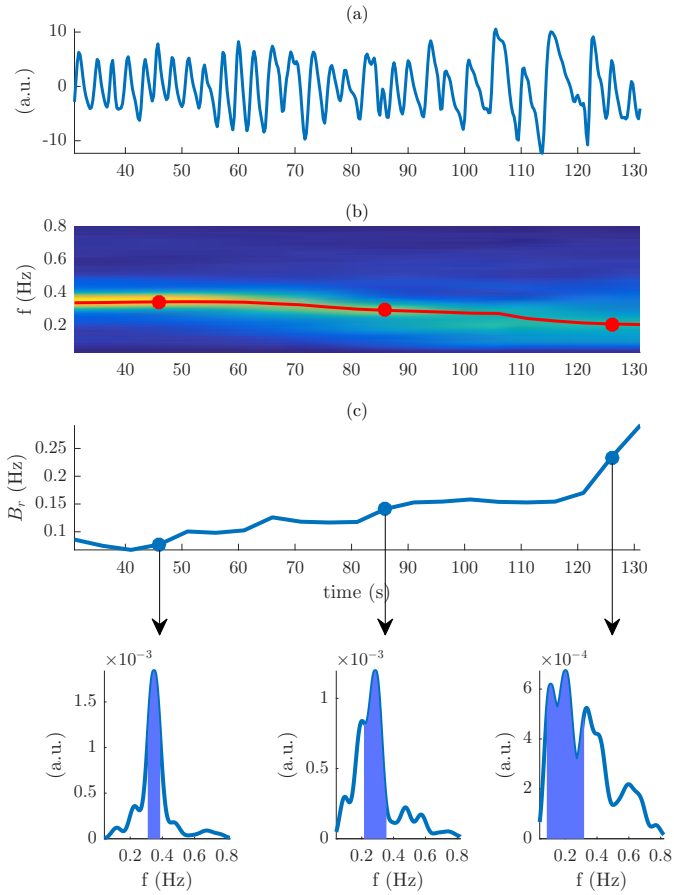

Figure 10.1: Estimation of respiratory spectrum bandwidth. (a) A respiratory signal during $\mathcal{S}_T$, (b) respiratory rate estimation (red line) from time–frequency spectra $S_k(f)$, (c) the bandwidth $B_r(k)$ around the absolute maximum. The spectra that correspond to the red and blue dots are displayed below.

required for filling the psychometric tests can differ among subjects or groups. The list of ANS biomarkers is composed of various features $\mathcal{F}$ summarized in Table 10.2.

Individual differences across conditions are assessed separately for HC and MDD group. A multicomparison test with Bonferroni correction is carried out for evaluating the individual differences across protocol stages using the paired t-test, and the Wilcoxon signed rank test when appropriate. Differences between groups are assessed with the t-test for independent samples, and the Mann-Whitney U non-parametric test when appropriate. Differences in ANS biomarkers between MDD patients and HC subjects are also assessed using the Cohen's d parameter and the area under the curve (AUC) of the receiver operating characteristic curve, which measure the size of an effect (depression) and the degree of separability between groups, respectively. Besides raw value, the intra-subject difference of a feature $\mathcal{F}$ between two conditions C_1 and C_2, denoted as $\Delta(\mathcal{F})_{C_1}^{C_2}$, is considered as an ANS biomarker. The reactivity indices are calculated by subtracting

Table 10.2: ANS biomarkers derived from multi-modal and model-based signal processing

	$\mathcal{F}$	Description
Chapter 6.1	$\overline{d}_{\text{HRM}}$	IPFM model-based HRM obtained from RR intervals
	SDNN	Standard deviation of the NN intervals
	RMSSD	RMSSD of the NN intervals
	P_{LF}	Spectral power in the classical LF band
	P_{HF}	Spectral power in the classical HF band
	P_{TOT}	Total spectral power
	P_{LFn}	Sympathovagal index based on normalized LF power
Chapter 6.2	P^{c}_{LFn}	Sympathovagal index where the HF band is centered around the respiratory rate
	$\overline{P}^{r}_{\text{LFn}}$	Sympathovagal index where respiratory-related power is calculated by means of TFC
	P^{u}_{LFn}	Sympathovagal index where respiratory-related components are separated from HRV by means of OSP
Chapter 6.3	$\overline{C}^{\Phi}_{\text{R,R}}$	QPC degree, assessed with RWB, between respiration and RSA component of HRV
	$\overline{C}^{\Phi}_{\text{L,R}}$	QPC degree, assessed with RWB, between respiration and LF component of HRV
	$\overline{E}_{\text{R,R}}$	QPC strength, assessed with NWB, between respiration and RSA component of HRV
	$\overline{E}_{\text{L,R}}$	QPC strength, assessed with NWB, between respiration and LF component of HRV
Chapter 7	$\overline{f}_r$	Mean respiratory rate estimated from the respiratory belt signal
	$\overline{f}^{\text{SR}}_r$	Mean respiratory rate estimated from the ECG using the SR method
	$\overline{B}_r$	Bandwidth of the respiratory spectrum estimated from the respiratory belt signal
Chapter 8	$\overline{\overline{\text{HR}}}$	HRM obtained from pulse-to-pulse intervals
	$\overline{A}_{12}$	Percentage of amplitude loss in the first reflection
	$\overline{A}_{13}$	Percentage of amplitude loss in the second reflection
	$\overline{W}_1$	Width of the main wave
	$\overline{T}_1$	Time occurrence of the main wave
	$\overline{T}_{12}$	Time delay between the main and the first reflected wave
	$\overline{T}_{13}$	Time delay between the main and the second reflected wave

the value of the feature $\mathcal{F}$ in C_1 from C_2. The changes from basal to stress, from stress to recovery or from basal to recovery stage are studied for assessing autonomic reactivity.

Correlation (Pearson) analyses are carried out for testing bivariate associations between the most significant ANS biomarkers and depression severity assessed with HDRS. Correlation coefficient r is also used for investigating the associations between depression severity and the scores of psychometric and cognitive tests. Differences in demographic data between groups are assessed with the t-test for independent samples, and the Mann-Whitney U non-parametric test when appropriate. The significance threshold in this study is set to $p < 0.01$. Furthermore, ANS biomarkers are fed into a classification pipeline that reaches a decision on the subject's status (MDD/HC). A leave-one-subject-out (LOSO) scheme is employed to evaluate the discrimination potential of the proposed approach. To avoid the *curse of dimensionality*, different feature selection methods, in-

cluding stepwise linear regression (SLR) [10], least absolute shrinkage and selection operator (LASSO) [325], and feature ranking (FR) [210], are carried out with an upper limit of six selected features. SLR is employed to add or remove predictors for creating a linear model that contains only an intercept. At each step, a term is added to the model only if p-value is lower than 0.05. Regularized least-squares regression using LASSO penalty is carried out with 5-fold cross-validation to remove predictors from the model. The cross validated mean square error of the resulting model is used to select the regularization parameter that forces some of the model coefficients to zero. FR is employed to rank the features based on class separability criteria. The evaluation criteria used in this dissertation are the absolute value of the standardized u-statistic of a two-sample unpaired Wilcoxon test and a cross-correlation weighting to exclude largely correlated ($r = 0.7$) features. Afterwards, each selected feature is normalized using the exponential function of the z-score. Note that the left-out subject is excluded from the calculation of the sample mean and standard deviation used in z-score transformation. Eventually, the LOSO scheme is completed when all subjects are left out and afterwards evaluated against MDD. A linear Support-Vector Machine (SVM) [74], a logistic regression (LR) [66], and a linear discriminant analysis (LDA) classifier [221] are examined in terms of classification performance, i.e., accuracy (ACC) and F1-score (F1).

10.2 Results

Fig. 10.2 and Fig. 10.3 show the boxplots of ANS biomarkers derived from the joint analysis of HRV and respiratory signals. Statistical differences between HC and MDD group as well as individual differences along the protocol stages are summarized in Table 10.3. As can be seen from Fig. 10.2(a), patients with depression show higher values of HR compared to healthy controls during non-stressful stages, i.e. $\mathcal{B}$ and $\mathcal{R}$ (see Table 10.3). The absence of statistical differences between groups during stressful stages, i.e. $\mathcal{S}_\mathrm{T}$ and $\mathcal{S}_\mathrm{C}$, is associated with an increased HR in HC group in the presence of stressful stimuli. In MDD group, HR is found to be higher in stressful stages only compared to $\mathcal{R}$. Participants of both groups exhibit a lower HR in post-task relaxation period $\mathcal{R}$ compared to $\mathcal{B}$.

Differences between groups are also observed for the respiratory rate during the recovery stage, in which HC subjects show lower values of $\overline{f}_r$ compared to MDD patients. During $\mathcal{S}_\mathrm{C}$, where the subjects were speaking, a significantly lower respiratory rate compared to $\mathcal{B}$ was found for both groups (see Fig. 10.2(b)). Similar results to $\overline{f}_r$ across all protocol stages are obtained when estimating the respiratory rate from EDR signals (see Fig. 10.2(c)) using the slope range method (see Table 10.3). Besides respiratory rate, results show significant individual differences in the bandwidth of the respiratory spectrum between stressful and relaxing stages (see Fig. 10.2(d)). An increased $\overline{B}_r$ is associated with less regular breathing, characterized by increased breath-to-breath variability in tidal volume or respiratory rate, owing to the presence of stressful stimuli.

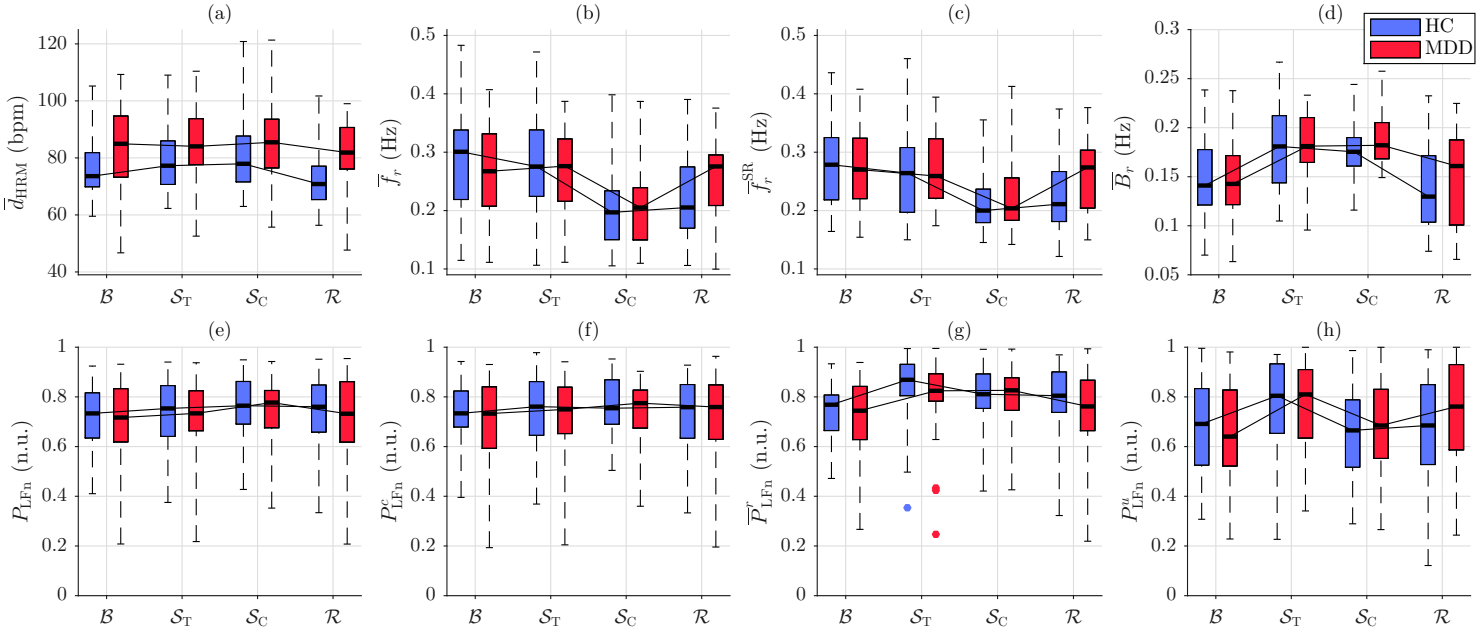

Figure 10.2: Functional boxplots of ANS biomarkers derived from the joint analysis of HRV and respiratory signals. (a) Heart rate ($\overline{d}_{HRM}$), (b) Reference respiratory rate ($\overline{f}_r$), (c) ECG-derived respiratory rate using the slope range method ($\overline{f}_r^{SR}$), (d) bandwidth of the respiratory spectrum ($\overline{B}_r$), (e) normalized LF power using the classical HF band (P_{LFn}), (f) normalized LF power using a HF band centered around the mean respiratory rate (P_{LFn}^c), (g) normalized LF power obtained by means of TFC ($\overline{P}_{LFn}^r$), and (h) normalized LF power obtained by means of OSP (P_{LFn}^u). The group of HC and MDD subjects are marked in blue and red, respectively.

Table 10.3: Values (Median±IQR) of ANS biomarkers derived from the joint analysis of HRV and respiratory signals

	$\mathcal{B}$		$\mathcal{S}_{\mathrm{T}}$		$\mathcal{S}_{\mathrm{C}}$		$\mathcal{R}$	
	HC	MDD	HC	MDD	HC	MDD	HC	MDD
$\overline{d}_{\mathrm{HRM}}$ (bpm)	**73.6 ± 11.9**$_{\dagger}$	**85.0 ± 21.4**$_{\dagger}$	77.3 ± 15.2$^{*}_{\dagger}$	84.0 ± 16.1$_{\dagger}$	77.9 ± 16.0$^{*}_{\dagger}$	85.5 ± 17.0$_{\dagger}$	**70.8 ± 11.6***	**81.9 ± 14.5***
$\overline{f}_r$ (Hz)	0.300 ± 0.120$_{\dagger}$	0.270 ± 0.120	0.280 ± 0.110$_{\dagger}$	0.280 ± 0.110	0.200 ± 0.083*	0.210 ± 0.089$^{*}_{\dagger}$	**0.210 ± 0.100***	**0.280 ± 0.086**
$\overline{f}_r^{\mathrm{SR}}$ (Hz)	0.280 ± 0.110$_{\dagger}$	0.270 ± 0.100	0.260 ± 0.110$_{\dagger}$	0.260 ± 0.100	0.200 ± 0.057*	0.200 ± 0.073$^{*}_{\dagger}$	**0.210 ± 0.086***	**0.270 ± 0.099**
$\overline{B}_r$ (Hz)	0.140 ± 0.056	0.140 ± 0.050	0.180 ± 0.068$^{*}_{\dagger}$	0.180 ± 0.046$^{*}_{\dagger}$	0.180 ± 0.029$^{*}_{\dagger}$	0.180 ± 0.037$^{*}_{\dagger}$	0.130 ± 0.068	0.160 ± 0.087
SDNN (ms)	**34.4 ± 21.3**$_{\dagger}$	**22.8 ± 22.3**$_{\dagger}$	**38.2 ± 22.4**$^{*}_{\dagger}$	**25.9 ± 25.2**$^{*}_{\dagger}$	**43.5 ± 22.8***	**30.6 ± 24.8***	**45.2 ± 26.1***	**30.5 ± 25.9***
RMSSD (ms)	**22.6 ± 15.1**$_{\dagger}$	**12.9 ± 15.2**$_{\dagger}$	**21.5 ± 15.5**$_{\dagger}$	**14.6 ± 12.0**	22.1 ± 13.8$^{*}_{\dagger}$	14.6 ± 15.4*	**26.3 ± 16.0***	**15.3 ± 13.8***
P_{LF} (a.u.)	0.20 ± 0.20$_{\dagger}$	0.11 ± 0.21$_{\dagger}$	0.19 ± 0.24$_{\dagger}$	0.13 ± 0.20	**0.35 ± 0.49***	**0.15 ± 0.29***	0.32 ± 0.50*	0.18 ± 0.35*
P_{HF} (a.u.)	0.08 ± 0.11$_{\dagger}$	0.04 ± 0.09$_{\dagger}$	0.06 ± 0.07$_{\dagger}$	0.04 ± 0.07	0.10 ± 0.15*	0.05 ± 0.10*	**0.10 ± 0.16***	**0.04 ± 0.10***
P_{TOT} (a.u.)	0.26 ± 0.27$_{\dagger}$	0.16 ± 0.28$_{\dagger}$	0.28 ± 0.30$_{\dagger}$	0.19 ± 0.28	**0.47 ± 0.58***	**0.21 ± 0.44***	0.54 ± 0.61*	0.24 ± 0.48*
P_{LFn} (n.u.)	0.73 ± 0.18	0.72 ± 0.21	0.75 ± 0.20	0.73 ± 0.16	0.76 ± 0.17	0.78 ± 0.15	0.76 ± 0.19	0.73 ± 0.24
P^{c}_{LFn} (n.u.)	0.73 ± 0.14	0.73 ± 0.25	0.76 ± 0.22	0.75 ± 0.19	0.75 ± 0.18	0.77 ± 0.15	0.76 ± 0.22	0.76 ± 0.22
$\overline{P}^{r}_{\mathrm{LFn}}$ (n.u.)	0.77 ± 0.14	0.74 ± 0.21	0.87 ± 0.13*	0.82 ± 0.11$^{*}_{\dagger}$	0.81 ± 0.14*	0.83 ± 0.13*	0.80 ± 0.16	0.76 ± 0.20
P^{u}_{LFn} (n.u.)	0.69 ± 0.31	0.64 ± 0.31$_{\dagger}$	0.80 ± 0.28*	0.81 ± 0.28*	0.67 ± 0.27	0.68 ± 0.28	0.69 ± 0.32	0.76 ± 0.34*
$\overline{E}_{\mathrm{R,R}}$ (a.u.)	0.16 ± 0.08	0.15 ± 0.09	**0.13 ± 0.08**	**0.17 ± 0.09**			0.13 ± 0.10	0.15 ± 0.08
$\overline{E}_{\mathrm{L,R}}$ (a.u.)	0.16 ± 0.07	0.18 ± 0.07	0.15 ± 0.10	0.18 ± 0.09			0.16 ± 0.09	0.17 ± 0.07
$\overline{C}^{\Phi}_{\mathrm{R,R}}$ (n.u.)	0.66 ± 0.10$_{\dagger}$	0.69 ± 0.09	**0.64 ± 0.10**$_{\dagger}$	**0.68 ± 0.10**			0.71 ± 0.06*	0.68 ± 0.09
$\overline{C}^{\Phi}_{\mathrm{L,R}}$ (n.u.)	0.69 ± 0.07	0.69 ± 0.06	0.72 ± 0.09*	0.70 ± 0.06			0.70 ± 0.07	0.70 ± 0.05

Note: In bold are marked the parameters with statistical differences ($p < 0.01$) between HC and MDD group. Statistically significant ($p < 0.01$) individual differences compared to $\mathcal{B}$ and $\mathcal{R}$ are denoted with * and †, respectively.

Table 10.4: Time percentages (Median±IQR) of linear and nonlinear cardiorespiratory coupling

	$\mathcal{T}_r$ (%)		$\mathcal{T}_{R,R}$ (%)		$\mathcal{T}_{L,R}$ (%)	
	HC	MDD	HC	MDD	HC	MDD
$\mathcal{B}$	$51.3 \pm 34.1_{\dagger}$	40.1 ± 38.8	30.0 ± 44.2	33.3 ± 34.2	40.0 ± 20.0	36.7 ± 30.8
$\mathcal{S}_T$	$30.9 \pm 37.6^{*}$	$29.6 \pm 22.5^{*}$	30.8 ± 34.0	41.2 ± 46.1	38.5 ± 43.2	46.7 ± 26.9
$\mathcal{S}_C$	$16.8 \pm 24.5^{*}_{\dagger}$	$22.6 \pm 22.1^{*}_{\dagger}$				
$\mathcal{R}$	$23.5 \pm 36.5^{*}$	39.4 ± 41.5	40.7 ± 51.3	44.4 ± 46.9	41.4 ± 32.2	50.0 ± 20.5

Note: In bold are marked the parameters with statistical differences ($p < 0.01$) between HC and MDD group. Statistically significant ($p < 0.01$) individual differences compared to $\mathcal{B}$ and $\mathcal{R}$ are denoted with * and †, respectively.

Regarding HRV indices, both SDNN and RMSSD are lower in MDD patients than in HC subjects during non-stressful stages, fact that is related to the higher HR in MDD group. Moreover, the values of temporal HRV indices are higher in $\mathcal{R}$ than in $\mathcal{B}$ for all participants, following the inverse relationship between HRV power and HR. In $\mathcal{R}$, a statistically significantly larger P_{HF} in HC group compared to MDD is associated, besides the lower HR, with the lower respiratory rate in the post-task relaxation period. However, during stressful stimuli, the interpretation of classical HRV indices might not be straightforward due to erratic respiratory patterns. For instance, while HR tends to increase, subjects exhibit higher values of SDNN in $\mathcal{S}_T$ and $\mathcal{S}_C$, compared to $\mathcal{R}$. An increase in the total power of HRV and in the LF band is associated with the mechanical effect of respiration. This effect on HRV is more pronounced in tasks that require speech production [27, 269, 311], thereby explaining the statistically significantly higher P_{LF} and P_{TOT} in $\mathcal{S}_C$ compared to $\mathcal{B}$.

Taking into account that a less regular breathing can blur the estimation of SNS and PNS activity using the classical HRV indices, no statistical differences were found for the sympathovagal balance index P_{LFn} (see Fig. 10.2(e)). Erratic respiratory pattern results in a broadband spectrum with significant power in the LF band, even if the average respiratory rate is higher than 0.15 Hz [28]. Thus, P^{c}_{LFn}, in which HF band is centered around the mean respiratory rate, shows no differences between stressful and relaxing stages (see Fig. 10.2(f)). On the contrary, higher values of $\overline{P}^{r}_{\text{LFn}}$ in both $\mathcal{S}_T$ and $\mathcal{S}_C$ compared to $\mathcal{B}$ are observed for all participants (see Fig. 10.2(g)). This definition of sympathovagal balance index based on a TFC approach allows time instants in which components at frequencies with different physiological meaning, e.g. LF and HF, are overlapping to be discarded. The time percentage of analyzed data $\mathcal{T}_r$ is given in the Table 10.4. The lowest values of $\mathcal{T}_r$ in both groups are observed for the stressful task $\mathcal{S}_C$, which is associated with speech production. For an unbiased estimation of sympathovagal balance, besides TFC, respiratory influences can be separated from the HRV signal by means of OSP. Results show a statistically significantly higher P^{u}_{LFn} during the non-verbal stressor $\mathcal{S}_T$ compared to $\mathcal{B}$ (see Fig. 10.2(h)). However, P^{u}_{LFn} shows no difference in $\mathcal{S}_C$ compared to $\mathcal{B}$. This suggests that the performance of OSP on separating respiratory influences from the HRV might be hindered during the stressful tasks involving speech.

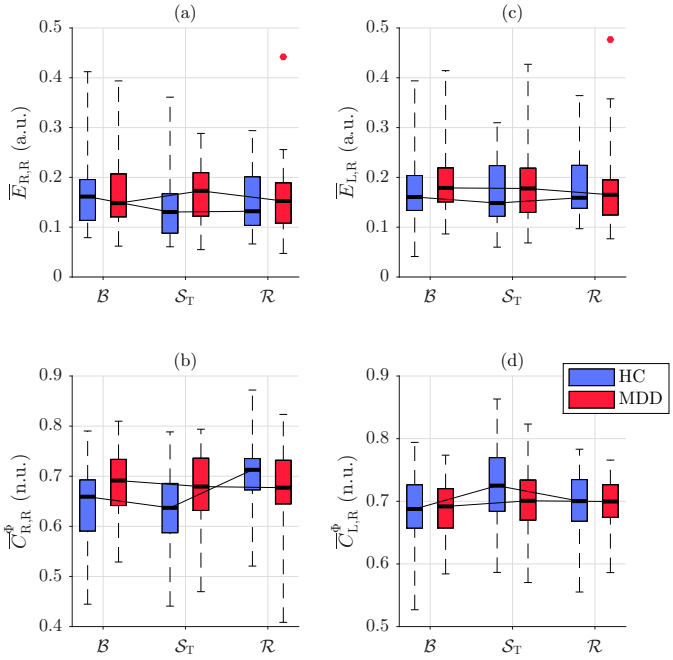

Figure 10.3: Functional boxplots of cardiorespiratory QPC indices. QPC strength and QPC degree between respiration and RSA component of HRV in (a) $\overline{E}_{R,R}$ and (b) $\overline{C}^{\Phi}_{R,R}$, respectively, and between respiration and LF component of HRV in (c) $\overline{E}_{L,R}$ and (d) $\overline{C}^{\Phi}_{L,R}$, respectively. The group of HC and MDD subjects are marked in blue and red, respectively.

Results in Fig. 10.3(a)-(b) show that the QPC strength $\overline{E}_{R,R}$ and the QPC degree $\overline{C}^{\Phi}_{R,R}$ are statistically significantly higher in MDD compared to HC subjects during the stressful stimuli $\mathcal{S}_T$. In the HC group, stress induced by the cognitive task execution increased the degree of QPC in $\Omega_{L,R}$ compared to basal stage $\mathcal{B}$ (see Fig. 10.3(d)). Furthermore, in HC group, the QPC degree $\overline{C}^{\Phi}_{R,R}$ increased after task execution. No significant differences were found for the time percentage of QPC in $\Omega_{L,R}$ ($\mathcal{T}_{L,R}$) and in $\Omega_{R,R}$ ($\mathcal{T}_{R,R}$), neither when evaluating individual differences nor group differences (see Table 10.4).

Results regarding the differences between MDD and HC subjects using the raw values of ANS biomarkers and autonomic reactivity indices derived from the joint analysis of HRV and respiratory signals are summarized in Table 10.5. Due to the limitations related to respiration described above, various ANS biomarkers are not evaluated in some stressful tasks. Results show that autonomic reactivity indices for $\overline{C}^{\Phi}_{R,R}$ are associated with larger effect sizes compared to other ANS biomarkers. A higher degree of separability between groups is observed when changes from the stressful stage $\mathcal{S}_T$ to recovery phase $\mathcal{R}$ are considered, yielding AUC value of 0.76. High AUC values related to $\mathcal{R}$, either using the raw values of ANS biomarkers or autonomic reactivity indices, are also obtained for HR and respiratory rate. Moreover, the results suggest that $\overline{f}_r^{SR}$ can be used instead of $\overline{f}_r$ since similar AUC values, of about 0.7, are obtained when changes from the basal $\mathcal{B}$ to recovery stage $\mathcal{R}$ are considered.

Table 10.5: AUC / Cohen's d values of ANS biomarkers derived from the joint analysis of HRV and respiratory signals

$\mathcal{F}$	$\mathcal{B}$	$\mathcal{S}_{\mathrm{T}}$	$\mathcal{S}_{\mathrm{C}}$	$\mathcal{R}$	$\Delta(\mathcal{F})_{\mathcal{B}}^{\mathcal{S}_{\mathrm{T}}}$	$\Delta(\mathcal{F})_{\mathcal{B}}^{\mathcal{S}_{\mathrm{C}}}$	$\Delta(\mathcal{F})_{\mathcal{R}}^{\mathcal{B}}$	$\Delta(\mathcal{F})_{\mathcal{R}}^{\mathcal{S}_{\mathrm{T}}}$	$\Delta(\mathcal{F})_{\mathcal{R}}^{\mathcal{S}_{\mathrm{C}}}$
$\overline{d}_{\mathrm{HRM}}$	0.69 / 0.60	0.62 / 0.35	0.58 / 0.21	**0.72** / **0.71**	0.67 / 0.56	0.68 / 0.60	0.56 / 0.24	**0.70** / **0.70**	**0.71** / **0.71**
$\overline{f}_r$	0.54 / 0.16	0.52 / 0.12	0.53 / 0.06	0.63 / 0.40	0.53 / 0.03	0.55 / 0.18	**0.70** / **0.61**	0.66 / 0.43	0.60 / 0.30
$\overline{f}_r^{\mathrm{SR}}$	0.52 / 0.09	0.54 / 0.08	0.53 / 0.19	0.69 / 0.65	0.52 / 0.16	0.56 / 0.21	**0.70** / **0.69**	0.65 / 0.47	0.64 / 0.41
$\overline{B}_r$	0.51 / 0.03	0.52 / 0.05	0.63 / 0.44	0.58 / 0.24	0.54 / 0.08	0.61 / 0.32	0.58 / 0.28	0.53 / 0.18	0.51 / 0.04
SDNN	0.66 / 0.56			0.66 / 0.55			0.55 / 0.26		
RMSSD	0.66 / 0.42			0.69 / 0.54			0.63 / 0.47		
P_{LF}	0.64 / 0.46			0.64 / 0.38			0.59 / 0.26		
P_{HF}	0.62 / 0.38			0.64 / 0.46			0.63 / 0.44		
P_{TOT}	0.64 / 0.46			0.64 / 0.38			0.59 / 0.26		
P_{LFn}	0.51 / 0.13			0.52 / 0.06			0.52 / 0.08		
P_{LFn}^{c}	0.52 / 0.25			0.52 / 0.04			0.59 / 0.36		
$\overline{P}_{\mathrm{LFn}}^{r}$	0.53 / 0.24	0.60 / 0.25	0.50 / 0.08	0.58 / 0.22	0.54 / 0.07	0.56 / 0.18	0.53 / 0.07	0.52 / 0.07	0.54 / 0.14
P_{LFn}^{u}	0.52 / 0.11	0.52 / 0.03		0.56 / 0.21	0.51 / 0.08		0.62 / 0.33	0.57 / 0.23	
$\overline{E}_{\mathrm{R,R}}$	0.51 / 0.01	0.65 / 0.34		0.52 / 0.08	0.62 / 0.37		0.54 / 0.23	0.54 / 0.11	
$\overline{E}_{\mathrm{L,R}}$	0.59 / 0.35	0.57 / 0.26		0.53 / 0.13	0.52 / 0.09		0.62 / 0.47	0.61 / 0.34	
$\overline{C}_{\mathrm{R,R}}^{\Phi}$	0.65 / 0.56	**0.71** / **0.72**		0.61 / 0.41	0.53 / 0.00		**0.71** / **0.75**	**0.76** / **0.85**	
$\overline{C}_{\mathrm{L,R}}^{\Phi}$	0.51 / 0.06	0.62 / 0.44		0.51 / 0.05	0.58 / 0.31		0.51 / 0.12	0.62 / 0.46	

Note: In bold are marked the parameters with AUC $\geq$ 0.7

Besides ANS biomarkers derived from the joint analysis of HRV and respiratory signals, various morphological parameters were obtained from PPG signals. The percentage (mean±SD) of discarded pulses for each stage was 2.3% ± 4.8% ($\mathcal{B}$), 4.4% ± 6.6% ($\mathcal{S}_\mathrm{T}$), 4.0% ± 6.7% ($\mathcal{S}_\mathrm{C}$), and 3.6% ± 5.7% ($\mathcal{R}$) suggesting that few distorted pulses are present in the PPG recordings. The number of analyzed pulses (mean±SD) was 370 ± 102 ($\mathcal{B}$), 262 ± 137 ($\mathcal{S}_\mathrm{T}$), 317 ± 105 ($\mathcal{S}_\mathrm{C}$), and 369 ± 102 ($\mathcal{R}$).

As can be seen from the boxplots in Fig. 10.4, patients with depression show higher values of $\overline{\mathrm{HR}}$ and vascular compliance-related parameters $\overline{A}_{12}$ and $\overline{A}_{13}$ compared to healthy controls. In contrast to that, healthy controls show higher values for the pulse transit time surrogates $\overline{T}_{12}$ and $\overline{T}_{13}$ and the temporal parameters related to the main wave, i.e, $\overline{W}_1$ and $\overline{T}_1$. Statistical differences between HC and MDD group as well as individual differences along the protocol stages are summarized in Table 10.6. Results show that HC subjects exhibit statistical differences in all characteristics during the verbal stressor compared either to basal or recovery stage. On the other hand, statistically significant individual differences were found in MDD patients mainly for HR and $\overline{A}_{13}$ indices, which were associated with changes from stress to recovery. An example of average pulse waveforms for a HC and a MDD subject (matched by sex, age and BMI) is shown in Fig. 10.5. For each stage, prior to averaging operation, the pulses are aligned to the position of the pulse start (basal point). This figure highlights the fact that across different stages within the same subject minimal changes of waveform characteristics, including $\overline{\mathrm{HR}}$, $\overline{T}_{13}$, and $\overline{A}_{13}$, are observed for the MDD compared to the HC subject.

Results regarding the differences between MDD and HC subjects using the raw values of ANS biomarkers and autonomic reactivity indices derived from the model-based PPG waveform analysis are summarized in Table 10.7. Results show that the amplitude loss in the second reflection $\overline{A}_{13}$ is associated with larger effect sizes compared to HR or other pulse waveform characteristics. A higher degree of separability between groups is observed when changes from stressful stages ($\mathcal{S}_\mathrm{T}$, $\mathcal{S}_\mathrm{C}$) to recovery phase ($\mathcal{R}$) are considered, yielding AUC values of 0.77, and 0.74 for $\Delta\left(\overline{A}_{13}\right)_{\mathcal{R}}^{\mathcal{S}_\mathrm{T}}$, and $\Delta\left(\overline{A}_{13}\right)_{\mathcal{R}}^{\mathcal{S}_\mathrm{C}}$, respectively. Note that similar results to $\overline{\mathrm{HR}}$ are also obtained with $\overline{d}_{\mathrm{HRM}}$ (see Table 10.5), thereby suggesting that, instead of ECG, PPG signal can be used to extract HR information.

The associations between the most significant ANS biomarkers and depression severity assessed with HDRS are summarized in Table 10.8. Note that depression severity scores are transformed using the squared root (log transformation is avoided due to zeros in HDRS) to increase the linear relationship with ANS biomarkers. The results indicate that, in the recovery stage $\mathcal{R}$, there is a statistically significant positive correlation between depression severity scores and ANS biomarkers $\overline{\mathrm{HR}}$, $\overline{f}_r^{\mathrm{SR}}$, and $\overline{A}_{13}$, while a negative correlation was found for $\overline{C}_{\mathrm{R,R}}^{\Phi}$. Positive correlation was found for those parameters in which higher values are related to increased SNS activity. Furthermore, autonomic reactivity indices show a better performance compared to raw values of ANS biomarkers. It can be seen that $\Delta\left(\overline{A}_{13}\right)_{\mathcal{R}}^{\mathcal{S}_\mathrm{C}}$ is associated with the highest (absolute) correlation values ($r = -0.50$).

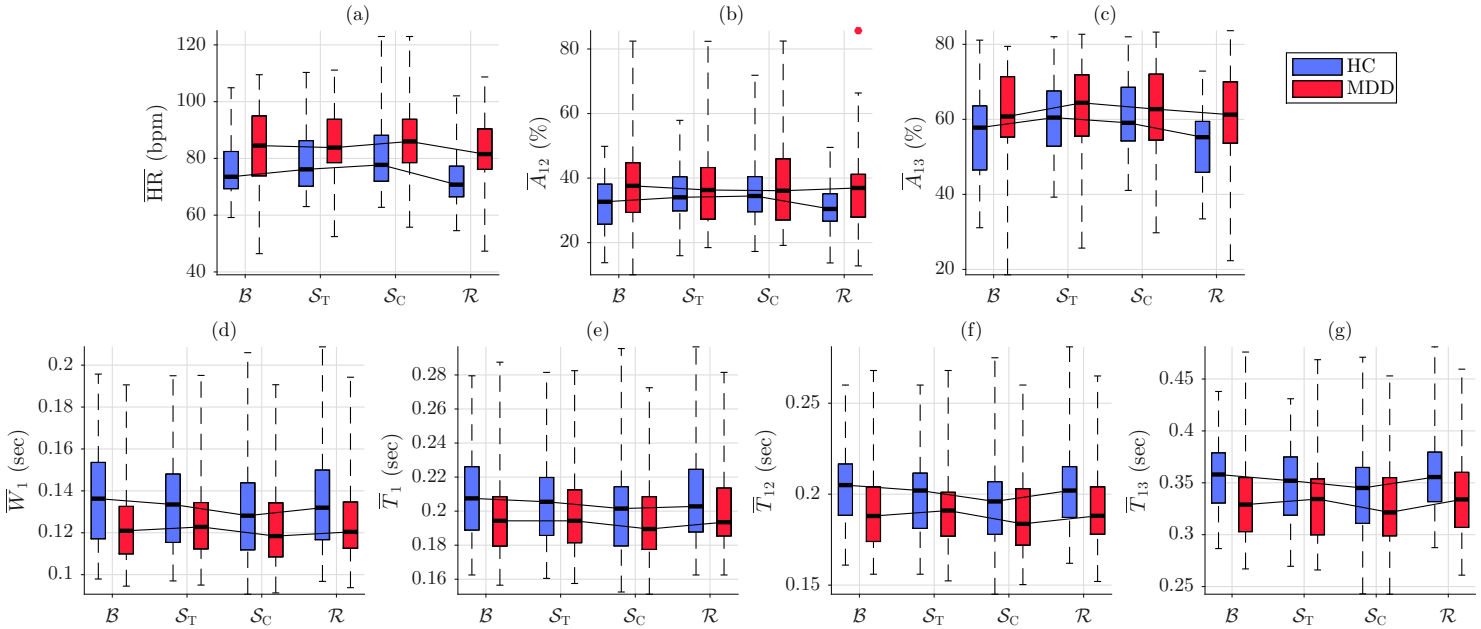

Figure 10.4: Functional boxplots of pulse waveform characteristics. (a) Heart rate (HR), (b) percentage of amplitude loss in the first reflection ($\overline{A}_{12}$), (c) percentage of amplitude loss in the second reflection ($\overline{A}_{13}$), (d) width of the main wave ($\overline{W}_1$), (e) time occurrence of the main wave ($\overline{T}_1$), (f) time delay between the main wave and the first reflected wave ($\overline{T}_{12}$), and (g) time delay between the main wave and the second reflected wave ($\overline{T}_{13}$). The group of HC and MDD subjects are marked in blue and red, respectively.

Table 10.6: Values (Median±IQR) of ANS biomarkers derived from the model-based PPG waveform analysis

	$\mathcal{B}$		$\mathcal{S}_T$		$\mathcal{S}_C$		$\mathcal{R}$	
	HC	MDD	HC	MDD	HC	MDD	HC	MDD
$\overline{HR}$ (bpm)	**73.5 ± 13.1**$_{\dagger}$	**84.5 ± 21.0**$_{\dagger}$	76.1 ± 15.9$^{*}_{\dagger}$	83.8 ± 15.2$_{\dagger}$	77.7 ± 16.1$^{*}_{\dagger}$	86.0 ± 15.2$_{\dagger}$	**70.8 ± 10.7***	**81.5 ± 14.2***
$\overline{A}_{12}$ (%)	32.7 ± 12.4	37.6 ± 15.4	34.1 ± 10.4$^{*}_{\dagger}$	36.2 ± 16.2	34.5 ± 10.8$^{*}_{\dagger}$	36.1 ± 18.8	30.3 ± 8.4	37.0 ± 13.1
$\overline{A}_{13}$ (%)	57.7 ± 16.6$_{\dagger}$	61.7 ± 15.1	60.2 ± 14.8$^{*}_{\dagger}$	64.7 ± 15.3$^{*}_{\dagger}$	59.2 ± 13.5$^{*}_{\dagger}$	62.7 ± 17.6$_{\dagger}$	**55.2 ± 13.6***	**61.4 ± 14.8**
$\overline{W}_1$ (ms)	**137.0 ± 35.9**	**121.9 ± 22.4**	133.7 ± 32.0	123.6 ± 21.7	129.1 ± 32.6$^{*}_{\dagger}$	119.3 ± 25.8	133.2 ± 32.5	121.3 ± 21.4
$\overline{T}_1$ (ms)	209.6 ± 37.4	196.0 ± 28.0	206.0 ± 34.3	195.3 ± 32.0	202.0 ± 33.4$^{*}_{\dagger}$	190.0 ± 32.0	204.8 ± 35.6	194.0 ± 28.0
$\overline{T}_{12}$ (ms)	**204.0 ± 27.5**	**188.0 ± 29.8**	204.0 ± 27.5	190.8 ± 24.0	196.0 ± 27.8$^{*}_{\dagger}$	184.9 ± 32.0	202.3 ± 27.0	188.0 ± 25.6
$\overline{T}_{13}$ (ms)	**357.7 ± 49.0**	**330.0 ± 52.0**	352.0 ± 54.9$_{\dagger}$	334.2 ± 59.1	344.8 ± 51.3$^{*}_{\dagger}$	321.0 ± 56.0$_{\dagger}$	**356.0 ± 47.3**	**334.7 ± 52.0**

Note: In bold are marked the parameters with statistical differences ($p < 0.01$) between HC and MDD group. Statistically significant ($p < 0.01$) individual differences compared to $\mathcal{B}$ and $\mathcal{R}$ are denoted with * and †, respectively.

Table 10.7: AUC / Cohen's d values of ANS biomarkers derived from the model-based PPG waveform analysis

$\mathcal{F}$	$\mathcal{B}$	$\mathcal{S}_T$	$\mathcal{S}_C$	$\mathcal{R}$	$\Delta(\mathcal{F})^{\mathcal{S}_T}_{\mathcal{B}}$	$\Delta(\mathcal{F})^{\mathcal{S}_C}_{\mathcal{B}}$	$\Delta(\mathcal{F})^{\mathcal{B}}_{\mathcal{R}}$	$\Delta(\mathcal{F})^{\mathcal{S}_T}_{\mathcal{R}}$	$\Delta(\mathcal{F})^{\mathcal{S}_C}_{\mathcal{R}}$
$\overline{HR}$	0.69 / 0.59	0.63 / 0.36	0.60 / 0.24	**0.72 / 0.69**	0.65 / 0.51	0.65 / 0.53	0.57 / 0.24	0.69 / 0.67	**0.71 / 0.67**
$\overline{A}_{12}$	0.63 / 0.52	0.54 / 0.27	0.54 / 0.18	0.65 / 0.59	0.68 / 0.60	**0.70 / 0.60**	0.51 / 0.07	0.65 / 0.58	0.67 / 0.61
$\overline{A}_{13}$	0.63 / 0.38	0.59 / 0.26	0.58 / 0.24	**0.72 / 0.70**	0.56 / 0.35	0.58 / 0.35	**0.72 / 0.68**	**0.77 / 0.85**	**0.74 / 0.81**
$\overline{W}_1$	0.69 / 0.55	0.60 / 0.37	0.59 / 0.30	0.62 / 0.46	0.66 / 0.51	**0.70 / 0.61**	0.59 / 0.17	0.59 / 0.26	0.62 / 0.49
$\overline{T}_1$	0.66 / 0.46	0.59 / 0.29	0.57 / 0.23	0.60 / 0.36	0.64 / 0.50	**0.70 / 0.62**	0.61 / 0.29	0.54 / 0.16	0.59 / 0.41
$\overline{T}_{12}$	0.69 / 0.56	0.62 / 0.34	0.59 / 0.25	0.65 / 0.50	0.65 / 0.57	**0.72 / 0.66**	0.55 / 0.11	0.62 / 0.37	0.67 / 0.63
$\overline{T}_{13}$	0.69 / 0.56	0.62 / 0.34	0.59 / 0.28	0.68 / 0.56	0.64 / 0.56	0.65 / 0.55	0.52 / 0.06	0.63 / 0.51	0.67 / 0.62

Note: In bold are marked the parameters with AUC ≥ 0.7

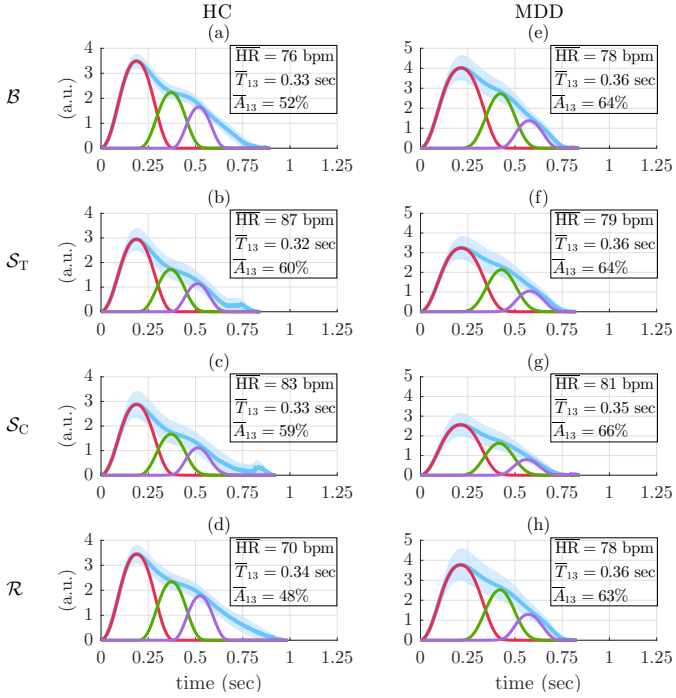

Figure 10.5: Average pulse waveforms for two subjects. Average pulse waveforms for (a)-(d) a HC, and (e)-(h) a MDD subject. Each row corresponds to one of the experimental protocol stages, i.e., $\mathcal{B}$, $\mathcal{S}_T$, $\mathcal{S}_C$, and $\mathcal{R}$. The blue lines and shaded areas represent the ensemble average and standard deviation, respectively, while the ensemble average for the three inner waves are marked with red, green, and purple lines. The waveform characteristics $\overline{HR}$, $\overline{T}_{13}$, and $\overline{A}_{13}$ are illustrated at the top right of each graph.

Figure 10.6 shows the scatter plots of depression severity with autonomic reactivity indices as well as with the scores of psychometric and cognitive tests. Self-reported depression and stress level, assessed with BDI and PSS, respectively, show a positive correlation with HDRS, yielding $r = 0.85$, and $r = 0.79$, respectively. Regarding cognitive tests, the time needed to perform the $\mathcal{S}_T$ ($\mathcal{T}_{AB}$) was positively correlated with HDRS, while the accuracy in $\mathcal{S}_C$ (W_C) was negatively correlated with depression level.

The results of classification are summarized in Table 10.9 and Table 10.10. Among all ANS biomarkers, $\overline{HR}$ and $\overline{f_r}^{SR}$ in recovery stage, as well as autonomic reactivity indices $\overline{C}^{\Phi}_{R,R}$ and $\overline{A}_{13}$ from basal and stress to recovery, respectively, are selected consistently using different feature selection methods (Table 10.9). The feature set with the minimum number of ANS biomarkers is obtained with SLR method, and it offers the best performance using a linear SVM classifier, yielding to ACC = 80.0% and F1 = 80.0% (Table 10.10). Note that the features with the best performance can differ depending on the type of analysis, i.e., classification or regression/correlation.

Table 10.8: Correlation coefficient r between ANS biomarkers and depression severity

$\mathcal{F}$	$\mathcal{R}$	$\Delta(\mathcal{F})^{\mathcal{B}}_{\mathcal{R}}$	$\Delta(\mathcal{F})^{\mathcal{S}_T}_{\mathcal{R}}$	$\Delta(\mathcal{F})^{\mathcal{S}_C}_{\mathcal{R}}$
$\overline{\overline{\text{HR}}}$	0.38^{**}	-0.09	-0.39^{**}	$\mathbf{-0.40}^{**}$
$\overline{f}_r^{\text{SR}}$	0.24	$\mathbf{-0.29}^{*}$	-0.24	-0.15
$\overline{C}^{\Phi}_{\text{R,R}}$	-0.23	0.44^{**}	$\mathbf{0.45}^{**}$	
$\overline{A}_{13}$	0.44^{**}	-0.37^{*}	-0.45^{**}	$\mathbf{-0.50}^{**}$

Note: In bold are marked the highest absolute correlation values of each ANS biomarker. Statistically significant correlation values are denoted with * for $p < 0.01$ and ** for $p < 0.001$.

Table 10.9: Selected ANS biomarkers in the classification pipeline

$\mathcal{F}$	$\mathcal{R}$	$\Delta(\mathcal{F})^{\mathcal{B}}_{\mathcal{R}}$	$\Delta(\mathcal{F})^{\mathcal{S}_T}_{\mathcal{R}}$	$\Delta(\mathcal{F})^{\mathcal{S}_C}_{\mathcal{R}}$
$\overline{\overline{\text{HR}}}$	♦▲■			
$\overline{f}_r^{\text{SR}}$	♦▲■	▲		
$\overline{C}^{\Phi}_{\text{R,R}}$		♦▲■	▲■	
$\overline{A}_{13}$	■		♦▲■	

Note: The features selected using SLR, LASSO, and FR approach are marked with ♦, ▲, and ■, respectively.

Table 10.10: Results of MDD classification

	SVM		LR		LDA	
	ACC	F1	ACC	F1	ACC	F1
SLR	**80.0**%	**80.0**%	76.2%	75.9%	68.7%	71.9%
LASSO	80.0%	78.9%	78.7%	77.9%	75.0%	76.2%
FR	73.7%	73.4%	75.5%	74.3%	75.0%	77.2%

Note: In bold is marked the classifier with the best performance.

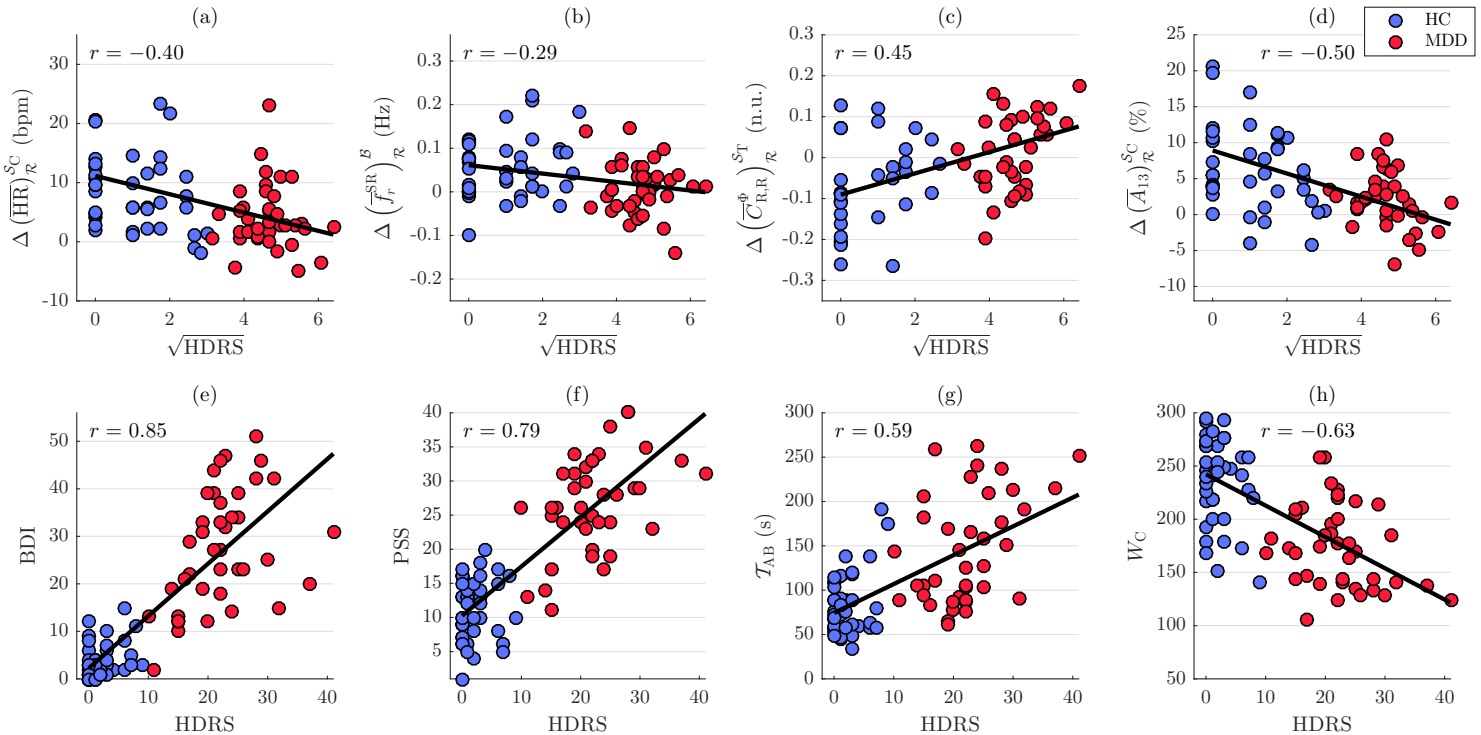

Figure 10.6: Scatter plots of depression severity scores and autonomic reactivity indices, scores of psychometric, and cognitive tests. (a) HR, (b) respiratory rate, (c) QPC degree between respiration and RSA component of HRV, (d) percentage of amplitude loss in the second reflection, (e) self-reported depression level, (f) self-reported stress level, (g) time required to accomplish $\mathcal{S}_T$, and (h) number of correct words in $\mathcal{S}_C$. Least-squares reference lines are superimposed on the scatter plots. Correlation coefficients between depression severity scores and autonomic reactivity indices are displayed at the top of each graph. The group of HC and MDD subjects are marked in blue and red, respectively.

10.3 Discussion

The present study investigates the differences in ANS function and stress response between MDD and healthy subjects by measuring changes in ANS biomarkers. ANS-related parameters are derived from the joint analysis of HRV and respiratory signal, and from a model-based PPG waveform analysis. The response to stress, induced by verbal and non-verbal cognitive tasks, is also evaluated by means of autonomic reactivity.

Results show that MDD patients, compared to HC subjects, exhibit higher HR values during non-stressful stages, i.e., $\mathcal{B}$ and $\mathcal{R}$ (see Table 10.3), thereby suggesting that depression is associated with ANS dysfunction. Increased SNS activity in MDD patients, due to ANS imbalance, has been also reported in previous studies [290]. Participants of both groups exhibit a lower HR in post-task relaxation period $\mathcal{R}$ compared not only to stressful stages $\mathcal{S}_{\mathrm{T}}$ and $\mathcal{S}_{\mathrm{C}}$, but also to the basal stage $\mathcal{B}$. This implies that both patients with depression and healthy subjects reacted to stressful stimuli. Filling psychometric tests, during $\mathcal{B}$, does not imply a cognitive stressor, but it may require the attention and effort of the subject, which could affect the ANS state. Moreover, results show that respiratory rate reduces significantly in HC group during the recovery stage $\mathcal{R}$ compared to $\mathcal{B}$, while no statistical differences were found in MDD group (see Table 10.3). An increased breath-to-breath variability measured by $\overline{B}_r$ was found for both groups in the presence of stressful stimuli (see Table 10.3). In [357], it was reported that, during sad mood, individuals with remitted depression show greater respiration pattern variability compared to HC subjects. In this study, although no significant differences were found between MDD and HC group, a tendency for higher value in $\overline{B}_r$ is observed in MDD group during recovery (see Fig. 10.2(d)). Respiratory activity can influence the emotional status since the phrenic and vagus nerves are involved in the function of the diaphragm [38].

However, a less regular breathing can hinder the interpretation of some HRV indices due to the mechanical effect of respiration. Erratic respiratory patterns in the presence of stressful stimuli result to spectra with significant power in the LF band, even if the average respiratory rate is higher than 0.15 Hz [28]. Thus, the spectral power in both LF and HF band might be more related to mechanical effect of respiration than to ANS activity. Furthermore, in tasks that require speech production, HRV increases when short inspiration is followed by long expiration [27, 269, 311]. Changes in respiratory patterns imposed by the exposure to stressful stimuli may mask the vagal withdrawal [46, 151]. In this study, results show that, in stressful tasks, subjects exhibit a higher HRV quantified either by temporal, e.g., SDNN, or spectral HRV indices, such as P_{LF} or P_{TOT} (see Table 10.3). However, an increased HR should be accompanied by lower values of HRV [317]. These inconsistencies due to the less regular breathing blur also the interpretation of sympathovagal balance indices. Only when respiratory information is taken into account by means of TFC, a correct estimation of sympathovagal balance is obtained, i.e., increased $\overline{P}^{r}_{\mathrm{LF}n}$ during stressful stages. The unconstrained estimation of sympathovagal balance using $P^{u}_{\mathrm{LF}n}$ shows similar results to $\overline{P}^{r}_{\mathrm{LF}n}$ only during $\mathcal{S}_{\mathrm{T}}$. During stressful tasks involving speech, the performance of OSP on separating respiratory influences from the HRV might be hindered when both respiratory rate is low and the bandwidth of the res-

piratory spectrum is large (see Fig. 10.2(b),(d)). Other ANS biomarkers related to HRV that are not evaluated during verbal stressors are nonlinear cardiorespiratory coupling indices.

Regarding nonlinear cardiorespiratory coupling function during ANS changes induced by $\mathcal{S}_T$, results show that QPC strength $\overline{E}_{R,R}$ and QPC degree $\overline{C}^{\Phi}_{R,R}$ between respiration and the RSA component of HRV are statistically significantly lower in HC compared to MDD subjects in the presence of stressful stimuli (see Table 10.3). These results indicate that HC subjects reacted more to the stressful stimuli, while the parasympathetic branch was less inhibited in MDD patients. In our previous study, it was shown that a vagal withdrawal induced by hemodynamic stress decreased also QPC strength (see Ch. 9). In healthy subjects, an increased degree of QPC $\overline{C}^{\Phi}_{L,R}$ between respiration and components of HRV in the low frequency band might be related to the less regular breathing during $\mathcal{S}_T$. This may explain the absence of a significantly lower $\overline{E}_{L,R}$, since QPC strength depends on not only the amplitude of the nonlinear oscillations in HRV, but also on the degree of QPC. A longer lasting phase synchronization, i.e. higher QPC degree, between the interacting oscillations may lead to higher values in $\overline{E}_{L,R}$. The inhibition of sympathetic branch after the cognitive load in healthy subjects, evidenced by lower HR and respiratory rate, is also reflected by higher values in $\overline{C}^{\Phi}_{R,R}$ during $\mathcal{R}$. On the contrary, no significant changes across protocol stages were found in MDD patients, thereby suggesting that depression is associated with minimal changes in ANS state during mental stress.

Results from ANS biomarkers measuring changes in PPG morphology show an increased amplitude loss in wave reflections, e.g. $\overline{A}_{13}$, and a reduction in pulse transit time surrogates, e.g. $\overline{T}_{13}$, during stress (see Table 10.6). A more pronounced effect is observed in $\mathcal{S}_C$, which is characterized by higher levels of sympathetic activity evidenced by higher HR values. Acute mental stress may increase aortic stiffness [341]. An increased arterial stiffness implies that the stroke volume flows through the arterial system and peripheral tissues mainly during systole due to the reduced distensibility of the elastic arteries and the aorta [358]. This causes both a larger peak in systolic part and a larger decline during diastolic part. Thus, in stressful tasks, a decrease in $\overline{T}_{13}$ is due to early wave reflection, while an increment in $\overline{A}_{13}$ is related to the inverse relationship between systolic (increased) and diastolic blood pressure (decreased).

Besides raw values of ANS biomarkers, autonomic reactivity indices obtained from intra-subject differences between two conditions, e.g., basal and stress, are considered when evaluating differences between MDD and HC group. Results in Table 10.5 and Table 10.7 show that stress induction may enhance differences in ANS regulation between MDD and HC subjects. In general, changes in ANS function quantified by autonomic reactivity indices are associated with a higher degree of separability between groups, i.e., larger AUC values, compared to raw values of ANS biomarkers. The best performance among ANS-related parameters is obtained for the mean HR, either derived from ECG or PPG signals, the respiratory rate, either derived from the respiratory belt signal or EDR signals using the SR method, for the QPC degree in $\Omega_{R,R}$, and the percentage of

amplitude loss in the second reflection $\overline{A}_{13}$. The pulse waveform characteristic $\overline{A}_{13}$ is associated with larger effect sizes ($d > 0.8$), thereby implying that vascular characteristics could provide complementary information about autonomic function. The discriminative power of ANS biomarkers is complemented by their high diagnostic performance for classifying subjects as having MDD or not. Feeding a linear SVM classifier in a LOSO scheme with only 4 features selected automatically with a SLR method (see Tables 10.9 and 10.10) yields to ACC = 80.0% and F1 = 80.0%. These findings suggest that the stress response can be used to assess depression.

A higher degree of depression is associated with a decreased autonomic reactivity. Autonomic reactivity indices and depression severity scores are negatively correlated (see Fig. 10.6). Note that $\overline{\text{HR}}$, $\overline{f}_r^{\text{SR}}$, and $\overline{A}_{13}$ are considered indices of stress since larger values are expected in tasks associated with higher levels of SNS activity. Thus, considering changes from stressful tasks to recovery, higher values in autonomic reactivity indices indicate that subjects reacted to stress and they were able to return in a resting condition. On the contrary, inverse relationship holds for ANS biomarkers reflecting PNS activity. Thus, instead of negative, a positive correlation is obtained with $\overline{C}_{\text{R,R}}^{\Phi}$ (see Fig. 10.6(c)). Stress response quantified by dynamic changes in vascular characteristics shows the best performance in terms of correlation, yielding to $r = -0.5$ (see Fig. 10.6(d)). In Figs. 10.6(g),(h), it can be seen that subjects with higher levels of depression need more time to accomplish $\mathcal{S}_{\text{T}}$ and their performance in $\mathcal{S}_{\text{C}}$ is lower. Significant correlation was also found between the ANS biomarker with the best performance and the scores $\mathcal{T}_{\text{AB}}$ and W_{C}, yielding to $r = -0.36$ and $r = 0.39$, respectively. Blunted autonomic reactivity to stress might reflect suboptimal functioning of the cortical and limbic brain regions that are involved in motivation and cognitive ability [53]. Thus, deviations from an optimal response, in the face of challenge, may indicate that MDD patients are less capable than healthy subjects, to adjust their mental state to abrupt behavioral changes. This can also be associated to the fact that MDD patients might be already stressed before the induction of cognitive load, since a significant positive correlation between HDRS and the stress level reported in $\mathcal{B}$ is observed in Fig. 10.6(f). Taking into account that the range of depression severity scores covers all types of depressive symptoms (mild, moderate, severe, and very severe), stress response quantified by dynamic changes in vascular characteristics might be useful for depression monitoring.

These results are in agreement with previous studies which showed that patients with depression are associated with blunted cardiovascular reactivity to psychological stressors. Reduced HR and systolic BP reactivity during a speech task and less HR recovery in depressed patients compared to healthy control subjects was reported in [281]. Other studies pointed out that high scores of depression or anxiety symptomatology are associated with blunted BP and HR reactivity to psychological stressors [79,355]. Although PPG signal has been widely used for quantifying mental stress [60, 114], few studies have explored the ability of PPG-derived indices to assess autonomic reactivity in MDD patients. One of the very few studies which analyzed morphological PPG features in MDD patients showed that entropy indices of systolic and diastolic amplitude of pulse waveform were positively correlated with suicidal score [182]. Seldenrijk et al. [296] showed that the

early wave reflection in depressive or anxiety disorders was associated with higher arterial stiffness, which agrees with the findings of the present study. Altered vasomotor tone in MDD patients, owing to the autonomic imbalance (increased sympathetic activity), has been related to changes in endothelial function, which is considered a gauge of vascular health [257]. Systematic reviews have shown that depressive symptoms are associated with subclinical atherosclerosis [333, 352]. Arterial stiffness may increase the risk for structural abnormalities in the mood regulatory centers of the brain due to small vessel lesions, contributing to the development of late-life depression (vascular depression hypothesis) [232,319,336]. Irrespective of whether depression is a cause or effect of arterial stiffness, impaired arterial compliance might constitute a biomarker of mental health and might contribute to the increased frequency of cardiovascular diseases observed in MDD patients [280, 329].

In [203], the PDA-based inner waves of a PPG pulse were modeled as Gaussian waves using a Trust-Region algorithm for the fitting procedure, while, in this work, waveform characteristics are derived from the inner waves without the use of fitting. Similar results (Table 1 in Appendix) are obtained for both approaches, thereby suggesting a faster feature extraction, which seems appealing for a future integration of PDA into wearable devices. A low sampling frequency might be also required for implementation in wearables, however, it may produce a jitter in fiducial point estimation [317]. To reduce the effect of jitter, an algorithm of interpolation (up-sampling) is commonly used for refining the fiducial point [228]. Based on additional analyses (Table 2 and Table 3 in Appendix), where the PPG signal $x_{\mathrm{PPG}}(n)$ was up-sampled from F_s = 250 Hz to 1000 and 2000 Hz, the effect of F_s on morphological indices was minimal leading to changes in the order of 1% for AUC values. Although up-sampling is crucial in HRV analyses, since the effect of jitter can alter spectral indices considerably [181], PPG signals recorded at low sampling frequency, e.g. F_s = 250 Hz, may suffice for deriving morphological indices. The main difference of the present technique with respect to other PDA techniques in the literature is that both main and reflected waves are assumed to be symmetrical and they are extracted one-by-one, instead of obtaining a modeled PPG by fitting several waves at once [122,152]. This facilitates the interpretation of model parameters based on the pulse wave propagation physiology. Moreover, this decomposition is based on the hypothesis that half of the incidence pulse does not overlap with the reflected one, and same with the following pulses. However, in cases where fast propagation occurs, there might be overlapping between waves, but it should be minimum since it is an overlap of the maximum incident pulse with the lower tails of the reflected one. This point deserves a simulation study for evaluating hemodynamic responses to controlled fluxes, which, however, is out of the scope of this thesis.

A limitation of the present study is that the performance of PDA was studied mainly on a fingertip PPG signal. PPG signals recorded at different places on the body (wrist, forehead, ear) exhibit quite different morphologies from that of the fingers. Therefore, the current methodology can not be generalized automatically to all PPG signals. However, the database did not include PPG recordings at a second location on the body. Further studies, where PPG signals acquired from various sites of the body are available, should

be conducted for evaluating the effect of the recording site on the PDA performance. Another limitation is that most of MDD patients were in antidepressant treatment. Results of a recent cross-sectional study have shown that there is no association between arterial stiffness and longitudinal exposure to antidepressants [49]. In [188, 253], it was found that depressed patients who responded to antidepressant treatment presented sustained improvement in vascular function. Moreover, in a large cohort study, Dregan et al. [89] showed that the association of depression with arterial stiffness in midlife was mediated via both metabolic syndrome and inflammatory processes rather than antidepressant medication. The hypothesized bidirectional relationship between depression and arterial stiffness can be also mediated by the lack of physical activity and poor diet, rather than the use of antidepressants [124, 174]. However, the reduced number of MDD patients without medication (3 out of 40, see Table 10.1) do not allow the impact of drug treatment on pulse waveform characteristics to be assessed. Although the effect of drug treatment on the results cannot be investigated, it is possible to evaluate how the relationship between depression level and reactivity might be influenced by whether a patient takes a combination of AD and BZ or is treated with only one of them. Results of an additional analysis (see Fig. 2 in Appendix) show that patients treated with AD and BZ have higher reactivity than those treated with only AD or BZ. Thus, a combination of drugs might improve the emotional reactivity of patients with depression. However, due to the small sample size, no firm statement about causality can be put forward.

10.4 Conclusions

This part of the dissertation explores the idea of monitoring depression level using ANS biomarkers derived from the joint analysis of HRV and respiratory signals, as well as from a model-based PPG waveform analysis. ANS biomarkers are acquired in MDD patients and HC subjects at basal conditions, during the execution of cognitive tasks, and at the post-task relaxation period. Differences in ANS function between MDD and HC subjects are investigated not only by using the raw values of ANS biomarkers but also autonomic reactivity indices. Autonomic reactivity to mental stress, which reflects the ability of an individual to cope with a challenging situation, is assessed by quantifying individual differences in ANS biomarkers across conditions.

Results show that depression is associated with autonomic imbalance, characterized by increased sympathetic activity, since MDD patients exhibit higher HR values, compared to HC subjects, during non-stressful stages. Increased breath-to-breath variability in the presence of stressful stimuli and reduced HR in recovery period after the stress induction in both groups imply that all participants reacted to stressful stimuli. However, significantly lower HR and respiratory rate in HC compared to MDD group at the post-task relaxation period indicate that patients with depression recover at a less extent after stress exposure. Furthermore, the inhibition of sympathetic branch in HC group after task execution increased significantly the QPC degree between respiration and RSA component of HRV. Regarding vascular characteristics, increased sympathetic activity,

which is associated with higher arterial stiffness, is evidenced by increased amplitude loss in wave reflections and reduced pulse transit time surrogates.

In general, changes in ANS function quantified by autonomic reactivity indices are associated with a higher degree of separability between groups, i.e., larger AUC values, compared to raw values of ANS biomarkers. Larger AUC values are obtained when changes from stressful stages to recovery phase are considered. The discriminative power of ANS biomarkers is supported by their high diagnostic performance for classifying subjects as having MDD or not. The best performance among all ANS biomarkers derived from the joint analysis of HRV and respiratory signals is achieved for the nonlinear cardiorespiratory coupling indices, while the amplitude loss in second wave reflection shows the best performance among all ANS biomarkers derived from the model-based PPG waveform analysis. Stress response quantified by dynamic changes in arterial compliance shows also the best performance in terms of correlation with depression severity. Autonomic reactivity indices and depression severity scores are negatively correlated, thereby implying that a higher degree of depression is associated with a decreased autonomic reactivity. Furthermore, subjects with higher levels of depression need more time to accomplish cognitive tasks and their performance is lower. Thus, blunted autonomic reactivity to mental stress may indicate that MDD patients are less capable than healthy subjects, to adjust their mental state to abrupt behavioral changes.

Therefore, it can be concluded that impaired arterial compliance might constitute a biomarker of mental health and can be an aid for the monitoring of depression.

Part IV

Conclusions

11

Conclusions and future work

11.1 Summary and final discussion

The main objective of this thesis is to derive autonomic nervous system (ANS) biomarkers from multi-modal and model-based signal processing techniques for assessing stress and monitoring depression. For this purpose, the present document was divided in three main parts.

In the first part, an introduction to mental health, and a theoretical framework for investigating the role of stress in mental illness are presented. Stress is common in our fast-paced society and strongly influences our mental health. In the short term, ANS controls the cardiovascular response to stressful stimuli. Regulation of physiological parameters, i.e., biomarkers, such as heart rate (HR), respiratory rate, and blood pressure (BP), allows the organism to respond to sudden changes in the environment. However, physiological adaptation to a regularly occurring environmental phenomenon alters biological systems involved in stress response. Neurobiological alterations in the brain can disrupt the function of the ANS. ANS dysfunction and structural brain changes have

a negative impact on cognitive, emotional, and behavioral processes, thereby leading to development of mental disorders. The most common mental disorder is depression. Major depressive disorder (MDD) has a negative impact on the quality of life, since it is associated with considerable losses in health and functioning, and increases significantly a person's risk for cardiovascular diseases (CVDs). While screening tools used in clinical practice, such as questionnaires, have considerable value, sometimes they are time-consuming and require the willingness of the patients to communicate their symptoms. Screening tools based on noninvasive ANS biomarkers could complement existing psychometric scales for improved accuracy in the monitoring of depression. Thus, ANS assessment is of paramount importance in mental health and illness.

In the second part, the methodological framework for deriving biomarkers related to the ANS from multi-modal and model-based signal processing techniques is provided. Such methodologies include the joint analysis of heart rate variability (HRV) and respiratory signals (Ch. 6), novel techniques for deriving the respiratory signal from ECG (Ch. 7), and a robust PPG waveform analysis based on a model-based approach (Ch. 8). In Ch. 6.3, a novel method, which takes into account both phase and frequency locking phenomena between respiration and HRV signals, for assessing quadratic nonlinear cardiorespiratory coupling is proposed. The novel method, named Real Wavelet Bisphase (RWB), is computationally simple and exhibits the most robust performance, compared to other previous published methods, when assessing the degree of Quadratic Phase Couping (QPC) between HRV and respiration. Moreover, the novel method, named Normalized Wavelet Biamplitude (NWB), can be used to quantify robustly the strength of QPC, once detection has been performed by RWB. In Ch. 7, a novel ECG-derived respiration (EDR) signal, named "slope range" (SR), and a technique for estimating the respiratory rate from EDR signals in patients with atrial fibrillation (AF) is proposed. Although retrieving respiratory parameters from EDR signals during sinus rhythm has been widely studied, EDR methods in arrhythmia remains largely unexplored. Methods exploring HR information cannot be used in AF since the rhythm is not controlled by the ANS, while the performance of techniques exploring beat morphology may deteriorate due to the presence of atrial fibrillatory waves (f-waves), which can mask the respiratory information. Using real ECG signals and reference respiratory signals, respiratory rate estimation without f-wave suppression resulted in a median error of 0.015 ± 0.021 Hz. The SR method showed the most robust performance, compared to other previous published EDR methods. SR is computationally simple since f-wave suppression is not needed. Novel techniques for improving the monitoring of respiration in cardiac arrhythmias, is also important in the field of mental disorders, since previous studies have found a high degree of comorbidity between MDD and CVDs. In Ch. 8, to increase the robustness for some morphological measurements reflecting BP and arterial tone change, the modeling of the PPG pulse as a main wave superposed with several reflected waves is considered. Deriving ANS biomarkers that rely on the detection of inflection points, which might not be always visible in the PPG waveform (e.g. under stressful situations), can be challenging. Therefore, the development of novel approaches for deriving noninvasive ANS biomarkers

offers the possibility to improve the assessment of stress in healthy individuals and ANS dysfunction in MDD patients.

In the third part, ANS biomarkers are evaluated in the assessment of different types of stress, either physiological or psychological, in healthy individuals (Ch. 9), and, then, biomarkers sensitive to stress are evaluated in the monitoring of depression (Ch. 10).

11.1.1 Stress assessment

Although focus should be put on behavioral, cognitive, and emotional responses evoked by mental stress, the study of physiological stress, e.g. hemodynamic or heat, that minimize the influence of stress perception on the stress-evoked arousal, can be useful for developing biomarkers of stress. The evaluation of ANS biomarkers in stress assessment, first in healthy subjects, and then in MDD patients, is particularly important, because stress is a highly subjective phenomenon and many factors, including mental health, can modulate the perception of stressful stimuli. In the presence of mental stress (Ch. 9.1), induced by cognitive tasks, healthy subjects show an increment in the respiratory rate and higher number of nonlinear interactions between respiration and HRV signal, fact that might be associated with a sympathetic activation, but also with a less regular breathing. In the presence of hemodynamic stress (Ch. 9.2), induced by a postural change, healthy subjects show a reduction in NWB between respiration and HRV components, which might be related to a vagal withdrawal. In the presence of heat stress (Ch. 9.3), induced by exposure to elevated environmental temperatures, healthy subjects show an increased sympathovagal balance. Hence, ANS biomarkers, derived from HRV and respiratory signals, can be used for assessing stress.

11.1.2 Depression monitoring

In Ch. 10, ANS biomarkers, derived from the joint analysis of HRV and respiratory signals, as well as from a model-based PPG waveform analysis, are explored in the context of depression monitoring. ANS biomarkers are acquired in MDD patients and healthy control (HC) subjects at basal conditions, during the execution of cognitive tasks, and at the post-task relaxation period. Differences in ANS function between MDD and HC subjects are investigated not only by using the raw values of ANS biomarkers but also autonomic reactivity indices. Autonomic reactivity to mental stress, which reflects the ability of an individual to cope with a challenging situation, is assessed by quantifying individual differences in ANS biomarkers across conditions. Results show that depression is associated with autonomic imbalance, characterized by increased sympathetic activity and reduced arterial compliance, which are evidenced by large HR values and increased PPG amplitude loss in wave reflections, respectively. Although, all participants reacted to stressful stimuli, MDD patients recover at a less extent after stress exposure. This implies that stress response is different between MDD and HC group. Autonomic reactivity indices, assessed by changes in ANS biomarkers from stressful stages to recovery phase,

are associated with high degree of separability between groups and large effect sizes, yielding to AUC>0.7 and Cohen's $d > 0.8$, respectively. The discriminative power of ANS biomarkers is supported by their high diagnostic performance for classifying subjects as having MDD or not, yielding to accuracy of 80.0%. The best performance among all ANS biomarkers derived from the joint analysis of HRV and respiratory signals is achieved for the nonlinear cardiorespiratory coupling indices, while the amplitude loss in second wave reflection shows the best performance among all ANS biomarkers derived from the model-based PPG waveform analysis. Stress response quantified by dynamic changes in arterial compliance shows also the best performance in terms of correlation with depression severity, yielding to correlation coefficient $r = -0.5$. The negative correlation implies that a higher degree of depression is associated with a decreased autonomic reactivity. Furthermore, subjects with higher levels of depression need more time to accomplish cognitive tasks and their performance is lower. Blunted autonomic reactivity to mental stress may indicate that MDD patients are less capable than healthy subjects, to adjust their mental state to abrupt behavioral changes. Therefore, it can be concluded that impaired arterial compliance might constitute a biomarker of mental health and can be an aid for the monitoring of depression.

11.2 Main conclusion

The development of noninvasive ANS biomarkers, derived from multi-modal and model-based signal processing of diverse biosignals, such as ECG, PPG, and respiration, offers the possibility to improve the assessment of stress in healthy individuals and ANS dysfunction in patients with depression. Autonomic reactivity to mental stress, quantified by dynamic changes in PPG waveform morphology, can be an aid for the monitoring of depression. Thus, wearable devices that are able to capture or track such biometric information offer the possibility to perform a more frequent and massive screening as well as a continuous monitoring of stress and depression level.

11.3 Future work

- Derive respiratory parameters from PPG recordings in patients with MDD. Respiratory rate constitutes one of the most promising ANS biomarkers for assessing depression. The extension of the framework presented in this dissertation to real environments requires the development of methods for deriving respiratory parameters from PPG signals. The potential of morphological features extracted from PPG-pulses using a model-based approach to obtain respiratory signals can be studied. The respiratory rate estimation method developed in this thesis and applied to EDR signals can be used in PPG-derived respiratory signals, once it has been validated.

- Derive ANS biomarkers from additional biosignals. Speech signals and electrodermal activity can provide valuable information for assessing stress and depression level. The inclusion of such information may improve the performance of ANS biomarkers obtained from ECG, PPG, and respiratory signals.

- Remote assessment of depression. Depression course is dynamic with multiple relapses and predictive information indicative of a future deterioration is of primary importance. Predict negative clinical outcomes by providing real time information on the patient's current clinical state could be possible in the foreseeable future via sensors in smartphones or wearable devices. The development of remote measurement technologies (RMT) is an innovation that the last years has inspired research for a remotely and passively monitoring of CNS disorders via unobtrusive on-body biosensors and smartphones. This vision is consequent to the overarching aim to develop a transformative platform of remote monitoring of disease state in three CNS diseases: epilepsy, multiple sclerosis and depression, of the European Horizon 2020 project "*Remote Assessment of Disease and Relapse in Central Nervous System Disorders (RADAR-CNS)*". To do so, the identification of clinically useful RMT-measured biomarkers is crucial. The findings of this dissertation could provide valuable information to remote assessment of depression.

Part V

Appendix

PLEASE COMPLETE THE SCALE BASED ON A STRUCTURED INTERVIEW

Instructions: for each item select the one "cue" which best characterizes the patient. Be sure to record the answers in the appropriate spaces (positions 0 through 4).

1 DEPRESSED MOOD (sadness, hopeless, helpless, worthless)
- 0 |__| Absent.
- 1 |__| These feeling states indicated only on questioning.
- 2 |__| These feeling states spontaneously reported verbally.
- 3 |__| Communicates feeling states non-verbally, i.e. through facial expression, posture, voice and tendency to weep.
- 4 |__| Patient reports virtually only these feeling states in his/her spontaneous verbal and non-verbal communication.

2 FEELINGS OF GUILT
- 0 |__| Absent.
- 1 |__| Self reproach, feels he/she has let people down.
- 2 |__| Ideas of guilt or rumination over past errors or sinful deeds.
- 3 |__| Present illness is a punishment. Delusions of guilt.
- 4 |__| Hears accusatory or denunciatory voices and/or experiences threatening visual hallucinations.

3 SUICIDE
- 0 |__| Absent.
- 1 |__| Feels life is not worth living.
- 2 |__| Wishes he/she were dead or any thoughts of possible death to self.
- 3 |__| Ideas or gestures of suicide.
- 4 |__| Attempts at suicide (any serious attempt rate 4).

4 INSOMNIA: EARLY IN THE NIGHT
- 0 |__| No difficulty falling asleep.
- 1 |__| Complains of occasional difficulty falling asleep, i.e. more than ½ hour.
- 2 |__| Complains of nightly difficulty falling asleep.

5 INSOMNIA: MIDDLE OF THE NIGHT
- 0 |__| No difficulty.
- 1 |__| Patient complains of being restless and disturbed during the night.
- 2 |__| Waking during the night – any getting out of bed rates 2 (except for purposes of voiding).

6 INSOMNIA: EARLY HOURS OF THE MORNING
- 0 |__| No difficulty.
- 1 |__| Waking in early hours of the morning but goes back to sleep.
- 2 |__| Unable to fall asleep again if he/she gets out of bed.

7 WORK AND ACTIVITIES
- 0 |__| No difficulty.
- 1 |__| Thoughts and feelings of incapacity, fatigue or weakness related to activities, work or hobbies.
- 2 |__| Loss of interest in activity, hobbies or work – either directly reported by the patient or indirect in listlessness, indecision and vacillation (feels he/she has to push self to work or activities).
- 3 |__| Decrease in actual time spent in activities or decrease in productivity. Rate 3 if the patient does not spend at least three hours a day in activities (job or hobbies) excluding routine chores.
- 4 |__| Stopped working because of present illness. Rate 4 if patient engages in no activities except routine chores, or if patient fails to perform routine chores unassisted.

8 RETARDATION (slowness of thought and speech, impaired ability to concentrate, decreased motor activity)
- 0 |__| Normal speech and thought.
- 1 |__| Slight retardation during the interview.
- 2 |__| Obvious retardation during the interview.
- 3 |__| Interview difficult.
- 4 |__| Complete stupor.

9 AGITATION
- 0 |__| None.
- 1 |__| Fidgetiness.
- 2 |__| Playing with hands, hair, etc.
- 3 |__| Moving about, can't sit still.
- 4 |__| Hand wringing, nail biting, hair-pulling, biting of lips.

10 ANXIETY PSYCHIC
- 0 |__| No difficulty.
- 1 |__| Subjective tension and irritability.
- 2 |__| Worrying about minor matters.
- 3 |__| Apprehensive attitude apparent in face or speech.
- 4 |__| Fears expressed without questioning.

11 ANXIETY SOMATIC (physiological concomitants of anxiety) such as:
gastro-intestinal– dry mouth, wind, indigestion, diarrhea, cramps, belching
cardio-vascular – palpitations, headaches
respiratory – hyperventilation, sighing
urinary frequency
sweating
- 0 |__| Absent.
- 1 |__| Mild.
- 2 |__| Moderate.
- 3 |__| Severe.
- 4 |__| Incapacitating.

12 SOMATIC SYMPTOMS GASTRO-INTESTINAL
- 0 |__| None.
- 1 |__| Loss of appetite but eating without staff encouragement. Heavy feelings in abdomen.
- 2 |__| Difficulty eating without staff urging. Requests or requires laxatives or medication for bowels or medication for gastro-intestinal symptoms.

13 GENERAL SOMATIC SYMPTOMS
- 0 |__| None.
- 1 |__| Heaviness in limbs, back or head. Backaches, headaches, muscle aches. Loss of energy and fatigability.
- 2 |__| Any clear-cut symptom rates 2.

14 GENITAL SYMPTOMS (symptoms such as loss of libido, menstrual disturbances)
- 0 |__| Absent.
- 1 |__| Mild.
- 2 |__| Severe.

15 HYPOCHONDRIASIS
- 0 |__| Not present.
- 1 |__| Self-absorption (bodily).
- 2 |__| Preoccupation with health.
- 3 |__| Frequent complaints, requests for help, etc.
- 4 |__| Hypochondriacal delusions.

16 LOSS OF WEIGHT (RATE EITHER a OR b)

a) According to the patient:	b) According to weekly measurements:
0 |__| No weight loss.	0 |__| Less than 1 lb weight loss in week.
1 |__| Probable weight loss associated with present illness.	1 |__| Greater than 1 lb weight loss in week.
2 |__| Definite (according to patient) weight loss.	2 |__| Greater than 2 lb weight loss in week.
3 |__| Not assessed.	3 |__| Not assessed.

17 INSIGHT
- 0 |__| Acknowledges being depressed and ill.
- 1 |__| Acknowledges illness but attributes cause to bad food, climate, overwork, virus, need for rest, etc.
- 2 |__| Denies being ill at all.

Total score: |__|__|

Figure 1: The Hamilton depression rating scale questionnaire.

Table 1: AUC / Cohen's d values of ANS biomarkers derived from the model-based PPG waveform analysis with a fitting procedure

$\mathcal{F}$	$\mathcal{B}$	$\mathcal{S}_\mathrm{T}$	$\mathcal{S}_\mathrm{C}$	$\mathcal{R}$	$\Delta(\mathcal{F})^{\mathcal{S}_\mathrm{T}}_{\mathcal{B}}$	$\Delta(\mathcal{F})^{\mathcal{S}_\mathrm{C}}_{\mathcal{B}}$	$\Delta(\mathcal{F})^{\mathcal{B}}_{\mathcal{R}}$	$\Delta(\mathcal{F})^{\mathcal{S}_\mathrm{T}}_{\mathcal{R}}$	$\Delta(\mathcal{F})^{\mathcal{S}_\mathrm{C}}_{\mathcal{R}}$
$\overline{\mathrm{HR}}$	0.69 / 0.59	0.63 / 0.36	0.60 / 0.24	**0.72** / **0.69**	0.65 / 0.51	0.65 / 0.53	0.57 / 0.24	0.69 / 0.67	**0.71** / **0.67**
$\overline{A}_{12}$	0.63 / 0.48	0.53 / 0.24	0.53 / 0.16	0.64 / 0.55	0.69 / 0.58	0.69 / 0.57	0.51 / 0.09	0.65 / 0.58	0.66 / 0.58
$\overline{A}_{13}$	0.63 / 0.36	0.59 / 0.24	0.57 / 0.21	**0.70** / **0.66**	0.55 / 0.33	0.57 / 0.35	**0.70** / **0.67**	**0.76** / **0.81**	**0.73** / **0.80**
$\overline{W}_1$	0.68 / 0.54	0.61 / 0.35	0.58 / 0.28	0.61 / 0.43	0.65 / 0.51	**0.71** / **0.63**	0.59 / 0.21	0.58 / 0.22	0.61 / 0.47
$\overline{T}_1$	0.66 / 0.47	0.59 / 0.29	0.57 / 0.23	0.60 / 0.36	0.65 / 0.53	**0.71** / **0.63**	0.61 / 0.30	0.55 / 0.17	0.61 / 0.42
$\overline{T}_{12}$	0.69 / 0.54	0.62 / 0.35	0.58 / 0.26	0.65 / 0.49	0.63 / 0.51	**0.71** / **0.63**	0.55 / 0.08	0.60 / 0.33	0.66 / 0.61
$\overline{T}_{13}$	0.69 / 0.55	0.62 / 0.34	0.59 / 0.29	0.67 / 0.55	0.66 / 0.57	0.66 / 0.53	0.51 / 0.06	0.62 / 0.49	0.65 / 0.59

Note: In bold are marked the parameters with AUC ≥ 0.7

Table 2: AUC / Cohen's d values of ANS biomarkers derived from the model-based PPG waveform analysis (F_s = 1000 Hz)

$\mathcal{F}$	$\mathcal{B}$	$\mathcal{S}_\mathrm{T}$	$\mathcal{S}_\mathrm{C}$	$\mathcal{R}$	$\Delta(\mathcal{F})_{\mathcal{B}}^{\mathcal{S}_\mathrm{T}}$	$\Delta(\mathcal{F})_{\mathcal{B}}^{\mathcal{S}_\mathrm{C}}$	$\Delta(\mathcal{F})_{\mathcal{R}}^{\mathcal{B}}$	$\Delta(\mathcal{F})_{\mathcal{R}}^{\mathcal{S}_\mathrm{T}}$	$\Delta(\mathcal{F})_{\mathcal{R}}^{\mathcal{S}_\mathrm{C}}$
$\overline{\overline{\mathrm{HR}}}$	0.69 / 0.59	0.63 / 0.36	0.60 / 0.24	**0.72 / 0.69**	0.65 / 0.51	0.65 / 0.53	0.57 / 0.24	0.69 / 0.67	**0.71 / 0.67**
$\overline{A}_{12}$	0.63 / 0.52	0.54 / 0.27	0.54 / 0.18	0.65 / 0.58	0.69 / 0.61	**0.70 / 0.60**	0.51 / 0.06	0.66 / 0.58	0.67 / 0.60
$\overline{A}_{13}$	0.63 / 0.37	0.59 / 0.25	0.57 / 0.22	**0.71 / 0.68**	0.55 / 0.34	0.58 / 0.36	**0.71 / 0.69**	**0.77 / 0.83**	**0.74 / 0.82**
$\overline{W}_1$	0.69 / 0.56	0.61 / 0.37	0.59 / 0.30	0.62 / 0.45	0.66 / 0.53	**0.70 / 0.63**	0.59 / 0.20	0.58 / 0.24	0.61 / 0.48
$\overline{T}_1$	0.66 / 0.47	0.59 / 0.29	0.57 / 0.23	0.60 / 0.36	0.65 / 0.53	**0.71 / 0.64**	0.61 / 0.30	0.56 / 0.16	0.61 / 0.42
$\overline{T}_{12}$	0.69 / 0.54	0.62 / 0.35	0.58 / 0.26	0.65 / 0.49	0.63 / 0.52	**0.71 / 0.65**	0.55 / 0.09	0.59 / 0.33	0.66 / 0.62
$\overline{T}_{13}$	0.69 / 0.55	0.62 / 0.34	0.59 / 0.29	0.67 / 0.55	0.66 / 0.58	0.65 / 0.54	0.51 / 0.05	0.62 / 0.49	0.65 / 0.59

Note: In bold are marked the parameters with AUC ≥ 0.7

Table 3: AUC / Cohen's d values of ANS biomarkers derived from the model-based PPG waveform analysis (F_s = 2000 Hz)

$\mathcal{F}$	$\mathcal{B}$	$\mathcal{S}_\mathrm{T}$	$\mathcal{S}_\mathrm{C}$	$\mathcal{R}$	$\Delta(\mathcal{F})_{\mathcal{B}}^{\mathcal{S}_\mathrm{T}}$	$\Delta(\mathcal{F})_{\mathcal{B}}^{\mathcal{S}_\mathrm{C}}$	$\Delta(\mathcal{F})_{\mathcal{R}}^{\mathcal{B}}$	$\Delta(\mathcal{F})_{\mathcal{R}}^{\mathcal{S}_\mathrm{T}}$	$\Delta(\mathcal{F})_{\mathcal{R}}^{\mathcal{S}_\mathrm{C}}$
$\overline{\overline{\mathrm{HR}}}$	0.69 / 0.59	0.63 / 0.36	0.60 / 0.24	**0.72 / 0.69**	0.65 / 0.51	0.65 / 0.53	0.57 / 0.24	0.69 / 0.67	**0.71 / 0.67**
$\overline{A}_{12}$	0.63 / 0.52	0.54 / 0.27	0.54 / 0.18	0.65 / 0.58	0.68 / 0.60	**0.70 / 0.60**	0.51 / 0.07	0.66 / 0.58	0.67 / 0.60
$\overline{A}_{13}$	0.63 / 0.37	0.59 / 0.25	0.57 / 0.22	**0.71 / 0.68**	0.55 / 0.34	0.58 / 0.36	**0.72 / 0.69**	**0.77 / 0.84**	**0.74 / 0.82**
$\overline{W}_1$	0.69 / 0.55	0.61 / 0.37	0.59 / 0.30	0.62 / 0.45	0.65 / 0.50	**0.70 / 0.62**	0.59 / 0.19	0.58 / 0.24	0.61 / 0.49
$\overline{T}_1$	0.66 / 0.47	0.59 / 0.29	0.57 / 0.23	0.60 / 0.36	0.65 / 0.51	**0.71 / 0.63**	0.61 / 0.29	0.56 / 0.16	0.61 / 0.43
$\overline{T}_{12}$	0.69 / 0.54	0.62 / 0.35	0.58 / 0.26	0.65 / 0.49	0.63 / 0.52	**0.70 / 0.63**	0.55 / 0.09	0.60 / 0.33	0.65 / 0.60
$\overline{T}_{13}$	0.69 / 0.54	0.62 / 0.34	0.59 / 0.28	0.67 / 0.55	0.65 / 0.56	0.65 / 0.53	0.50 / 0.07	0.62 / 0.49	0.66 / 0.60

Note: In bold are marked the parameters with AUC ≥ 0.7

The effect of depression on autonomic reactivity in medicated MDD patients

To identify the strength of the effect that the depression level has on the reactivity in medicated MDD patients, two linear models were fitted to observed data. In the first model, $\sqrt{\text{HDRS}}$ is considered to be the explanatory variable, and $\Delta\left(\overline{A}_{13}\right)_{\mathcal{R}}^{\mathcal{S}_C}$ is considered to be the dependent variable. In the second model, whether a subject takes a combination of antidepressants (AD) and benzodiazepines (BZ), which could bias the estimate, is added as a covariate.

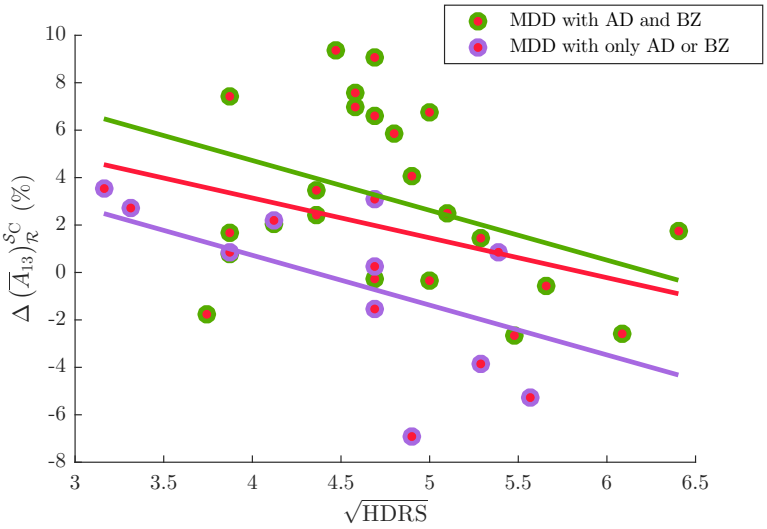

Figure 2: Linear regression analysis to evaluate the effect of depression level ($\sqrt{\text{HDRS}}$) on the reactivity ($\Delta\left(\overline{A}_{13}\right)_{\mathcal{R}}^{\mathcal{S}_C}$) in medicated MDD patients. A red line is fitted to the data of all medicated MDD patients without taking into account the combination of drugs. A green line is fitted to the data of MDD patients treated with AD and BZ, while a purple line is fitted to the data of MDD patients treated with only AD or BZ.

The effect of depression on reactivity without taking into account the combination of drugs in medicated MDD patients (red line in Fig. 2) was not significant. However, adjusting for whether a subject takes a combination of AD and BZ the effect of depression on reactivity (green and purple lines in Fig. 2) was significant. Patients treated with AD and BZ have higher reactivity than those treated with only AD or BZ. Thus, a combination of drugs might improve the emotional reactivity of patients. However, due to the small sample size, no firm statement about causality can be put forward.

Scientific contributions and awards

Scientific contributions

Journal publications

- **Kontaxis, S.**, Gil, E., Marozas, V., Lázaro, J., García, E., Posadas-de Miguel, M., Siddi, S., Bernal, M. L., Aguiló, J., Haro, J. M., de la Camara, C., Laguna, P., and Bailón, R. Photoplethysmographic Waveform Analysis for Autonomic Reactivity Assessment in Depression. *IEEE Trans Biomed Eng*, 2020. DOI: 10.1109/TBME.2020.3025908.

- Varon, C., Morales, J., Lázaro, J., Orini, M., Deviaene, M., **Kontaxis, S.**, Testelmans, D., Buyse, B., Borzée, P., Sörnmo, L., Laguna, P., Gil, E., and Bailón, R. A Comparative Study of ECG-derived Respiration in Ambulatory Monitoring using the Single-lead ECG. *Sci Rep*, 2020, vol. 10, n. 5704, pp.1–14. DOI: 10.1038/s41598-020-62624-5.

- **Kontaxis, S.**, Lázaro, J., Corino, V. D. A., Sandberg, F., Bailón, R., Laguna, P., and Sörnmo, L. ECG-derived Respiratory Rate in Atrial Fibrillation. *IEEE Trans Biomed Eng*, 2019. vol. 67, n. 3, pp.905–914. DOI: 10.1109/TBME.2019.2923587.

- **Kontaxis, S.**, Lázaro, J., Gil, E., Laguna, P., and Bailón, R. Assessment of Quadratic Nonlinear Cardiorespiratory Couplings During Tilt Table Test by Means of Real Wavelet Biphase. *IEEE Trans Biomed Eng*, 2019. vol. 66, n. 1, pp.187–198. DOI: 10.1109/TBME.2018.28211827.

Conference publications derived from the thesis

- **Kontaxis, S.**, Laguna, P., García, E., Posadas-de Miguel, M., Siddi, S., Bernal, M. L., Haro, J. M., Aguiló, J., de la Camara, C., Bailón, R., and Gil, E., Blunted Autonomic Reactivity to Mental Stress in Depression Quantified by Nonlinear Cardiorespiratory Coupling Indices. *2020 Computing in Cardiology Conference (CinC)*, Rimini, Italy, 2020. Accepted for publication.

- **Kontaxis, S.**, Yebra, A. M., Petrėnas, A., Marozas, V., Bailón, R., Laguna, P., and Sörnmo, L. Investigating Respiratory Rate Estimation During Paroxysmal Atrial

Fibrillation Using an Improved ECG Simulation Model. *2020 Computing in Cardiology Conference (CinC)*, Rimini, Italy, 2020. Accepted for publication.

- Martínez, C., **Kontaxis, S.**, Posadas-de Miguel, M., García, E., Siddi, S., Bernal, M. L., Aguiló, J., Haro, J. M., and Bailón, R. Analysis of prosodic features during cognitive load in patients with depression. *11th International Workshop on Spoken Dialog System Technology*, Madrid, Spain, 2020, pp. 1–8. Accepted for publication.
- **Kontaxis, S.**, Bailón, R., Rapalis, A., Brazaitis, M., Cernych, M., Lázaro, J., Laguna, P., Gil, E., and Marozas, V. Autonomic Nervous System Response to Heat Stress Exposure by Means of Heart Rate Variability. *2019 Computing in Cardiology Conference (CinC)*, Singapore, 2019, pp. 1–4. DOI: 10.23919/CinC49843.2019.9005474.
- Armañac, P., **Kontaxis, S.**, Lázaro, J., Laguna, P., Bailón, R., and Gil, E. Cardiovascular Changes Induced by Acute Emotional Stress Estimated from the Pulse Transit Time Difference. *2019 Computing in Cardiology Conference (CinC)*, Singapore, 2019, pp. 1–4. DOI: 10.23919/CinC49843.2019.9005922.
- Rinkevicius, M., **Kontaxis, S.**, Gil, E., Bailón, R., Lázaro, J., Laguna, P., and Marozas, V. Cardiovascular Photoplethysmogram Signal Morphology-Based Stress Assessment. *2019 Computing in Cardiology Conference (CinC)*, Singapore, 2019, pp. 1–4. DOI: 10.23919/CinC49843.2019.9005748.
- Lázaro, J., **Kontaxis, S.**, Bailón, R., Laguna, P., and Gil, E. Respiratory Rate Derived from Pulse Photoplethysmographic Signal by Pulse Decomposition Analysis. *2018 40th Annual International Conference of the IEEE Engineering in Medicine and Biology Society (EMBC)*, Honolulu, HI, 2018, pp. 5282–5285. DOI: 10.23919/CinC49843.2019.9005748.
- **Kontaxis, S.**, Orini, M., Gil, E., Posadas-de Miguel, M., Bernal, M. L., Aguiló, J., de la Camara, C., Laguna, P., and Bailón, R. Heart Rate Variability Analysis Guided by Respiration in Major Depressive Disorder. *2018 Computing in Cardiology Conference (CinC)*, Maastricht, Netherlands, 2018, pp. 1–4. DOI: 10.22489/CinC.2018.319.
- **Kontaxis, S.**, Lázaro, J., Hernando, A., Arza, A., Garzón, J. M., Gil, E., Laguna, P., Aguiló, J., and Bailón, R. Mental Stress Detection Using Cardiorespiratory Wavelet Cross-Bispectrum. *2016 Computing in Cardiology Conference (CinC)*, Vancouver, BC, 2016, pp. 725-728. DOI: 10.22489/CinC.2016.211-454.

Conference publications not related to the thesis

- Milagro, J., Martínez, M., **Kontaxis, S.**, Hernando, D., Gil, E., Bailón, R., Heras, C., and Laguna, P. In Bed Contactless Cardiorespiratory Signals Monitoring Using Optical Fiber Interferometry. *2020 Computing in Cardiology Conference (CinC)*, Rimini, Italy, 2020, pp. 1–4. Accepted for publication.

Patent applications associated with the thesis

- Aguiló, J., Garzón, J. M., Arza, A., Tsapikouni, T., García, E., **Kontaxis, S.**, Laguna, P., Bailón, R., Lázaro, J. *Methods and systems for measuring a stress indicator, and for determining a level of stress in an individual*, Application number: P4175EP00, 2018.

Supervision of master theses related to the thesis

- Armañac, P., Robust Estimation of Pulse Transit Time Difference from Photoplethysmographic Signals. TAF-TFM-2018-1222, University of Zaragoza.

Awards

- *Mortara mobility fellowship.* Heart Rate Variability Analysis Guided by Respiration in Major Depressive Disorder. *XLV International Conference on Computing in Cardiology*, 2018, Maastricht, The Netherlands.

List of acronyms

ABS	Average beat substraction
ACTH	Adrenocorticotropic hormone
ACC	Accuracy
ARs	Adrenoreceptors
AM	Amplitude modulation
ANS	Autonomic nervous system
AV	Atrioventricular
aVNS	Auricular vagus nerve stimulation
BDI	Beck's depression inventory-II
BP	Blood pressure
BRWB	Biphase randomization wavelet bicoherence
CNS	Central nervous system
CRH	Corticotropin-releasing hormone
CWT	Continuous wavelet transform
CVDs	Cardiovascular diseases
DSM-5	Diagnostic and Statistical Manual of Mental Disorders, 5th edition
DRG	Dorsal respiratory group
ECG	Electrocardiogram
ECT	Electroconclusive therapy
EDR	Electrocardiogram-derived respiration
F1	F1-score
FM	Frequency modulation

FR Feature ranking

FT Fourier transform

f-waves atrial fibrillatory waves

GCs Glucocorticoids

GRs Glucocorticoid receptors

HOS Higher order spectra

HPA Hypothalamic-pituitary-adrenal

HR Heart rate

HRV Heart rate variability

ICD-11 International Classification of Diseas, 11th version

LA QRS loop rotation angle

LDA Linear discriminant analysis

LED Light-emitting diode

LASSO Least absolute shrinkage and selection operator

LOSO Leave-one-subject-out

LR Logisitic regression

MAO Monoamine oxidase

MAOIs Monoamine oxidase inhibitors

MDD Major depressive disorder

MRs Minrealcorticoid receptors

NA noradrenaline

NTS Nucleus of the tractus solitarius

OSP Orthogonal subspace projection

PD Photodetector

PDA Pulse decomposition analysis

PNS Parasympathetic nervous system

PPG Photoplethysmogram

PRG Pontine respiratory group

QPC Quadratic phase coupling

QPU Quadratic phase uncoupling

QoL Quality of life

RA R-wave angle

RSA Respiratory sinus arrhythmia

RWB Real wavelet biphase

RVLM Rostral ventrolateral medulla

SA Sinoatrial

SDB Sleep disorder breathing

SLR Stepwise linear regression

SNRIs Serotonin norepinephrine re-uptake inhibitors

SNS Sympathetic nervous system

SPRB Surogate phase randomized bicoherence

SR Slope range

SSRIs Selective serotonin re-uptake inhibitors

SVM Support-vector machine

TCAs Tricyclic antidepressants

TF Time-frequency

TFC Time-frequency coherence

TRD Treatment-resistant depression

TVIPFM Time-varying integral pulse frequency modulation

VCG Vectrocardiogram

VN Vagus nerve

VNS Vagus nerve stimulation

VRG Ventral respiratory group

WB Wavelet bicoherence

WBS Wavelet cross-bispectrum

WHO World Health Organism

List of figures

List of tables

References

[1] Accorsi-Mendonça, D. *et al.* Pacemaking property of RVLM presympathetic neurons. Front Physiol 7:424, 2016.

[2] AL-Khalidi, F. Q. *et al.* Respiration rate monitoring methods: A review. Pediatr Pulmonol 46:523–529, 2011.

[3] Alam, N. *et al.* The impact of the use of the early warning score EWS on patient outcomes: a systematic review. Resuscitation 85:587–594, 2014.

[4] Allen, J. Photoplethysmography and its application in clinical physiological measurement. Physiol Meas 28:R1, 2007.

[5] Anacker, C. *et al.* Early life adversity and the epigenetic programming of hypothalamic-pituitary-adrenal function. Dialogues in clinical neuroscience 16:321, 2014.

[6] Andersen, E. H. *et al.* Aberrant parasympathetic reactivity to acute psychosocial stress in male patients with schizophrenia spectrum disorders. Psychiatry Res 265:39–47, 2018.

[7] Antelmi, I. *et al.* Influence of age, gender, body mass index, and functional capacity on heart rate variability in a cohort of subjects without heart disease. Am J Cardiol 93:381–385, 2004.

[8] Appelhans, B. M. *et al.* Heart rate variability as an index of regulated emotional responding. Rev Gen Psychol 10:229–240, 2006.

[9] Armanac, P. *et al.* Cardiovascular changes induced by acute emotional stress estimated from the pulse transit time difference. In: 2019 Comput Cardiol (CinC), pp. Page–1, IEEE2019.

[10] Armstrong, R. A. and A. C. Hilton. Stepwise multiple regression. Statistical analysis in microbiology: Statnotes pp. 135–138, 2010.

[11] Arza, A. *et al.* Measuring acute stress response through physiological signals: towards a quantitative assessment of stress. Med Biol Eng Comput 57:271–287, 2019.

[12] Association, A. P. *et al.* Diagnostic and statistical manual of mental disorders (DSM-5®), American Psychiatric Pub2013.

[13] Åström, M. *et al.* Vectorcardiographic loop alignment and the measurement of morphologic beat-to-beat variability in noisy signals. IEEE Trans Biomed Eng 47:497–506, 2000.

[14] Atlantis, E. *et al.* Bidirectional associations between clinically relevant depression or anxiety and COPD: a systematic review and meta-analysis. Chest 144:766–777, 2013.

[15] Baekey, D. M. *et al.* Effect of baroreceptor stimulation on the respiratory pattern: Insights into respiratory–sympathetic interactions. Resp Physiol Neurobiol 174:135–145, 2010.

[16] Bailón, R. *et al.* A robust method for ECG-based estimation of the respiratory frequency during stress testing. IEEE Trans Biomed Eng 53:1273–1285, 2006.

[17] Bailón, R. *et al.* Analysis of heart rate variability using time-varying frequency bands based on respiratory frequency. In: 2007 29th Annual International Conference of the IEEE Engineering in Medicine and Biology Society, pp. 6674–6677, IEEE2007.

[18] Bailón, R. *et al.* Analysis of heart rate variability during exercise stress testing using respiratory information. Biomed Signal Process Control 5:299–310, 2010.

[19] Bailón, R. *et al.* The integral pulse frequency modulation model with time-varying threshold: application to heart rate variability analysis during exercise stress testing. IEEE Trans Biomed Eng 58:642–652, 2010.

[20] Baruch, M. C. *et al.* Pulse decomposition analysis of the digital arterial pulse during hemorrhage simulation. Nonlinear Biomed Phys 5:1–15, 2011.

[21] Baumert, M. *et al.* Joint symbolic dynamics for the assessment of cardiovascular and cardiorespiratory interactions. Philos Trans A Math Phys Eng Sci 373:20140097, 2015.

[22] Baumert, M. *et al.* Mean nocturnal respiratory rate predicts cardiovascular and all-cause mortality in community-dwelling older men and women. Eur Respir J 54:1802175, 2019.

[23] Beck, A. T. Cognitive therapy and the emotional disorders, Penguin1979.

[24] Beck, A. T. The evolution of the cognitive model of depression and its neurobiological correlates. Am J Psychiatry 165:969–977, 2008.

[25] Beck, A. T. *et al.* Manual for the beck depression inventory-II. San Antonio , 1996.

[26] Beck, A. T. *et al.* A unified model of depression: Integrating clinical, cognitive, biological, and evolutionary perspectives. Clin Psychol Sci 4:596–619, 2016.

[27] Beda, A. *et al.* Heart-rate and blood-pressure variability during psychophysiological tasks involving speech: Influence of respiration. Psychophysiology 44:767–778, 2007.

[28] Beda, A. *et al.* Low-frequency heart rate variability is related to the breath-to-breath variability in the respiratory pattern. Psychophysiology 51:197–205, 2014.

[29] Belleau, E. L. *et al.* The impact of stress and major depressive disorder on hippocampal and medial prefrontal cortex morphology. Biol Psychiatry 85:443–453, 2019.

[30] Belzung, C. *et al.* Depression: from psychopathology to pathophysiology. Curr Opin Neurobiol 30:24–30, 2015.

[31] Ben-Tal, A. *et al.* Evaluating the physiological significance of respiratory sinus arrhythmia: looking beyond ventilation–perfusion efficiency. J Physiol 590:1989–2008, 2012.

[32] Berger, S. *et al.* Cardio-respiratory coupling in untreated patients with major depression. J Affect Disord 139:166–171, 2012.

[33] Billman, G. E. *et al.* An introduction to heart rate variability: methodological considerations and clinical applications. Front Physiol 6:55, 2015.

[34] Blakeley, P. M. *et al.* Maternal prenatal symptoms of depression and down regulation of placental monoamine oxidase A expression. J Psychosom Res 75:341–345, 2013.

[35] Bockting, C. L. *et al.* A lifetime approach to major depressive disorder: The contributions of psychological interventions in preventing relapse and recurrence. Clin Psychol Rev 41:16–26, 2015.

[36] Bonnin, A. *et al.* A transient placental source of serotonin for the fetal forebrain. Nature 472:347–350, 2011.

[37] Booij, L. *et al.* Genetic and early environmental influences on the serotonin system: consequences for brain development and risk for psychopathology. J Psychiatry Neurosci 40:5, 2015.

[38] Bordoni, B. *et al.* A review of analgesic and emotive breathing: a multidisciplinary approach. J Multidiscip Healthc 9:97, 2016.

[39] Borst, C. *et al.* Mechanisms of initial blood pressure response to postural change. Clin Sci 67:321–327, 1984.

[40] Botros, M. *et al.* The long-lasting neurobiological scars of early-life stress: implications for the neurobiology of depression. In: Neurobiology of Depression, pp. 111–121, Elsevier2019.

[41] Boudreau, P. *et al.* Circadian variation of heart rate variability across sleep stages. Sleep 36:1919–1928, 2013.

[42] Braun, S. R. Respiratory rate and pattern. In: Clinical Methods: The History, Physical, and Laboratory Examinations. 3rd edition, Butterworths1990.

[43] Brody, D. A. A theoretical analysis of intracavitary blood mass influence on the heart-lead relationship. Circ Res 4:731–738, 1956.

[44] Brown, T. A. *et al.* The direct and interactive effects of neuroticism and life stress on the severity and longitudinal course of depressive symptoms. J Abnorm Psychol 120:844, 2011.

[45] Bruce-Low, S. S. *et al.* Heart rate variability during high ambient heat exposure. Aviat Space Environ Med 77:915–920, 2006.

[46] Brugnera, A. *et al.* Heart rate variability during acute psychosocial stress: A randomized cross-over trial of verbal and non-verbal laboratory stressors. Int J Psychophysiol 127:17–25, 2018.

[47] Buch, P. *et al.* Reduced lung function and risk of atrial fibrillation in the copenhagen city heart study. Eur Respir J 21:1012–1016, 2003.

[48] Bylsma, L. M. *et al.* A meta-analysis of emotional reactivity in major depressive disorder. Clin Psychol Rev 28:676–691, 2008.

[49] Camacho, Á. *et al.* Antidepressant use and subclinical measures of atherosclerosis: The multi-ethnic study of atherosclerosis (MESA). J Clin Pharmacol 36:340, 2016.

[50] Cardinali, D. P. Autonomic nervous system: basic and clinical aspects, Springer2017, 1–17 pp.

[51] Cardoso, R. *et al.* Associations between autonomic nervous system function, voice, and dysphonia: A systematic review. J Voice , 2019.

[52] Carnevali, L. *et al.* Autonomic and brain morphological predictors of stress resilience. Front Neurosci 12:228, 2018.

[53] Carroll, D. *et al.* The behavioural, cognitive, and neural corollaries of blunted cardiovascular and cortisol reactions to acute psychological stress. Neurosci Biobehav Rev 77:74–86, 2017.

[54] Caspi, A. *et al.* Influence of life stress on depression: moderation by a polymorphism in the 5-HTT gene. Science 301:386–389, 2003.

[55] Censi, F. *et al.* Coupling patterns between spontaneous rhythms and respiration in cardiovascular variability signals. Comput Methods Programs Biomed 68:37–47, 2002.

[56] Censi, F. *et al.* Nonlinear coupling among heart rate, blood pressure, and respiration in patients susceptible to neuromediated syncope. Ann Biomed Eng 31:1097–1105, 2003.

[57] Chalmers, J. A. *et al.* Anxiety disorders are associated with reduced heart rate variability: a meta-analysis. Front Psychiatry 5:80, 2014.

[58] Charkoudian, N. Mechanisms and modifiers of reflex induced cutaneous vasodilation and vasoconstriction in humans. J Appl Physiol 109:1221–1228, 2010.

[59] Charlton, P. H. *et al.* An assessment of algorithms to estimate respiratory rate from the electrocardiogram and photoplethysmogram. Physiol Meas 37:610, 2016.

[60] Charlton, P. H. *et al.* Assessing mental stress from the photoplethysmogram: a numerical study. Physiol Meas 39:054001, 2018.

[61] Chen, C. *et al.* The exercise-glucocorticoid paradox: How exercise is beneficial to cognition, mood, and the brain while increasing glucocorticoid levels. Front Neuroendocrinol 44:83–102, 2017.

[62] Chida, Y. *et al.* Greater cardiovascular responses to laboratory mental stress are associated with poor subsequent cardiovascular risk status: a meta-analysis of prospective evidence. Hypertension 55:1026–1032, 2010.

[63] Chireh, B. *et al.* Diabetes increases the risk of depression: a systematic review, meta-analysis and estimates of population attributable fractions based on prospective studies. Prev Med Rep p. 100822, 2019.

[64] Chua, C. K. *et al.* Cardiac health diagnosis using higher order spectra and support vector machine. The open medical informatics journal 3:1, 2009.

[65] Chua, K. C. and othres. Application of higher order statistics/spectra in biomedical signals-a review. Med Eng Phys 32:679–689, 2010.

[66] Collett, D. Modelling binary data, CRC press2002.

[67] Colzato, L. S. *et al.* Variable heart rate and a flexible mind: Higher resting-state heart rate variability predicts better task-switching. Cogn Affect Behav Neurosci 18:730–738, 2018.

[68] Compare, A. *et al.* Emotional regulation and depression: A potential mediator between heart and mind. Cardiovasc Psychiatry Neurol 2014, 2014.

[69] Costa-Silva, J. H. *et al.* Glutamatergic antagonism in the NTS decreases post-inspiratory drive and changes phrenic and sympathetic coupling during chemoreflex activation. J Neurophysiol 103:2095–2106, 2010.

[70] Couceiro, R. *et al.* Assessment of cardiovascular function from multi-gaussian fitting of a finger photoplethysmogram. Physiol Meas 36:1801, 2015.

[71] Courtney, R. The functions of breathing and its dysfunctions and their relationship to breathing therapy. Int J Osteopath 12:78–85, 2009.

[72] Crandall, C. and J. Gonzalez-Alonso. Cardiovascular function in the heat-stressed human. Acta Physiol 199:407–423, 2010.

[73] Cretikos, M. A. *et al.* Respiratory rate: the neglected vital sign. Med J Aust 188:657–659, 2008.

[74] Cristianini, N. *et al.* An introduction to support vector machines and other kernel-based learning methods, Cambridge university press2000.

[75] Cummins, N. *et al.* A review of depression and suicide risk assessment using speech analysis. Speech Commun 71:10–49, 2015.

[76] Dagdanpurev, S. *et al.* Development and clinical application of a novel autonomic transient response-based screening system for major depressive disorder using a fingertip photoplethysmographic sensor. Front Bioeng Biotechnol 6:64, 2018.

[77] Dai, H. *et al.* Atrial activity extraction from single lead ECG recordings: Evaluation of two novel methods. Comput Biol Med 43:176–183, 2013.

[78] Daugherty, S. L. *et al.* Incidence and prognosis of resistant hypertension in hypertensive patients. Circulation 125:1635–1642, 2012.

[79] de Rooij, S. R. *et al.* Depression and anxiety: Associations with biological and perceived stress reactivity to a psychological stress protocol in a middle-aged population. Psychoneuroendocrinology 35:866–877, 2010.

[80] Dean, J. *et al.* The neurobiology of depression: An integrated view. Asian J Psychiatr 27:101–111, 2017.

[81] Dekker, J. M. *et al.* Low heart rate variability in a 2-minute rhythm strip predicts risk of coronary heart disease and mortality from several causes: the ARIC study. Circulation 102:1239–1244, 2000.

[82] Dergacheva, O. *et al.* Respiratory modulation of premotor cardiac vagal neurons in the brainstem. Resp Physiol Neurobiol 174:102–110, 2010.

[83] Di Simplicio, M. *et al.* Decreased heart rate variability during emotion regulation in subjects at risk for psychopathology. Psychol Med 42:1775–1783, 2012.

[84] Dick, T. E. *et al.* Cardio-respiratory coupling depends on the pons. Resp Physiol Neurobiol 168:76–85, 2009.

[85] Douglas, N. J. *et al.* Respiration during sleep in normal man. Thorax 37:840–844, 1982.

[86] Dower, G. E. *et al.* On deriving the electrocardiogram from vectorcardiographic leads. Clin Cardiol 3:87–95, 1980.

[87] Dowlati, Y. *et al.* A meta-analysis of cytokines in major depression. Biol Psychiatry 67:446–457, 2010.

[88] Downey, C. *et al.* Strengths and limitations of early warning scores: a systematic review and narrative synthesis. Int J Nurs 76:106–119, 2017.

[89] Dregan, A. *et al.* Associations between depression, arterial stiffness, and metabolic syndrome among adults in the uk biobank population study: a mediation analysis. JAMA Psychiatry 77:598–606, 2020.

[90] Eberhart, N. K. *et al.* Maladaptive schemas and depression: Tests of stress generation and diathesis-stress models. J Soc Clin Psychol 30:75–104, 2011.

[91] Eckberg, D. L. Physiological basis for human autonomic rhythms. Ann Med 32:341–349, 2000.

[92] Egloff, B. *et al.* Spontaneous emotion regulation during evaluated speaking tasks: associations with negative affect, anxiety expression, memory, and physiological responding. Emotion 6:356, 2006.

[93] Elgar, S. *et al.* Statistics of bicoherence and biphase. J Geophys Res Oceans 94:10993–10998, 1989.

[94] Elgendi, M. On the analysis of fingertip photoplethysmogram signals. Curr Cardiol Rev 8:14–25, 2012.

[95] Elstad, M. *et al.* Cardiorespiratory interactions in humans and animals: rhythms for life. Am J Physiol Heart Circ Physiol 315:H6–H17, 2018.

[96] Ernst, G. Heart-rate variability—more than heart beats? Public Health Front 5:240, 2017.

[97] Faes, L. *et al.* Bivariate nonlinear prediction to quantify the strength of complex dynamical interactions in short-term cardiovascular variability. Med Biol Eng Comput 44:383–392, 2006.

[98] Faes, L. *et al.* Information domain approach to the investigation of cardio-vascular, cardio-pulmonary, and vasculo-pulmonary causal couplings. Front Physiol 2:80, 2011.

[99] Faes, L. *et al.* Lag-specific transfer entropy as a tool to assess cardiovascular and cardiorespiratory information transfer. IEEE Trans Biomed Eng 61:2556–2568, 2014.

[100] Faes, L. *et al.* Information decomposition in bivariate systems: theory and application to cardiorespiratory dynamics. Entropy 17:277–303, 2015.

[101] Fang, J. *et al.* Transcutaneous vagus nerve stimulation modulates default mode network in major depressive disorder. Biol Psychiatry 79:266–273, 2016.

[102] Fatouleh, R. *et al.* Cardiorespiratory coupling of sympathetic outflow in humans: a comparison of respiratory and cardiac modulation of sympathetic nerve activity to skin and muscle. Exp Physiol 98:1327–1336, 2013.

[103] Feher, J. J. Quantitative human physiology: an introduction, Academic press2017, 672–685 pp.

[104] Fink, G. Stress: Concepts, cognition, emotion, and behavior: Handbook of stress series, volume 1, Academic Press2016, 103–107 pp.

[105] Firth, J. *et al.* The Lancet Psychiatry Commission: a blueprint for protecting physical health in people with mental illness. Lancet Psychiatry 6:675–712, 2019.

[106] Friedman, E. S. *et al.* Handbook of depression, Springer2014, 5 pp.

[107] Galts, C. P. *et al.* Depression in neurodegenerative diseases: common mechanisms and current treatment options. Neurosci Biobehav Rev , 2019.

[108] Gao, Y.-h. *et al.* The relationship between depression and asthma: a meta-analysis of prospective studies. PLoS One 10, 2015.

[109] Garcia III, A. J. *et al.* Cardiorespiratory coupling in health and disease. Auton Neurosci 175:26–37, 2013.

[110] Garcia-Retortillo, S. *et al.* Cardiorespiratory coordination in repeated maximal exercise. Front Physiol 8:387, 2017.

[111] Garg, P. K. *et al.* Negative affect and risk of atrial fibrillation: MESA. J Am Heart Assoc 8:e010603, 2019.

[112] Gaspersz, R. *et al.* Patients with anxious depression: overview of prevalence, pathophysiology and impact on course and treatment outcome. Curr Opin Psychiatry 31:17–25, 2018.

[113] Ghosh, R. K. *et al.* Depression in heart failure: Intricate relationship, pathophysiology and most updated evidence of interventions from recent clinical studies. Int J Cardiol 224:170–177, 2016.

[114] Giannakakis, G. *et al.* Review on psychological stress detection using biosignals. IEEE Trans Affective Comput , 2019.

[115] Giardino, N. D. *et al.* Respiratory sinus arrhythmia is associated with efficiency of pulmonary gas exchange in healthy humans. Am J Physiol Heart Circ Physiol 284:H1585–H1591, 2003.

[116] Gil, E. *et al.* Photoplethysmography pulse rate variability as a surrogate measurement of heart rate variability during non-stationary conditions. Physiol Meas 31:1271, 2010.

[117] Ginty, A. T. *et al.* Disordered eating behaviour is associated with blunted cortisol and cardiovascular reactions to acute psychological stress. Psychoneuroendocrinology 37:715–724, 2012.

[118] Glaser, R. *et al.* Stress-induced immune dysfunction: implications for health. Nat Rev Immunol 5:243–251, 2005.

[119] Glover, V. Annual research review: prenatal stress and the origins of psychopathology: an evolutionary perspective. J Child Psychol Psychiatry 52:356–367, 2011.

[120] Glover, V. *et al.* Prenatal maternal stress, fetal programming, and mechanisms underlying later psychopathology—a global perspective. Dev Psychopathol 30:843–854, 2018.

[121] Goren, Y. *et al.* Individual time-dependent spectral boundaries for improved accuracy in time-frequency analysis of heart rate variability. IEEE Trans Biomed Eng 53:35–42, 2005.

[122] Goswami, D. *et al.* A new two-pulse synthesis model for digital volume pulse signal analysis. Cardiovasc Eng 10:109–117, 2010.

[123] Gotlib, I. H. *et al.* Cognition and depression: current status and future directions. Annu Rev Clin Psychol 6:285–312, 2010.

[124] Gottsäter, M. *et al.* Non-hemodynamic predictors of arterial stiffness after 17 years of follow-up: the malmö diet and cancer study. J Hypertens 33:957, 2015.

[125] Goudis, C. A. *et al.* Obstructive sleep and atrial fibrillation: Pathophysiological mechanisms and therapeutic implications. Int J Cardiol 230:293–300, 2017.

[126] Grossman, P. *et al.* Toward understanding respiratory sinus arrhythmia: Relations to cardiac vagal tone, evolution and biobehavioral functions. Biol Psychol 74:263–285, 2007.

[127] Guyenet, P. G. Regulation of breathing and autonomic outflows by chemoreceptors. Compr Physiol 4:1511–1562, 2011.

[128] Hadjileontiadis, L. J. EEG-based tonic cold pain characterization using wavelet higher order spectral features. IEEE Trans Biomed Eng 62:1981–1991, 2015.

[129] Hadjileontiadis, L. J. Continuous wavelet transform and higher-order spectrum: combinatory potentialities in breath sound analysis and electroencephalogram-based pain characterization. Philos Trans A Math Phys Eng Sci 376:20170249, 2018.

[130] Hagihira, S. *et al.* Practical issues in bispectral analysis of electroencephalographic signals. Anesth Analg 93:966–970, 2001.

[131] Hainsworth, R. Physiology of the cardiac autonomic system. In: Clinical guide to cardiac autonomic tests, pp. 256–281, Springer1998.

[132] Halaris, A. Inflammation-associated co-morbidity between depression and cardiovascular disease. In: Inflammation-Associated Depression: Evidence, Mechanisms and Implications, pp. 45–70, Springer2016.

[133] Hall, J. E. Guyton and Hall Textbook of Medical Physiology, Jordanian Edition E-Book, Elsevier2016, 751–786 pp.

[134] Hamer, M. and L. Malan. Psychophysiological risk markers of cardiovascular disease. Neurosci Biobehav Rev 35:76–83, 2010.

[135] Hamilton, J. L. *et al.* Atypical reactivity of heart rate variability to stress and depression across development: Systematic review of the literature and directions for future research. Clin Psychol Rev 50:67–79, 2016.

[136] Hamilton, M. A rating scale for depression. J Neurol Neurosurg Psychiatry 23:56, 1960.

[137] Hammen, C. Generation of stress in the course of unipolar depression. J Abnorm Psychol 100:555, 1991.

[138] Hammen, C. Stress and depression. Annu Rev Clin Psychol 1:293–319, 2005.

[139] Hammen, C. *et al.* Chronic and acute stress and the prediction of major depression in women. Depress Anxiety 26:718–723, 2009.

[140] Hannuksela, M. L. and S. Ellahham. Benefits and risks of sauna bathing. Am J Med 110:118–126, 2001.

[141] Harkness, K. L. *et al.* The role of childhood abuse and neglect in the sensitization to stressful life events in adolescent depression. J Abnorm Psychol 115:730, 2006.

[142] Haroon, E. *et al.* Psychoneuroimmunology meets neuropsychopharmacology: translational implications of the impact of inflammation on behavior. Neuropsychopharmacol 37:137–162, 2012.

[143] Hayashi, K. *et al.* Anesthesia depth–dependent features of electroencephalographic bicoherence spectrum during sevoflurane anesthesia. Anesthesiology 108:841–850, 2008.

[144] Hayashi, K. *et al.* Simultaneous bicoherence analysis of occipital and frontal electroencephalograms in awake and anesthetized subjects. Clin Neurophysiol 125:194–201, 2014.

[145] Hernando, A. *et al.* Inclusion of respiratory frequency information in heart rate variability analysis for stress assessment. IEEE J Biomed Health Inform 20:1016–1025, 2016.

[146] Hill, B. *et al.* Monitoring respiratory rate in adults. Br J Nurs 29:12–16, 2020.

[147] Holsen, L. M. *et al.* Brain hypoactivation, autonomic nervous system dysregulation, and gonadal hormones in depression: a preliminary study. Neurosci Lett 514:57–61, 2012.

[148] Hölzel, B. K. *et al.* How does mindfulness meditation work? proposing mechanisms of action from a conceptual and neural perspective. Perspect Psychol Sci 6:537–559, 2011.

[149] Hoyer, D. *et al.* Determinism in bivariate cardiorespiratory phase-space sets. IEEE Eng Med Biol Mag 17:26–31, 1998.

[150] Hoyer, D. *et al.* Mutual information and phase dependencies: measures of reduced nonlinear cardiorespiratory interactions after myocardial infarction. Med Eng Phys 24:33–43, 2002.

[151] Hu, M. X. *et al.* Differential autonomic nervous system reactivity in depression and anxiety during stress depending on type of stressor. Psychosom Med 78:562–572, 2016.

[152] Huotari, M. *et al.* Photoplethysmography and its detailed pulse waveform analysis for arterial stiffness. J Struct Mech 44:345–362, 2011.

[153] Hussain, J. and M. Cohen. Clinical effects of regular dry sauna bathing: a systematic review. Evid Based Complement Alternat Med 2018, 2018.

[154] Iatsenko, D. *et al.* Evolution of cardiorespiratory interactions with age. Phil Trans R Soc A 371:20110622, 2013.

[155] Infurna, M. R. *et al.* Associations between depression and specific childhood experiences of abuse and neglect: A meta-analysis. J Affect Disord 190:47–55, 2016.

[156] Ingram, R. E. and D. D. Luxton. Vulnerability-stress models. Dev Psychopathol: A vulnerability-stress perspective 46, 2005.

[157] Irwin, M. R. *et al.* Reciprocal regulation of the neural and innate immune systems. Nat Rev Immunol 11:625–632, 2011.

[158] Ivanov, P. C. *et al.* Multifractality in human heartbeat dynamics. Nature 399:461–465, 1999.

[159] James, S. L. *et al.* Global, regional, and national incidence, prevalence, and years lived with disability for 354 diseases and injuries for 195 countries and territories, 1990–2017: a systematic analysis for the global burden of disease study 2017. Lancet 392:1789–1858, 2018.

[160] Jamšek, J. *et al.* Nonlinear cardio-respiratory interactions revealed by time-phase bispectral analysis. Phys Med Biol 49:4407, 2004.

[161] Jamšek, J. *et al.* Wavelet bispectral analysis for the study of interactions among oscillators whose basic frequencies are significantly time variable. Phys Rev E 76:046221, 2007.

[162] Jamšek, J. *et al.* Detecting couplings between interacting oscillators with time-varying basic frequencies: Instantaneous wavelet bispectrum and information theoretic approach. Phys Rev E 81:036207, 2010.

[163] Jänig, W. Integrative action of the autonomic nervous system: Neurobiology of homeostasis, Cambridge University Press2008, 1–34 pp.

[164] Jeon, S. W. *et al.* Neuroinflammation and cytokine abnormality in major depression: cause or consequence in that illness? World J Psychiatr 6:283, 2016.

[165] Jha, M. K. *et al.* Screening and management of depression in patients with cardiovascular disease: JACC state-of-the-art review. J Am Coll Cardiol 73:1827–1845, 2019.

[166] Jia, Y. *et al.* Depression and cancer risk: a systematic review and meta-analysis. Public Health 149:138–148, 2017.

[167] Johnson, J. N. *et al.* Prevalence of early-onset atrial fibrillation in congenital long QT syndrome. Heart Rhythm 5:704–709, 2008.

[168] Johnson, R. L. *et al.* A review of vagus nerve stimulation as a therapeutic intervention. J Inflamm Res 11:203, 2018.

[169] Joormann, J. Cognitive inhibition and emotion regulation in depression. Curr Dir Psychol Sci 19:161–166, 2010.

[170] Joormann, J. *et al.* Emotion regulation in depression: Relation to cognitive inhibition. Cogn Emot 24:281–298, 2010.

[171] Joormann, J. *et al.* Examining emotion regulation in depression: A review and future directions. Behav Res Ther 86:35–49, 2016.

[172] Kabir, M. M. *et al.* Cardiorespiratory phase-coupling is reduced in patients with obstructive sleep apnea. PLoS One 5:e10602, 2010.

[173] Kaess, B. M. *et al.* Aortic stiffness, blood pressure progression, and incident hypertension. Jama 308:875–881, 2012.

[174] Kandola, A. *et al.* Depressive symptoms and objectively measured physical activity and sedentary behaviour throughout adolescence: a prospective cohort study. Lancet Psychiatry 7:262–271, 2020.

[175] Kaniusas, E. *et al.* Current directions in the auricular vagus nerve stimulation I-a physiological perspective. Front Neurosci 13:854, 2019.

[176] Kaniusas, E. *et al.* Current directions in the auricular vagus nerve stimulation II-an engineering perspective. Front Neurosci 13:772, 2019.

[177] Karg, K. *et al.* Gene× environment interaction models in psychiatric genetics. In: Behav Neurogenetics, pp. 441–462, Springer2011.

[178] Kelava, A. *et al.* A new approach for the quantification of synchrony of multivariate non-stationary psychophysiological variables during emotion eliciting stimuli. Front Psychol 5:1507, 2015.

[179] Kendler, K. S. *et al.* Causal relationship between stressful life events and the onset of major depression. Am J Psychiatry 156:837–841, 1999.

[180] Kendler, K. S. *et al.* The impact of environmental experiences on symptoms of anxiety and depression across the life span. Psychol Sci 22:1343–1352, 2011.

[181] Khandoker, A. H. *et al.* Comparison of pulse rate variability with heart rate variability during obstructive sleep apnea. Med Eng Phys 33:204–209, 2011.

[182] Khandoker, A. H. *et al.* Suicidal ideation is associated with altered variability of fingertip photo-plethysmogram signal in depressed patients. Front Physiol 8:501, 2017.

[183] Kiecolt-Glaser, J. K. *et al.* Inflammation: depression fans the flames and feasts on the heat. Am J Psychiatry 172:1075–1091, 2015.

[184] Kim, E. J. *et al.* Relationship between blood pressure parameters and pulse wave velocity in normotensive and hypertensive subjects: invasive study. J Hum Hypertens 21:141–148, 2007.

[185] Kim, T. *et al.* A novel QPC detector for the health monitoring of rotating machines. In: 2007 IEEE Instrumentation & Measurement Technology Conference IMTC 2007, pp. 1–6, IEEE2007.

[186] Kinsella, M. T. *et al.* Impact of maternal stress, depression & anxiety on fetal neurobehavioral development. Clin Obstet Gynecol 52:425, 2009.

[187] Kjeldsen, S. E. Hypertension and cardiovascular risk: General aspects. Pharmacol Res 129:95–99, 2018.

[188] Kokras, N. *et al.* The effect of treatment response on endothelial function and arterial stiffness in depression. a prospective study. J Affect Disord 252:190–200, 2019.

[189] Kontaxis, S. *et al.* Investigating respiratory rate estimation during paroxysmal atrial fibrillation using an improved ECG simulation model. In: 2020 Comput Cardiol, pp. 1–4, IEEE2020.

[190] Kors, J. *et al.* Reconstruction of the frank vectorcardiogram from standard electrocardiographic leads: diagnostic comparison of different methods. Eur Heart J 11:1083–1092, 1990.

[191] Kuehner, C. Why is depression more common among women than among men? Lancet Psychiatry 4:146–158, 2017.

[192] Kupfer, D. J. Lessons to be learned from long-term treatment of affective disorders: Potential utility in panic disorder. J Clin Psychiatry , 1991.

[193] Laborde, S. *et al.* Heart rate variability and cardiac vagal tone in psychophysiological research–recommendations for experiment planning, data analysis, and data reporting. Front Psychol 8:213, 2017.

[194] Laborde, S. *et al.* Vagal tank theory: the three rs of cardiac vagal control functioning–resting, reactivity, and recovery. Front Neurosci 12:458, 2018.

[195] Lackner, H. K. *et al.* Phase synchronization of hemodynamic variables and respiration during mental challenge. Int J Psychophysiol 79:401–409, 2011.

[196] Laguna, P. *et al.* Power spectral density of unevenly sampled data by least-square analysis: performance and application to heart rate signals. IEEE Trans Biomed Eng 45:698–715, 1998.

[197] Lamb, L. E. The effects of respiration on the electrocardiogram in relation to differences in right and left ventricular stroke volume: A clinical observation. Am Heart J 54:342–351, 1957.

[198] Larsen, P. *et al.* Respiratory sinus arrhythmia in conscious humans during spontaneous respiration. Respir Physiol Neurobiol 174:111–118, 2010.

[199] Larsen, V. H. *et al.* Impedance pneumography for long-term monitoring of respiration during sleep in adult males. Clin Physiol 4:333–342, 1984.

[200] Lázaro, J. *et al.* Deriving respiration from photoplethysmographic pulse width. Med Biol Eng Comput 51:233–242, 2013.

[201] Lázaro, J. *et al.* Pulse rate variability analysis for discrimination of sleep-apnea-related decreases in the amplitude fluctuations of pulse photoplethysmographic signal in children. IEEE J Biomed Health Inform 18:240–246, 2013.

[202] Lázaro, J. *et al.* Electrocardiogram derived respiratory rate from QRS slopes and R-wave angle. Ann Biomed Eng 42:2072–2083, 2014.

[203] Lázaro, J. *et al.* Baroreflex sensitivity measured by pulse photoplethysmography. Front Neurosci 13:339, 2019.

[204] Levesque, M. L. *et al.* Epigenetic mechanisms in depression. In: Systems Neuroscience in Depression, pp. 181–207, Elsevier2016.

[205] Lewis, M. *et al.* Autonomic nervous system control of the cardiovascular and respiratory systems in asthma. Respir Med 100:1688–1705, 2006.

[206] Li, Y. *et al.* Biphase randomization wavelet bicoherence for mechanical fault diagnosis. Measurement 49:407–420, 2014.

[207] Limmer, J. *et al.* Panic and comorbid depression and their associations with stress reactivity, interoceptive awareness and interoceptive accuracy of various bioparameters. J Affect Disord 185:170–179, 2015.

[208] Lin, T.-W. *et al.* Exercise benefits brain function: the monoamine connection. Brain Sci 3:39–53, 2013.

[209] Lippi, G. *et al.* Global epidemiology of atrial fibrillation: An increasing epidemic and public health challenge. Int J Stroke pp. 1–5, 2020.

[210] Liu, H. and H. Motoda. Feature extraction, construction and selection: A data mining perspective, volume 453, Springer Science & Business Media1998.

[211] Liu, R. T. *et al.* Stress generation in depression: A systematic review of the empirical literature and recommendations for future study. Clin Psychol Rev 30:582–593, 2010.

[212] Luppino, F. S. *et al.* Overweight, obesity, and depression: a systematic review and meta-analysis of longitudinal studies. Arch Gen psychiatry 67:220–229, 2010.

[213] Madsen, I. E. *et al.* Job strain as a risk factor for clinical depression: systematic review and meta-analysis with additional individual participant data. Psychol Med 47:1342–1356, 2017.

[214] Maheshwari, A. *et al.* Low heart rate variability in a 2-minute electrocardiogram recording is associated with an increased risk of sudden cardiac death in the general population: the atherosclerosis risk in communities study. PloS One 11, 2016.

[215] Malhi, G. S. and J. J. Mann. Seminar depression. Lancet 392:2299–2312, 2018.

[216] Martínez, J. P. *et al.* A wavelet-based ECG delineator: evaluation on standard databases. IEEE Trans Biomed Eng 51:570–581, 2004.

[217] Massaroni, C. *et al.* Contact-based methods for measuring respiratory rate. Sensors 19:908, 2019.

[218] Mateo, J. and P. Laguna. Analysis of heart rate variability in the presence of ectopic beats using the heart timing signal. IEEE Trans Biomed Eng 50:334–343, 2003.

[219] Maydych, V. The interplay between stress, inflammation, and emotional attention: relevance for depression. Front Neurosci 13, 2019.

[220] McEwen, B. S. *et al.* Central role of the brain in stress and adaptation: links to socioeconomic status, health, and disease. Ann N Y Acad Sci 1186:190, 2010.

[221] McLachlan, G. J. Discriminant analysis and statistical pattern recognition, volume 544, John Wiley & Sons2004.

[222] McLaughlin, K. A. *et al.* Childhood adversity, adult stressful life events, and risk of past-year psychiatric disorder: a test of the stress sensitization hypothesis in a population-based sample of adults. Psychol Med 40:1647–1658, 2010.

[223] McMorris, T. History of research into the acute exercise–cognition interaction: A cognitive psychology approach, Elsevier Academic Press2016, 1–28 pp.

[224] Melanson, E. L. Resting heart rate variability in men varying in habitual physical activity. Med Sci Sports Exerc 32:1894–1901, 2000.

[225] Mendelowitz, D. Advances in parasympathetic control of heart rate and cardiac function. Physiology 14:155–161, 1999.

[226] Meo, M. *et al.* Spatial variability of the 12-lead surface ECG as a tool for noninvasive prediction of catheter ablation outcome in persistent atrial fibrillation. IEEE Trans Biomed Eng 60:20–27, 2012.

[227] Meredith, D. J. *et al.* Photoplethysmographic derivation of respiratory rate: a review of relevant physiology. J Med Eng Technol 36:1–7, 2012.

[228] Merri, M. *et al.* Sampling frequency of the electrocardiogram for spectral analysis of the heart rate variability. IEEE Trans Biomed Eng 37:99–106, 1990.

[229] Michael-Titus, A. *et al.* The nervous system: basic science and clinical conditions, Edinburgh: Churchill Livingstone2010, 1–30 pp.

[230] Milagro, J. *et al.* Electrocardiogram-derived tidal volume during treadmill stress test. IEEE Trans Biomed Eng 67:193–202, 2019.

[231] Mitchell, G. F. Arterial stiffness and hypertension. Hypertension 64:13–18, 2014.

[232] Mitchell, G. F. *et al.* Arterial stiffness, pressure and flow pulsatility and brain structure and function: the age, gene/environment susceptibility–reykjavik study. Brain 134:3398–3407, 2011.

[233] Monahan, K. *et al.* Triggering of nocturnal arrhythmias by sleep-disordered breathing events. J Am Coll Cardiol 54:1797–1804, 2009.

[234] Monroe, S. M. and L. F. Cummins. Diathesis-stress models. The encyclopedia of clinical psychology pp. 1–6, 2014.

[235] Monroe, S. M. *et al.* Diathesis-stress theories in the context of life stress research: implications for the depressive disorders. Psychol Bull 110:406, 1991.

[236] Montano, N. *et al.* Presence of vasomotor and respiratory rhythms in the discharge of single medullary neurons involved in the regulation of cardiovascular system. J Auton Nerv Syst 57:116–122, 1996.

[237] Moody, G. B. *et al.* Derivation of respiratory signals from multi-lead ECGs. Comput Cardiol 12:113–116, 1985.

[238] Mookiah, M. R. K. *et al.* Data mining technique for automated diagnosis of glaucoma using higher order spectra and wavelet energy features. Knowl Based Syst 33:73–82, 2012.

[239] Morrison, S. F. Central control of body temperature. F1000Research 5, 2016.

[240] Müller, H. H. *et al.* Vagus nerve stimulation (VNS) and other augmentation strategies for therapy-resistant depression (TRD): review of the evidence and clinical advice for use. Front Neurosci 12:239, 2018.

[241] Murison, R. The neurobiology of stress. In: Neuroscience of Pain, Stress, and Emotion, pp. 29–49, Elsevier2016.

[242] Myint, A.-M. *et al.* Network beyond IDO in psychiatric disorders: revisiting neurodegeneration hypothesis. Prog Neuropsychopharmacol Biol Psychiatry 48:304–313, 2014.

[243] Ng, C. Y. *et al.* Meta-analysis of obstructive sleep apnea as predictor of atrial fibrillation recurrence after catheter ablation. Am J Cardiol 108:47–51, 2011.

[244] Organization, W. H. *et al.* Depression and other common mental disorders: global health estimates. Technical report, World Health Organization, 2017.

[245] Orini, M. *et al.* Characterization of dynamic interactions between cardiovascular signals by time-frequency coherence. IEEE Trans Biomed Eng 59:663–673, 2011.

[246] Orini, M. *et al.* Assessment of the dynamic interactions between heart rate and arterial pressure by the cross time–frequency analysis. Physiol Meas 33:315, 2012.

[247] Orini, M. *et al.* A multivariate time-frequency method to characterize the influence of respiration over heart period and arterial pressure. EURASIP J Adv Signal Process 2012:214, 2012.

[248] Orini, M. *et al.* Synthesis of HRV signals characterized by predetermined time-frequency structure by means of time-varying ARMA models. Biomed Signal Process Control 7:141–150, 2012.

[249] Orphanidou, C. Derivation of respiration rate from ambulatory ECG and PPG using ensemble empirical mode decomposition: Comparison and fusion. Comput Biol Med 81:45–54, 2017.

[250] Osório, C. *et al.* Adapting to stress: understanding the neurobiology of resilience. Behav Med 43:307–322, 2017.

[251] Ott, C. V. *et al.* Structural changes in the hippocampus as a biomarker for cognitive improvements in neuropsychiatric disorders: A systematic review. Eur Neuropsychopharmacol 29:319–329, 2019.

[252] Otte, C. *et al.* Major depressive disorder. Nature reviews Disease primers 2:1–20, 2016.

[253] Oulis, P. *et al.* Reversal of increased arterial stiffness in severely depressed women after 6-week antidepressant treatment. J Affect Disord 122:164–166, 2010.

[254] Paluš, M. and A. Stefanovska. Direction of coupling from phases of interacting oscillators: An information-theoretic approach. Phys Rev E 67:055201, 2003.

[255] Pan, A. *et al.* Bidirectional association between depression and metabolic syndrome: a systematic review and meta-analysis of epidemiological studies. Diabetes Care 35:1171–1180, 2012.

[256] Pascoe, M. C. *et al.* A systematic review of randomised control trials on the effects of yoga on stress measures and mood. J Psychiatr Res 68:270–282, 2015.

[257] Patvardhan, E. A. *et al.* Assessment of vascular endothelial function with peripheral arterial tonometry: information at your fingertips? Cardiol Rev 18:20–28, 2010.

[258] Pavlov, V. A. *et al.* The vagus nerve and the inflammatory reflex—linking immunity and metabolism. Nat Rev Endocrinol 8:743, 2012.

[259] Penninx, B. W. Depression and cardiovascular disease: epidemiological evidence on their linking mechanisms. Neurosci Biobehav Rev 74:277–286, 2017.

[260] Petrėnas, A. *et al.* An echo state neural network for QRST cancellation during atrial fibrillation. IEEE Trans Biomed Eng 59:2950–2957, 2012.

[261] Petrėnas, A. *et al.* Electrocardiogram modeling during paroxysmal atrial fibrillation: application to the detection of brief episodes. Physiol Meas 38:2058, 2017.

[262] Peupelmann, J. *et al.* Cardio-respiratory coupling indicates suppression of vagal activity in acute schizophrenia. Schizophr Res 112:153–157, 2009.

[263] Pichot, V. *et al.* ECG-derived respiration: A promising tool for sleep-disordered breathing diagnosis in chronic heart failure patients. Int J Cardiol 186:7, 2015.

[264] Pinhas, I. *et al.* Bicoherence analysis of new cardiovascular spectral components observed in heart-transplant patients: statistical approach for bicoherence thresholding. IEEE Trans Biomed Eng 51:1774–1783, 2004.

[265] Pongratz, G. *et al.* The sympathetic nervous response in inflammation. Arthritis Res Ther 16:504, 2014.

[266] Porta, A. *et al.* Conditional self-entropy and conditional joint transfer entropy in heart period variability during graded postural challenge. PLoS One 10:e0132851, 2015.

[267] Post, R. M. Transduction of psychosocial stress into the neurobiology of recurrent affective disorder. Am J Psychiatry , 1992.

[268] Post, R. M. Epigenetic basis of sensitization to stress, affective episodes, and stimulants: implications for illness progression and prevention. Bipolar Disord 18:315–324, 2016.

[269] Quintana, D. S. *et al.* Considerations in the assessment of heart rate variability in biobehavioral research. Front Psychol 5:805, 2014.

[270] Rabe, K. F. *et al.* Global strategy for the diagnosis, management, and prevention of chronic obstructive pulmonary disease: GOLD executive summary. Am J Respir Crit Care Med 176:532–555, 2007.

[271] Raj, S. *et al.* Development of robust, fast and efficient QRS complex detector: a methodological review. Australas Phys Eng Sci Med 41:581–600, 2018.

[272] Rakel, D. Integrative medicine-E-book, Elsevier health sciences2017, 36–45 pp.

[273] Richards, D. Prevalence and clinical course of depression: a review. Clin Psychol Rev 31:1117–1125, 2011.

[274] Rinkevičius, M. *et al.* Photoplethysmogram signal morphology-based stress assessment. In: 2019 Computing in Cardiology (CinC), pp. Page–1, IEEE2019.

[275] Ritz, T. *et al.* Modulation of respiratory sinus arrhythmia by respiration rate and volume: Stability across posture and volume variations. Psychophysiology 38:858–862, 2001.

[276] Rolfe, S. The importance of respiratory rate monitoring. Br J Nurs 28:504–508, 2019.

[277] Rosenblum, M. G. *et al.* Identification of coupling direction: application to cardiorespiratory interaction. Phys Rev E 65:041909, 2002.

[278] Rudy, Y. *et al.* The effects of variations in conductivity and geometrical parameters on the electrocardiogram, using an eccentric spheres model. Circ Res 44:104–111, 1979.

[279] Russell, G. *et al.* The human stress response. Nat Rev Endocrinol 15:525–534, 2019.

[280] Rybakowski, J. K. *et al.* Impairment of endothelial function in unipolar and bipolar depression. Biol Psychiatry 60:889–891, 2006.

[281] Salomon, K. *et al.* Major depressive disorder is associated with attenuated cardiovascular reactivity and impaired recovery among those free of cardiovascular disease. Health Psychol 28:157, 2009.

[282] Sameni, R. *et al.* Multichannel ECG and noise modeling: Application to maternal and fetal ECG signals. EURASIP J Adv Sig Pr 2007:043407, 2007.

[283] Santamore, W. P. *et al.* Ventricular interdependence: significant left ventricular contributions to right ventricular systolic function. Prog Cardiovasc Dis 40:289–308, 1998.

[284] Sapolsky, R. M. *et al.* How do glucocorticoids influence stress responses? Integrating permissive, suppressive, stimulatory, and preparative actions. Endocr Rev 21:55–89, 2000.

[285] Sarchiapone, M. *et al.* The association between electrodermal activity (EDA), depression and suicidal behaviour: A systematic review and narrative synthesis. BMC Psychiatry 18:22, 2018.

[286] Saul, J. P. *et al.* Transfer function analysis of autonomic regulation. II. respiratory sinus arrhythmia. Am J Physiol Heart Circ Physiol 256:H153–H161, 1989.

[287] Scarpina, F. and S. Tagini. The stroop color and word test. Front Psychol 8:557, 2017.

[288] Schäfer, C. *et al.* Heartbeat synchronized with ventilation. Nature 392:239–240, 1998.

[289] Scher, C. D. *et al.* Cognitive reactivity and vulnerability: Empirical evaluation of construct activation and cognitive diatheses in unipolar depression. Clin Psychol Rev 25:487–510, 2005.

[290] Schiweck, C. *et al.* Heart rate and high frequency heart rate variability during stress as biomarker for clinical depression. a systematic review. Psychol Med 49:200–211, 2019.

[291] Schmidt, H. D. *et al.* Functional biomarkers of depression: diagnosis, treatment, and pathophysiology. Neuropsychopharmacol 36:2375–2394, 2011.

[292] Scholkmann, F. and U. Wolf. The pulse-respiration quotient: A powerful but untapped parameter for modern studies about human physiology and pathophysiology. Front Physiol 10:371, 2019.

[293] Schulz, S. *et al.* Cardiovascular and cardiorespiratory coupling analyses: a review. Philos Trans A Math Phys Eng Sci 371:20120191, 2013.

[294] Sclocco, R. *et al.* The influence of respiration on brainstem and cardiovagal response to auricular vagus nerve stimulation: a multimodal ultrahigh-field (7T) fMRI study. Brain Stimul 12:911–921, 2019.

[295] Scully, C. G. *et al.* Detecting interactions between the renal autoregulation mechanisms in time and space. IEEE Trans Biomed Eng 64:690–698, 2017.

[296] Seldenrijk, A. *et al.* Depression, anxiety, and arterial stiffness. Biol Psychiatry 69:795–803, 2011.

[297] Shaffer, F. *et al.* An overview of heart rate variability metrics and norms. Public Health Front 5:258, 2017.

[298] Shah, V. *et al.* The association between chronic obstructive pulmonary disease (COPD) and atrial fibrillation: A review. Chron Obstruct Pulmon Dis 1:2, 2016.

[299] Silverthorn, D. U. *et al.* Human physiology: an integrated approach, Pearson/Benjamin Cummings San Francisco2010, 605–606 pp.

[300] Slavich, G. M. *et al.* From stress to inflammation and major depressive disorder: a social signal transduction theory of depression. Psychol Bull 140:774, 2014.

[301] Smeets, T. Autonomic and hypothalamic–pituitary–adrenal stress resilience: Impact of cardiac vagal tone. Biol Psychol 84:290–295, 2010.

[302] Sörnmo, L. Vectorcardiographic loop alignment and morphologic beat-to-beat variability. IEEE Trans Biomed Eng 45:1401–1413, 1998.

[303] Sörnmo, L. Databases and simulation. In: Atrial fibrillation from an engineering perspective, pp. 49–72, Springer2018.

[304] Sörnmo, L. Extraction of f waves. In: Atrial fibrillation from an engineering perspective, pp. 137–220, Springer2018.

[305] Sörnmo, L. and P. Laguna. Bioelectrical signal processing in cardiac and neurological applications, volume 8, Academic Press2005, 411–627 pp.

[306] Stange, J. P. *et al.* Flexible parasympathetic responses to sadness facilitate spontaneous affect regulation. Psychophysiol 54:1054–1069, 2017.

[307] Stein, P. K. *et al.* Heart rate variability, sleep and sleep disorders. Sleep Med Rev 16:47–66, 2012.

[308] Steingrub, J. S. *et al.* Hemodynamic consequences of heart-lung interactions. J Intensive Care Med 18:92–99, 2003.

[309] Sternberg, E. M. Neural regulation of innate immunity: a coordinated nonspecific host response to pathogens. Nat Rev Immunol 6:318–328, 2006.

[310] Stevenson, I. H. *et al.* Prevalence of sleep disordered breathing in paroxysmal and persistent atrial fibrillation patients with normal left ventricular function. Eur Heart J 29:1662–1669, 2008.

[311] Strauss-Blasche, G. *et al.* Relative timing of inspiration and expiration affects respiratory sinus arrhythmia. Clin Exp Pharmacol Physiol 27:601–606, 2000.

[312] Strawbridge, R. *et al.* Biomarkers for depression: recent insights, current challenges and future prospects. Neuropsychiatr Dis Treat , 2017.

[313] Stroud, C. B. The stress sensitization model, The Oxford Handbook of Stress and Mental Health2018.

[314] Szyf, M. Nongenetic inheritance and transgenerational epigenetics. Mol Med 21:134–144, 2015.

[315] Taelman, J. *et al.* Influence of mental stress on heart rate and heart rate variability. In: 4th European conference of the international federation for medical and biological engineering, pp. 1366–1369, Springer2009.

[316] Tamura, T. *et al.* Wearable photoplethysmographic sensors—past and present. Electronics 3:282–302, 2014.

[317] Task Force of the European Society of Cardiology and the North American Society of Pacing and Electrophysiology. Heart rate variability: Standards of measurement, physiological interpretation, and clinical use. Eur Heart J 17:354–381, 1996.

[318] Taylor, E. W. *et al.* Central control of the cardiovascular and respiratory systems and their interactions in vertebrates. Physiol Rev 79:855–916, 1999.

[319] Taylor, W. D. *et al.* The vascular depression hypothesis: mechanisms linking vascular disease with depression. Mol Psychiatry 18:963–974, 2013.

[320] Teasdale, J. D. Cognitive vulnerability to persistent depression. Cogn & Emot 2:247–274, 1988.

[321] Terzano, C. *et al.* Atrial fibrillation in the acute, hypercapnic exacerbations of COPD. Eur Rev Med Pharmacol Sci 18:2908–2917, 2014.

[322] Thayer, J. F. *et al.* Heart rate variability, prefrontal neural function, and cognitive performance: the neurovisceral integration perspective on self-regulation, adaptation, and health. Ann Behav Med 37:141–153, 2009.

[323] Theiler, J. *et al.* Testing for nonlinearity in time series: the method of surrogate data. Physica D 58:77–94, 1992.

[324] Theorell, T. *et al.* A systematic review including meta-analysis of work environment and depressive symptoms. BMC public health 15:738, 2015.

[325] Tibshirani, R. Regression shrinkage and selection via the lasso. Journal of the Royal Statistical Society: Series B (Methodological) 58:267–288, 1996.

[326] Tipton, M. J. *et al.* The human ventilatory response to stress: rate or depth? J Physiol 595:5729–5752, 2017.

[327] Tonello, L. *et al.* The role of physical activity and heart rate variability for the control of work related stress. Front Physiol 5:67, 2014.

[328] Torrence, C. and G. P. Compo. A practical guide to wavelet analysis. Bull Am Meteorol Soc 79:61–78, 1998.

[329] Vaccarino, V. *et al.* Depression and coronary heart disease: 2018 position paper of the esc working group on coronary pathophysiology and microcirculation. Eur Heart J 41:1687–1696, 2020.

[330] Valderas, M. T. *et al.* Mutual information between heart rate variability and respiration for emotion characterization. Physiol Meas 40:084001, 2019.

[331] Valenza, G. *et al.* Oscillations of heart rate and respiration synchronize during affective visual stimulation. IEEE Trans Inf Technol Biomed 16:683–690, 2012.

[332] Valenza, G. *et al.* Instantaneous transfer entropy for the study of cardiovascular and cardiorespiratory nonstationary dynamics. IEEE Trans Biomed Eng 65:1077–1085, 2017.

[333] van Agtmaal, M. J. *et al.* Association of microvascular dysfunction with late-life depression: a systematic review and meta-analysis. JAMA psychiatry 74:729–739, 2017.

[334] van Gestel, A. J. *et al.* Autonomic dysfunction in patients with chronic obstructive pulmonary disease (COPD). J Thorac Dis 2:215, 2010.

[335] Van Milligen, B. P. *et al.* Wavelet bicoherence: a new turbulence analysis tool. Phys Plasmas 2:3017–3032, 1995.

[336] van Sloten, T. T. *et al.* Carotid artery stiffness and incident depressive symptoms: the paris prospective study III. Biol Psychiatry 85:498–505, 2019.

[337] Varon, C. and thers. A comparative study of ECG-derived respiration in ambulatory monitoring using the single-lead ECG. Sci Rep 10:1–14, 2020.

[338] Varon, C. *et al.* Unconstrained estimation of hrv indices after removing respiratory influences from heart rate. IEEE J Biomed Health Inform 23:2386–2397, 2018.

[339] Virtanen, R. *et al.* Reduced heart rate variability in hypertension: associations with lifestyle factors and plasma renin activity. J Hum Hypertens 17:171–179, 2003.

[340] Visted, E. *et al.* Emotion regulation in current and remitted depression: A systematic review and meta-analysis. Front Psychol 9:756, 2018.

[341] Vlachopoulos, C. *et al.* Acute mental stress has a prolonged unfavorable effect on arterial stiffness and wave reflections. Psychosom Med 68:231–237, 2006.

[342] von Wowern, E. *et al.* Digital photoplethysmography for assessment of arterial stiffness: repeatability and comparison with applanation tonometry. PloS One 10:e0135659, 2015.

[343] Voss, A. *et al.* Short-term heart rate variability—influence of gender and age in healthy subjects. PloS One 10, 2015.

[344] Walker, E. F. *et al.* Schizophrenia: a neural diathesis-stress model. Psychol Rev 104:667, 1997.

[345] Weiss, E. H. *et al.* An optimized method for the estimation of the respiratory rate from electrocardiographic signals: implications for estimating minute ventilation. Am J Physiol Heart Circ Physiol 307:H437–H447, 2014.

[346] Widjaja, D. *et al.* ECG-derived respiration: comparison and new measures for respiratory variability. In: 2010 Comput Cardiol, pp. 149–152, IEEE2010.

[347] Widjaja, D. *et al.* Separation of respiratory influences from the tachogram: a methodological evaluation. PloS One 9:e101713, 2014.

[348] Widjaja, D. *et al.* Cardiorespiratory information dynamics during mental arithmetic and sustained attention. PLoS One 10:e0129112, 2015.

[349] Willner, P. *et al.* The neurobiology of depression and antidepressant action. Neurosci Biobehav Rev 37:2331–2371, 2013.

[350] Witte, H. *et al.* Technique for the quantification of transient quadratic phase couplings between heart rate components. Biomed Eng 46:42–49, 2001.

[351] Wohleb, E. S. *et al.* Integrating neuroimmune systems in the neurobiology of depression. Nat Rev Neurosci 17:497, 2016.

[352] Wu, Y. *et al.* The relationship of depressive symptoms and functional and structural markers of subclinical atherosclerosis: A systematic review and meta-analysis. Eur J Prev Cardiol 25:706–716, 2018.

[353] Yap, J. Y. *et al.* Critical review of transcutaneous vagus nerve stimulation: Challenges for translation to clinical practice. Front Neurosci 14, 2020.

[354] Yousef, Q. *et al.* The analysis of PPG morphology: investigating the effects of aging on arterial compliance. Meas Sci Rev 12:266–271, 2012.

[355] Yuenyongchaiwat, K. *et al.* Symptoms of anxiety and depression are related to cardiovascular responses to active, but not passive, coping tasks. Braz. J. Psychiatry 39:110–117, 2017.

[356] Zalewski, P. *et al.* Cardiovascular and thermal response to dry-sauna exposure in healthy subjects. J Physiol 2014, 2014.

[357] Zamoscik, V. E. *et al.* Respiration pattern variability and related default mode network connectivity are altered in remitted depression. Psychol Med 48:2364–2374, 2018.

[358] Zanoli, L. *et al.* Arterial structure and function in inflammatory bowel disease. World J Gastroenterol 21:11304, 2015.

[359] Zhang, J. Effect of age and sex on heart rate variability in healthy subjects. J Manipulative Physiol Ther 30:374–379, 2007.

[360] Zhao, L. *et al.* Cardiorespiratory coupling analysis based on entropy and cross-entropy in distinguishing different depression stages. Front Physiol 10:359, 2019.

[361] Zoccal, D. B. *et al.* The nucleus of the solitary tract and the coordination of respiratory and sympathetic activities. Front Physiol 5:238, 2014.